EXPERIMENTAL AND THEORETICAL STUDY ON CAVITATION INCEPTION AND BUBBLY FLOW DYNAMICS

I. Design, Development and Operation of a Cavitation Susceptibility Meter

II. Linearized Dynamics of Bubbly and Cavitating Flows with Bubble Dynamics Effects

Thesis by

Luca d'Agostino

In Partial Fulfillment of the Requirements

for the Degree of

Doctor of Philosophy

California Institute of Technology

Pasadena, California

1987

(Submitted May 20, 1987)

ACKNOWLEDGEMENTS

It is in the nature of engineering experiments that many people collaborate to their completion. The present work is no exception in this respect and I am sincerely grateful to all of them, even if they are not mentioned here, for their contribution.

I feel particularly thankful to my advisor, Prof. A. J. Acosta, who stimulated, directed, encouraged and supported my efforts and displayed patience, appreciation and human understanding during the most difficult phases of my work.

I share the same feelings for Prof. C. E. Brennen who supervised the second part of this thesis. I am especially grateful to him for having been the first to display interest in my situation and to provide much needed guidance and encouragement during the crucial period at the beginning of my research.

I want to express my deep gratitude to Prof. Rolf Sabersky, who was my temporary – but much caring – advisor during my first year, and to Prof. Renzo Lazzeretti of the University of Pisa, Italy, for his role in securing the Rotary Award that brought me to Caltech in the first place.

Many of my former and current colleagues at Caltech have helped me in many ways; among them: Tim O'Hern, whom I directly collaborated with, and Eric Matthys, Harri Kytomäa, Enrique Geffroy, Scott Patton, Charlie Campbell, Joe Katz, with their suggestions and criticism.

I wish to acknowledge the blissful contribution of Joe Fontana in reviewing the machine design of the experimental apparatus, and the friendly assistance of Elton Daly, Rich Eastvedt and Leonard Montenegro of the W. M. Keck Laboratory of Hydraulics and Water Resources.

I thank very much Dr. Haskel Shapiro, Mr. Bob Kirkpatrick and their whole group for the design and implementation of the custom-made electronics of the experiment and for their caring, patient and prompt assistance during the

whole period of my research. I am also very grateful to Mr. John Lee, for his friendly help in solving electronic and data acquisition problems.

Several students have helped me at various stages during the course of my research and I would especially like to mention the effective collaboration of Olivier Jarrault, Raymond Moberly, Judy Goldish and Steve Ceccio.

I very much appreciated the financial support from the Rotary Foundation Educational Award for pursuing my M. S. degree during my first year at Caltech. Later, this research has been funded by the Office of Naval Research and by the Naval Sea Systems Command General Hydromechanics Research Program administered by the David W. Taylor Naval Ship Research and Development Center, whose support I gratefully acknowledge. Special thanks to Dr. T.T. Huang of DTNSRDC for his interest in this work.

I also would like to express my gratitude to my native country, Italy, which liberally provided for most of my formal education and showed its support during my studies at Caltech by granting me a 1982 and a 1985 North Atlantic Treaty Organization - Consiglio Nazionale delle Ricerche Fellowships for Technological Research.

I finally thank my parents. I regard this thesis as a tangible token of their lifelong efforts and ambitions.

TABLE OF CONTENTS

LIST OF FIGURES

30 bar (downward triangles) for $T = 20\,^{\circ}\mathrm{C}$ (water temperature) and $D_t = 1\,\mathrm{mm}$ (throat diameter).

Figure 2.9. Bubble detection length L_f necessary for a bubble to reach a detectable radius $R_f = 150\,\mu\mathrm{m}$ v/s equilibrium bubble radius R_o at various initial pressures: $p_o = 1\,\mathrm{bar}$ (squares), 10 bar (upward triangles) and 30 bar (downward triangles) for $T = 20\,^{\circ}\mathrm{C}$ (water temperature) and $D_t = 1\,\mathrm{mm}$ (throat diameter).

Figure 2.10. Volume flow rate q v/s equilibrium bubble radius R_o in water at various pressures: $p_o = 1$, 10 and 30 bar for $T = 20\,^{\circ}\mathrm{C}$ (water temperature) and $D_t = 1\,\mathrm{mm}$ (throat diameter).

Figure 2.11. Average cavitation event rate $\overline{\nu}_b$ v/s equilibrium bubble radius R_o in water at various pressures: $p_o = 1$, 10 and 30 bar for $D_t = 1\,\mathrm{mm}$ (throat diameter), $K_N = 0.001\,\mathrm{m}^{-1}$ (nuclei number distribution parameter) and $T = 20\,^{\circ}\mathrm{C}$ (water temperature).

Figure 2.12. Sampling time t_s v/s equilibrium bubble radius R_o in water at various pressures: $p_o = 1$, 10 and 30 bar. Here $\varepsilon = 0.20$ (estimated relative r.m.s. error of the cavitation event rate), $D_t = 1\,\mathrm{mm}$ (throat diameter), $T = 20\,^{\circ}\mathrm{C}$ (water temperature) and $K_N = 0.001\,\mathrm{m}^{-1}$ (nuclei number distribution parameter).

Figure 2.13. Liquid sample volume V_s v/s bubble equilibrium radius R_o in water at $p_o = 1\,\mathrm{bar}$ and $T = 20\,^{\circ}\mathrm{C}$ for $K_N = 0.001\,\mathrm{m}^{-1}$ (nuclei number distribution parameter) and various values of the estimated relative r.m.s. error of the cavitation event rate: $\varepsilon = 0.01$, 0.05 and 0.20.

Figure 2.14. Duct shape of prototype CSM venturi in normalized coordinates $2x/D_i$ (axial) and $D(x)/D_i$ (radial) with: $D_i = 10\,\mathrm{mm}$ (throat diameter),

$C_c = 1/100$ (contraction ratio) and $\beta_d = 0.76$ deg (diffuser semi-aperture angle). The lenghts of the various sections are: $L_i = 11.4$ mm (inlet), $L_c = 10.4$ mm (contraction), $L_t = 7.7$ mm (throat), $L_d = 10.4$ mm (diffuser).

Figure 2.15. Relative displacement thickness, $2\delta^*/D(x)$, and momentum thickness, $2\theta/D(x)$, v/s normalized axial coordinate $2x/D_i$ in the laminar venturi of Fig. 2.14 for $Re_i = 1400$ (inlet Reynolds number).

Figure 2.16. Pressure coefficient $C_p = 2(p - p_i)/\rho u_i^2$ at the venturi centerline v/s normalized axial coodinate $2x/D_i$ for the venturi of Fig. 2.14.

Figure 2.17. Stratford's laminar separation criterion S_c and Thwaites' shear and shape correlation parameter $\lambda = \theta^2 U'/\nu$ v/s normalized axial coordinate $2x/D_i$, for the venturi of Fig. 2.14. Laminar separation is predicted when S_c drops to zero or $\lambda \simeq -0.09$.

Figure 2.18. Maximum nominal diameter ratio $D(x)/D_t$ theoretically attainable according to Stratford's criterion in the diffuser of the venturi of Fig. 2.14 without incurring in laminar separation as a function of the distance x from the diffuser inlet.

Figure 3.1. Schematic of the CSM optical components (dimensions in mm). Continuous wave laser (L), beam displacer (BD), beamsplitter cube (BS), telescopic relay lenses (L1 and L2), focusing and receiving lens (L3), venturi tube (V), front surface mirror (M) with slit for transmission of laser beams, photomultiplier collimating lens (L4), field stop aperture (FS), photomultiplier tube (PM).

Figure 4.1. General view of the CSM experimental apparatus. In the foreground on the right: the I-beams supporting the laser and the baseplate where

most of the optical and fluidic components are mounted. In the background: the electronic instrumentation rack (left) and the data acquisition computer (center).

Figure 4.2. Schematic of the various components of the CSM experimental apparatus: water inlet (WI), sampling valve (SV), upstream pressure transducer (UPT), venturi tube (VT), exhaust valve (EV), exhaust tank (ET), regulated air pressure line (RA), return valve (RV), water return (WR), laser Doppler velocimeter (LDV).

Figure 4.3. Schematic of the CSM fluidic circuits: mercury barometer (B), bleed valve (BV), compressed air supply (CA), constant level tank (CLT), exhaust valve (EV), exhaust tank (ET), exhaust pressure valve (EPV), exhaust pressure regulator (EPR), air filter (AF), high pressure regulator (HPR), needle valve (NV), pressure gage (PG), return valve (RV), three-way sampling valve (SV), vacuum gage (VG), vacuum pump (VP), vacuum reservoir (VR), venturi tube (VT), three-way valve (V3), four-way valve (V4), water inlet (WI), water return (WR), water trap (WT).

Figure 4.4. Machine drawing of the CSM optical lay-out, top and side views: laser (1) on its mount (2), beam displacer (3) on its micrometric side translation stage (4), beamsplitter cube (5), lenses (6 and 8) of the telescopic relay (7), front surface mirror (9), longitudinal translation stage (10) of the focusing and receiving lens (13), transverse translation stage (14) of the venturi tube mount (15), inlet (16) and outlet (19) lines of the venturi tube (18), pressure tap (17), photomultiplier collimating lens (20), mount (21) of the field stop aperture (22), photomultplier (23).

Figure 4.5. General view of the CSM optical set-up. The optical components are mounted on the baseplate in the center, while most of the fluidic components

are mounted below it. The laser installed on its positionable mount on the longitudinal I-beam is barely visible on the left edge of the picture.

Figure 4.6. Close-up view of CSM venturi tube No. 1. A cylindrical shell of cast transparent resin contains the glass-blown venturi tube for mechanical protection and easy installation. The contraction ratio of the tube is about 1/100, the throat diameter is about 1 mm and the exit diameter is about 1.2 mm.

Figure 4.7. Close-up view of CSM venturi tube No. 2. This blown-glass venturi has thicker walls, a contraction ratio of about 1/100, a throat diameter of about 1 mm, a long straight section after the diffuser and an exhaust diameter of about 1.2 mm.

Figure 4.8. Detailed view of the CSM venturi tube No. 2 installed in its positionable mount at the LDV focal point. On the left: the pressure tap connection from the inlet water line to the upstream pressure transducer mounted below the baseplate. On the bottom right corner of the picture is the exhaust valve mounted on the venturi outlet water line.

Figure 4.9. Block diagram of the information flow in the CSM Signal Processor.

Figure 4.10. Close-up view of the CSM Signal Processor in its slide-mounted drawer. The modular bus frame contains three electronic boards wired to the front panel commands, controls and I/O connectors. On the right inside the drawer is the unit's DC power supply.

Figure 4.11. The CSM electronic rack, on the left. From the top to the bottom: the digital multimeter, the pressure transducer exciter and amplifier, the laser power supply, the oscilloscope, the electronic filters, the CSM Signal Processor, the photomultiplier power supply. Also shown in the picture: the

Figure 7.2. Cavitation-separation of a tap water sample initially at atmospheric pressure in the CSM venturi tube No. 2. The flow is from left to right. The cavitation-separation bubble originates in the diffuser and terminates in the exit section without reaching the exhaust. The exhaust pressure is about 5000 Pa and the throat velocity about 13.5 m/s.

Figure 7.3. Histogram chart of the observed density distribution of time intervals between cavitation events in resonant cavitation conditions in the CSM venturi tube No. 1. The continuous line indicates the expected (Poissonian) distribution corresponding to the observed value of the average arrival rate.

Figure 7.4. Travelling bubble cavitation of a tap water sample initially at atmospheric pressure in the CSM venturi tube No. 1. The flow is from right to left. The throat pressure is about -15 kPa and the throat velocity about 14.8 m/s.

Figure 7.5. Travelling bubble cavitation of a tap water sample initially at atmospheric pressure in the CSM venturi tube No. 2. The flow is from left ot right. The throat pressure is about -15 kPa and the throat velocity about 14.8 m/s.

Figure 7.6. Zero crossing data N_{zc} as a function of the data index I in a typical CSM run. The data refer to a tap water sample with the following initial properties: initial pressure $p_o = 1$ atm, temperature $T = 21\,^{\circ}$C and air content $\alpha = 20.5$ ppm. The throat pressure and velocity are: $p_t = -15$ kPa, $u_t = 14.8$ m/s.

Figure 7.7. Doppler frequency data f_D as a function of the data index I in a typical CSM run. The data refer to the tap water sample of Fig. 7.6: initial

pressure $p_o = 1\,\text{atm}$, temperature $T = 21\,^\circ\text{C}$, air content $\alpha = 20.5\,\text{ppm}$, throat pressure $p_t = -15\,\text{kPa}$ and throat velocity $u_t = 14.8\,\text{m/s}$.

Figure 7.8. Upstream pressure data p_u as a function of the data index I in a typical CSM run. The data refer to the tap water sample of Fig. 7.6: initial pressure $p_o = 1\,\text{atm}$, temperature $T = 21\,^\circ\text{C}$, air content $\alpha = 20.5\,\text{ppm}$, throat pressure $p_t = -15\,\text{kPa}$ and throat velocity $u_t = 14.8\,\text{m/s}$.

Figure 7.9. Filtered Doppler frequency data f_D as a function of the data index I in a typical CSM run. The data refer to the tap water sample of Fig. 7.6: initial pressure $p_o = 1\,\text{atm}$, temperature $T = 21\,^\circ\text{C}$, air content $\alpha = 20.5\,\text{ppm}$, throat pressure $p_t = -15\,\text{kPa}$ and throat velocity $u_t = 14.8\,\text{m/s}$. Readings deviating from the mean more than three standard deviations have been eliminated.

Figure 7.10. Histogram chart of the observed distribution of filtered throat velocity data compared to the Gaussian distribution (solid line) of equal mean and standard deviation in a typical CSM run. The data refer to the tap water sample of Fig. 7.6: initial pressure $p_o = 1\,\text{atm}$, temperature $T = 21\,^\circ\text{C}$, air content $\alpha = 20.5\,\text{ppm}$, throat pressure $p_t = -15\,\text{kPa}$ and throat velocity $u_t = 14.8\,\text{m/s}$. Readings deviating from the mean more than three standard deviations have been eliminated.

Figure 7.11. Arrival time data T_p of velocity tracers (particles) as a function of the data index I in a typical CSM run. The data refer to the tap water sample of Fig. 7.6: initial pressure $p_o = 1\,\text{atm}$, temperature $T = 21\,^\circ\text{C}$, air content $\alpha = 20.5\,\text{ppm}$, throat pressure $p_t = -15\,\text{kPa}$ and throat velocity $u_t = 14.8\,\text{m/s}$.

Figure 7.12. Arrival time data T_b of cavitation events (bubbles) as a function of the data index I in a typical CSM run. The data refer to the tap water sample

Figure 7.19. Cavitating nuclei concentration $n(p_t)$ measured by the CSM as a function of the venturi throat pressure p_t in a sample of tap water with temperature $T = 21\,^{\circ}\mathrm{C}$ and air content $\alpha = 20.8\,\mathrm{ppm}$.

Figure 7.20. Standard deviation of the throat velocity data σ_{u_t} as a function of the throat pressure p_t in the tap water sample of Fig. 7.17 with temperature $T = 21\,^{\circ}\mathrm{C}$ and air content $\alpha = 20.8\,\mathrm{ppm}$.

Figure 7.21. Average arrival time interval between cavitating nuclei $\overline{\tau}_b$ as a function of the throat pressure p_t in the tap water sample of Fig. 7.17: temperature $T = 21\,^{\circ}\mathrm{C}$ and air content $\alpha = 20.8\,\mathrm{ppm}$.

ABSTRACT

The first and main part of this work presents the design, development and operation of a Cavitation Susceptibility Meter based on the use of a venturi tube for the measurement of the content of active cavitation nuclei in water samples. The pressure at the venturi throat is determined from the upstream pressure and the local flow velocity without corrections for viscous effects because the flow possesses a laminar potential core in all operational conditions. The detection of cavitation and the measurement of the flow velocity are carried out optically. The apparatus comprises a Laser Doppler Velocimeter for the measurement of the flow velocity and the detection of cavitation, a custom-made electronic Signal Processor for real time generation and temporary storage of the data and a computerized system for the final acquisition and reduction of the collected data. The various steps and considerations leading to the present design concept are discussed in detail and the implementation of the whole system is described in order to provide the all the information necessary for its calibration and operation. Finally, the results of application of the Cavitation Susceptibility Meter to the measurement of the water quality of tap water samples are presented and critically discussed with reference to other similar or alternative methods of cavitation nuclei detection and to the current state of knowledge on cavitation inception.

The second part of the present work presents the results of an investigation on the linearized dynamics of two-phase bubbly flows with the inclusion of bubble dynamics effects. Two flow configurations have been studied: the time dependent one-dimensional flow of a spherical bubble cloud subject to harmonic excitation of the far field external pressure and the steady state two-dimensional flow of a bubbly mixture on a slender profile of arbitrary shape. The inclusion of bubble dynamic damping and of the relative motion between the two phases and the extension of the results to the case of arbitrary excitation are discussed when examining the second flow configuration. The simple linearized dynamical

analysis developed so far clearly demonstrates the importance of the complex phenomena connected to the interaction of the dynamics of the bubbles with the flow and provides an introduction to the study of the same flows with non-linear bubble dynamics.

NOMENCLATURE

Symbols

A	cross-sectional area
$A(x)$	venturi cross-sectional area at location x
A_e	venturi exit cross-sectional area
A_i	venturi inlet cross-sectional area
A_m	venturi cross-sectional area at LDV measuring section
A_t	venturi throat cross-sectional area
A_1	barometer tube cross-sectional area
A_2	barometer pot cross-sectional area
c	sonic speed
C_c	venturi contraction coefficient
C_e	venturi expansion coefficient
C_p	pressure coefficient
C_{pe}	exhaust pressure coefficient
d_x	LDV probe volume diameter in the x direction
d_y	LDV probe volume diameter in the y direction
d_z	LDV probe volume diameter in the z direction
D	diameter, venturi diameter
$D(x)$	venturi diameter at location x
D_e	venturi exit diameter
D_i	venturi inlet diameter
D_m	venturi diameter at LDV measuring section
D_t	venturi throat diameter
E_i	i-th expected frequency
f	frequency, focal length
f_D	Doppler frequency or its data value
$\overline{f}_D$	average of Doppler frequency data

F_c	data filtering criterion in standard deviations from the mean
K_N	nuclei number distribution parameter
L	length
L_d	length of the venturi diffuser section
L_e	length of the venturi exit section
L_f	detection length of a bubble or cavitation nucleus
L_i	length of the venturi inlet section
L_t	length of the venturi throat section
m	index of refraction
M	number of data groups
n	integer index
$n(p_t)$	concentration of nuclei with critical pressure not smaller than p_t
$n(R_o)$	concentration of nuclei with radius not smaller than R_o
N_b	number of cavitation events or bubbles
N_{fr}	number of fringes
N_p	number of velocity tracers or particles
$N(R_o)$	nuclei number concentration density distribution
N_{zc}	number of zero crossings
$N_{zc_{min}}$	minimum number of zero crossings
O_i	i-th observed frequency
p	pressure
p_b	bubble internal pressure
p_e	venturi exhaust pressure
p_i	venturi inlet pressure
p_o	reference equilibrium pressure
p_t	venturi throat pressure or its reading
$\overline{p}_t$	average of venturi throat pressure data
p_u	venturi upstream pressure or its reading
$\overline{p}_u$	average of venturi upstream pressure data
p_v	vapor pressure

Pr	probability
q	volume flux, Gaussian beam complex parameter
q_i	volume flux in the venturi inlet
q_e	volume flux in the venturi exit
r	radial coordinate
R	radius of a bubble or cavitation nucleus
R_f	detection radius radius of a bubble or cavitation nucleus
R_f	radius of curvature of the laser beam at the LDV focal point
R_m	radius of venturi tube at the LDV measuring section
R_o	bubble reference radius
Re	Reynolds number
Re_i	Reynolds number at the venturi inlet
s	spatial semi-separation, LDV beams semi-separation
s_{fr}	fringe spacing
S	surface tension
t	time
t_f	detection time of a bubble or cavitation nucleus
t_s	sampling time
T	period, temperature
T_b	arrival time of a cavitation event or bubble
T_g	Doppler gate time
T_p	arrival time of a velocity tracer or particle
u	velocity
u_e	venturi exhaust flow velocity
u_i	venturi inlet flow velocity
u_m	venturi measured flow velocity
$\overline{u}_m$	average of venturi measured flow velocity data
u_t	venturi throat flow velocity or throat flow velocity reading
$\overline{u}_t$	average of venturi throat flow velocity data
U	velocity component measured by the LDV

V	volume
V_s	sample volume
V_t	venturi throat volume
w	radius of the laser beam
w_f	radius of the laser beam at the LDV focal point
w_o	waist radius of the laser beam
x	venturi axial coordinate
y	coordinate in the direction of the LDV main optical axis
y_1	barometer's upper mercury level
y_2	barometer's lower mercury level
z	vertical coordinate
α	void fraction, dissolved air content
α_{Al}	linear thermal expansion coefficient of aluminum
α_{Hg}	volumetric thermal expansion coefficient of mercury
β	nuclei interference probability
β_d	semi-aperture angle of the venturi diffuser
$\delta(x - x_o)$	Dirac function centered at x_o
δ_{BL}	boundary layer thickness
δ^*	displacement boundary layer thickness
ε	error
θ	momentum boundary layer thickness
λ	wave length of LDV laser beams
λ_o	wave length of LDV laser beams in air
ν	kinematic viscosity
$\overline{\nu}_b$	mean cavitation event rate
ρ	water density
ρ_{Al}	aluminum density
ρ_{Hg}	mercury density
σ	standard deviation

σ^2	variance
σ_{f_D}	standard deviation of Doppler frequency data
$\sigma_{\overline{f}_D}$	standard deviation of average Doppler frequency
σ_{p_t}	standard deviation of throat pressure data
$\sigma_{\overline{p}_t}$	standard deviation of average throat pressure
σ_{p_u}	standard deviation of upstream pressure data
$\sigma_{\overline{p}_u}$	standard deviation of average upstream pressure
σ_n	standard deviation of unstable cavitation nuclei
σ_{u_m}	standard deviation of measured velocity data
$\sigma_{\overline{u}_m}$	standard deviation of average measured velocity
σ_{u_t}	standard deviation of throat velocity data
$\sigma_{\overline{u}_t}$	standard deviation of average throat velocity
σ_{χ^2}	standard deviation of χ^2 parameter
$\overline{\tau}_b$	mean time between cavitation events
φ	semi-aperture angle of the LDV beams in air
χ^2	χ^2 parameter for χ^2 test of agreement
$\overline{\chi^2}$	expected value of χ^2 parameter
ξ	Poisson distribution parameter

Subscripts

b	bubble or cavitation event
c	venturi tube contraction
cr	critical
d	venturi tube diffuser
e	venturi tube exhaust
i	venturi tube inlet
m	venturi tube LDV measuring section
o	reference conditions
p	particle or velocity tracer
t	venturi tube throat

v	vapor
zc	zero crossing

Acronyms

BAC	Bubble Address Counter
CSM	Cavitation Susceptibility Meter
EPS	Enable Particle Stuff signal
ETC	Elapsed Time Counter
GT	particle Gate Time
LDV	Laser Doppler Velocimetr
PDC	Particle Duration Counter
PAC	Particle Address Counter
ZC	gated Zero Crossing pulse train
ZCC	Zero Crossing Counter

Part I

DESIGN, DEVELOPMENT AND OPERATION OF A CAVITATION SUSCEPTIBILITY METER

Chapter 1. INTRODUCTION

Early studies have shown [Knapp et al., 1970] that the maximum tensile strength that liquids can sustain is considerably reduced by the presence of weak spots, generically called "nuclei". Although their nature has not yet been fully understood, it has been recognized that small gas bubbles [Plesset, 1969], certain types of solid impurities, and gas pockets contained inside crevices and cracks of a liquid-solid interface [Harvey et al., 1947] are nuclei, since they act as preferred points for the onset of liquid rupture [Holl, 1970].

The presence of nuclei is considerably important in many flows of technical interest, where they are responsible for originating or variously modifying the occurrence of cavitation, a generally undesired phenomenon which severely limits the performances of hydraulic operating machinery [Arndt, 1981]. In this respect the concentration of nuclei which become unstable at a given level of tension is therefore a fundamental parameter in the attempt to predict the onset of cavitation, to model its development and to deduce scaling laws capable to extend the results obtained from model tests to full-scale operation.

The effect of the presence of nuclei inside liquids is not limited to cavitation. Inhomogeneities and, in particular, micro-bubbles, considerably change the optical and acoustical properties of liquids in a way which also depends in general on their concentration and size distribution [van Wijngäarden, 1972]. Such phenomena, as well as cavitation, are of great practical importance in many technological applications of underwater acoustics [Apfel, 1984; Akulichev and Ilychev, 1986] and optics. The presence of bubbles and particles in natural waters is also of interest in various fields of geophysics and biology.

Therefore significant efforts have been made in developing methods to detect nuclei contained inside liquids, whose effects usually dominate the ones due to the nuclei localized at the flow boundaries. The various techniques currently developed for the measurement of cavitation nuclei have been recently reviewed by Billet, 1986 a, 1985.

Some methods, such as photography or holography, which produce a recorded image of a sample volume in the liquid, allow one to detect nuclei whose size is larger than about 10 μm (holography) or even 2 μm (photography), depending on the resolution of the optical system. They also can safely discriminate between bubbles and particles, but have the disadvantage that results are not immediately and continuously available because the analysis of the obtained data requires a considerable time [Feldberg, 1973; Gates, 1978], unless complex but not very reliable image analysis automated techniques are used [Hentschel et al., 1984].

Other methods, based on the measurement of acoustical or optical radiation scattered by the nuclei [Keller, 1972], can operate continuously providing results which are readily available, but do not allow one to safely distinguish between bubbles and particles, unless all bubbles are known to be nearly spherical. For satisfactory operation, a careful calibration using a liquid sample of known characteristics is needed. Non-uniform illumination and finite size of the scattering volume also generate systematic errors which are difficult to take into account. Besides, when particles are prevalent, considerable uncertainty is introduced by the fact that both their shape and index of refraction are unknown.

Similar problems are also encountered when the content of particulates and microbubbles in water samples is monitored electrically using Coulter Counters [Oba et al., 1981]. These instruments measure the volume of cavitation nuclei from the amplitude of the electrical perturbation they produce passing through a small orifice in a conducting liquid. The uncertainty in this case lies in the fact that the nuclei electrical properties necessary to deduce the nuclei volume are generally unknown and that no information is anyway provided by Coulter Counters on the nature of the nuclei themselves. Coulter Counters have also been extensively used in monitoring the particulate content of ocean waters [Sheldon et al., 1972; Carder et al., 1971; Thorpe, 1982], with little concern on the above limitations of these instruments when used to monitor particles of unknown electrical properties.

The development of a field test for the holographic determination of cavitation nuclei content in ocean waters as a part of a wider ongoing investigation on cavitation inception at Caltech provided a good opportunity to assess the importance of these limitations. Holographic and Coulter Counter techniques were jointly used to measure the concentration density distribution of cavitation nuclei in the ocean. The results of this study are documented and discussed in detail in Appendix 3. In general discrepancies by up to an order of magnitude have been found between the nuclei number concentration density distribution deduced from holographic observation and the one measured using the Coulter Counter. Clearly holography is the most reliable of the two nuclei detection methods. Therefore the results of Appendix 3 confirm that Coulter Counters can be affected by significant errors in the determination of the nuclei size distribution.

Bubbles in liquids can also be detected from the large attenuation experienced by acoustical radiation which resonates with the bubble natural frequency of oscillation [Medwin, 1970, 1977]. Detection systems based on this concept do not require long times for data analysis, but are unable to detect particles and need comparatively large and homogeneous sample volumes.

For the purpose of cavitation research a common disadvantage of all the above methods is that only size distribution and concentration of the nuclei are measured. The value of the critical tension that makes each nucleus unstable, as required for cavitation studies, must therefore be deduced indirectly from size measurements, which can be done only in the case of micro-bubbles. Solid particles, when detected and recognized, can be included or not in the measurement of nuclei concentration, but no information is provided about their critical tension, yet it is known that only part of the solid particulates are active as cavitation nuclei. To overcome these difficulties, cavitation events occurring in a known pressure field can be detected and counted. When applied to bodies of standardized form and size, this method has indeed the advantage of providing a direct measurement. However, since many nuclei are simultaneously exposed

to the tension, the response of the weakest ones inevitably dominates the flow, so that only cavitation susceptibility evaluations can be obtained.

Recently Oldenziel [1982a, 1982b, 1982c] proposed a new instrument, the Cavitation Susceptibility Meter (CSM), in which the internal flow of a liquid through a glass venturi is used to induce cavitation at the throat and bubbles are detected optically. The CSM developed at Neyrtec [Le Goff et al., 1983] is based on the same principle, but it utilizes a stainless steel venturi, where cavitation bubbles are counted by recording the noise generated by their collaspe in the diffuser downstream the throat section [Lecoffre and Bonnin, 1979]. In both these applications the flow in the venturi is turbulent due to the relatively high velocity in the inlet line before the throat section. In CSM's the effects of mutual interference between cavitating nuclei can be reduced by decreasing the size the cavitation region. Therefore venturi systems can determine the concentration of unstable nuclei as a function of the applied tension from the observed number of cavitation events and the measurement of the sampled volume of liquid. Cavitation observations in restricted flows using electrical and optical detection have also been recently reported in the literature [Oba and Ito, 1980], [Oba et al., 1979], [Ito and Oba, 1980], although not with the specific purpose of measuring the liquid quality of the sample.

Various methods to monitor the cavitation nuclei population of water samples, including the above two CSM's, have been recently compared together at Delft Hydraulics Laboratory [Godefroy et al., 1981]. The results confirm that C.S.M.'s can reliably measure the critical tension of the weakest nuclei and their concentration up to a maximum of the order of $10\,\mathrm{cm}^{-3}$, after which the venturi throat becomes saturated with bubbles and the flow chokes. Reportedly the Neyrtec system can also measure the nuclei critical pressure in the range 0 to -2 bar without significant saturation effects, provided that the concentration of unstable nuclei does not exceed about $1\,\mathrm{cm}^{-3}$. Nevertheless such low values of the pressure correspond to bubbles having an equilibrium radius between $0.1\,\mu\mathrm{m}$ and $1\,\mu\mathrm{m}$, whose concentration in most water samples is expected to be consid-

erably larger than $1\,cm^{-3}$. Therefore it appears that, during operation in these conditions, several unstable nuclei are simultaneously present in the cavitation region of the CSM. When this happens, the pressure in the throat increases significantly with respect to its nominal steady state non-caviating value. The CSM is then partially saturated and the actual range over which reliable measurements of both the nuclei critical tension and concentration are possible is significantly reduced.

The Cavitation Susceptibility Meter developed at Neyrtec is described in detail by Shen, Gowing and Pierce, 1984, and has been extensively used in conjuction with light scattering nuclei detection to monitor the cavitation nuclei content in natural and laboratory waters [Shen et al., 1986]. Also in this case nuclei critical pressures as low as -1.7 bar have been reported. The possible occurrence of scaling effects in the operation of this venturi system due to Reynolds number effects is discussed in [Shen and Gowing, 1985], and the relationships of cavitation inception to the flow perturbations due to the dynamics of one or more bubbles in the venturi are examined by [Chaine and Shen, 1986].

On the basis of the available operational experience Cavitation Susceptibility Meters are not free from problems apart from saturation effects. All previous investigators in this research area, for example, reported the intermittent occurrence of separation in the diffuser of the venturi tube even in the presence of turbulent flow. In addition, sheet cavitation at the throat has also been occasionally observed. Yet, when compared to other techniques, CSM's seem to have several attractive features:

- they provide a direct measure of both the nuclei critical tension and concentration, thus eliminating the problem of the uncertain behaviour of particles as cavitation nuclei;
- data analysis only requires a comparatively short time, so that the liquid quality measurement can be carried out in an almost continuous way;
- there is no limitation on the size of the smallest detectable nuclei.

Despite their limitations CSM's seem to be promising devices in cavitation research. In the next chapter the principles of CSM operation are analyzed and those considerations are presented which are mostly relevant to their design.

Chapter 2. CSM OPERATION ANALYSIS

2.1. General Approach

The configuration of the axisymmetric CSM venturi pipe considered in the present study is shown in Fig. 2.1. The flow originates from the far field on the left (subscript o), representing the sampled liquid, through the venturi inlet to the exhaust region on the right. Both the upstream and downstream conditions are supposed to be independent on time t. Let x and r be the space coordinates along the venturi centerline and in the radial direction. A volume flux $q(t)$ of liquid with density ρ and kinematic viscosity ν flows with axial velocity $u(x,r,t)$ and radial velocity $v(x,r,t)$ through the venturi duct of local diameter $D(x)$ and cross-sectional area $A(x) = \pi D(x)^2/4$, divided in five segments: a cylindrical inlet (subscript i), a contraction (subscript c), a cylindrical throat (subscript t), a diffuser (subscript d) and a cylindrical exhaust (subscript e). The length L of each segment of the duct is shown in the same figure; the inlet contraction area ratio is: $C_c = A_t/A_i$ and the diffuser expansion area ratio is: $C_e = A_e/A_t$.

The main parameters used to describe the overall performance of CSM's are shown in the block diagram of Fig. 2.2. The existence of functional relations between two parameters is indicated by arrows connecting the two corresponding blocks. The nature of these relations will be discussed in detail later. Some of the parameters in the diagram represent given data, some can be considered as independent requirements and some as resulting or dependent factors. However, the subdivision in such categories is somewhat arbitrary, since it depends on the view point chose to approach the whole problem of CSM design. The one implicitly adopted in the present anlysis can be summarized as follows:

- it is assumed that the sample initial conditions and properties are given;
- a nuclei number distribution (i.e. the liquid quality) of the sample is postulated, which is generally representative of typical water samples of technological interest;

- for simplicity all the nuclei are supposed to be gas bubbles with equilibrium radius equal to their size;
- the most important relationships among the CSM parameters are investigated;
- the main conditions are deduced for the measurement of unstable nuclei concentration to be possible over the assigned nuclei radius range with the required precision.

This point of view is particularly useful for design orientation. On the other hand, for performance assessment of a given design, the obtainable precision in the measurement of unstable nuclei concentration over a certain radius range is the result of the specific CSM geometry and can also be analyzed with the methods contained herein.

2.2. Liquid Quality and Critical Tension

In cavitation research literature the liquid quality of a sample is usually expressed by means of the nuclei number concentration density distribution: $N(R_o) = -dn(R_o)/dR_o$, where $n(R_o)$ is the number concentration of nuclei whose equilibrium radius is not smaller than R_o. The nuclei number distributions of water samples of technological interest spread in practice over a very large range and in most cases approximatively follow a hypergeometric distribution [Bader, 1970]. Here, for simplicity, we assume $N(R_o) = K_N/R_o^3$, with $K_N = 10^{-3}\,\mathrm{m}^{-1}$. This value is generally representative of the data from technical waters reported in the literature for the radius range from 10 to 100 μm considered in this analysis. However, errors by an order of magnitude on both sides are quite possible in practice because of the large dispersion of liquid quality data reported in the literature. From the above assumption it follows that:

$$n(R_o) = \frac{K_N}{2R_o^2} \tag{2.1}$$

In order to relate the nuclei number distribution to the corresponding critical pressure, we make use of the hypothesis that all the nuclei consist of equilibrium

gas bubbles, for which the critical tension with respect to dynamic stability [Knapp et al., 1970] is expressed by:

$$(p_v - p)_{cr} = \frac{4S}{3R_o}\left[3\left(1 + \frac{p_o - p_v}{2S/R_o}\right)\right]^{-1/2} \tag{2.2}$$

where p_o and R_o are the equilibrium pressure and radius of the bubble, p_v is the vapor pressure and S the surface tension (see Fig. 2.3). The corresponding "critical" velocity at the venturi throat deduced from ideal, incompressible, one-dimensional, steady flow calculations is shown in Fig. 2.4. Similarly, the exhaust pressure coefficient $C_{pe} = (p_e - p_v)/(p_o - p_v)$ is plotted in Fig. 2.5 for the case $p_o = 1\,\text{bar}$ and various expansion ratios. When the equilibrium pressure p_o increases, the C_{pe} curves shift to the left in the diagram.

Note that the critical tensions of bubbles in the radius range of interest from 10 to 100 μm are quite small. Also note, on the other hand, that in the same range the radius of marginally stable bubbles (critical radius) is a very sensitive function of the applied tension. These facts have several important (and unfortunate) consequences for the design of CSM's. The first is that it is virtually impossible to measure these small pressures at the throat because of inadequate sensitivity and, if done intrusively, separation and/or cavitation would surely be induced in such an extremely unstable flow. The second is that the throat pressure must be evaluated accurately to avoid large errors in the determination of the nuclei number distribution. A third consequence has to do with the problem of regulating the flow. Since the pressure upstream cannot be changed without seriously affecting the sample and therefore interfering with the liquid quality measurement, this must be done by varying the exhaust pressure. The curves of Fig. 2.5 deduced for $p_o = 1\,\text{bar}$ show that very low sensitivity is obtained, unless diffusers with a very small expansion ratio are used. Besides, due to the shift of the curves to the left when the equilibrium pressure p_o increases, the same sensitivity cannot be achieved throughout the radius range of interest with the same diffuser geometry.

2.3. Saturation and Throat Section Volume

As pointed out briefly in the introduction, the problem of saturation poses a significant limitation to the operation of CSM's. It also introduces a systematic error, since the unsteady pressure perturbations due to the presence of a growing or collapsing bubble in the cavitation region of the CSM can prevent the normal growth of other neighbouring nuclei. To control such an error the probability of finding more than one unstable nucleus in the throat volume V_t of the CSM must be minimized. When the nuclei concentration is uniform, the occurrence of N_b unstable nuclei in V_t is expected to follow the Poisson distribution:

$$Pr(N_b) = \frac{\xi^{N_b}}{N_b!} e^{-\xi} \tag{2.3}$$

where $\xi = n(R_o)V_t$ is the average number of unstable nuclei in V_t. Therefore the cumulative probability of observing two or more unstable nuclei in V_t (bubble interaction probability, see Fig. 2.6) is:

$$\beta = 1 - Pr(0) - Pr(1) = 1 - (1 + \xi)e^{-\xi} \tag{2.4}$$

It is now possible to express the throat volume of the CSM as a function of the equilibrium bubble radius and of the bubble interference probability. The results of Fig. 2.7 show that in the radius range from 10 to 100 μm the volume of the throat section of the CSM should not exceed about 100 mm^3 if the interference error is to be reduced to an acceptable level, say less than 20%. In this respect a throat diameter of 1 mm ca. appears to be both feasible and adequate, therefore further considerations and analysis are based on such a choice.

2.4. Bubble Dynamic Response and Throat Section Geometry

The problem of the response of an isolated bubble in the throat of the CSM is now approached. The solution of such a problem is expressed in terms of the detection time t_f and detection length L_f, respectively defined as the time and the length necessary for the bubble to grow from its initial size R_o

to a final detectable radius R_f. The choice of the final radius R_f is somewhat arbitrary, since it clearly depends on the sensitivity of the method used to detect cavitation. The solution of the above problem provides a way to estimate the minimum necessary length of the throat volume, thus completing its geometrical definition.

A number of assumptions are made in order to construct a simplified set of equations which nevertheless models the interactions between the bubble and the liquid. First the flow is supposed to be one-dimensional, ideal, incompressible and the relative motion of the bubble with respect to the surrounding liquid is neglected. The bubble, moving along the centerline of the duct with istantaneous position $x_b(t)$, remains spherical and its radius $R(t)$ is determined by the Rayleigh-Plesset equation [Plesset and Prosperetti, 1977; Knapp, Daily and Hammit, 1970]:

$$p_v - p_b = \rho \left[R\frac{d^2R}{dt^2} + \frac{3}{2}\left(\frac{dR}{dt}\right)^2 \right] - p_g \left(\frac{R_o}{R}\right)^3 + \frac{2S}{R} \tag{2.5}$$

where S is the surface tension and diffusive and thermal effects are neglected, i.e. p_v and p_g are constant. Here p_b is the external pressure driving the bubble volume changes and it is assumed to be equal to the pressure of the liquid in the proximity of the bubble. Then, from the continuity and unsteady Bernoulli's equations for the inlet flow upstream of the bubble (subscript i) and the exit flow downstream of the bubble (subscript e):

$$q_i - q_b + 2\pi R^2 \frac{dR}{dt} = 0 \tag{2.6}$$

$$q_e - q_b - 2\pi R^2 \frac{dR}{dt} = 0 \tag{2.7}$$

$$-I_i \frac{dq_i}{dt} + \frac{p_i - p_b}{\rho} - \frac{1}{2}\frac{q_b^2}{A_b^2} = 0 \tag{2.8}$$

$$-I_e \frac{dq_e}{dt} + \frac{p_b - p_e}{\rho} + \frac{1}{2}\frac{q_b^2}{A_b^2} - \frac{q_e^2}{A_e^2} = 0 \tag{2.9}$$

where $A_b = A(x_b)$, p_i and p_e are constant and:

$$I_i \simeq \int_{x_i}^{x_b} \frac{dx}{A(x)} \quad ; \qquad I_e \simeq \int_{x_b}^{x_e} \frac{dx}{A(x)} \tag{2.10}$$

Equations (2.6) through (2.9) are then transformed by introducing perturbation quantities with respect to the steady state solution and linearized for small changes in the volume fluxes. Finally, if $I_i \simeq x_b/A_b = u_t t/A_t \ll I_i + I_e$, which is essentially equivalent to consider the dynamics of a bubble entering a semi-infinite pipe of constant cross-sectional area A_t, the perturbation and Rayleigh-Plesset equations can be reduced to the following second order differential equation for the bubble radius $R(t)$:

$$\frac{2\pi\rho u_t}{A_t}\left[2tR^2\frac{d^2R}{dt^2}+4tR\left(\frac{dR}{dt}\right)^2+R^2\frac{dR}{dt}\right]+$$
$$+\rho R\frac{d^2R}{d^2t}+\frac{3}{2}\rho\left(\frac{dR}{dt}\right)^2-p_v-p_g\left(\frac{R_o}{R}\right)^3+\frac{2S}{R}+p_t=0 \quad (2.11)$$

where p_t and u_t are the steady state pressure and velocity at the throat. Note that the solution of the above equation depends on A_t, the throat cross-sectional area. The detection time t_f and detection length L_f, computed for a final detection radius $R_f = 150\,\mu$m and a throat diameter $D_t = 1$ mm by numerically integrating the above equation, are shown in Fig. 2.8 and Fig. 2.9. The maximum in the results separates two regimes: in the lower radius range the inertial effects of the displaced liquid dominate, while in the upper one the effect of bubble gas content prevails, therefore accelerating the bubble dynamic response. Note that, in the radius range of interest, the detection length is almost independent of the equilibrium bubble pressure and that the length of the throat section should not be shorter than 5 to 10 mm. In view of the throat diameter initially assumed this choice is compatible with the need to control the bubble interference error (see Sec. 2.3) over the nuclei radius range in cosideration. Also note that the solution of the above equation depends on A_t, the throat cross-sectional area.

2.5. Cavitation Rate and Liquid Quality Measurements

Once the throat cross-sectional area has been determined, the volume flux $q = u_t A_t$ and the mean cavitation event rate $\overline{\nu}_b = qn(R_o)$ can be computed. Results shown in Fig. 2.10 and Fig. 2.11 for a throat diameter $D_t = 1$ mm

indicate that in the radius range from 10 to 100 μm as many as maybe a thousand cavitation events per second are to be expected. In steady state conditions, if the liquid quality of the sample is constant and the cavities do not appreciably interfere with each other, the occurrence of cavitation at the venturi throat is described by a Poisson process with average arrival time $\overline{\tau}_b = 1/\overline{\nu}_b$ and the probability of observing N_b cavities during the time t is expressed by:

$$Pr(N_b) = \frac{(\overline{\nu}_b t)^{N_b}}{N_b!} e^{-\overline{\nu}_b t} \tag{2.12}$$

This also implies that the probability density distribution of the delay time t between cavitation events follows the exponential distribution:

$$f(t) = \overline{\nu}_b e^{-\overline{\nu}_b t} \tag{2.13}$$

The agreement of the observed distribution of cavitation delay times with the above theoretical one provides a rational and quantitative way to assess the importance of interference effects among the cavities in the CSM venturi flow and to introduce corrections when appropriate. A large portion of cavitation events will thus occur with a separation in time considerably smaller than the average arrival time $\overline{\tau}_b$. Therefore the CSM data acquisition system must be designed to handle as many as, say, order of ten thousand cavitation events per second for a reliable measurement of the water quality to be made. In addition, it also must record the arrival times with comparable precision if the importance of cavitation interference effects is to be assessed from consideration of the delay time statistics.

For a given pressure at the throat, the corresponding concentration of unstable nuclei can be estimated from the count N_b of the cavitation bubbles observed during the sampling time t_s. Since t_s can be conveniently measured, the problem of estimating ν_b now reduces to the estimation of the Poisson parameter $\xi = \overline{\nu}_b t_s$. It is known from the theory of probability distributions, [Browlee, 1960], that the best estimator of the Poisson parameter ξ is the observed frequency N_b, whose expected value and variance are respectively:

$E[N_b] = V[N_b] = \xi$. Thus the estimated root mean square relative error in the measurement of ξ and of any other linearly related quantity such as $\overline{\nu}_b$, $n(R_o)$ and $N(R_o)$ is $\varepsilon = 1/\sqrt{N_b}$.

The sampling time $t_s = 1/\overline{\nu}_b\varepsilon^2$ and liquid sample volume $V_s = qt_s$ necessary for achieving the required precision are plotted in Fig. 2.12 and Fig. 2.13. From them it appears that the liquid sample volume and sampling time required for one single measurement of unstable nuclei concentration of acceptable precision (say, $\varepsilon = .20$) are at most of the order of $10\,\mathrm{dm}^3$ and 10 s respectively. Clearly, the overall sampling time and volume of liquid necessary for the evaluation of the nuclei number distribution will depend on the total number of points where the measurement of the unstable nuclei concentration is carried out. Finally, the unstable nuclei concentration is estimated as $n(R_o) = N_b/V_s$, with standard deviation $\sigma_n = \sqrt{N_b}/V_s$.

In existing CSM's cavitation detection has been made either optically [Oldenziel,1982a, 1982b, 1982c], [Ito and Oba, 1980] or acoustically [Shen et al., 1984] from the noise generated by the rapid volume changes of the cavities and in particular by their collapses. Acoustical detection is relatively simple and has the distinct advantage of not requiring optical access to the cavitation region. However, rebounds are possible and frequently occur in practice during the collapse of cavitation bubbles, leading to multiple acoustical signals of decreasing amplitude from the same original cavity. Optical detection is clearly preferable whenever feasible because it safely locates the occurrence of cavitation in space, eliminating the possibility of spurious multiple counts, and preserves the information on the arrival time of cavitation events, which represents a powerful diagnostic tool in monitoring the operation of CSM's. In addition the possibility of direct optical observation of cavitation in the venturi is an important advantage of optical methods for cavitation detection.

2.6. Throat Pressure Measurement

It was previously mentioned that one of the most difficult problems of CSM's

consists in measuring the throat pressure with the required precision. Since direct methods appear to be impossible, indirect methods must be used. Most naturally a representative value of the inception pressure at the venturi throat may be deduced from the measurements of the inlet pressure and of the throat velocity using Bernoulli's equation for ideal, incompressible, steady flow:

$$p_t = p_i - \frac{1}{2}\rho u_t^2(1 - C_c^2) \tag{2.14}$$

An unavoidable problem associated with this technique is that the throat pressure, being inherently small compared to the inlet pressure and kinetic pressure drop, is expressed as the difference of two almost equal quantities. Thus, small relative errors in the evaluation of these quantities lead to a much larger relative error for the throat pressure.

In existing CSM's, [Oldenziel,1982a, 1982b, 1982c], [Godefroy et al., 1981], [Le Goff and Lecoffre, 1983], [Shen et al., 1984] the velocity measurement was carried out either in the inlet or in the outlet sections of the duct, relatively far from the venturi throat. This method appears to be rather unsatisfactory for various reasons. First, any intrinsic error in the measurement of the velocity or due to inaccurate estimate of boundary layer effects is amplified proportionally to the reciprocal of the contraction ratio when the throat velocity is derived by means of continuity arguments. This limitation is particularly severe since in CSM's the contraction ratio should be as small as possible in order not to appreciably affect the conditions of the sampled liquid during its flow in the inlet section. Morover, it is generally necessary to make the inlet section longer, which is also likely to affect the conditions of the sampled liquid, especially when a second venturi of smaller contraction ratio is used to monitor the velocity.

These difficulties are overcome if the velocity measurement is carried out at the throat. In consideration of the various requirements and limitations involved, the use of a Laser Doppler Velocimeter (LDV) seems to be the best solution. In this case it is advisable to consider the more general situation when the pressure is measured at an upstream station (subscript u) and the velocity at a location

indicated by the subscript m, near but not necessarily coincident with the throat section. Then the throat pressure can be calculated from:

$$p_t = p_u - \frac{1}{2}\rho u_m^2 \frac{A_m^2}{A_t^2}(1 - C_c^2) \tag{2.15}$$

The error analysis of this measurement can be easily developed if the two independent variables p_u and u_m are assumed to be normally distributed about their expected values $\overline{p}_u$ and $\overline{u}_m$ with variances $\sigma_{p_u}^2$ and $\sigma_{u_m}^2$. Standardizing p_u and u_m and using the properties of the moments of the standard normal distribution one obtains the following expressions for the expected value and the variance of p_t:

$$\overline{p}_t = \overline{p}_u - \frac{\rho c}{2}(\overline{u}_m{}^2 + \sigma_{u_m}^2) \tag{2.16}$$

$$\sigma_{p_t}^2 = \sigma_{p_u}^2 + \rho^2 c^2 \sigma_{u_m}^2 \left(\overline{u}_m{}^2 + \frac{\sigma_{u_m}^2}{2}\right) \tag{2.17}$$

where $c = (1 - C_c^2)A_m^2/A_t^2$. Note the "shift" due to the dispersion of the measured velocity together with the quadratic nature of the equation (2.15).

2.7. Boundary Layer Effects

For the pressure to be correctly deduced from velocity measurements, the presence of a potential core at the CSM throat must be demonstrated. Viscous effects have therefore been estimated by matching an axisymmetric laminar boundary layer [White, 1974] to the quasi one-dimensional ideal flow solution based on the duct geometry, [Chmielewski, 1974; Mikhail, 1978]. The assumption of laminar flow in the venturi is justified by the low value of the Reynolds number at the inlet ($Re_i \simeq 1500$) and, further downstream where the Reynolds number increases beyond the transition value, by the effect of the steep contraction which tends to laminarize the flow by drastically reducing pre-existing velocity fluctuations. The turbulent transition length for a flat plate with equal free stream velocity is of the order of 20 cm and it seems likely that it would not be shorter for the guided flow in the CSM venturi. Thus there is strong

reason to believe that at least the non-cavitating flow remains laminar throughout the whole venturi. In the boundary layer computation the duct profile has been assumed to be continuous with continuous first and second derivatives, as required from fluid mechanical considerations to avoid separation. In the contraction and the transitions at the inlet and outlet of the diffuser the duct radius was supposed to have sinusoidal second derivative in the streamwise direction. The inlet and throat sections were taken to be cylindrical and the central part of the diffuser to be conical, of given semi-aperture angle β_d.

The results of such boundary layer calculations obtained for a prototype venturi made of acrylic plastic with inlet Reynolds $Re_i = u_i D_i/\nu = 1400$ (the lowest expected value during operation) are summarized in Fig. 2.14 through Fig. 2.17. The geometrical characteristics of the above prototype venturi are: inlet length $L_i = 11.4\,\text{mm}$, contraction length $L_c = 10.4\,\text{mm}$, throat length $L_t = 7.7\,\text{mm}$, diffuser length $L_d = 9.6\,\text{mm}$ with a 3.3 mm long inlet transition and a semi-aperture angle $\beta_d = 0.80\,\text{deg}$, throat diameter $D_t = 1\,\text{mm}$, contraction ratio $C_c = 1/100$, exhaust diameter $D_e = 1.23\,\text{mm}$. The duct shape profile is shown in Fig. 2.14, where the scales on the two axes are different. The boundary layer displacement and momentum thicknesses δ^* and θ are plotted in Fig. 2.15, where they are normalized with respect to the local duct radius. They clearly demonstrate the presence of a potential core in the throat section of the CSM. In Fig. 2.16 the pressure coefficients $C_p = 2(p - p_i)/\rho u_i^2$ at the centerline of the venturi is shown as functions of the axial coordinate of the duct. Note the very steep pressure drop in the contraction and the milder recovery in the diffuser.

Another effect of the boundary layer is the reduction of the flux-averaged cross-sectional area of the venturi with respect to its geometrical area. This effect is particularly important in the diffuser, whose performance is very sensitive to even very small changes of the expansion ratio (see Fig. 2.5). In theory it would be possible to compute the boundary layer displacement thickness for the assigned, nominal profile of the potential core velocity and to correct accordingly the venturi geometry. In practice this possibility should be regarded

with some skepticism because boundary layer computations for flows with a highly unfavourable pressure gradient as the one in the diffuser are rather imprecise. Furthermore, it is questionable that their results could be accurately implemented in the manufacturing of small size venturis. However, if the results of these computations are to be trusted, in a venturi equal to the one previously considered but with a 20 mm long diffuser the presence of the boundary layer would, for example, increase the expansion ratio from its nominal value of 1.10 to a geometric value of 1.37.

2.8. Laminar Separation

Another problem to be expected in the venturi as a consequence of viscous effects is the occurrence of laminar separation in the diffuser when too large negative pressure gradients are present. If laminar separation takes place, cavitation nuclei from the main flow are likely to be trapped in the recirculation region, where they eventually grow and possibly develop into an attached cavity, whose unsteady behaviour greatly disturbes the rest of the flow. The situation is furtherly worsened if this cavity propagates downstream and reaches the exit. In this case the exhaust pressure is established throughout the cavity and the useful portion of the diffuser is proportionally shortened. A cylindrical section of appropriate length downstream of the diffuser promotes the stability of the exhaust flow and usually prevents the separation-cavitation from extending to the exit.

Preliminary tests on the prototype venturi of Fig. 2.14 and later experience with operational ones showed that steady or intermittent separation in the diffuser can indeed occur, a problem also reported by Oldenziel [1982]. In view of this, the boundary layer correlation parameter $\lambda = \theta^2 U'/\nu$ (where U' is the streamwise derivative of the flow velocity at the boundary layer edge) and the Stratford laminar boundary layer separation criterion S_c [Stratford, 1954] have been plotted in Fig. 2.17. Separation is predicted when $\lambda = -0.09$ or $S_c = 0$. The two methods agree well with each other and also with the observed location

of separation in the prototype venturi, thus indicating that less steep diffusers should be used.

Indeed, the constraint imposed by the need to avoid laminar separation on the design and the performance of the diffuser is extremely severe. In order to qualitatively assess this point let us consider the application of Stratford's laminar separation criterion to the flow in the venturi:

$$(x - x_B)C_p \left(\frac{dC_p}{dx}\right)^2 = 0.0104 \tag{2.18}$$

Here $C_p = 1 - A_t^2/A^2$ and x_B is the distance for the momentum thickness of a Blasius boundary layer (with zero pressure gradient) to reach the actual value of θ at the diffuser inlet, say $x = 0$. The above equation can be written as a differential equation for $C_p(x)$ with initial condition $C_p(0) = 0$, whose solution is:

$$\frac{A}{A_t} = \left[1 - \left(0.153 \ln \frac{x + x_B}{x_B}\right)^{2/3}\right]^{-1/2} \tag{2.19}$$

The results of this mathematical exercise are shown in Fig. 2.18 in terms of the nominal diameter ratio as a function of the diffuser length for the venturi of Fig. 2.14 ($x_B = 8.57\,\text{mm}$) with, of course, a different diffuser. They represent the maximum expansion ratio which could in theory be achieved without incurring in laminar separation, neglecting any other consideration. The cusp of the duct profile at the origin clearly betrays the practical limits of this approach, which, nevertheless, still forcefully illustrates how severe is the constraint imposed by the insurgence of separation on the performance of diffusers operating with laminar flows.

Ideally these limitations could be considerably alleviated in a venturi with turbulent flow in the diffuser. In practice this situation would be very difficult to reconcile with the conflicting need of preserving a potential core in the flow at least through the venturi throat for the local pressure to be measured as discussed in Sec. 2.6. This difficulty is particularly evident when the fact is considered that the use of transition promoting devices at or close to the venturi throat is clearly out of the question due to the extreme instability of the flow.

2.9. Summary and Conclusions

The operation of CSM's has been analyzed in order to clarify the most relevant factors affecting their design. By means of various assumptions and approximations, a simplified model has been derived which adequately represents the operation of CSM's in terms of a limited number of relevant parameters. The investigation of their mutual relations led to a functional description of CSM operation which enables one to address the problem of their design in a systematic and organic way. The above model has been applied to simulate CSM operation for the case of a typical nuclei number distribution in water. The results can be summarized as follows:

- the pressure in the CSM cavitation region is an extremely sensitive parameter and cannot be measured directly with the necessary accuracy;
- the existence of a potential core at the throat has been demonstrated in venturi tubes of proper geometry by estimating the boundary layer thickness;
- the indirect measurement of the pressure in the cavitation region appears to be best accomplished by measuring the upstream pressure with an absolute pressure transducer and the potential core velocity at the CSM throat with non-intrusive direct methods such as, for example, a LDV;
- the detection of cavitation at the venturi throat is best accomplished by optical techniques;
- it is clearly advantageous for the purpose of monitoring the flow to preserve the optical access to the cavitation region whenever possible;
- the flow is likely to remain laminar throughout the venturi's throat section and the first portion of the diffuser;
- in the case of the nuclei number distributions typically encountered in technical waters the errors and limitations due to saturation can be effectively controlled by decreasing the volume of the cavitation region to less than a

few tens of cubic millimeters;

- for a throat diameter of 1 mm the time response of the cavitating nuclei imposes a lower bound of about 5 to 10 mm to the length of the CSM throat section;
- the flow is extremely sensitive to laminar separation in the diffuser, which limits the maximum achievable expansion ratio to less than 1.1;
- in the case of the nuclei number distributions typically encountered in technical waters it appears that CSM's can be designed which are capable to detect gas bubbles having an equilibrium radius larger than about 10 μm within the errors characteristic of the other alternative techniques currently available;
- due to the considerable complexity of the phenomena involved, the interpretation of the data obtained from CSM's requires a careful analysis.

It is therefore proposed to develop a CSM with a transparent venturi tube where the throat velocity is measured by a LDV and the upstream pressure by an absolute pressure transducer. At the same time LDV signal is also used to detect the occurrence of cavitation at the throat of the venturi tube. The analysis of the signals from the LDV and the upstream pressure transducer is carried out by an especially designed electronic Signal Processor for real time acquisition of the relevant data. Finally, the data reduction is performed by a microcomputer.

The next chapter presents the main considerations for the design of the LDV optical system for the CSM.

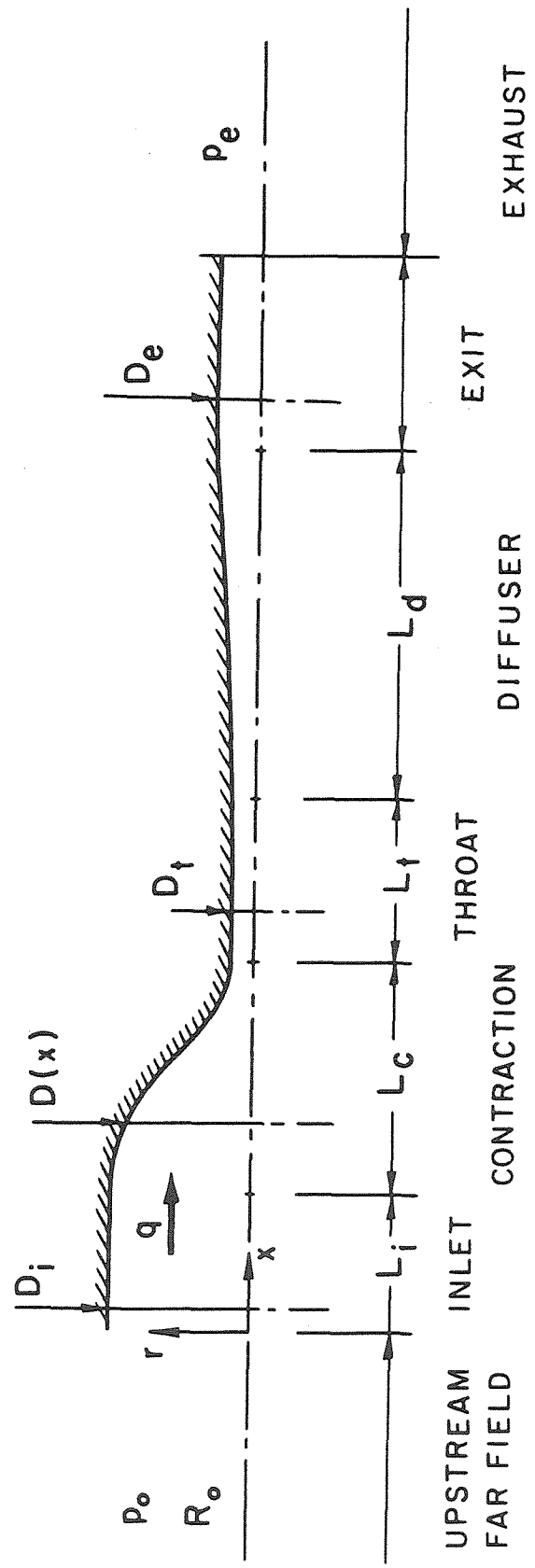

Figure 2.1. Geometry and nomenclature of axisymmetric CSM venturi duct.

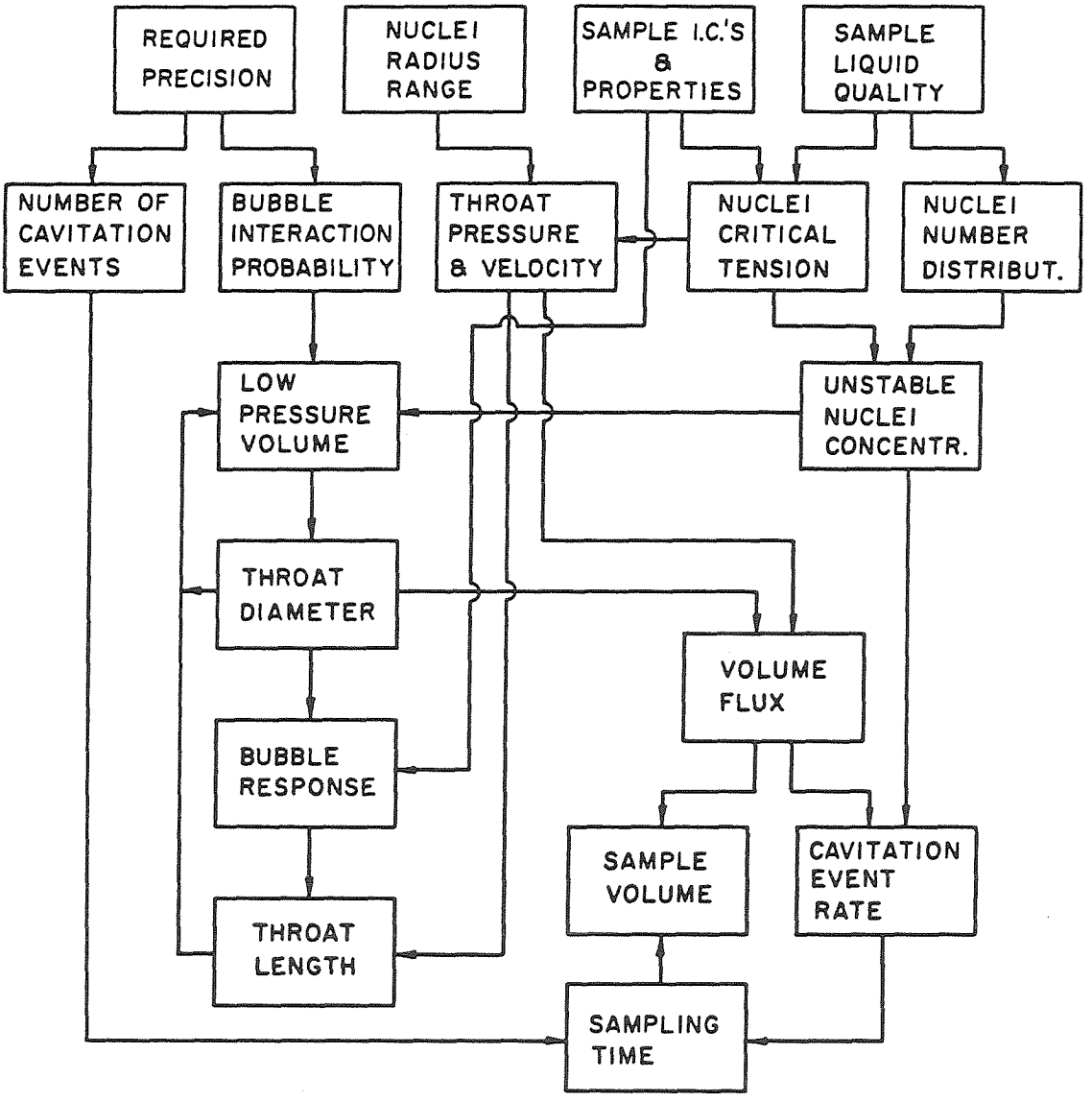

Figure 2.2. Block diagram of CSM parameters.

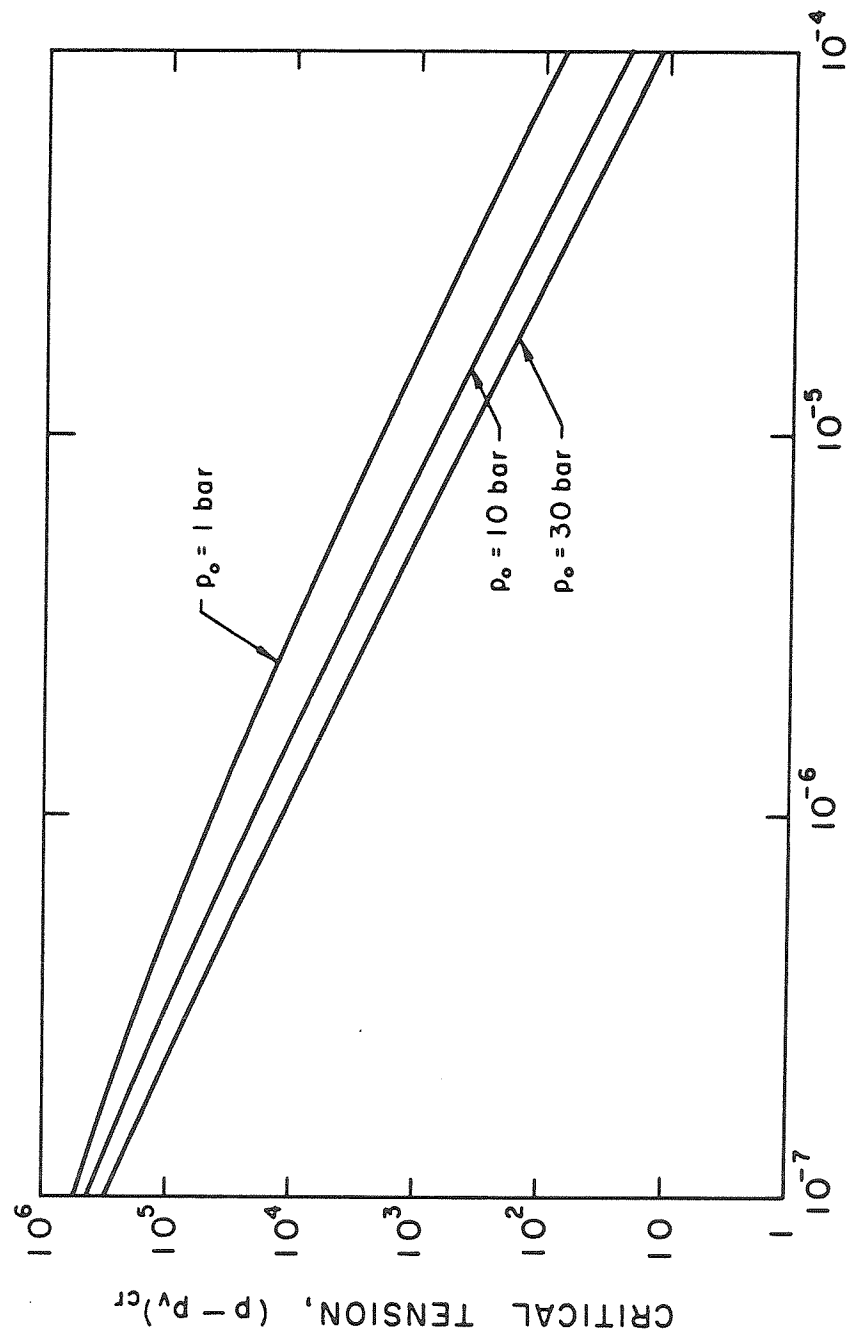

Figure 2.3. Critical tension $(p - p_v)_{cr}$ of a spherical air bubble v/s its equilibrium radius R_o in water at various pressures: $p_o = 1$, 10 and 30 bar and $T = 20\,^{\circ}\mathrm{C}$ (surface tension $S = 0.073\,\mathrm{N/m}$, vapor pressure $p_v = 1919\,\mathrm{Pa}$, water density $\rho = 1000\,\mathrm{kg/m^3}$).

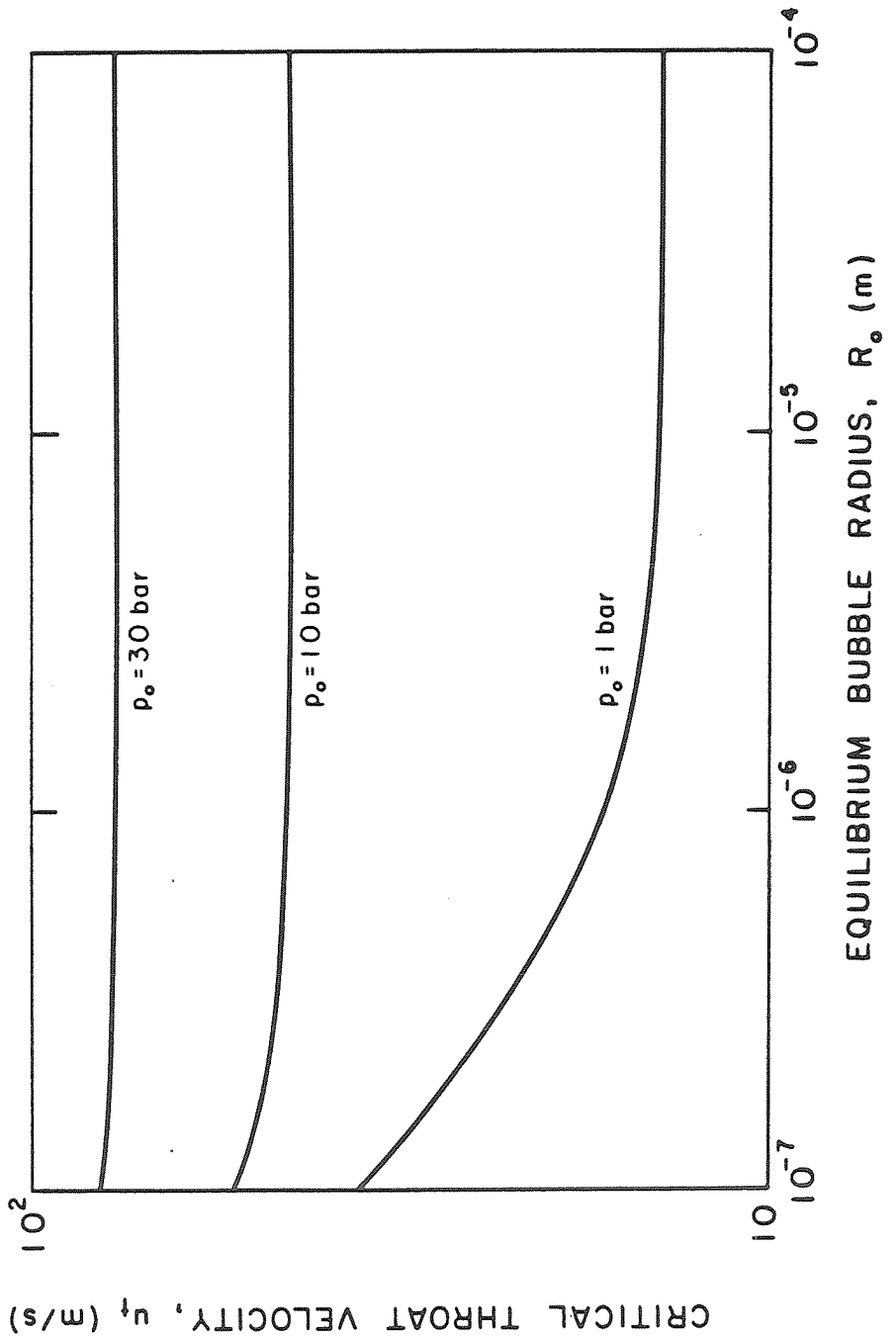

Figure 2.4. Throat velocity u_t v/s equilibrium bubble radius R_o in water at various pressures: $p_o = 1$, 10 and 30 bar and $T = 20\,^{\circ}\mathrm{C}$.

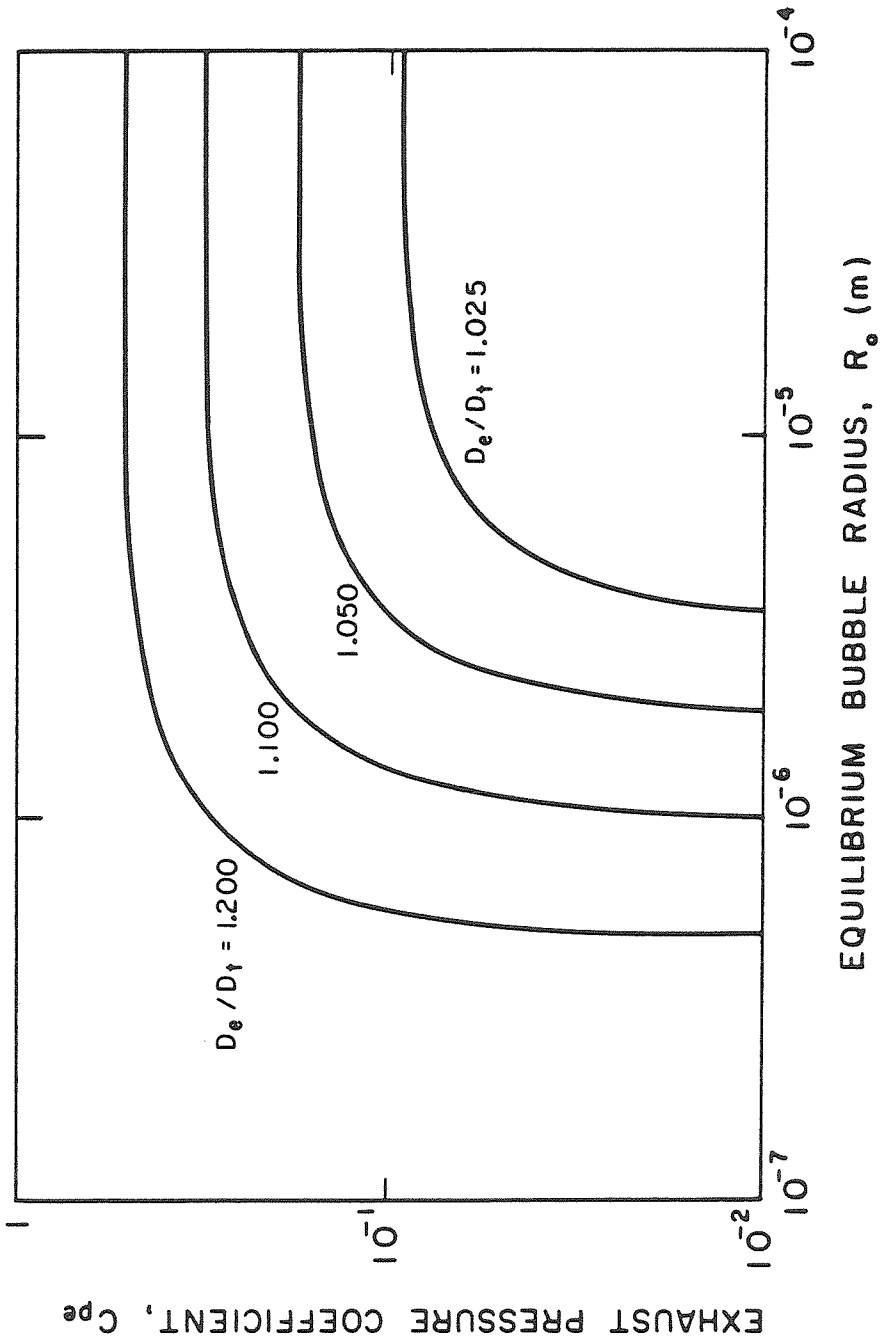

Figure 2.5. Exhaust pressure coefficient $C_{pe} = (p_e - p_v)/(p_o - p_v)$ v/s equilibrium bubble radius R_o in water at $p_o = 1$ bar and $T = 20$ °C for various values of the diffuser's exhaust to throat diameter ratio: $D_e/D_t = 1.025$, 1.050, 1.100 and 1.200.

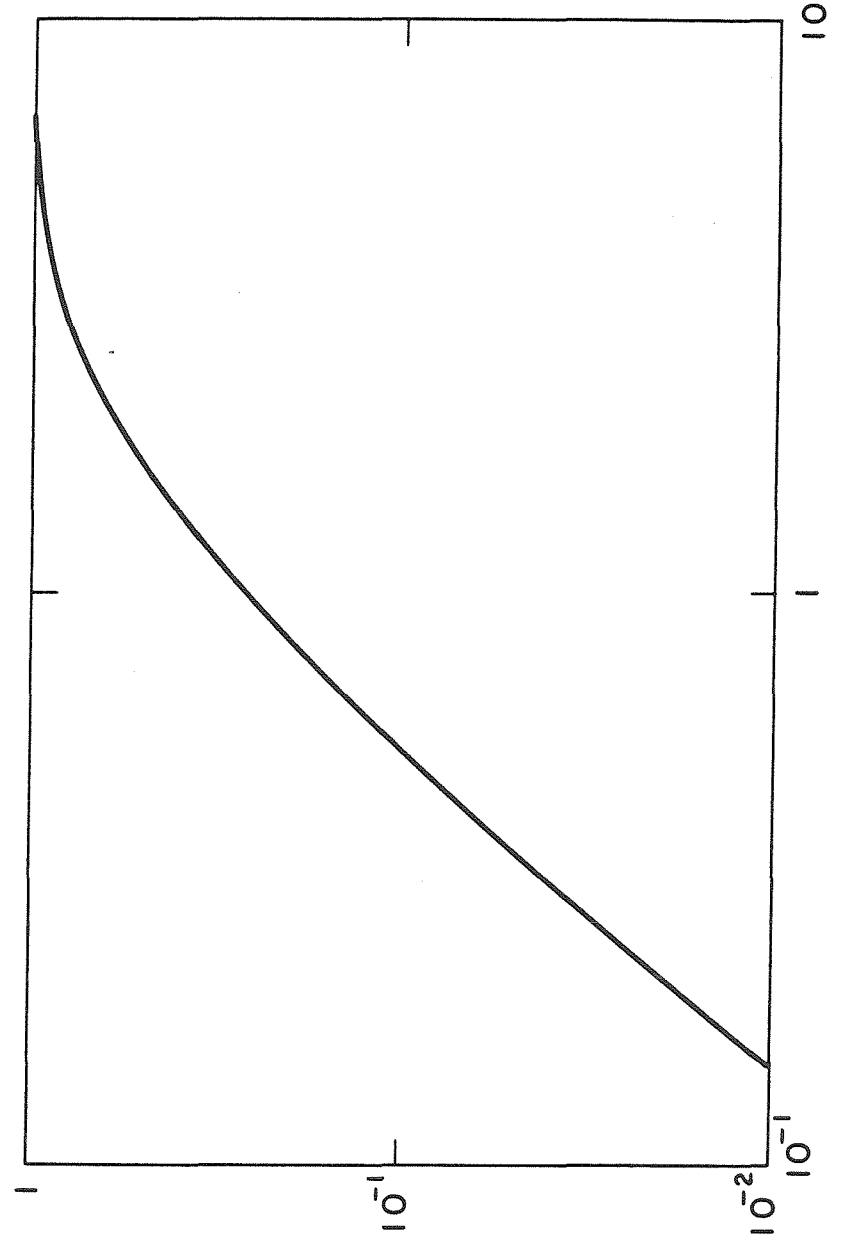

Figure 2.6. Bubble interference probability β v/s average number of unstable nuclei in the CSM throat section $\xi = n(R_o)V_t$ calculated assuming Poissonian occurrence of cavitation nuclei.

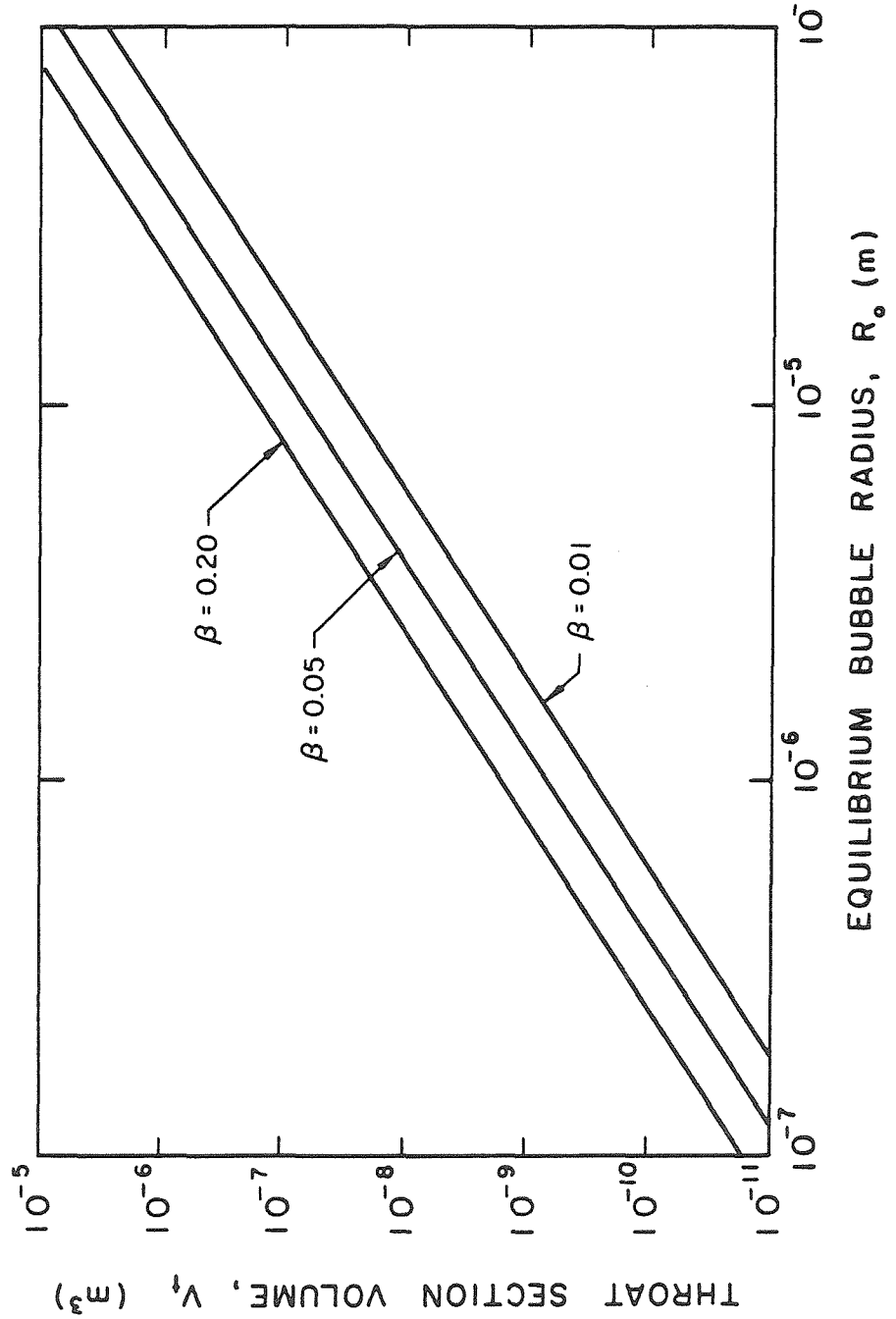

Figure 2.7. CSM venturi throat section volume V_t v/s equilibrium bubble radius R_o for $K_N = 0.001\,m^{-1}$ (nuclei number distribution parameter) and various values of the bubble interference probability: $\beta = 0.01$, 0.05 and 0.20.

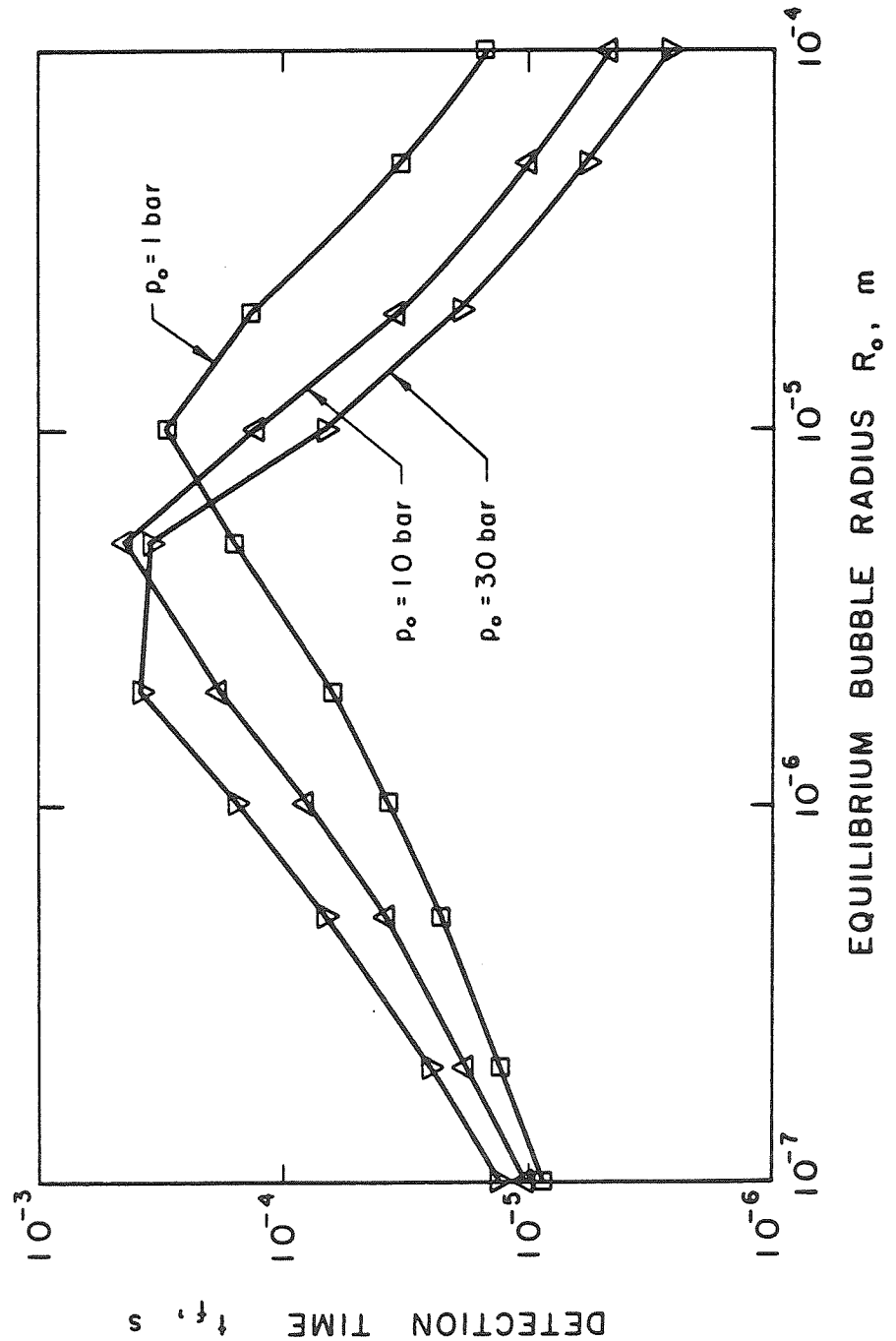

Figure 2.8. Bubble detection time t_f necessary for a bubble to reach a detectable radius $R_f = 150\,\mu$m v/s equilibrium bubble radius R_o in water at various initial pressures: $p_o = 1$ bar (squares), 10 bar (upward triangles) and 30 bar (downward triangles) for $T = 20\,^{\circ}$C (water temperature) and $D_t = 1$ mm (throat diameter).

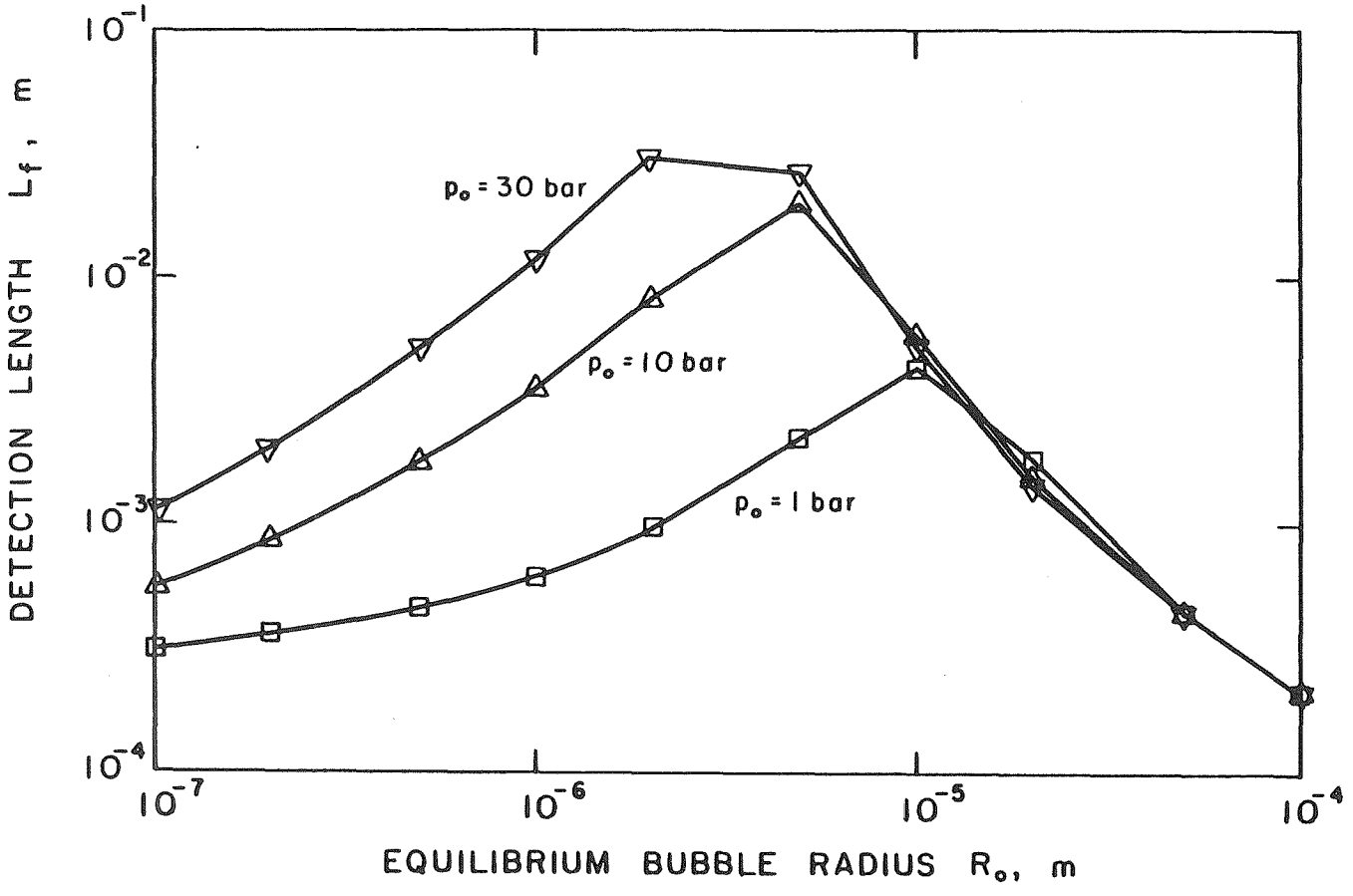

Figure 2.9. Bubble detection length L_f necessary for a bubble to reach a detectable radius $R_f = 150\,\mu$m v/s equilibrium bubble radius R_o at various initial pressures: $p_o = 1$ bar (squares), 10 bar (upward triangles) and 30 bar (downward triangles) for $T = 20\,^{\circ}$C (water temperature) and $D_t = 1$ mm (throat diameter).

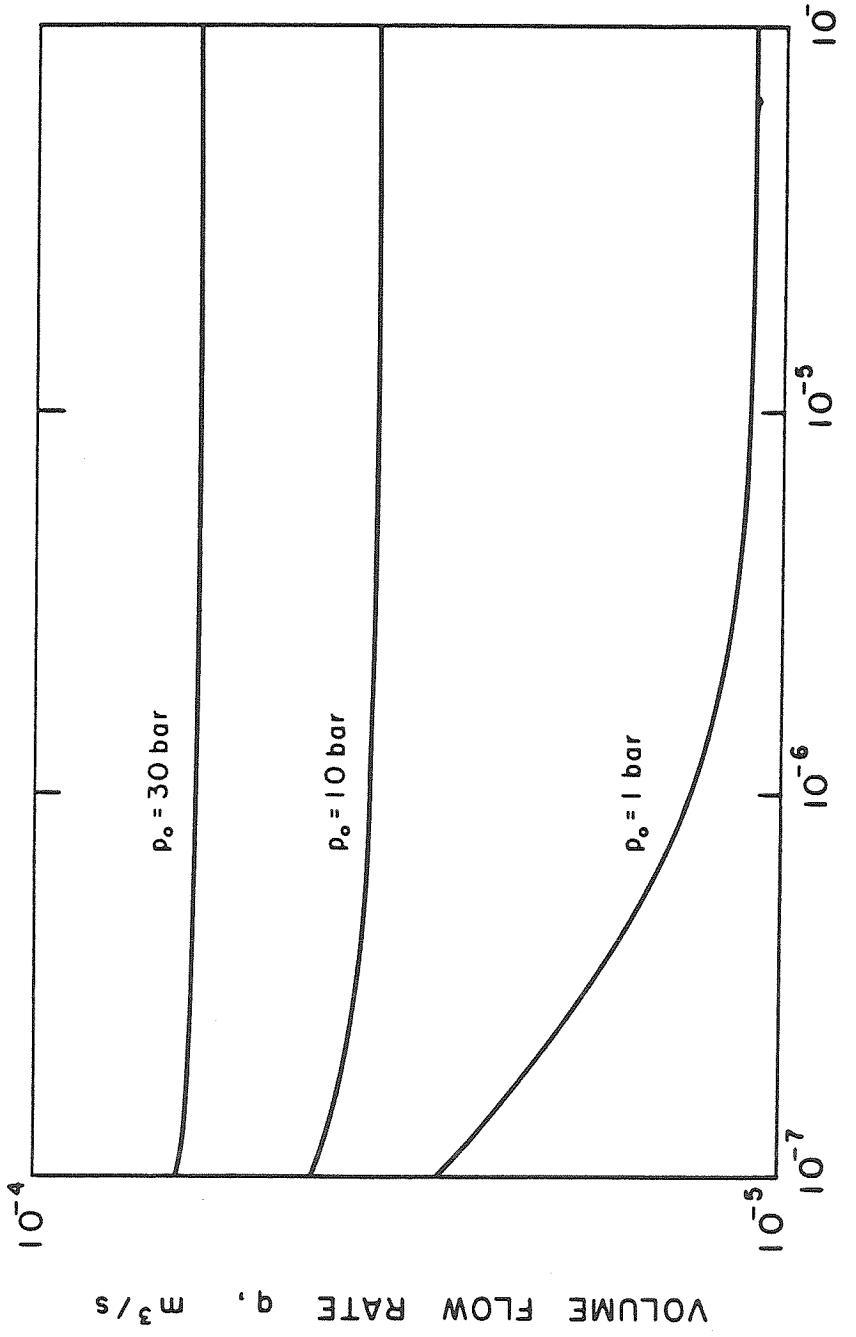

Figure 2.10. Volume flow rate q v/s equilibrium bubble radius R_o in water at various pressures: $p_o = 1$, 10 and 30 bar for $T = 20\,^{\circ}\mathrm{C}$ (water temperature) and $D_t = 1\,\mathrm{mm}$ (throat diameter).

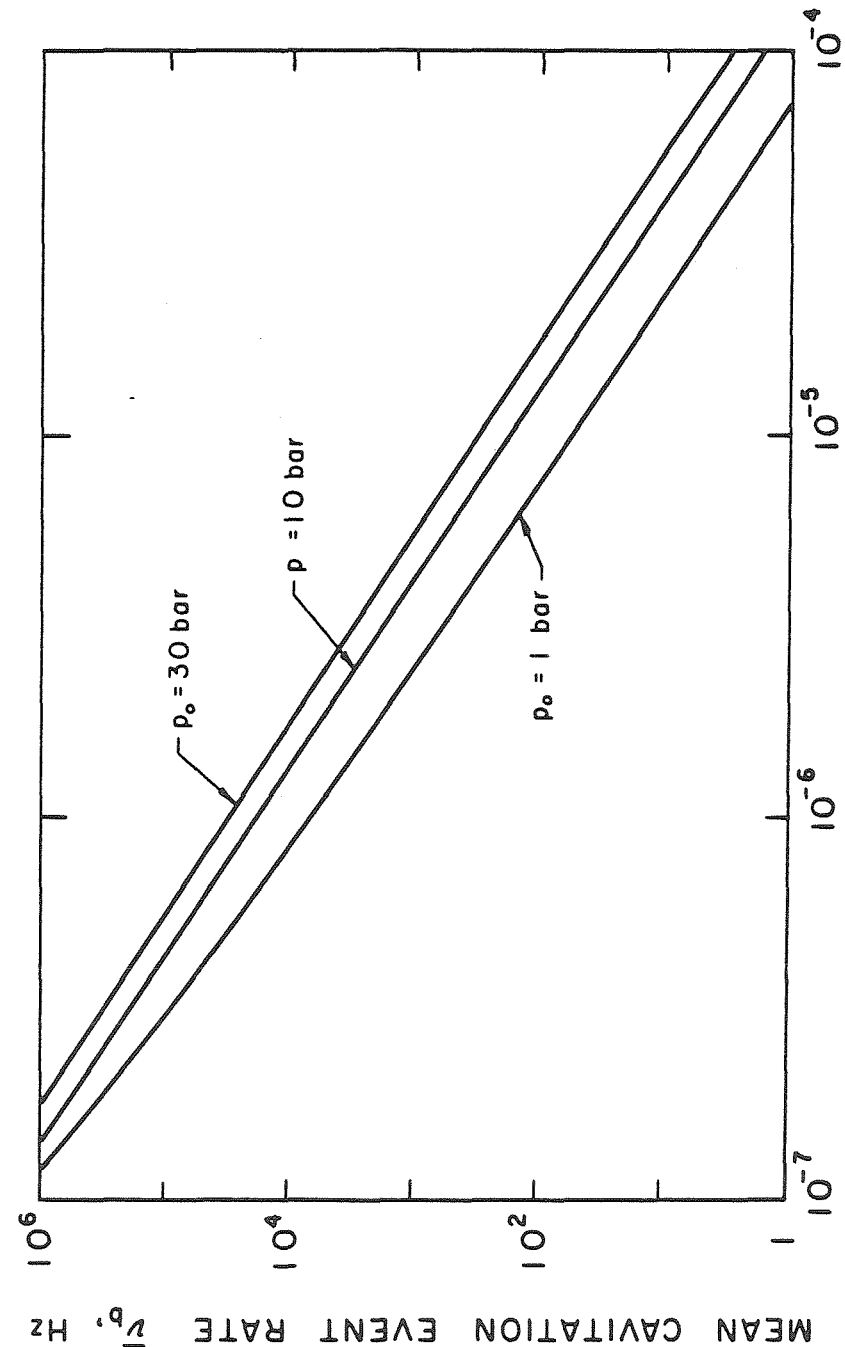

Figure 2.11. Average cavitation event rate $\overline{\nu}_b$ v/s equilibrium bubble radius R_o in water at various pressures: $p_o = 1$, 10 and 30 bar for $D_t = 1$ mm (throat diameter), $K_N = 0.001\,\mathrm{m}^{-1}$ (nuclei number distribution parameter) and $T = 20\,^{\circ}\mathrm{C}$ (water temperature).

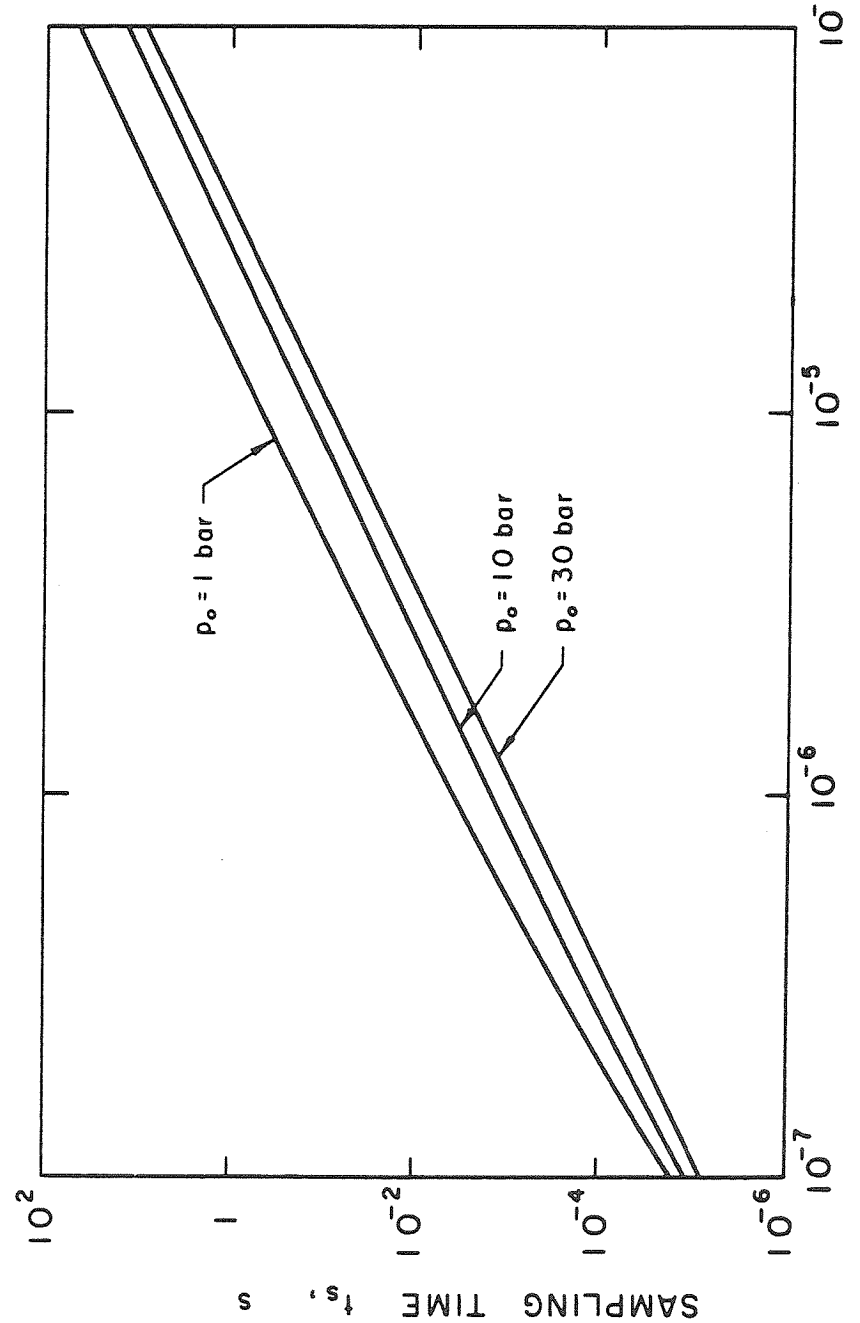

Figure 2.12. Sampling time t_s v/s equilibrium bubble radius R_o in water at various pressures: $p_o = 1$, 10 and 30 bar. Here $\varepsilon = 0.20$ (estimated relative r.m.s. error of the cavitation event rate), $D_t = 1$ mm (throat diameter), $T = 20\,^{\circ}$C (water temperature) and $K_N = 0.001\,\mathrm{m}^{-1}$ (nuclei number distribution parameter).

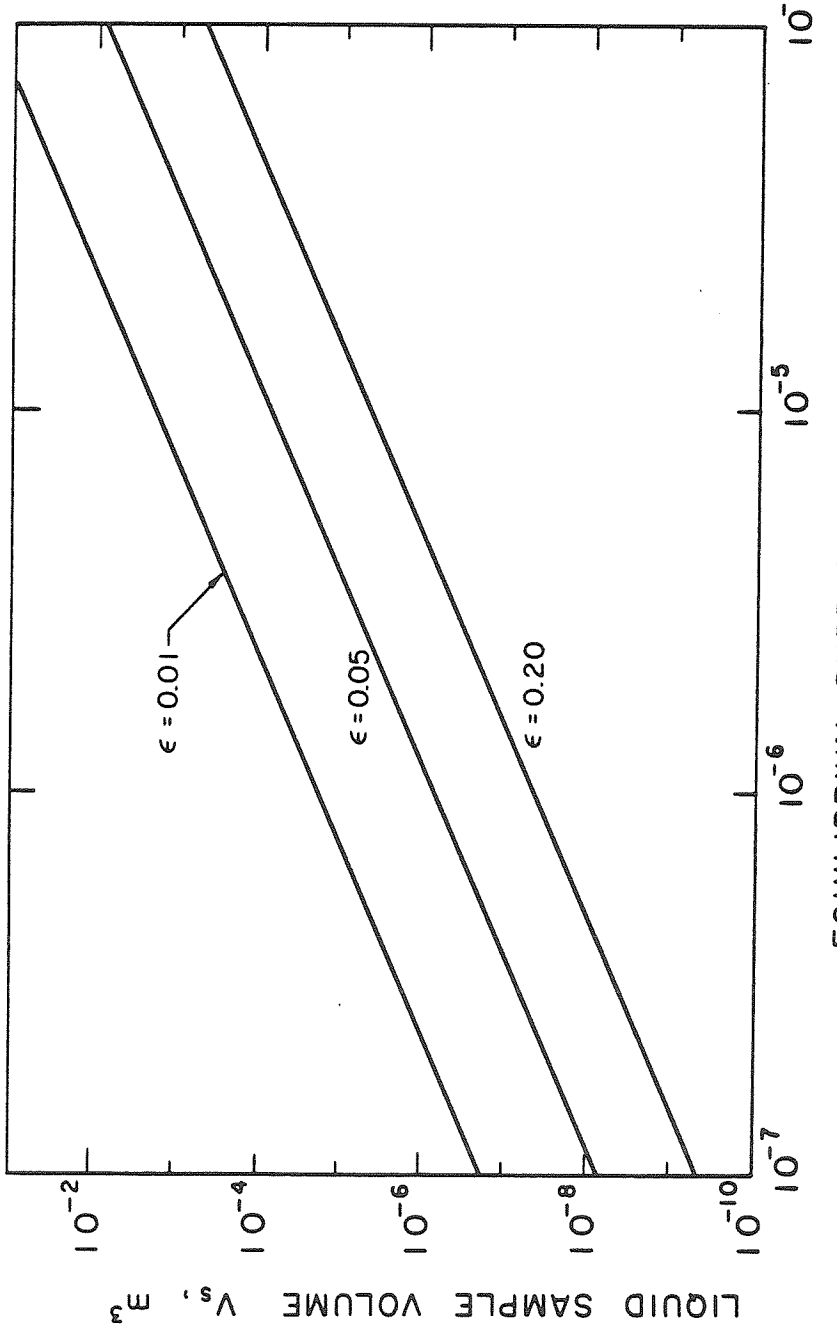

Figure 2.13. Liquid sample volume V_s v/s bubble equilibrium radius R_o in water at $p_o = 1$ bar and $T = 20\,^{\circ}$C for $K_N = 0.001\,\mathrm{m}^{-1}$ (nuclei number distribution parameter) and various values of the estimated relative r.m.s. error of the cavitation event rate: $\epsilon = 0.01$, 0.05 and 0.20.

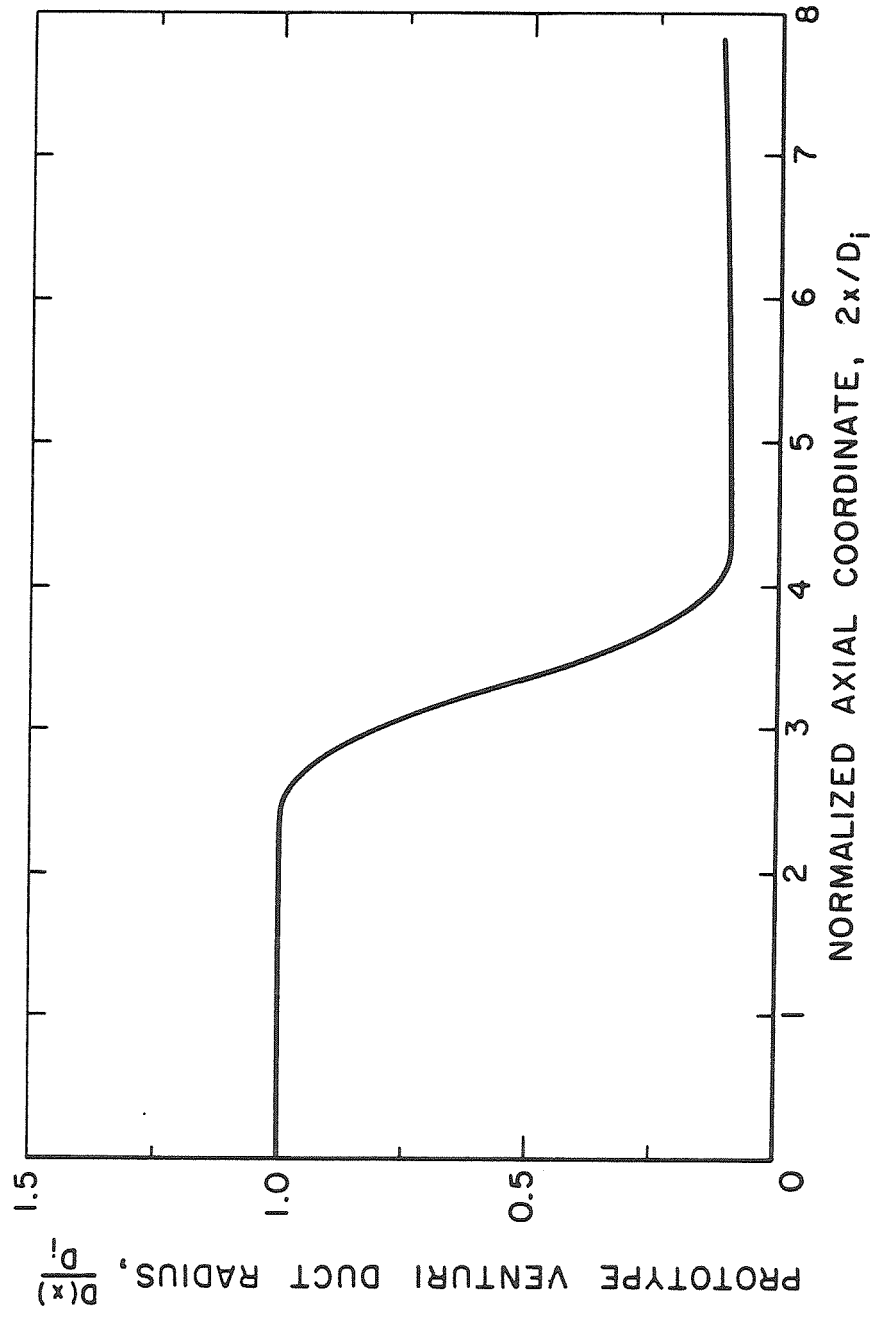

Figure 2.14. Duct shape of prototype CSM venturi in normalized coordinates $2x/D_i$ (axial) and $D(x)/D_i$ (radial) with: $D_i = 10\,\text{mm}$ (throat diameter), $C_c = 1/100$ (contraction ratio) and $\beta_d = 0.76\,\text{deg}$ (diffuser semi-aperture angle). The lenghts of the various sections are: $L_i = 11.4\,\text{mm}$ (inlet), $L_c = 10.4\,\text{mm}$ (contraction), $L_t = 7.7\,\text{mm}$ (throat), $L_d = 10.4\,\text{mm}$ (diffuser).

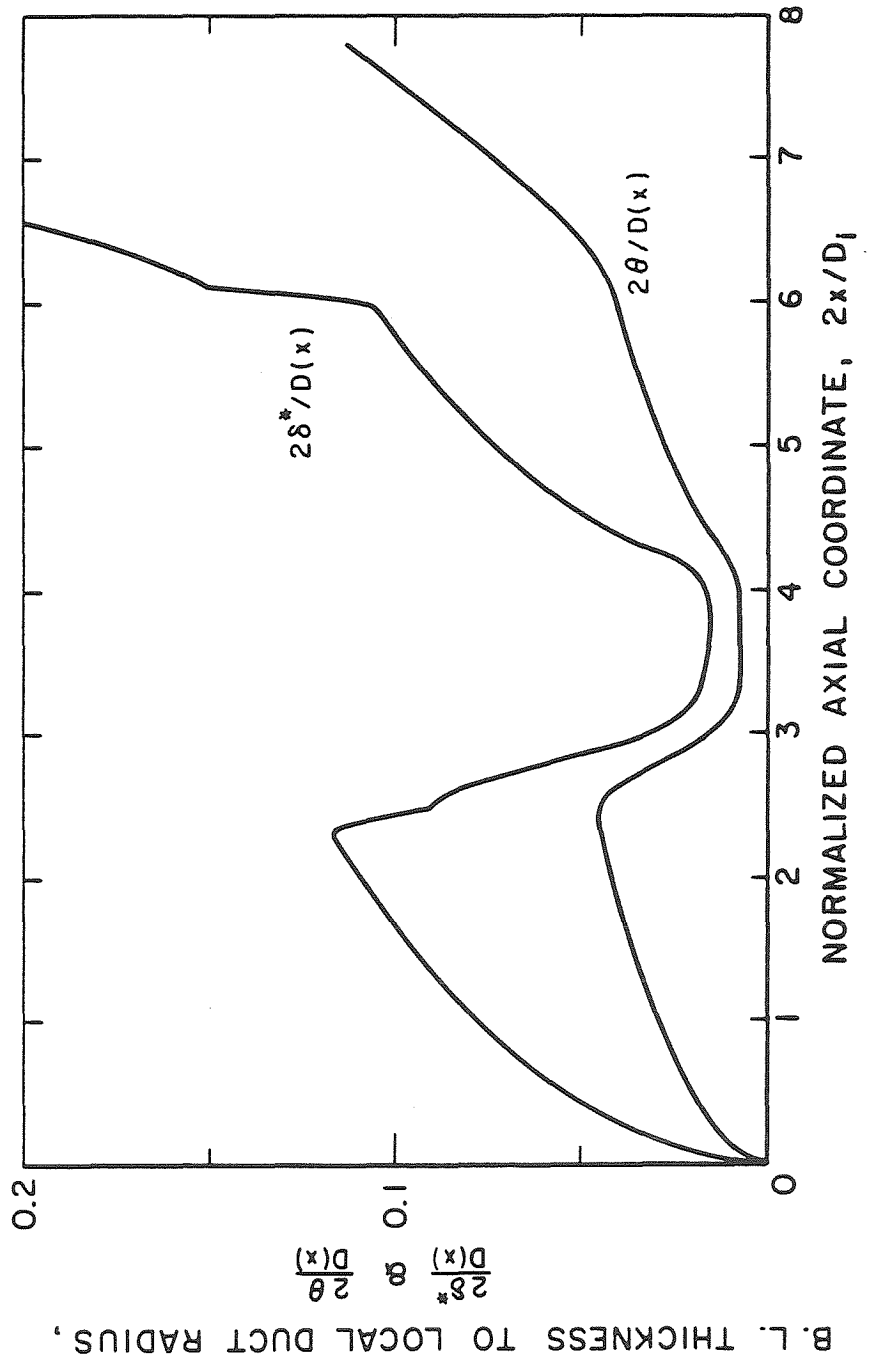

Figure 2.15. Relative displacement thickness, $2\delta^*/D(x)$ (upper curve), and momentum thickness, $2\theta/D(x)$ (lower curve), v/s normalized axial coordinate $2x/D_i$ in the laminar venturi of Fig. 2.14 for $Re_i = 1400$ (inlet Reynolds number).

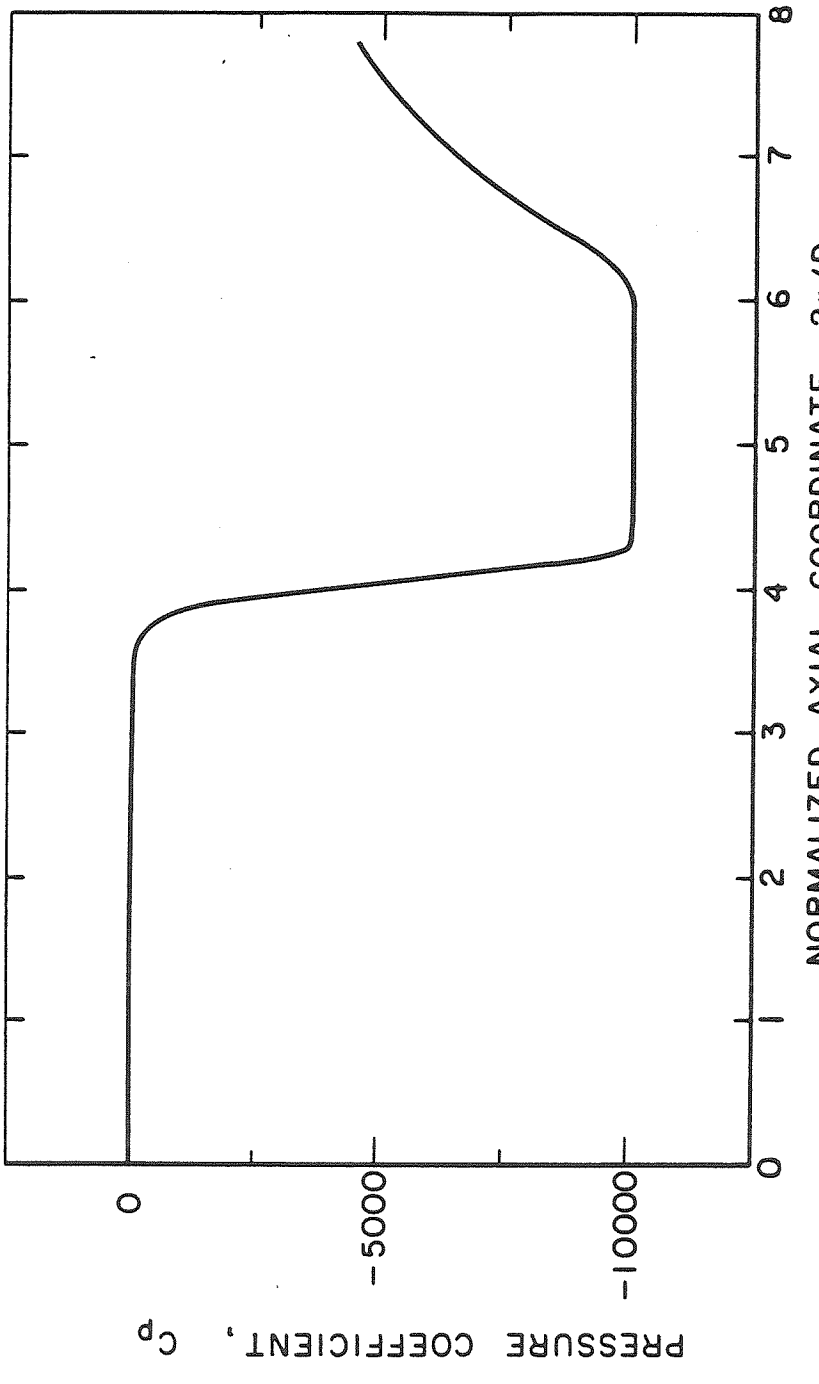

Figure 2.16. Pressure coefficient $C_p = 2(p - p_i)/\rho u_i^2$ at the venturi centerline v/s normalized axial coodinate $2x/D_i$ for the venturi of Fig. 2.14.

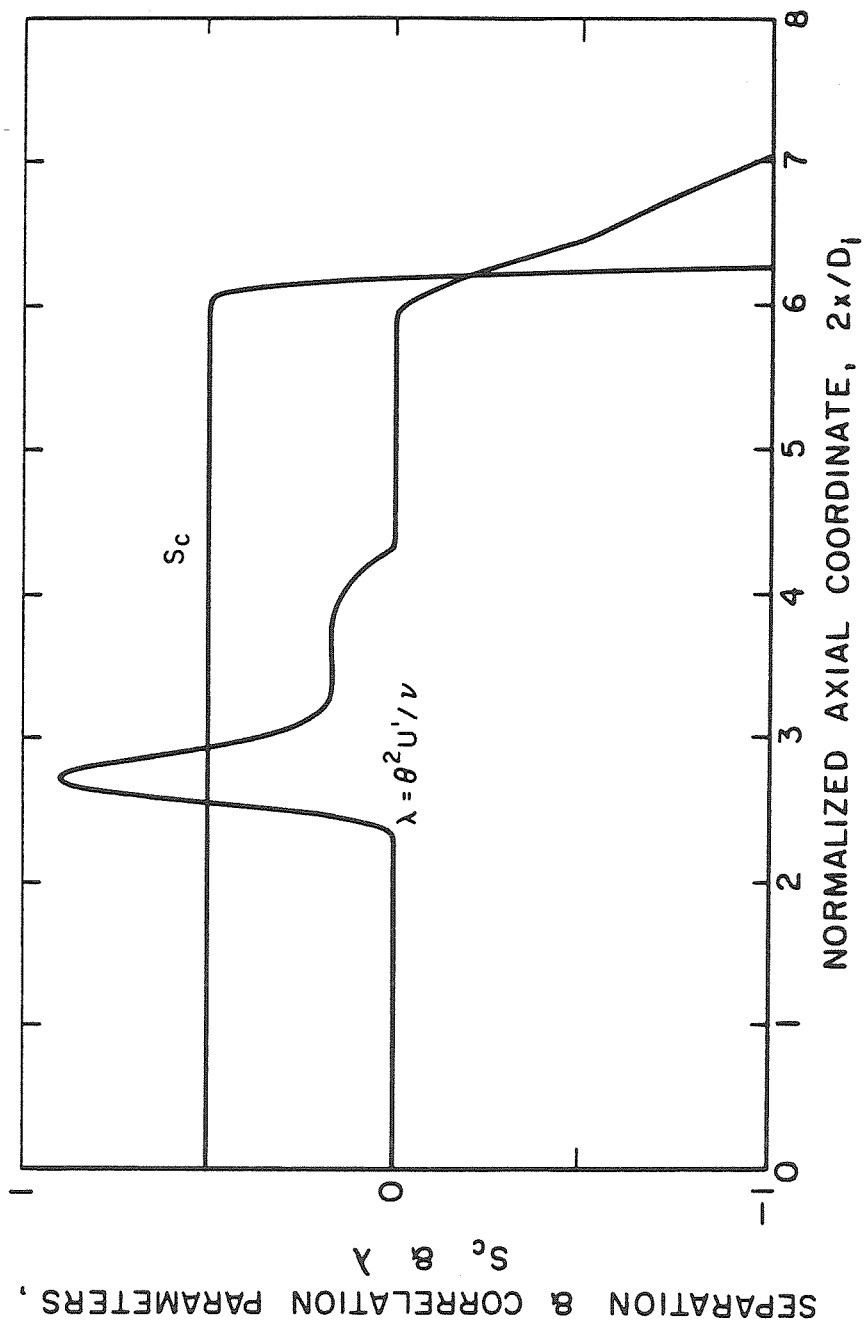

Figure 2.17. Stratford's laminar separation criterion S_c (upper curve) and Thwaites' shear and shape correlation parameter $\lambda = \theta^2 U'/\nu$ (lower curve) v/s normalized axial coordinate $2x/D_i$, for the venturi of Fig. 2.14. Laminar separation is predicted when S_c drops to zero or $\lambda \simeq -0.09$.

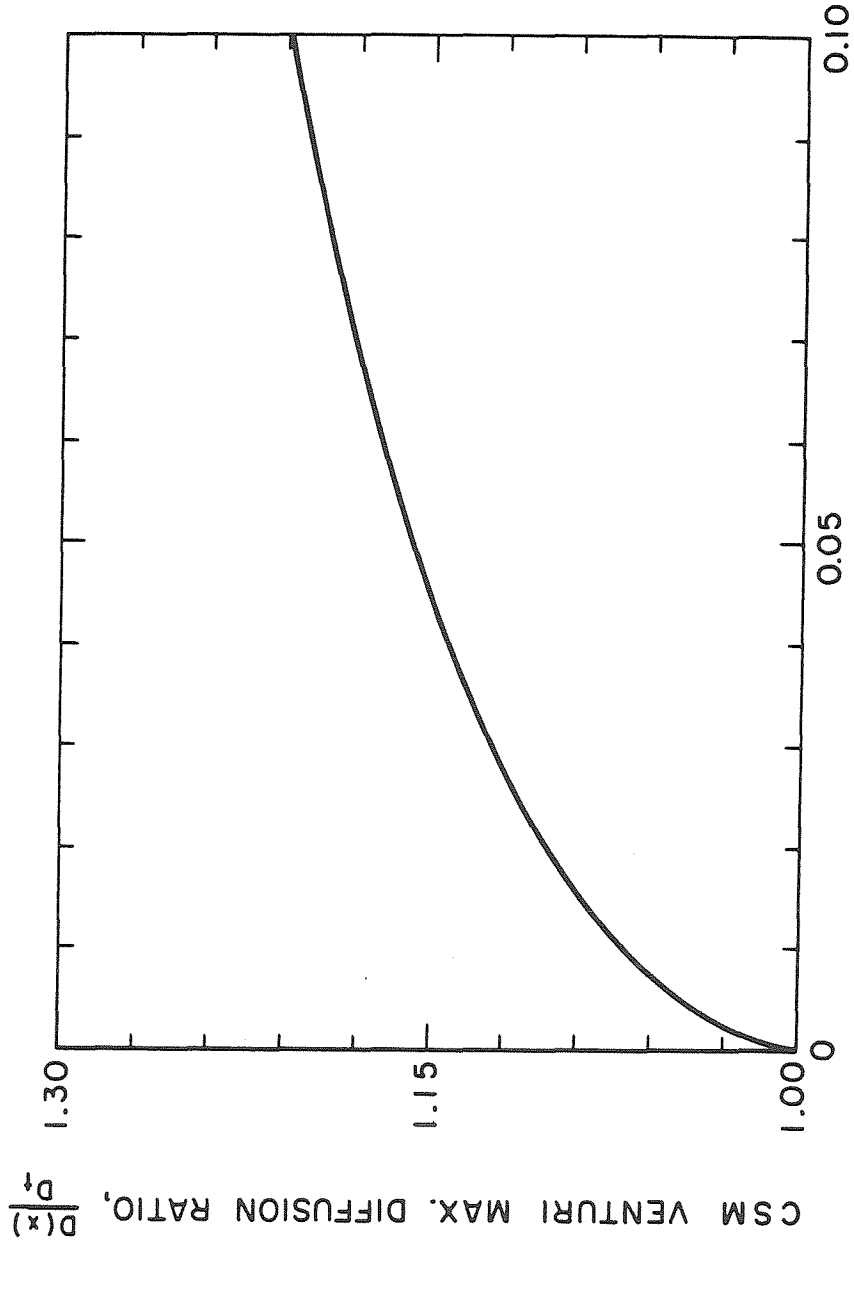

Figure 2.18. Maximum nominal diameter ratio $D(x)/D_t$ theoretically attainable according to Stratford's criterion in the diffuser of the venturi of Fig. 2.14 without incurring in laminar separation as a function of the distance x from the diffuser inlet.

Chapter 3. LDV DESIGN ANALYSIS

3.1. LDV General Configuration

In this section the main considerations and electro-optical analysis are presented which led to the design of the LDV used in the CSM. These considerations mostly concern the choice of the optical configuration and the connected problem of the LDV signal processing. Here the basic principles of operation of LDV's are recalled as required for clarity of the presentation, but a general knowledge of this subject is assumed. For more details the reader is referred to the vast literature available on this complex field (see, for example, Durst, Melling and Whitelaw, 1981).

Laser Doppler velocimetry is a photoelectric interferometric technique for determining the velocity of suspended optical scatterers in transparent fluids. The velocity is measured from the frequency of the signal generated by the scatterer motion through an interference fringe pattern. Presently LDV's can be divided in three categories according to the way this interference pattern is created by the intersection of two coherent light beams:

- reference beam configuration, where the unperturbed light of a weaker reference beam interferes with the light scattered from a stronger scattering beam at their intersection;
- dual beam configuration, where the light scattered from two intersecting beams of about equal intensity is collected and combined to generate the interference signal;
- two-scattered beam configuration, where the light scattered from a point on a single beam is collected in two symmetric directions about the optical axis and combined to create the interference signal.

The first configuration was also historically the first to be developed and is sometimes considered more advantageous in fluids containing a high density of scatterers. The optical aperture for the collection of the scattered light must be

limited to a relatively small angle in order to obtain good signal quality. The dual-beam configuration does not suffer from this limitation and is generally thought to be superior, especially in fluids with low concentration of scatterers. The last arrangement is rarely used because it is more complex to implement and does not seem to present significant advantages over the others.

With respect to the location of the receiving optics relative to the light source LDV systems can be categorized as operating in forward-scattering or back-scattering mode. The relative merits of these two modes mostly depend on the radius r_s of the scatterer with respect to the wave length λ of the illuminating radiation. Forward-scattering is more efficient in the Mie scattering regime occurring when $r_s \ll \lambda$ because in this case most of the scattered light propagates forward. The reverse happens in the Rayleigh scattering regime when $r_s \gg \lambda$ and therefore back-scattering is preferable in this case. The back-scattering configuration also has the advantage that it can be implemented using the same optics for focusing the illuminating radiation and collecting the scattered light, thereby greatly simplifying the problem of ensuring the coincidence of the focal points of the collimating and receiving optics.

At the CSM throat the number of scatterers on the beam path is not expected to be high in consideration of the small size of the flow. The average radius of the scatterers cannot be anticipated with any degree of accuracy, since it depends on the individual characteristics of the sampled water and no artificial seeding can be used without greatly interfering with the water quality measurement. However, cavities will clearly be present at the end of the throat section as long as measurements with the CSM can be made. Since the pressure gradient in the throat section is ideally zero, so is the slip velocity of the two phases and the cavities themselves can therefore be safely used as velocity tracers. Their size is expected to be much larger of the wave length of the impinging radiation (632.8 nm for a He-Ne gas laser) as a consequence of their growth under the influence of the applied tension. In view of these considerations a dual beam LDV operating in back-scattering configuration has been selected for measuring

the CSM throat velocity.

For this arrangement the Doppler frequency of the LDV signal is expressed by:

$$f_D = \frac{2Um\sin\varphi}{\lambda_o} \tag{3.1}$$

where φ is the semi-aperture angle of the two intersecting beams, λ_o is the wave length of the beams in vacuum, m is the index of refraction of the optical medium and U is the velocity component perpendicular to the optical axis in the plane of the two beams. The fringe spacing is:

$$s_{fr} = \frac{\lambda_o}{2m\sin\varphi} \tag{3.2}$$

while clearly the number of fringes is given by:

$$N_{fr} = \frac{d_x}{s_{fr}} = \frac{d_x f_D}{U} \tag{3.3}$$

where d_x is the size of the LDV probe volume in the flow direction.

The Doppler frequency and the fringe spacing are not affected by the refraction of the two beams through a plane interface separating two optical media with index of refraction m and m', because in this case from Snell's law: $m\sin\varphi = m'\sin\varphi'$, where φ' is the beam semi-aperture angle in the second medium. This result can be easily generalized to the case of a sequence of planar, parallel interfaces. Also note that the Doppler frequency is only sensitive to the orientation of the impinging radiation in the plane of the two beams, which coincides with the meridional plane of the CSM venturi. Within the limits of gaussian or paraxial optics the effects due to the cylindrical geometry of the venturi optical interfaces can be separately analyzed in the meridional and cross-sectional planes. The curvature of these interfaces in the cross-sectional plane produces therefore a refraction of the impinging beams in the same plane but has no effect on the direction of the beam propagation in the meridional plane. The above considerations imply that the LDV Doppler frequency only depends on the venturi geometry in the meridional plane and that its relation to

the velocity is the same in air as it is in the CSM flow, provided that the walls of the venturi are parallel. This is a very fortunate situation, since it implies that the calibration of the LDV can be carried out in air and that its results can be directly extended to the flow in the CSM venturi.

3.2. LDV Signal Processing

The measurement of the Doppler frequency can be made either in the time domain or in the frequency domain. The most commonly used methods are:

- spectrum analyzers;
- frequency trackers;
- frequency counters.

Frequency spectrum analyzers require a signal with low drop-out rate and are less sensitive to noise, but have the disadvantage of destroying the information individually contained in each Doppler burst. They also require the analysis of relatively long signals and some care is necessary in the interpretation of their results due, among other things, to frequency broadening effects.

These disadvantages are not present in frequency counters, which operate in the time domain. Each burst is recognized, isolated and its Doppler frequency is counted by comparing the LDV signal to properly adjusted threshold levels. For proper operation frequency counters necessitate of a relatively strong, noise-free signal with high drop-out rate and the maximum frequency that can be measured is more severely limited by the speed of the counting electronics.

In the CSM it is imperative to preserve the information on the individual bursts if the LDV signal is to be used to measure the flow velocity and to monitor the occurrence of cavitation at the same time. In addition, the drop-out rate and the signal level are expected to be high, at least as long as tiny cavities are used as velocity tracers. Therefore a frequency counter has been selected for measuring the LDV Doppler frequency.

3.3. LDV Optical Design and Analysis

A few other considerations must be kept in mind in the optical design of the LDV. For the flow velocity range expected at the venturi throat (about 15 m/s) the Doppler frequency is relatively large, unless the angular separation of the two beams is dramatically reduced. Beyond about 1 or 2 MHz it becomes increasingly difficult to measure the Doppler frequency with a counter incorporating today's "off the shelf" electronic technology. In order to decrease the Doppler frequency below this limit the CSM optics must be capable to reduce the angle between the two interfering beams to about 0.01 rad or lower. Furthermore, the best LDV signal quality is obtained when the fringe spacing is of the same order of magnitude as the size of the scatterer, whose characteristic dimensions cannot be safely anticipated. It seems therefore advisable to keep the beam separation adjustable within a relatively large range.

The above considerations led to the arrangement schematically shown in Fig. 3.1 for the dual beam back-scattering LDV used to measure the CSM throat velocity. The laser beam, generated by a 5 mw He-Ne continuous wave laser (L), goes through a beam displacer (dove prism, BD) and a metal-coated beamsplitter cube (BS). The separation of the two outcoming beams can be widely adjusted using the beam displacer to change the transversal position of the beam entering the beamsplitter. In order to reduce the Doppler frequency of the LDV signal and consequently simplify the processing electronics, the beam separation is then four times reduced by a telescopic lens relay (L1 and L2). After passing through a slit in the front surface mirror (M), the two beams are finally focused by the lens (L3) to the test section of the CSM venturi tube (VT).

The back-scattered light is then collected by the whole aperture of the same lens (L3) and mostly reflected by the front surface mirror (M) towards the photomultiplier collimating lens (L4). The resulting image of the test section is filtered by a field stop aperture (FS) to reduce the optical background noise and finally reaches the photomultiplier tube (PM), where it is converted into an

electric signal. All lenses have a back focal length of 200 mm, except the second lens (L2) of the telescopic relay, whose focal length is 50 mm.

Since the deviation of the laser beams from the optical axis is small, the theory of propagation of paraxial gaussian beams can now be used to analyze the optical system in order to deduce the focal volume and the expected number of fringes of the LDV signal. The first step in this process consists in the computation of the ray transfer matrix:

$$\underline{A} = \begin{bmatrix} a & b \\ c & d \end{bmatrix} \tag{3.4}$$

of the optical system. The propagation of a ray through an optical system can be described in terms of the modifications of its distance r from the optical axis y and of its slope r'. In the paraxial approximation the output ray parameters (subscript 2) are linearly related to the input ones (subscript 1) through the ray transfer matrix:

$$\begin{vmatrix} r_2 \\ r_2' \end{vmatrix} = \underline{A} \begin{vmatrix} r_1 \\ r_1' \end{vmatrix} \tag{3.5}$$

From this definition it follows that the ray transfer matrix of a system of n optical elements $a_1, \ldots a_n$ in the direction of propagation is simply equal to the product of the individual ray transfer matrices of each element: $\underline{A} = \underline{A}_n \cdots \underline{A}_1$. In particular, the ray transfer matrices for the transmission of a beam over the distance Δy and for a thin lens with back focal length f in air [Kogelnik and Li, 1966] are:

$$\underline{A}_t = \begin{bmatrix} 1 & \Delta y \\ 0 & 1 \end{bmatrix}; \qquad \underline{A}_l = \begin{bmatrix} 1 & 0 \\ -1/f & 1 \end{bmatrix} \tag{3.6}$$

Then, with the data of Fig. 2.1, the ray transfer matrices of the focusing optics from the laser window to the LDV focal point and of receiving optics from the probe volume to the photomultiplier are:

$$\underline{A}_F = \begin{bmatrix} 0 & -800 \\ 1.250 \cdot 10^{-3} & -0.3063 \end{bmatrix}; \qquad \underline{A}_R = \begin{bmatrix} -1 & 0 \\ -4.5 \cdot 10^{-3} & -1 \end{bmatrix} \tag{3.7}$$

where optical lengths are in mm. The elements a and $-c$ of these matrices are respectively the magnification and the inverse of back focal length of the

optical system. As expected, the magnification of the receiving optics is equal to -1. Furthermore, the ray transfer matrix of the focusing optics gives the relation: $s = 800 \cdot \varphi$ between the initial semi-separation of the LDV beams in millimeters and the semi-aperture angle φ in radians. Thus, for a flow velocity $U = 15\,\mathrm{m/s}$ the Doppler frequency can be decreased to less than 200 kHz with a beam separation of a few millimiters, still large enough to be achieved with a cube beamsplitter.

In the theory of paraxial optics the propagation of a gaussian beam is expressed in terms of the complex beam parameter [Kogelnik and Li, 1966]:

$$\frac{1}{q} = \frac{1}{R} - i\frac{\lambda}{\pi w^2} \tag{3.8}$$

where R is the radius of curvature of the beam wave front and w is the beam radius, defined as the distance from the beam axis where the field amplitude drops to $1/e$ times its maximum value. At the beam waist the wave front curvature is zero and the beam radius is minimum. The size and location of the beam waist depend on the internal geometry of the laser optics: in the Spectra Physics He-Ne gas laser model Stabilite 120 to be used in the CSM the beam waist radius is $w_o = 0.325\,\mathrm{mm}$ and coincides with the output window of the laser. In the propagation of a gaussian beam through an optical system with ray transfer matrix $\underline{A}$ the complex beam parameter at the output q_2 is related to the input value q_1 by [Kogelnik and Li, 1966]:

$$q_2 = \frac{aq_1 + b}{cq_1 + d} \tag{3.9}$$

From this equation and the above results the beam radius and the curvature of the wave front at the LDV focal point are: $R_f = 2.61\,\mathrm{m}$ and $w_f = 0.496\,\mathrm{mm}$.

In the final operational configuration of the LDV the beam angular semi-separation is $\varphi = 5.27 \cdot 10^{-3}\,\mathrm{rad}$ and the fringe spacing $s_{fr} = 60\,\mu\mathrm{m}$, which experience has shown to give the best results. With this choice the axes of the LDV focal ellipsoid are: $d_x = 2w_f/\cos\varphi = 0.992\,\mathrm{mm}$ in the direction of the

flow, $d_y = 2w_f / \sin\varphi = 188\,\text{mm}$ in the direction of the optical axis, $d_z = 2w_f = 0.992\,\text{mm}$ in the vertical direction.

Then the number of fringes and the duration (gate time) of a typical Doppler burst can be estimated to be $N_{fr} = d_x/s_{fr} \simeq 17$ and $T_g = d_x/U \simeq 66\,\mu\text{s}$. Clearly the fringe spacing must be as uniform as possible throughout the LDV focal volume in order to obtain consistent velocity readings regardless of the location of the scatterer's trajectory. For this to happen the beam divergence angle $w_f/R_f = 1.90 \cdot 10^{-4}\,\text{rad}$ must be much smaller than the angular semi-separation φ between the two beams. This condition is indeed satisfied in the configuration examined here.

Finally, since the magnification of the receiving optics is equal to -1, the diameter of the photomultiplier field stop aperture should be about 1 mm. However, in practice better results have been obtained with larger field stop apertures, probably because of the magnification of the focal point image in the cross-sectional plane caused by the cylindrical geometry of the venturi tube.

Note that for a throat diameter $D_t = 1\,\text{mm}$ the LDV focal volume extends far across the venturi walls in the direction of the optical axis and also covers the whole throat in the vertical direction. Therefore the LDV signal can effectively monitor the occurrence of cavitation, but at the same time velocity readings in the boundary layer are likely to occur. This situation is taken into account in the reduction of the data in order to introduce the appropriate corrections when necessary. The occurrence of velocity readings in the boundary layer also provides a direct way to check the presence of a potential core in the flow at the venturi throat, which is essential for the correct deduction of the throat pressure (see Chapter 5).

In theory the intensity of the LDV output signal could now be estimated from the laser power, the transmittance of the optical system, the focal point dimensions and the photomultiplier's sensitivity. However, in practice the scattering and collecting efficiencies are too uncertain for a useful estimate to be made because they depend in a very complex way on the optical and geometri-

cal properties of both the tracer itself and of the collecting optics.

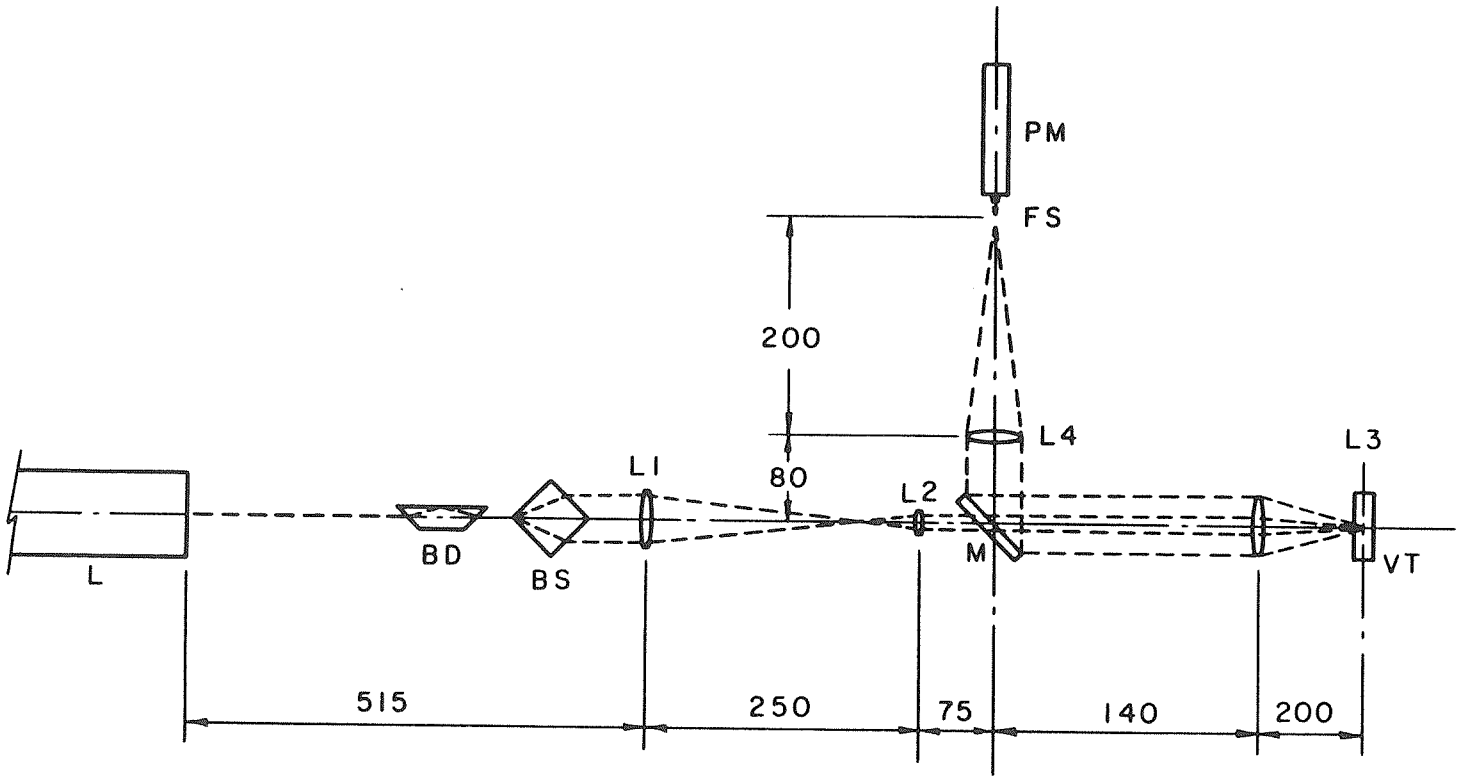

Figure 3.1. Schematic of the CSM optical components (dimensions in mm). Continuous wave laser (L), beam displacer (BD), beamsplitter cube (BS), telescopic relay lenses (L1 and L2), focusing and receiving lens (L3), venturi tube (V), front surface mirror (M) with slit for transmission of laser beams, photomultiplier collimating lens (L4), field stop aperture (FS), photomultiplier tube (PM).

Chapter 4. CSM EXPERIMENTAL APPARATUS

4.1. General Description

The CSM experimental apparatus can be divided into the following subsystems:

- fluidic circuitry, for the flow management and control;
- optics (LDV), for the measurement of the throat velocity and the detection of cavitation;
- electronic Signal Processor, for real time data collection and temporary storage;
- instrumentation, both fluidic and electronic, for data measurement, system's operation monitoring, and data reduction.

A general view of the experimental apparatus is shown in Fig. 4.1. The electronic instrumentation rack is on the left, the data acquisition and reduction computer is in the center and the optical and fluidic components of the CSM are in the foreground on the right. The connections of the various parts comprising the CSM are illustrated in Fig. 4.2. The water from the water inlet (WI) passes through the sampling valve (SV), the venturi tube (VT), the exhaust valve (EV) and is finally collected in the exhaust tank (ET). The pressure in the exhaust tank is kept constant by the regulated air pressure line (RA), which is used to control the flow rate and therefore the pressure generated at the throat of the venturi. The static pressure of the sampled water is measured by a pressure transducer (UPT) located upstream of the test venturi. Provisions have been made for the installation of a second pressure transducer downstream of the CSM test section to monitor also the exhaust pressure, if necessary. Periodically the sampled water is removed from the exhaust tank through the return valve (RV) and the water return line (WR) by increasing the regulated air pressure. During test runs the dual beam back-scattering Laser Doppler Velocimeter (LDV) monitors the occurrence of cavitation and the flow velocity at the throat

of the transparent venturi (VT). The LDV signal is band-pass filtered and sent, together with the amplified output signal of the upstream pressure transducer, to the CSM Signal Processor. Here data relevant to CSM operation are generated and temporarily stored. At conclusion of each run they are transferred to the minicomputer for final acquisition, storage and reduction. The LDV signal is normally monitored by an oscilloscope and the signal of the upstream pressure transducer by a digital multimeter.

4.2. CSM Fluidic Circuitry

The fluidic circuits of the CSM are shown in Fig. 4.3. The sampling water from the inlet (WI) passes through a three-way sampling valve (SV), which operates either the by-pass line or the CSM testing line to the venturi tube (VT), and is finally collected in the exhaust tank (ET). The flow is controlled by changing the pressure in the exhaust tank. During normal operation the three-way exhaust pressure valve (EPV) connects the exhaust tank to the regulated air line. The pressure in this line is measured by the mercury barometer (B) and can be controlled from 0 to 1.5 bar with the exhaust pressure regulator (EPR), which bleeds the excess air to the vacuum pump (VP) through the vacuum reservoir (VR) and the cryogenic water trap (WT). Alternatively, the exhaust pressure valve (EPV) can connect the exhaust tank to the high pressure line for periodically expelling the sampled water to the water return (WR) or for purging the water lines. The high pressure line originates from the high pressure regulator (HPR), which in turn is connected to the compressed air supply (CA) through an air filter (AF). The needle valve (NV) can be used to establish the slowly rising pressure in the exhaust tank necessary for proper operation of the exhaust pressure regulator. The the gauges (PG) and (VG) indicate the pressure in the vacuum reservoir and in the high pressure line.

The constant level tank (CLT) is used to calibrate and keep flooded the upstream pressure transducer. The water level in the tank is kept equal to the one of the venturi throat section, about 12.5 cm above the upstream pressure trans-

ducer, using the overflow line to the exhaust tank. Therefore the air pressure in the constant level tank is equal to the venturi throat pressure during operation and can be conveniently measured with the barometer (B) to calibrate or check the upstream pressure transducer. The constant level tank is normally connected to the exhaust pressure during CSM operation. Occasionally it can be opened to the atmosphere by properly switching the three-way valve (V3).

The four-way valve (V4) can connect together the upsteam pressure transducer, the constant level tank and the upstream section of the venturi in four possible configurations:

- Operation: for normal CSM operation: the upstream pressure transducer is connected to the venturi; the constant level tank is isolated;
- Calibration: for calibrating or checking the upstream pressure transducer: the upstream pressure transducer is connected with the constant level tank; the venturi is isolated;
- Refill: for refilling the constant level tank with water from the venturi: the upstream transducer is isolated; the venturi is connected to the constant level tank;
- Off: for shutting off the system: the venturi is connected to itself; the upstream pressure transducer and the constant level tank are isolated.

The bleed valve (BV) is used during CSM operation, when the pressure in the constant level tank is low, to purge the pressure transducer line of unwanted air bubbles. Finally, in the water trap (WT) a mixture of isopropanol and dry ice is used to condense most of the moisture contained in the air reaching the vacuum pump (VP) to prevent rusting.

4.3. CSM Optics

The lay-out of the dual beam back-scattering LDV used in the CSM is shown in Fig. 4.4, with the plant view at the top of the picture and the side view at the bottom. Two I-beams in a T-shaped configuration support both

the laser (1) and the base plate, where all the other optical components are installed. Most of the mounting and positioning equipment of the CSM elecro-optical and fluidic compoments, including the I-beams and the base plate, are made of black anodized aluminum. The holders of delicate optical parts (such as lenses, mirrors etc.) are made of softer materials, usually PVC. Plastic mounts are also used where electrical insulation is important, as for example in the case of the photomultiplier tube, whose outer shield is at high voltage (up to 1800 VDC) during normal operation.

The laser mount (2) allows fine positioning and orientation of the laser in both the horizontal and vertical planes for accurate and easy alignment of the beam. The beam displacer (3) is mounted on a micrometric lateral translation stage (4) which provides repeatable and accurate control of the separation of the two beams emerging from the beamsplitter cube (5). The distance between the two lenses of the telescopic relay (6 and 8) is also adjustable in order to insure perfect parallelism of the emerging beams. Similarly, the focusing lens (11) is mounted on a longitudinal translation stage, in order to allow coarse positioning and to compensate for possible deviations from its nominal focal length. Finally, the photomultiplier field stop aperture (22) can also be accurately positioned and locked along and about the optical axis for optimal reduction of the optical background noise.

The CSM glass venturi is connected with O-ring fittings to the hydraulic lines (16 and 9) for easy installation and removal. The whole CSM test section (18), including the hydraulic lines, can be finely translated, rotated and fastened in the horizontal plane and in the vertical transversal plane for accurate location of the venturi at the focal point of the optical system. The test section is also mounted on a transversal translation stage in order to allow the measurement of the flow velocity along the venturi's centerline. Pressure taps (17) are located in the water inlet and outlet of the test section and a ball valve (not appearing in Fig. 4.4) is mounted on the exhaust line. A comprehensive picture of the CSM optical set-up appears in Fig. 4.5 which shows the optical components installed

on the CSM base plate. Most of the fluidic components, on the other hand, are mounted below the base plate in order to protect the electro-optical equipment from the damaging effects of possible water spills.

Two types of glass venturi tubes have actually been used. The first type is an extremely fragile blown-glass venturi contained in a cylindrical shell of transparent acrylic resin for mechanical protection and connection to the hydraulic lines. Fig. 4.6 shows a detailed picture of this tube, whose throat diameter is about 1 mm. In what follows this tube will be indicated as tube No. 1. The second type of glass venturi, which will be referred to as tube No. 2, has much thicker walls and can therefore be directly connected to the hydraulic lines without mechanical protection. It is shown in detail in Fig. 4.7 and, installed in its positionable mount, in Fig. 4.8. The exhaust valve on the outlet water line appears in the foreground on the right. On the left is visible the pressure tap connection from the inlet water line to the upstream pressure transducer which is mounted underneath the base plate.

The characteristics of the passive optical components are:

- dove prism, Melles Griot No. 01 PDE 005/079, 84.5 × 20 mm, 2λ flat, anti-reflection coated;
- metal-dielectric beamsplitter cube, Melles Griot No. 03 BSC 015/079, 50.8 × 50.8 × 50.8 mm, 2λ flat, anti-reflection coated;
- first plano-convex spherical glass lens of the telescopic relay, Melles Griot No. 01 LPX 277/079, $f = 200$ mm, $\phi = 50$ mm, anti-reflection coated;
- second plano-convex spherical glass lens of the telescopic relay, Melles Griot No. 01 LPX 107/079, $f = 50$ mm, $\phi = 20$ mm, anti-reflection coated;
- focusing and receiving plano-convex spherical glass lens, Melles Griot No. 01 LPX 277/079, $f = 200$ mm, $\phi = 50$ mm, anti-reflection coated;
- two front surface rectangular mirrors, Ealing Corp. No. 23-4187, $\lambda/4$ flat, 25.4 × 76.2 × 9.65 mm;

- photomultiplier focusing bi-convex spherical glass lens, Ealing Corp. No. 23-8964, $f = 200\,\text{mm}$, $\phi = 50\,\text{mm}$.

Note that all optical components, except the venturi tube and the photomultiplier focusing lens, have a multilayer anti-reflection coating which reduces their reflection losses from about 4% to less than 0.5%. The transmissivity of the beamsplitter cube (BS) is about 45% per each outcoming beam due to the metal film coating at the splitting surface.

4.4. CSM Signal Processor

The custom-made CSM Signal Processor responds to the band-pass filtered LDV signal from the photomultiplier and to the amplified output of the upstream pressure transducer. The photomultiplier generates a burst when an inhomogeneity such as a cavity or a suspended particle scatters light during its motion through the LDV focal point. After band-pass filtering this burst ideally consists of a Doppler carrier frequency modulated by a Gaussian-shaped envelope. The Doppler frequency is proportional to the velocity of the scatterer. The amplitude of the burst's envelope is instead mostly related to the size of the scatterer, although it also depends in a complex way on its shape, optical properties and on the location of its trajectory through the LDV focal point. The CSM Signal Processor uses the intensity and the Doppler modulated frequency of the LDV bursts to respectively monitor the occurrence of cavitation and to measure the flow velocity. The instantaneous upstream pressure of the water is provided by the output of the pressure transducer.

A simplified block diagram of the CSM signal processing and data acquisition is shown in Fig. 4.9. The output of the photomultiplier is band-pass filtered for separating the Doppler frequency from the electronic noise and sent to the CSM Signal Processor, where it is amplified before entering the threshold circuits. Here a zero level and two couples of adjustable, symmetric threshold levels are used to reject the residual noise and to discriminate valid Doppler bursts coming from a velocity tracer from the ones coming from a cavitation event. For

simplicity cavitation events will be indicated as bubbles and velocity tracers as particles, although in practice smaller cavities probably represent the majority of the velocity tracers recognized by the Signal Processor in the flow at the venturi throat. A burst whose amplitude is contained between the smaller couple of threshold levels (particle thresholds) and the larger one (bubble thresholds) is considered to be coming from a velocity tracer. A cavitation event is recognized when the burst amplitude exceeds the bubble thresholds and a preset minimum number of fringes is counted. The LDV signal not exceeding the smaller couple of threshold levels (particle thresholds) is rejected as noise.

This information is used to deduce the occurrence time of valid bursts from the run's Elapsed Time Counter (ETC) and to increment the cavitation event counter (Bubble Address Counter, BAC), whose capacity is adjustable from 1 to 1024. A CSM run is normally concluded when the capacity of the Bubble Address Counter is exceeded, unless it has already been terminated by overtime or externally by the operator. The same threshold levels are also used in proper sequence to reject the spurious zero crossings which may be caused by the presence of high frequency noise in the LDV signal and to operate the Particle Address Counter (PAC) for the storage of particle data and the counters for measurement of the duration (Particle Duration Counter, PDC) and the number of zero crossings (Zero Crossing Counter, ZCC) of each valid burst coming from a velocity tracer.

During a CSM run the Signal Processor generates, collects and temporarily stores in real time the following data:

- when a cavitation event is recognized:
  - the occurrence time measured from the beginning of the run (bubble elapsed time, T_b), represented by a 24 bit digit with 50 μs resolution;
- when a velocity tracer is recognized:
  - the occurrence time measured from the beginning of the run (particle elapsed time, T_p), represented by a 12 bit digit with 204.8 ms resolution;

- the duration of the Doppler burst (particle gate time, T_g), represented by a 12 bit digit with 50 ns resolution;
- the number of zero crossings of the Doppler burst N_{zc}, represented by a 12 bit digit;
- the upstream water pressure p_u, represented with 12 bit resolution over the transducer range (about 1 bar).

The resident memory of the CSM Signal Processor is organized in 9 Kbytes, where the data are written in order of acquisition according to the following map:

kbyte No.	High Nibble/Low Nibble
1	Bubble Time Low Byte
2	Bubble Time Mid Byte
3	Bubble Time High Byte
4	Particle Time Low Byte
5	Particle Duration Low Nibble/Particle Time High Nibble
6	Particle Duration High Byte
7	Zero Crossing Low Byte
8	Upstream Pressure High Nibble/Zero Crossing High Nibble
9	Upstream Pressure Low Byte

When the capacity of the particle data registers is exceeded during a run the storage of the following data continues starting from the first memory location of each Kbyte and the pre-existing data are lost. This situation cannot occur for bubble data because the CSM run is automatically terminated when the bubble count exceeds 1024 at most. At the conclusion of each run the data collected by the CSM Signal Processor can be serially transferred at the operator's request to the microcomputer for final acquisition, storage on a magnetic disk and reduction.

The CSM Signal Processor is installed inside a slide mounted drawer in a standard relay rack together with the rest of the CSM electronic instrumenta-

tion. It consists of a power supply and a modular bus frame containing three electronic boards (see Fig. 4.10). The electrical connections to the photomultiplier, to the pressure transducer and to the computer are mounted both on front panel and the rear side of the bus frame. Also mounted on the front panel are the Signal Processor's commands and controls: the power switch; the push-buttons for system reset, run start, run stop, data unloading to the computer; the light indicators of power on, of the execution of the run and of the data unloading operations.

A more detailed description of the CSM Signal Processor operation and a general overview of its most important components can be found in Appendix 1.

4.5. CSM Instrumentation

Most of the CSM electronic instrumentation is mounted in the standard relay rack of Fig. 4.11. Besides the CSM Signal Processor itself, it includes:

- the photomultiplier power supply: Power Design High Volatage Calibrated DC Power Source, Model 2K20, 1 – 2000 V, 20 mA;
- the He-Ne laser exciter: Spectra Physics 256;
- the electronic filters, Krohn-Hite Solid State Variable Filter, Model 3202(R), 20 Hz - 2 MHz;
- an oscilloscope, for monitoring the LDV input signal to the CSM Signal Processor: Tektronix, Model 465B;
- the pressure transducer exciter and amplifier: Vishay Strain Gage Conditioning Amplifier, 2300 Series;
- a multimeter for calibrating the pressure transducer output: HP Digital Multimeter, Model 3465B.

The instrumentation not mounted in the electronic rack includes:

- the He-Ne laser: Spectra Physics Stabilite TM, Model 120;
- the photomultiplier tube: RCA type 8645;

- the data acquisition and reduction microcomputer: a Compaq Plus Desktop personal computer, with a total resident memory of 640 Kbytes, a video screen display and two 5.25 in diameter floppy disk drives (see Fig. 4.11);
- a function generator, occasionally used to simulate the LDV signal and to set the thresholds of CSM Signal Processor: Exact Function Generator, Model 519G;
- an optical pick-up (see Sec. 4.6), for LDV calibration;
- a LDV calibration unit (see Sec. 4.6), also used for LDV calibration;
- the upstream pressure transducer: Gould Instruments Statham Absolute Pressure Transducer, 0 to 22 psia, 5 V, 350 Ω;
- a mercury barometer, for calibrating the upstream pressure transducer and monitoring the exhaust pressure;
- the vacuum pump.

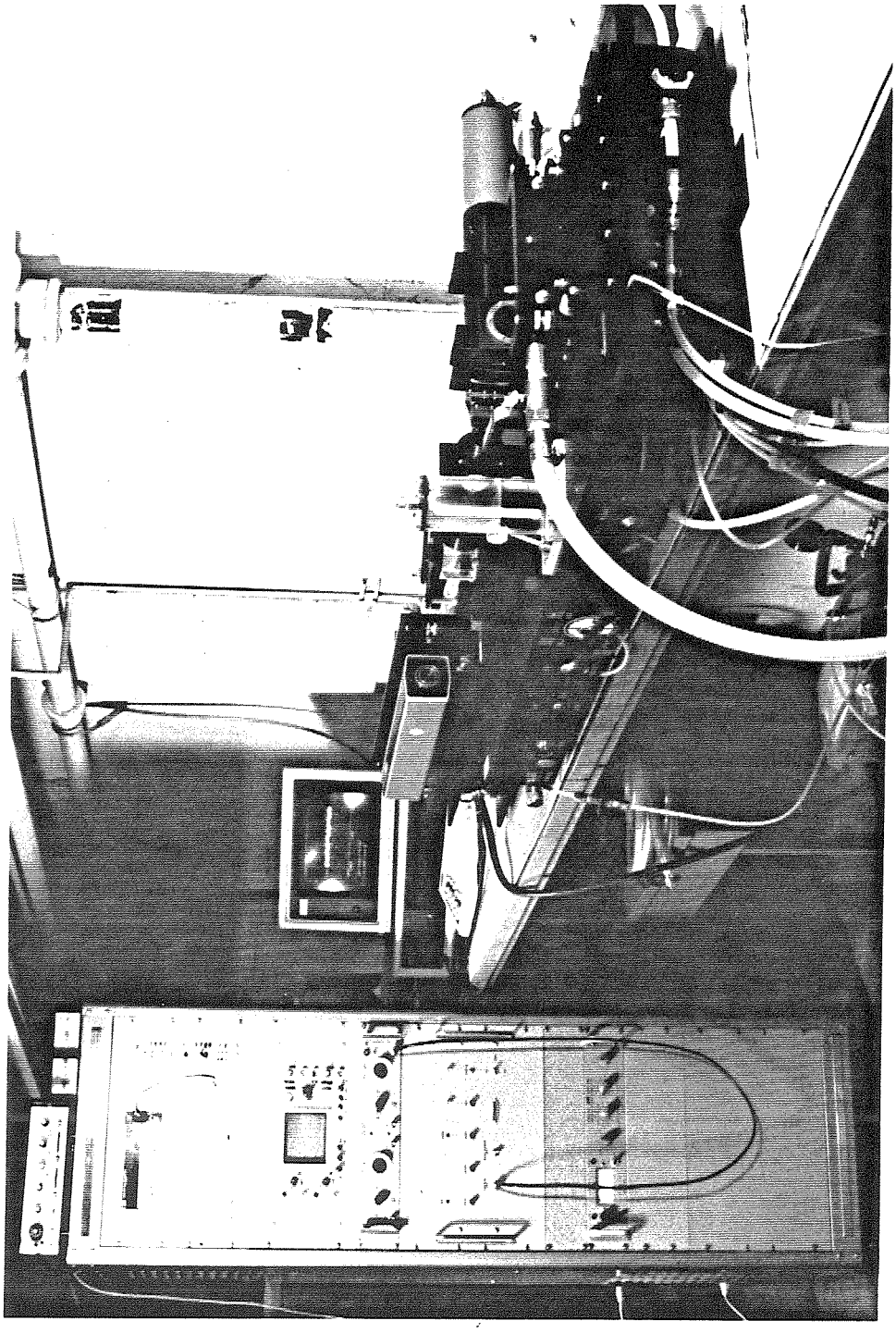

Figure 4.1. General view of the CSM experimental apparatus. In the foreground on the right: the I-beams supporting the laser and the baseplate where most of the optical and fluidic components are mounted. In the background: the electronic instrumentation rack (left) and the data acquisition computer (center).

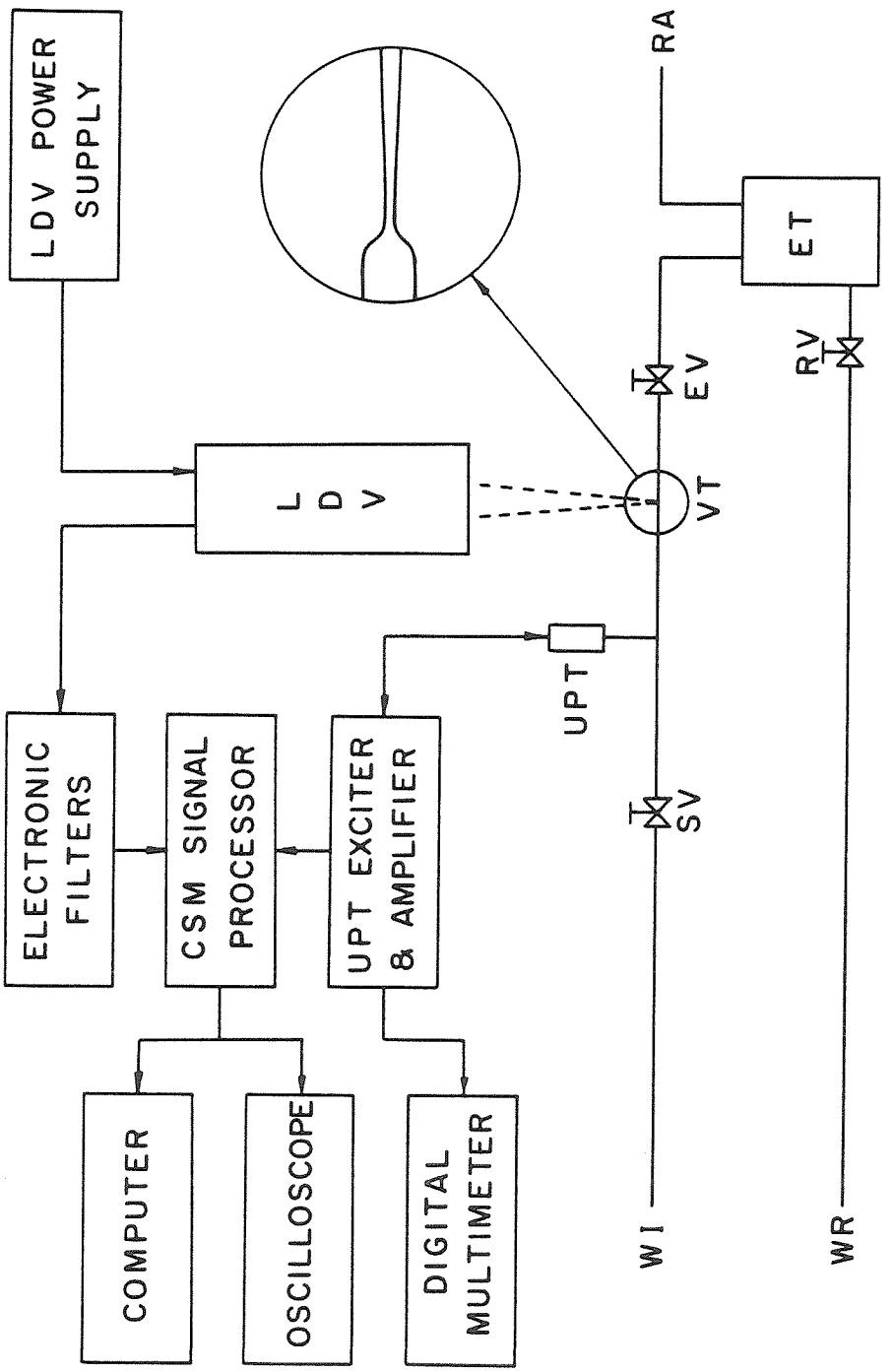

Figure 4.2. Schematic of the various components of the CSM experimental apparatus: water inlet (WI), sampling valve (SV), upstream pressure transducer (UPT), venturi tube (VT), exhaust valve (EV), exhaust tank (ET), regulated air pressure line (RA), return valve (RV), water return (WR), laser Doppler velocimeter (LDV).

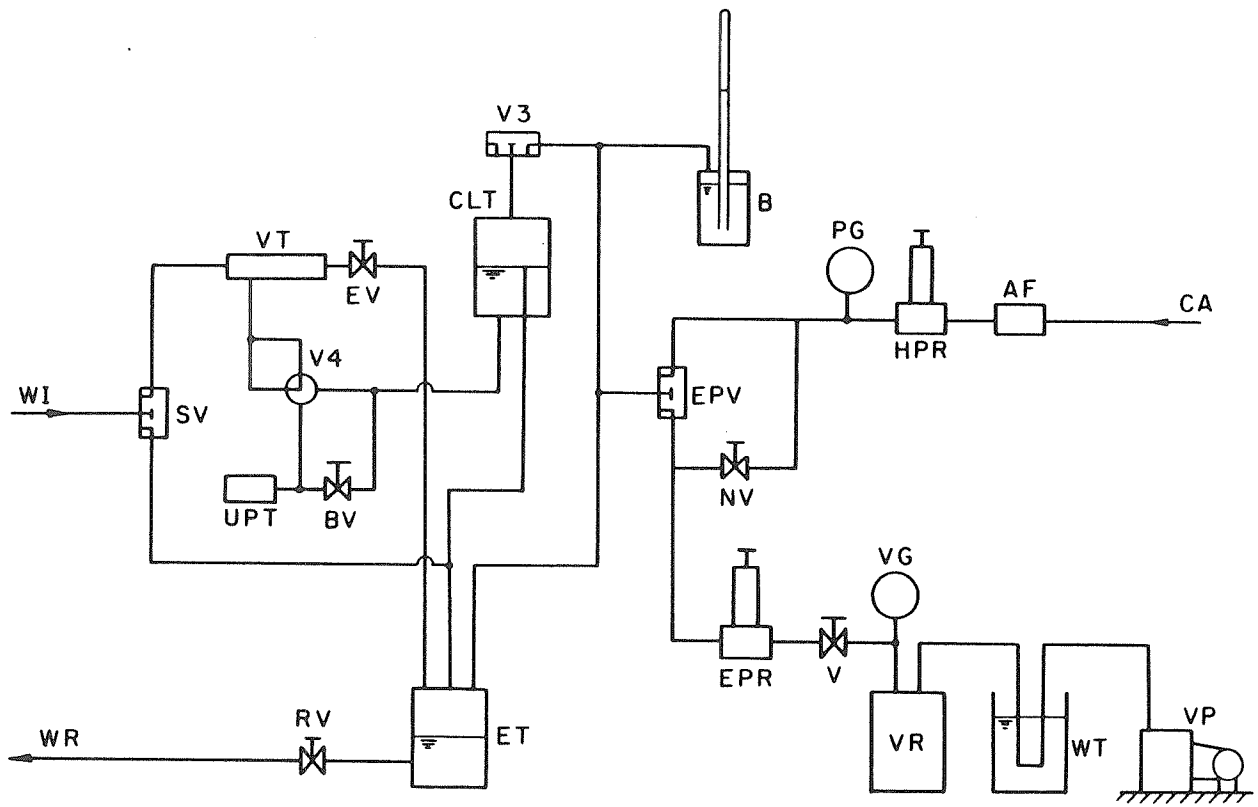

Figure 4.3. Schematic of the CSM fluidic circuits: mercury barometer (B), bleed valve (BV), compressed air supply (CA), constant level tank (CLT), exhaust valve (EV), exhaust tank (ET), exhaust pressure valve (EPV), exhaust pressure regulator (EPR), air filter (AF), high pressure regulator (HPR), needle valve (NV), pressure gage (PG), return valve (RV), three-way sampling valve (SV), vacuum gage (VG), vacuum pump (VP), vacuum reservoir (VR), venturi tube (VT), three-way valve (V3), four-way valve (V4), water inlet (WI), water return (WR), water trap (WT).

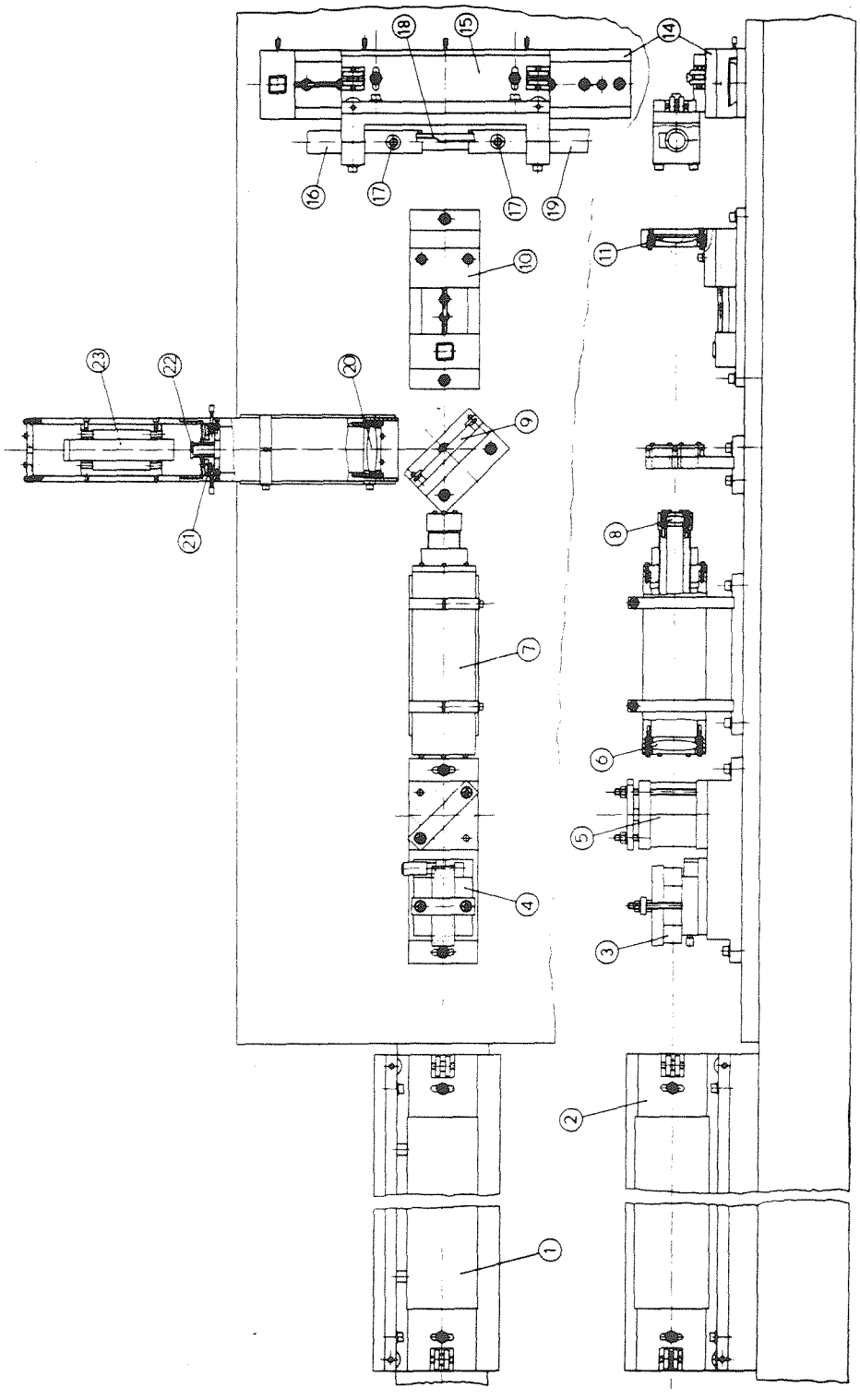

Figure 4.4. Machine drawing of the CSM optical lay-out, top and side views: laser (1) on its mount (2), beam displacer (3) on its micrometric side translation stage (4), beamsplitter cube (5), lenses (6 and 8) of the telescopic relay (7), front surface mirror (9), longitudinal translation stage (10) of the focusing and receiving lens (13), transverse translation stage (14) of the venturi tube mount (15), inlet (16) and outlet (19) lines of the venturi tube (18), pressure tap (17), photomultiplier collimating lens (20), mount (21) of the field stop aperture (22), photomultplier (23).

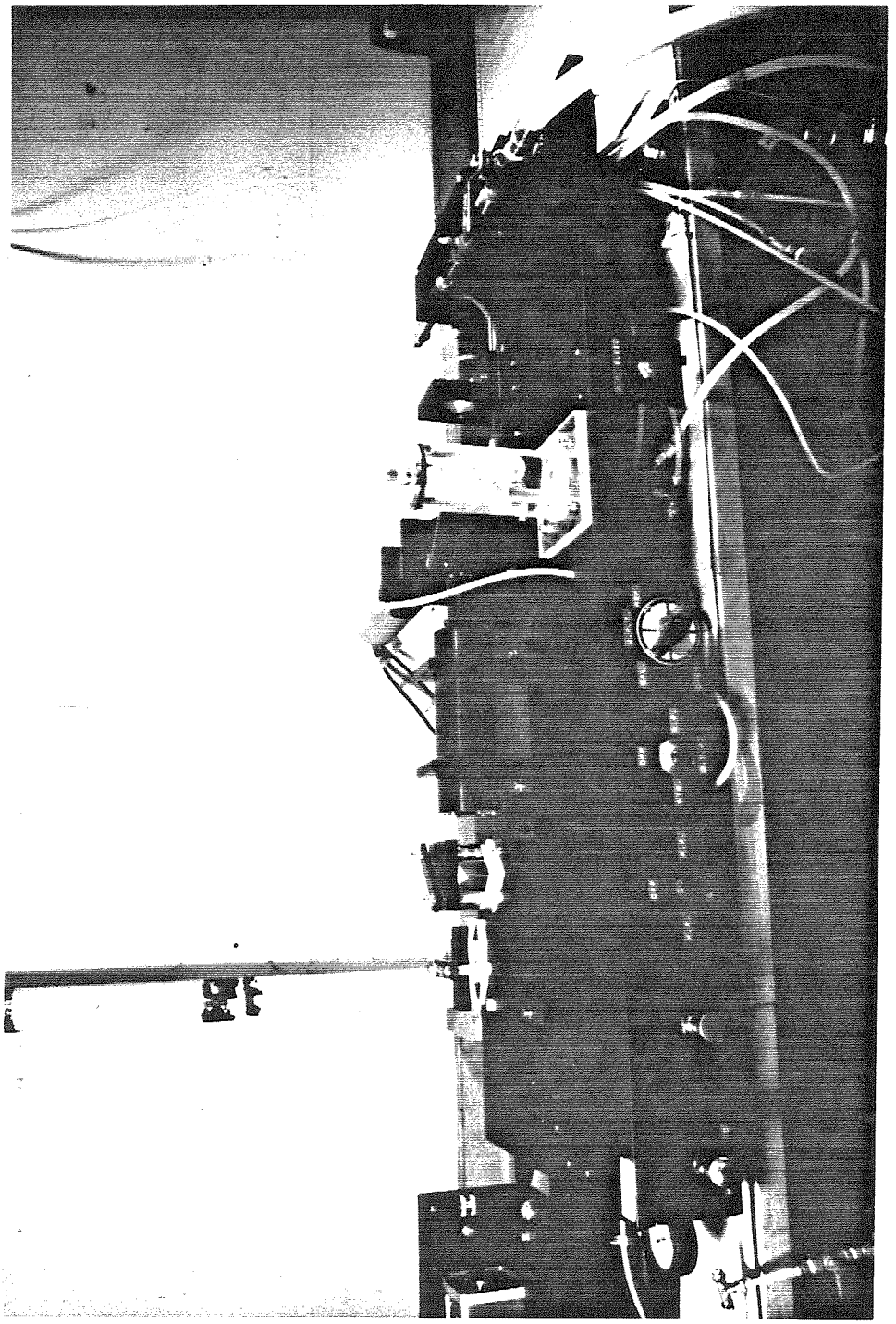

Figure 4.5. General view of the CSM optical set-up. The optical components are mounted on the baseplate in the center, while most of the fluidic components are mounted below it. The laser installed on its positionable mount on the longitudinal I-beam is barely visible on the left edge of the picture.

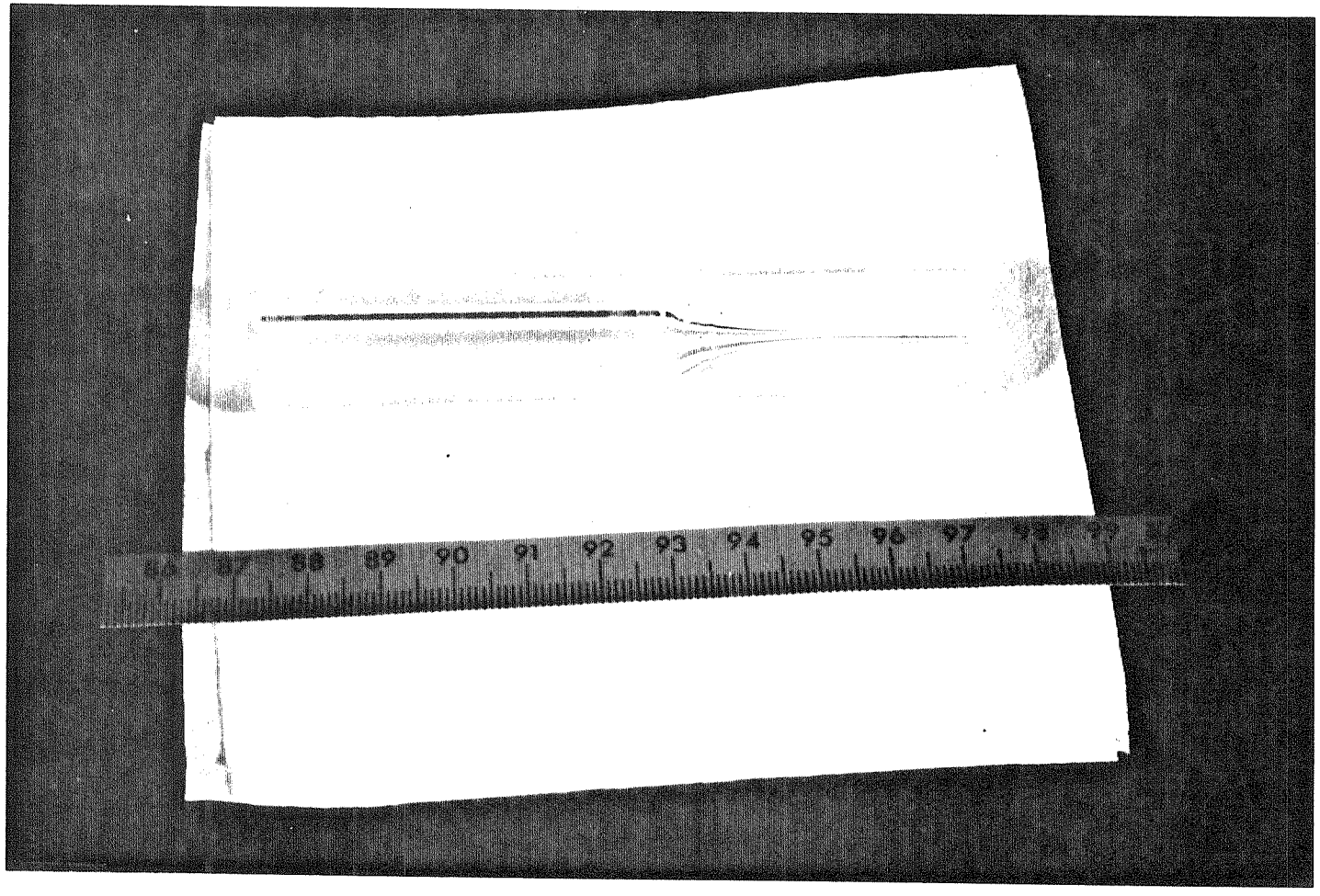

Figure 4.6. Close-up view of CSM venturi tube No. 1. A cylindrical shell of cast transparent resin contains the glass-blown venturi tube for mechanical protection and easy installation. The contraction ratio of the tube is about 1/100, the throat diameter is about 1 mm and the exit diameter is about 1.2 mm.

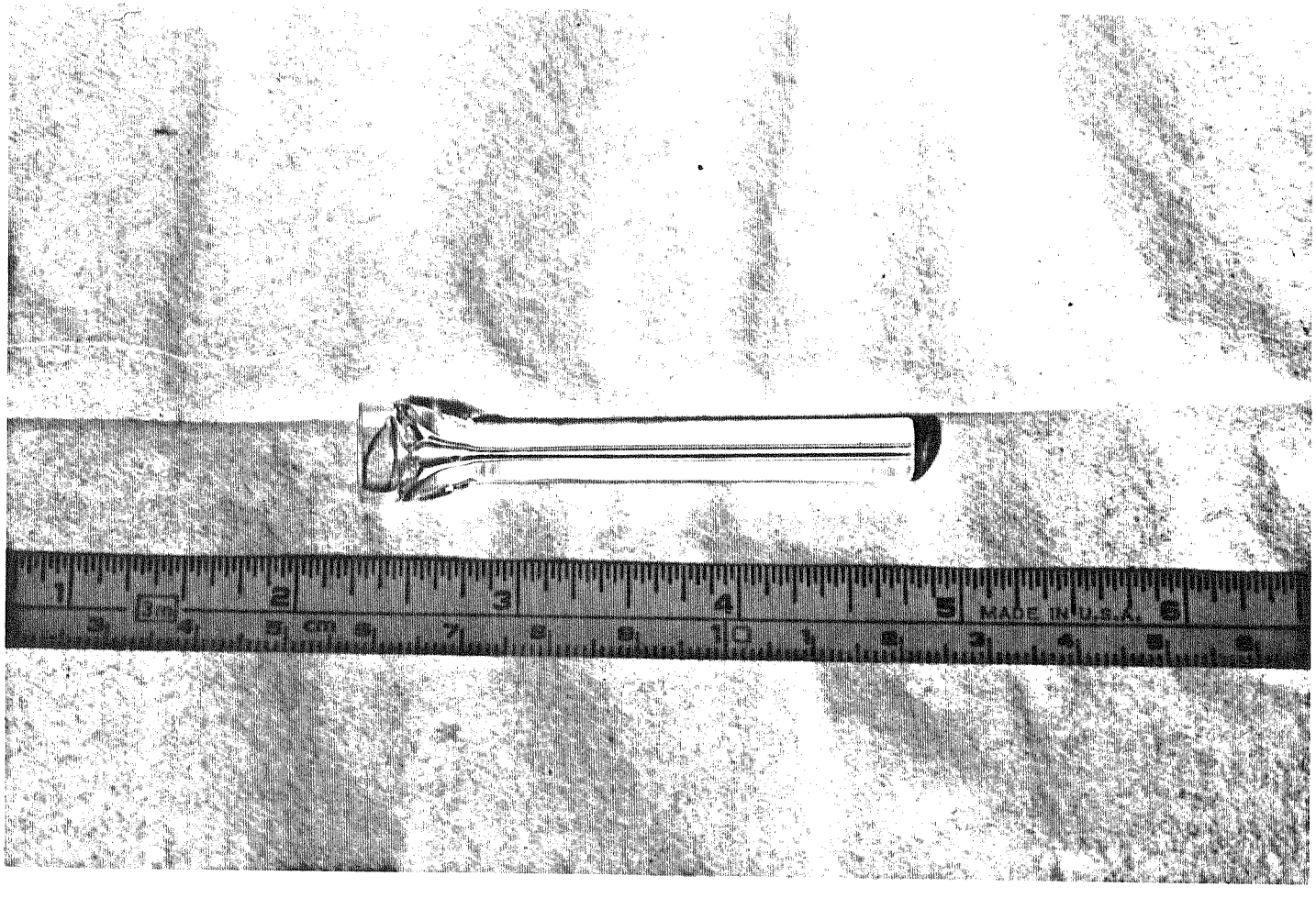

Figure 4.7. Close-up view of CSM venturi tube No. 2. This blown-glass venturi has thicker walls, a contraction ratio of about 1/100, a throat diameter of about 1 mm, a long straight section after the diffuser and an exhaust diameter of about 1.2 mm.

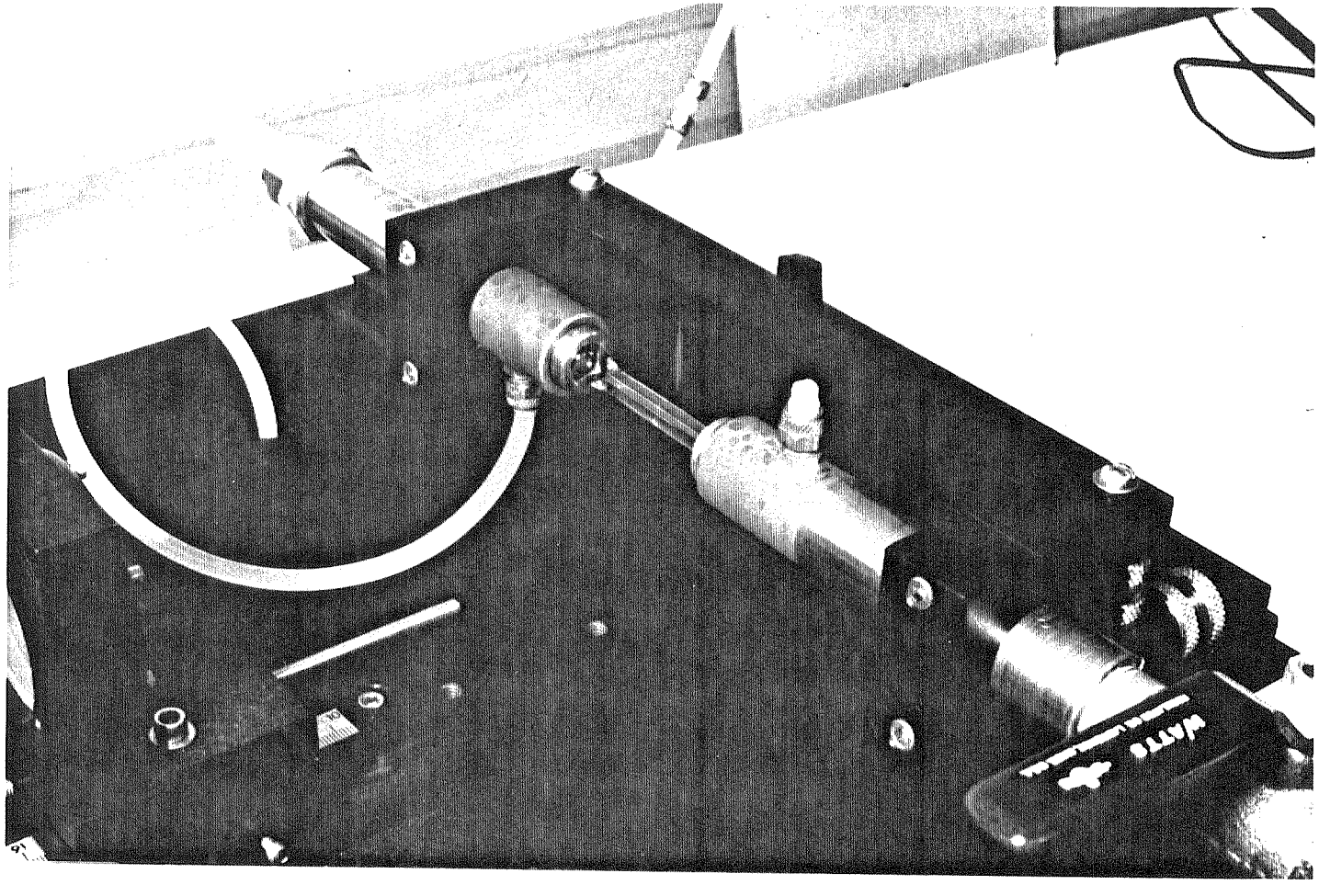

Figure 4.8. Detailed view of the CSM venturi tube No. 2 installed in its positionable mount at the LDV focal point. On the left: the pressure tap connection from the inlet water line to the upstream pressure transducer mounted below the baseplate. On the bottom right corner of the picture is the exhaust valve mounted on the venturi outlet water line.

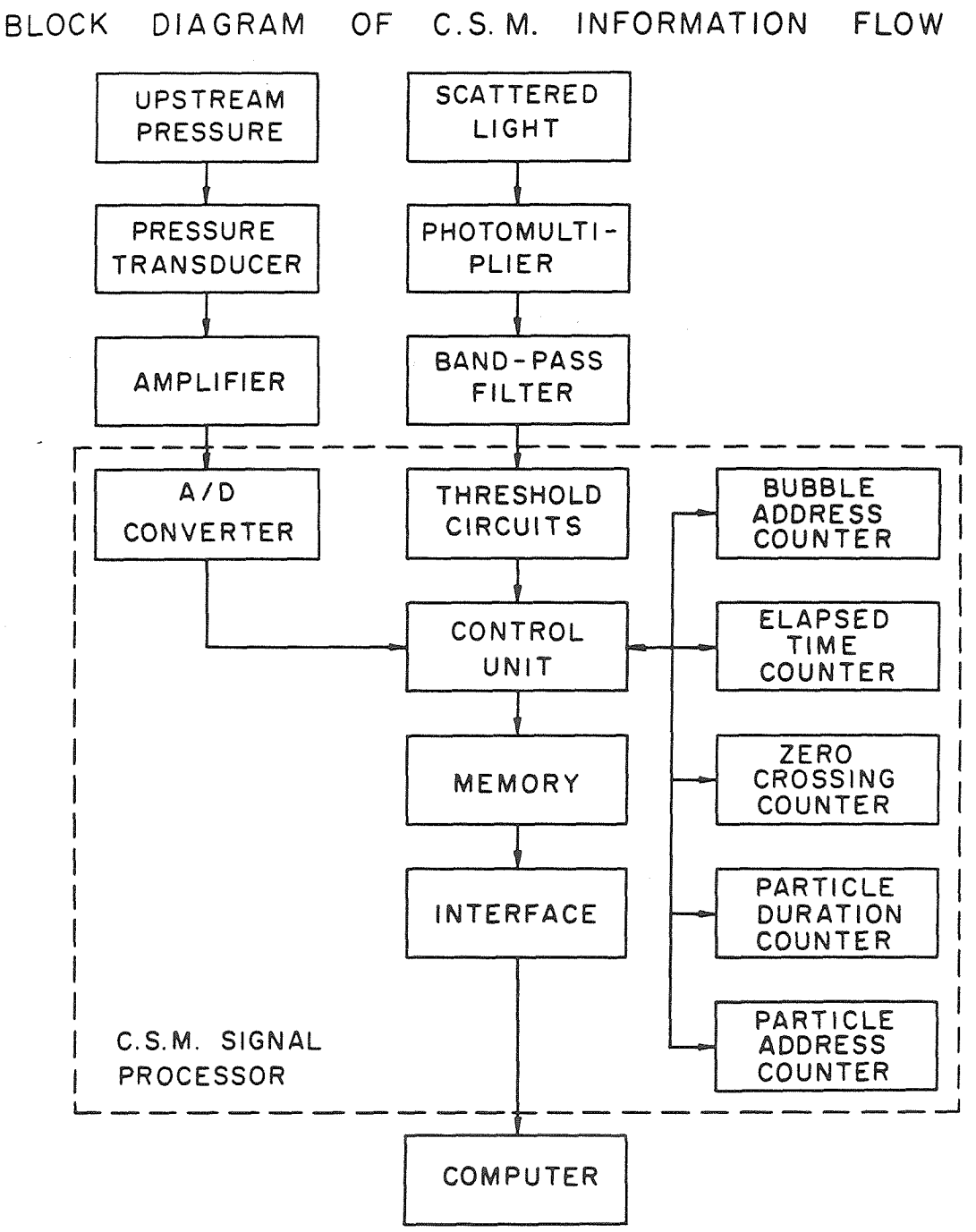

Figure 4.9. Block diagram of the information flow in the CSM Signal Processor.

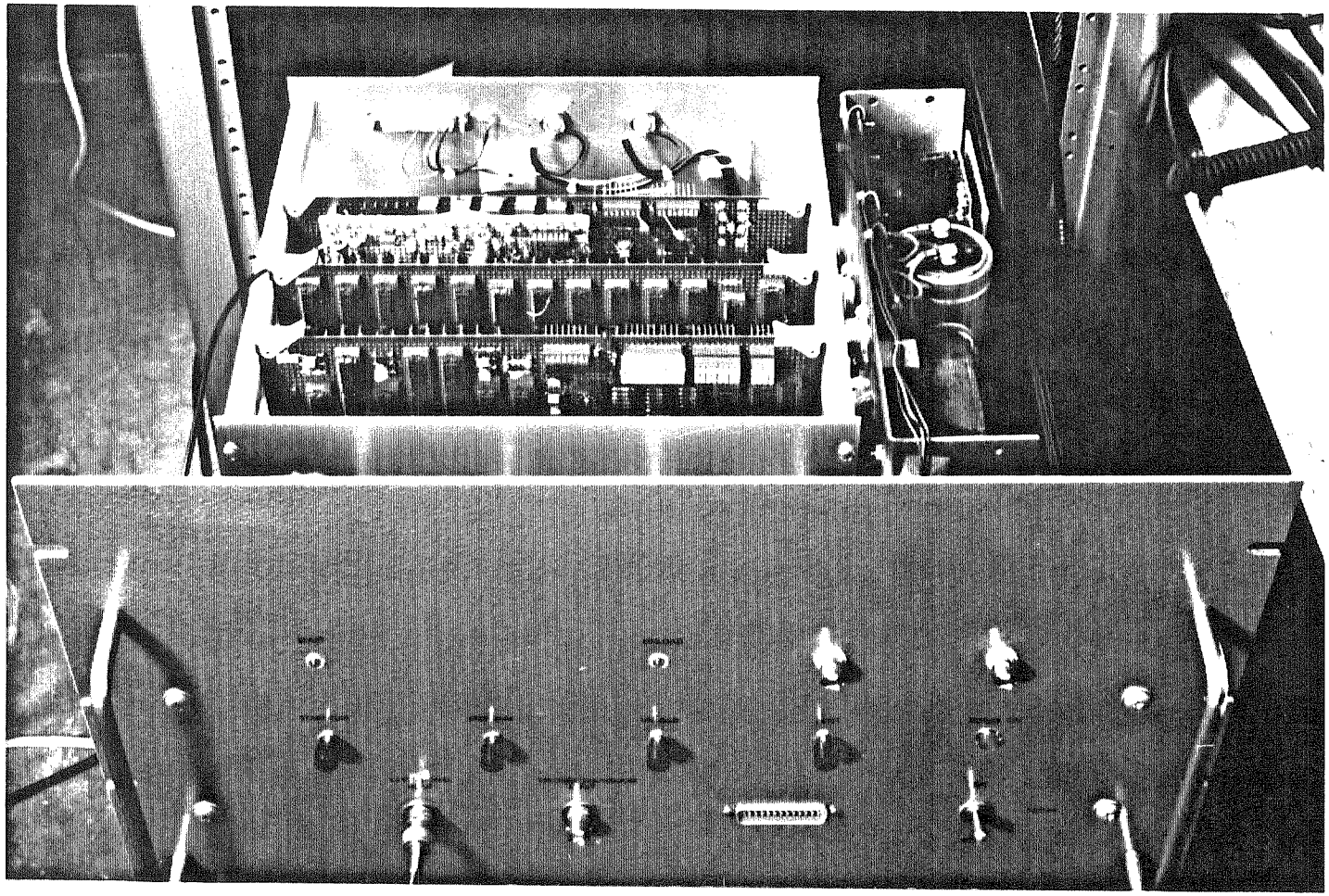

Figure 4.10. Close-up view of the CSM Signal Processor in its slide-mounted drawer. The modular bus frame contains three electronic boards wired to the front panel commands, controls and I/O connectors. On the right inside the drawer is the unit's DC power supply.

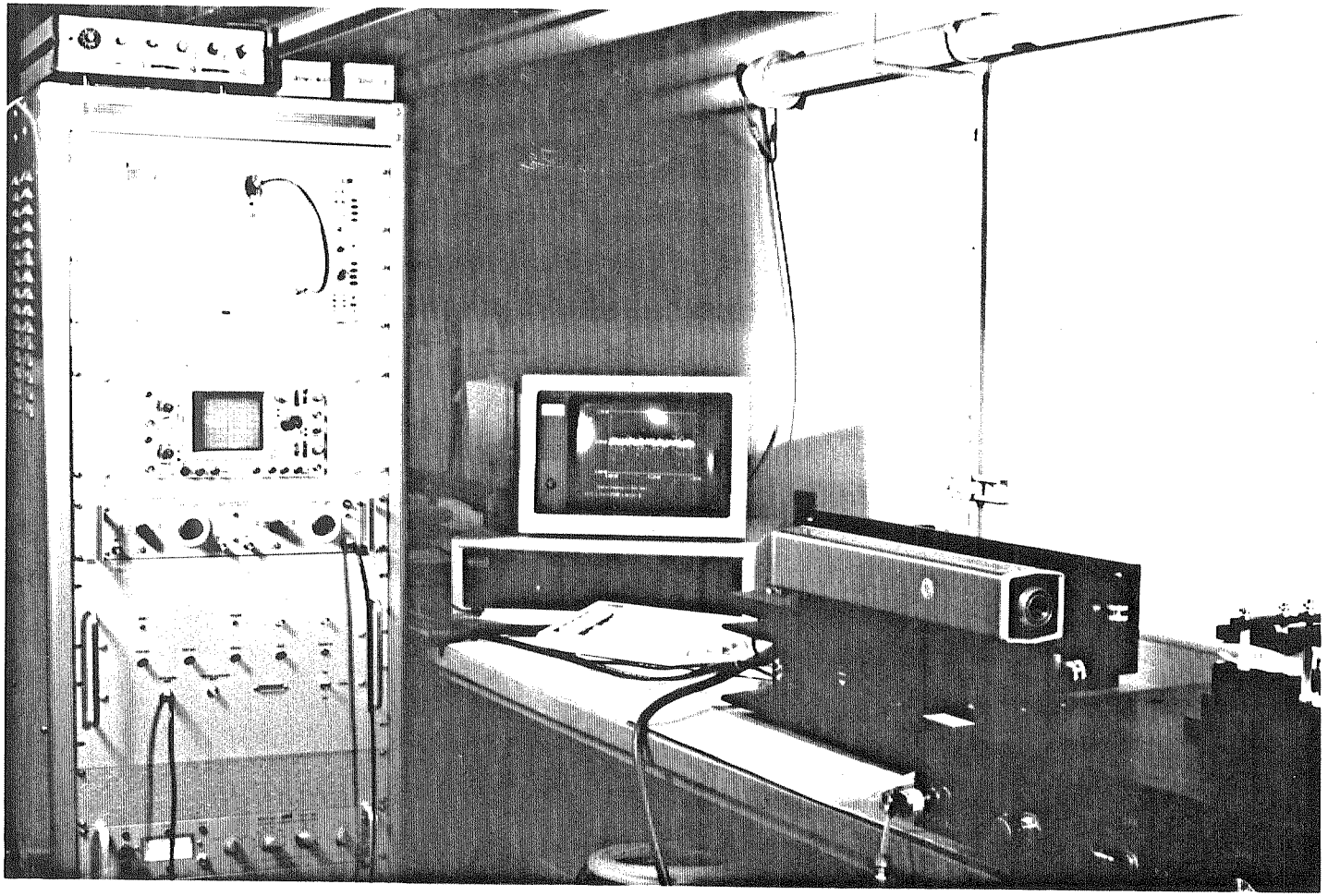

Figure 4.11. The CSM electronic rack, on the left. From the top to the bottom: the digital multimeter, the pressure transducer exciter and amplifier, the laser power supply, the oscilloscope, the electronic filters, the CSM Signal Processor, the photomultiplier power supply. Also shown in the picture: the data acquisition and reduction computer (center) and the LDV laser (right) installed in its positionable mount.

Chapter 5. CSM DATA ACQUISITION AND REDUCTION

5.1. Raw Data Acquisition

The final acquisition of the CSM data and their reduction is currently made by a Compaq Plus Desktop personal computer with a total resident memory of 640 kbytes, provided with a video screen display and two 5.25 in diameter floppy disk drives (see Fig. 4.11). However the data transfer has been designed in such a way that virtually any other micro-computer could alternatively be used.

As explained in Sec. 4.4, the data collected during each test run are organized in 9 Kbytes which contain in compacted form the information on the occurrence time of cavitation events, the corresponding upstream water pressure, the occurrence time, the duration and the number of zero crossings of the valid Doppler bursts. They can be sent to the computer by the CSM Signal Processor at the operator's request after the conclusion of each run through a standard RS232 serial port. The data are transmitted in the order of their address, starting, of course, with the first Kbyte.

An interactive compiled BASIC program named "REDUCE9.BAS" (whose listing is reported in Appendix 2) performs the acquisition and the reduction of the raw data from the CSM Signal Processor under the supervision of the operator. The main functions carried out by the CSM data acquisition and reduction program are:

- raw data input from the CSM Signal Processor;
- raw data display on the video screen and/or storage in a disk file;
- reconstruction of the physical data from the raw data;
- display and/or plotting of the physical data;
- interactive raw data reduction;
- display and/or plotting of the reduced data;
- input/output of the reduced data from/to disk files;

- some automated sequences of the above operations to accelerate the input of the raw data from the Signal Processor, the reduction of sets of raw data and the plotting of sets of reduced data.

The acquisition of the raw data is made in two steps: first the raw data are transferred from the CSM Signal Processor to the computer and then they are written to magnetic disk files, when required. During the data transfer a machine language subroutine continuously interrogates the serial input port of the computer and sequentially loads the data in the resident memory in the same order as they are received from the CSM Signal Processor starting from the location with hexadecimal address &H3000. The raw data can then be stored on a magnetic disk as a sequential file together with the general information pertaining the CSM run, namely: operator's comments, calibration constants, settings of the apparatus. In this case each raw data byte is converted in its two-character hexadecimal string representation and 64 consecutive bytes are arranged in a 128 character long string, which is sequentially written in the file until all the nine Kbytes of raw data have been exhausted. This encoding method combines the advantage of preserving the ASCII representation of the information (for easy and universal access) with an efficient use of the disk space. The acquisition of the data from the CSM Signal Processor can be directly controlled by the operator or can be automatically executed by the computer in order to simplify and accelerate the handling of data from sets of multiple CSM runs in rapid sequence.

5.2. Data Reduction

The first step of the data reduction is the reconstruction of the physical data from the raw binary data using the clock frequencies which drive the counters of the CSM Signal Processor and the pressure transducer calibration curves. In order to reduce the number of directly addressable variables in the program, the data reconstruction is done by a set of user defined functions which directly

return the values of the various physical quantities from the relevant binary information stored in the computer high memory.

The data reduction develops through the following steps:

1. zero crossing validation and statistical filtering of the Doppler frequency and upstream pressure data;
2. computation of the average potential core velocity, of the potential core velocity data standard deviation and of the boundary layer thickness;
3. computation of the average throat pressure and of the throat pressure data standard deviation;
4. validation of the arrival times of cavitation events;
5. computation of the observed and expected occurrence frequency distributions of the delay times between cavitation events;
6. computation of the unstable nuclei concentration.

During the first step Doppler frequency data are computed by dividing the number of zero crossings of each burst by twice its duration. To reject spurious bursts only counts with a preselected minimum number of zero crossings are used (zero crossing validation). Both the Doppler frequency data and the upstream pressure data contain a relatively small number of outliers due to various noise sources in the electronics. In addition, the Doppler frequency data may sometimes contain a more significant number of low readings from scatterers deep inside the venturi boundary layers. To eliminate the noise and to isolate the velocity information primarily coming from the venturi's potential core the Doppler frequency data are statistically filtered by only retaining those readings whose deviation from their average values does not exceed a preset multiple of their standard deviation (usually three standard deviations). The same procedure is also applied to the upstream pressure data, leading to the determination of the average upstream pressure $\overline{p}_u$ and of the upstream pressure data standard deviation σ_{p_u}.

The computation of the average potential core velocity, of the potential core velocity data standard deviation and of the boundary layer thickness is carried out as follows. First the observed occurrence frequency distribution of the measured velocity data is calculated in the form of a histogram chart. When boundary layer effects are important (and their role is not masked by other factors such as, for example, an upper drift of the flow velocity during the run) this distribution should be negatively skewed and therefore its third central moment should be negative. If this is not the case the expected value and the standard deviation of the observed distribution are simply used to compute the average potential core velocity $\overline{u}_m$ and the standard deviation of the potential core velocity data σ_{u_m}, while the boundary layer thickness δ_{BL} is taken to be zero. Otherwise, a theoretical probability distribution of the measured velocity is derived which parametrically depends on $\overline{u}_m$, σ_{u_m} and the ratio of the boundary layer thickness to the local duct radius δ_{BL}/R_m. These parameters are then determined by fitting the theoretical distributiom to the observed one. This process results in a slightly higher estimate of the average throat velocity and in a small reduction of the standard deviation of the throat velocity data depending on the value of the parameter δ_{BL}/R_m.

For simplicity the analysis is carried out assuming that the LDV probe volume extends across the whole venturi tube in the direction of the optical axis but that it does not include appreciable portions of the boundary layers in the vertical direction. Indeed only the outer, dimmer region of the LDV beams extends towards the venturi walls in this direction and therefore it is reasonable to expect that relatively few velocity readings will be recorded there. Let the true velocity profile at the measurement section of the CSM venturi be: $u = u(y)$ with $u = \overline{u}_m$ for $0 \leq y \leq R_m - \delta_{BL}$ where y is the distance from the venturi centerline in the direction of the optical axis. Also assume that the velocity tracers are uniformely distributed on the venturi cross-section in the direction of the optical axis with density distribution $1/R_m$. Then the probability density

distribution of the true velocity u is:

$$f_u(u) = \begin{cases} (dy/du)/R_m & \text{for } 0 \le u < \overline{u}_m \\ \delta(u-\overline{u}_m)(R_m - \delta_{BL})/R_m & \text{for } u = \overline{u}_m \end{cases} \tag{5.1}$$

where $\delta(u-\overline{u}_m)$ indicates the Dirac function centered at $u = \overline{u}_m$. Let the dispersion of the measured velocity u_m corresponding to the true velocity u be described by the probability density distribution function:

$$h(u_m - u) = \frac{1}{\sigma_{u_m}\sqrt{2\pi}} \exp\left(-\frac{(u_m-u)^2}{2\sigma_{u_m}^2}\right) \tag{5.2}$$

Under these assumptions the probability density distribution of the measured velocity in the venturi is expressed by the convolution of the above two equations:

$$f_{u_m}(u_m) = \int_{-\infty}^{+\infty} f_u(u)\, h(u_m - u)\, du \tag{5.3}$$

The velocity profile in the boundary layer must now be specified. Experience showed that the result is not very sensitive to the precise shape of the velocity profile, therefore let assume $u(y) = \overline{u}_m \sqrt[3]{(R_m - y)/\delta_{BL}}$. This profile is not very realistic since, for example, its transition to the potential core flow is not smooth, but has the advantage of providing the following explicit expression for the probability density distribution of the measured velocity:

$$\begin{aligned} f_{u_m}(u_m) = {} & \frac{3\delta_{BL}}{\overline{u}_m^3}\frac{u_m^2+\sigma_{u_m}^2}{2}\left[\operatorname{erf}\left(\frac{u_m}{\sqrt{2\pi}}\right) - \operatorname{erf}\left(\frac{u_m-\overline{u}_m}{\sqrt{2\pi}}\right)\right] + \\ & + \frac{3\delta_{BL}}{\overline{u}_m^3}\left[\frac{u_m\sigma_{u_m}}{\sqrt{2\pi}}\exp\left(-\frac{u_m^2}{2\sigma_{u_m}^2}\right) - \frac{\sigma_{u_m}(u_m+\overline{u}_m)}{\sqrt{2\pi}}\exp\left(-\frac{(u_m-\overline{u}_m)^2}{2\sigma_{u_m}^2}\right)\right] + \\ & + \frac{R_m-\delta_{BL}}{R_m}\frac{1}{\sigma_{u_m}\sqrt{2\pi}}\exp\left(-\frac{(u_m-\overline{u}_m)^2}{2\sigma_{u_m}^2}\right) \end{aligned} \tag{5.4}$$

This function represents a negatively skewed probability density distribution for $\delta_{BL} \neq 0$ and reduces to a simple Gaussian when $\delta_{BL} = 0$. Let N_p be the total number of velocity data and O_i the observed occurrence frequency of the measured velocity in each of the M intervals $[u_{m_i}, u_{m_i} + \Delta u_m[$. Then the expected frequency in these intervals is: $E_i = N_p f_{u_m}(\overline{u}_{m_i})\Delta u_m$, where $\overline{u}_{m_i}$ is

internal to $[u_{m_i}, u_{m_i} + \Delta u_m[$. Finally, the values of the parameters $\overline{u}_m$, σ_{u_m} and δ_{BL} which minimize the quadratic error:

$$\varepsilon^2(\overline{u}_m, \sigma_{u_m}, \delta_{BL}) = \sum_{i=1}^{M} (E_i - O_i)^2 \tag{5.5}$$

are chosen as the average potential core velocity, the standard deviation of the potential core velocity data and the boundary layer thickness. At this stage the computation of the average throat pressure and of the standard deviation of the throat pressure data is performed in a straightforward fashion as previously described in Sec. 2.6.

In steady conditions the average arrival rate of cavitation events is constant and therefore their arrival times are monotonically increasing and approximatively proportional to their index. However, a relatively small number of outliers can also be present due to various noise sources in the electronics. In order to eliminate spurious data the linear regression curve of the bubble occurrence time data as a function of their arrival index is calculated. Then the arrival time data which are not in monotonically increasing order with respect to the neighbouring ones and whose deviation from the regression line is the largest are eliminated, until a set of data in the proper order is obtained (bubble time data validation).

The observed occurrence frequency distribution of the delay time τ between cavitation events is easily calculated from their arrival times. A histogram chart is constructed by sorting the data in, say, M groups equally spaced in time and the average arrival time is estimated from the sampling time t_s and the total number of cavitation events N_b as $\overline{\tau}_b = t_s/N_b = 1/\overline{\nu}_b$. On the other hand, The expected occurrence frequency distribution is computed from equation (2.13) multiplied by N_b:

$$f_e(t) = N_b \overline{\nu}_b e^{-\overline{\nu}_b t} \tag{5.6}$$

for comparison with the above observed frequency distribution.

Finally, the unstable nuclei concentration and its standard deviation are calculated as indicated in Sec. 2.5 from: $n(R_o) = N_b/u_m A_m t_s$ and $\sigma_n = \sqrt{N_b}/u_m A_m t_s$.

Chapter 6. SYSTEM CALIBRATION

6.1. Upstream Pressure Transducer Calibration

The calibration of the CSM upstream pressure transducer has been made in a relatively straightforward way using the constant level tank connected in the "Calibration" configuration of previous Sec. 4.2. The amplified output of the pressure transducer has been recorded while the air pressure in the tank was measured using a mercury barometer. The response of the A/D converter which digitizes the pressure signal in the CSM Signal Processor has been separately checked with simulated DC inputs. In the current configuration the A/D binary output ranges linearly from 0 to 4095 when the input varies from 0 to 5 V. Its response and range can be varied by properly changing the jumper connections of some of its pins, as explained in Appendix 1. Both the response of the pressure transducer and the A/D converter have been tested for linearity, stability and repeatability with satisfactory results. The final calibration has been made using eleven points in one step from the pressure input of the transducer to the A/D output from the Signal Processor and the linear regression line has been used for the data conversion. The values of the two calibration constants (off-set and slope) depend on the adjustable zero of the pressure transducer exciter and amplifier and on its other settings: transducer excitation (3.5 VDC), signal amplification gain (500) and signal frequency filtering (wide band). In the specific case they were:

$$C_{off-set} = 21123.46\,\text{Pa}; \qquad C_{slope} = 35.0019\,\text{Pa/bit} \tag{6.1}$$

The results of the upstream pressure transducer calibration are shown in Fig. 6.1, where the calibration points are plotted together with the linear regression line. The resulting regression coefficient is extremely high ($r \simeq 0.999997$) and the maximum deviation of the calibration points from the regression line is smaller than about 200 Pa, as shown in Fig. 6.2.

A pot mercury barometer has been built for measuring the pressure in the constant level tank and it has been calibrated using an atmospheric barometer. Let the subscripts 1 and 2 respectively refer to the upper and lower mercury levels and y be the level reading on the barometer scale. Then the pressure has been computed from the equation:

$$p = \rho_{Hg}(T) g \left\{ (y_1 - y_1^*) \left(1 + \frac{A_1}{A_2} \right) + (y_1^* - y_2^*) \right\} \tag{6.2}$$

where $\rho_{Hg}(T)$ is the mercury density at the temperature T, $g = 9.796\,\mathrm{m/s^2}$ is the acceleration of gravity, $A_1/A_2 = 9.049 \cdot 10^{-3}$ is the area ratio for mercury continuity compensation and the superscript $*$ indicates calibration conditions. Corrections due to thermal expansions of the mercury and the scale with respect to calibration conditions have been included by assuming:

$$\rho_{Hg}(T) = \rho_{Hg}(T^*)[1 + \alpha_{Hg}(T - T^*)] \tag{6.3}$$

and:

$$(y_1 - y_1^*) = (y_1' - y_1^*)[1 + \alpha_{Al}(T - T^*)] \tag{6.4}$$

where $\rho_{Hg}(T^*) = 13595.4\,\mathrm{kg/m^3}$ is the mercury density at the calibration temperature $T^* = 20\,^\circ\mathrm{C}$, $\alpha_{Hg} = 1.806 \cdot 10^{-4}\ ^\circ\mathrm{C}^{-1}$ is the volumetric thermal expansion coefficient of mercury, $\alpha_{Al} = 2.322 \cdot 10^{-5}\ ^\circ\mathrm{C}^{-1}$ is the linear thermal expansion coefficient of the barometer's aluminum scale and y_1' is the uncorrected reading of the upper mercury level elevation.

6.2. LDV Alignment and Calibration

The alignment of the optical components is greatly simplified in the present back-scattering configuration of the LDV. First the laser has been positioned using its adjustable mount until its beam was located at the proper height (76.2 mm) parallel to the longitudinal axis of the baseplate. Then the other components of the focusing optics were mounted in the order of the light propagation. Care must be taken to ensure that the beamsplitter produces two

parallel beams symmetrically located with respect to the vertical longitudinal plane of the baseplate and that their separation can be continuously changed by the beam displacer from about zero to its maximum possible value. The telescopic relay was also positioned and the separation of its two lenses adjusted to the same purpose. Because of the imperfection of the lenses, perfect parallelism of the outcoming beams cannot be obtained over the entire range of beam separation. However this error is small, especially if the two laser beams emerge parallel to each other for some intermediate value of their separation. The gap between the two mirrors of the receiving optics has been reduced as much as possible without interfering with the transmission of the incoming laser beams. Then the diameter and the position of the photomultiplier field stop aperture has been chosen by optimizing the Doppler signal from the photomultiplier during the LDV calibration.

The LDV has been calibrated in two steps by focusing it on the side of a rotating disk made of black-anodized aluminum and driven by an electrical induction motor. The calibration disk was mounted on a vertical translation stage so that the peripheral velocity U at the LDV focal point could be continuously changed by varying its distance r from the axis of rotation. At first two fine parallel traces symmetrically located on one side of the disk at a distance $s = 25.4\,\text{mm}$ from its center were used to accurately determine the location of the LDV focal point with respect to axis of rotation. These two traces were accurately drawn on one half only of the disk side surface so that their passage through the LDV focal point generated two electric pulses per revolution. These pulses were used to trigger a counter and to measure both the time interval τ between the occurrence of the two traces and the disk rotational period T. In this process only one of the two LDV beams was used to illuminate the focal point in order to eliminate the Doppler effect. Furthermore, the filtering of the electric signal from the photomultiplier was properly chosen in order to obtain sharp clean pulses at the passage of the traces through the LDV focal point.

An especially designed electronic unit transformed the electric pulses from

the phomultiplier in a rectangular wave form signal for triggering and stopping the counter on the appropriate transitions of the signal (see Fig. 6.3). It consists of three simple integrated circuits: a comparator (311), a pulse generator (4538) and a flip-flop (4013), all powered by a 9 V battery. The output (pin 7) of the comparator trasitions when the photomultiplier input signal (pin 2) crosses the threshold level (pin 3), which can be adjusted using the 10 kΩ variable resistor. The signal from the comparator is then transformed by the second unit (4538) in a short pulse, whose duration can be varied acting on the 100 kΩ potentiometer. Finally, the flip-flop (4013) generates the alternating rectangular output for the counter in response to the signal received from the pulse generator (4538).

During the LDV calibration the angular velocity of the disk was very nearly constant due to its relatively large inertia and to the small irregularity of the electric induction motor, so both τ and T could be measured very accurately with a precision of, say, 0.1% or better. Then the distance r of the LDV focal point from the disk center was calculated assuming uniform angular velocity from:

$$r = \frac{s}{\sin(\pi\tau/T)} \tag{6.5}$$

thus providing a reference position on the disk surface. Next, the disk was flipped in order to expose the side without traces to the LDV beams and the vertical translation stage was used to change the distance of the LDV focal point from the disk axis. At the same time the rotational period was measured with an optical pick-up and the peripheral velocity at the LDV focal point was calculated from: $U = 2\pi r/T$.

In order to run the LDV calibration the two laser beams were allowed to illuminate the focal point on the disk and the following settings had to be chosen:

- the beam separation;
- the location of the focal point with respect to the focusing and collecting lens;
- the position and diameter of the photomultiplier field stop aperture;

- the excitation of the photomultiplier;
- the cut-off frequencies of the band-pass filters;
- the electronic threshold settings.

All of the above settings except the last two have been determined empirically by maximizing the LDV signal intensity.

In the choice of the beam separation it appeared that the best results were obtained when the Doppler frequency was contained in the range from about 100 kHz to 400 kHz. In particular, the LDV signal intensity tended to decrease rather quickly when the Doppler frequency exceeded about 800 kHz and almost disappeared in the noise level beyond 1 MHz. This behaviour was first appearent with the LDV signal generated by the surface of the rotating disk, but has also been observed later in the operation of the CSM with cavitating flows. Two contributing factors are thought to be responsible for this situation: the reduced sensitivity of the electronics due to band width limitations and the decrease of the fringe spacing in the LDV focal point when the beam angular separation increases. Since the intensity of the LDV signal is maximum when the size of the scatteres is of the same order of magnitude as the fringe spacing, an increase of the beam intersection angle has the effect of focusing on smaller and smaller scatterers. However, the Doppler signals coming from these scatterers are generally less intense due to their reduced scattering cross-section and are more likely to be smeared together because of their more frequent occurrence (smaller drop-out rate).

Clearly in the optical configuration chosen for the CSM the nominal location of the LDV probe volume is the focal point of focusing and collecting optics, about 200 mm from the lens L3. However, slightly better results have been obtained by moving the rotating disk a bit closer to the lens. Most likely the resulting increase of the solid angle available to the collecting optics compensated the penalty involved in displacing the scattering source away from the geometric center of the probe volume. Alternatively, slight imperfections in the optical

components and in their positioning may have been the cause of this situation.

The optimal excitation of the photomultiplier greatly depends on the nature of the LDV signal. Although it can range nominally from 0 to 1600 V, it rarely seemed advantageous to increase it beyond 1200 V, due to saturation of the photomultiplier, or decrease it below 700 V, because of insufficient sensitivity. Therefore it was normally kept between 800 to 950 V.

The cut-off frequencies of the band-pass filters have been found to have a non-negligible effect on frequency measurements from non-monocromatic signals as the ones coming from Doppler bursts. In particular, the frequency readings tended to be biased towards the center of the frequency band, at least when one of the cut-off frequencies was relatively close to the measured frequency. For this reason during the LDV calibration some iterations were made until the cut-off frequencies were safely set at 80% (high-pass) and 125% (low-pass) of the measured frequency. In this way the Doppler frequency was very carefully isolated from the superimposed noise and the biasing error was virtually eliminated. In the operation of the CSM, where no accurate predictions of the frequency to be measured were possible, a much wider band-pass window was used (100 to 400 kHz) in order to reduce the biasing in the measurement of the Doppler frequency, while still providing adequate high-pass filtering and rejection of high frequency noise.

During the LDV calibration only the zero and particle thresholds have been used, while the bubble thresholds have been set very high, so that virtually all Doppler bursts were counted as velocity tracers. As explained in Appendix 2, these thresholds are best set by observing the output of the corresponding comparators in the presence of a simulated DC filtered LDV signal from a signal generator, instead of monitoring the inputs to the comparators.

The Doppler frequency data measured by the CSM Signal Processor in response to the LDV signal generated by the rotating disk appeared to be about normally distributed and showed little dispersion and skewness. In general their standard deviation was less than a few percent of the mean. Data deviating from

the average by more than three standard deviations were rejected and the mean of the remaining population was used as the representative value of the Doppler frequency for calibration purposes. For normally distributed data the standard deviation of the Doppler frequency calculated in this way is equal to the standard deviation of the sample divided by the square root of its size, here about 900 points. Therefore the relative r.m.s. error of the Doppler frequency value used in the LDV calibration was usually lower than a few parts in one thousand. In practice the dispersion of the velocity measurement was even lower than the intrinsic spread of the measured velocity due to the finite radial size of the LDV focal spot on the disk surface.

The LDV calibration has been made using eight groups of four velocity points ranging from about 9 to 22 m/s and in this case also the linear regression line has been used for the data conversion (see Fig. 6.4). Each group has been recorded at the same location on the disk surface and therefore should lead to the same results, apart from the small difference in the rotational velocity from one reading to the next. The regression coefficient is extremely high ($r \simeq 0.999991$) and the maximum deviation of the calibration points from the regression line is smaller than about 0.05 m/s, as shown in Fig. 6.5. Clearly, the values of the two calibration constants (off-set and slope) depend on the setting of the optics, in particular on the separation of the two laser beams and of the telescopic relay lenses, which are both adjustable. In the specific case they were:

$$C_{off-set} = -0.157543\,\mathrm{m/s}; \qquad C_{slope} = 5.156469 \cdot 10^{-5}\,\mathrm{m/sHz} \qquad (6.6)$$

The Doppler frequency, on the other hand, was practically unaffected by the position of the velocity field in the probe volume along the direction of the optical axis, thus proving that the fringe spacing was essentially uniform. This was no longer the case when faster focusing lenses were tried with the purpose of increasing the signal intensity, because the beam divergence angle increased as a consequence of the larger power of the lenses while the beam angular separation had to remain approximatively constant in order to mantain the Doppler

frequency in the desired range.

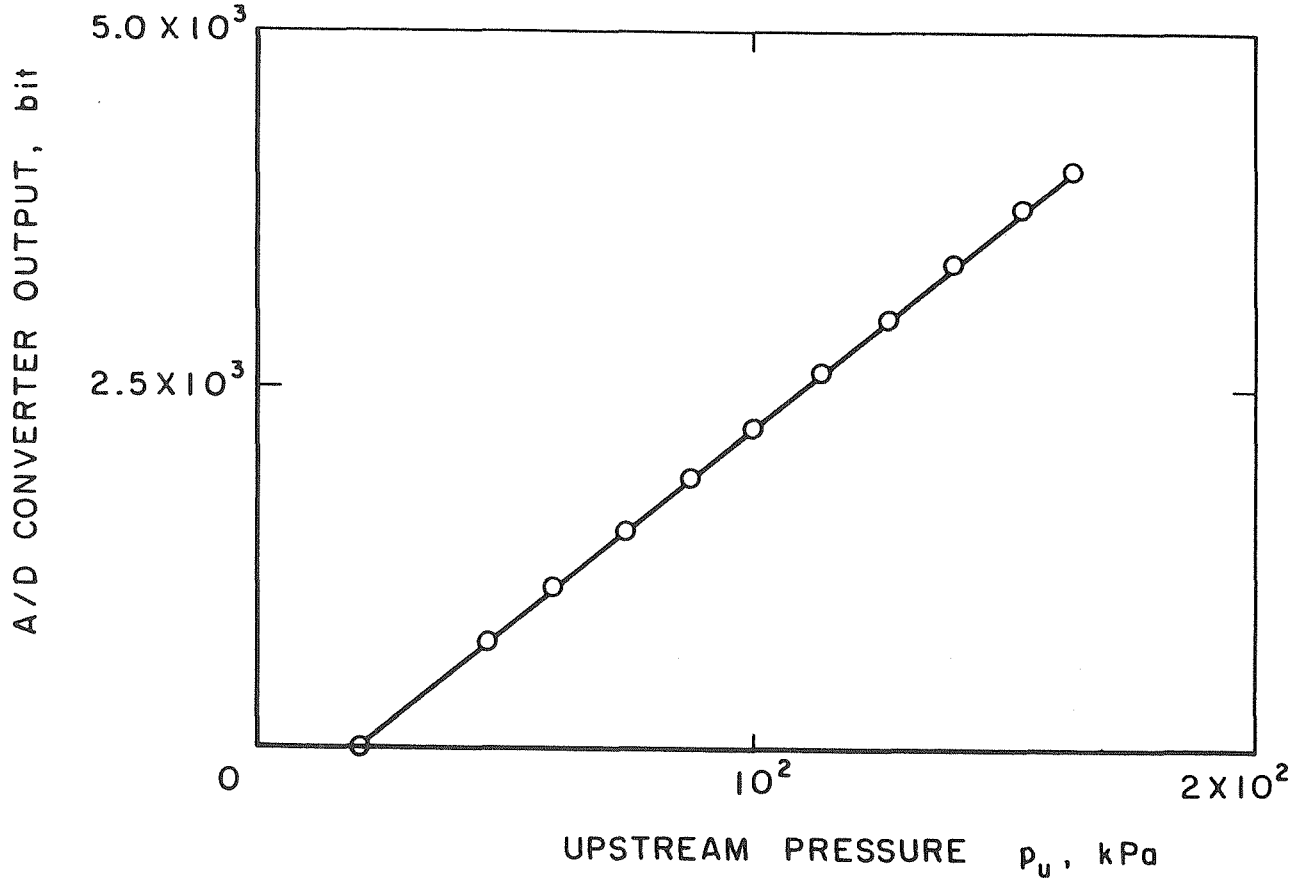

Figure 6.1. Upstream pressure transducer calibration points and linear regression line. The the digital output of the CSM Signal Processor A/D converter is plotted v/s the upstream pressure.

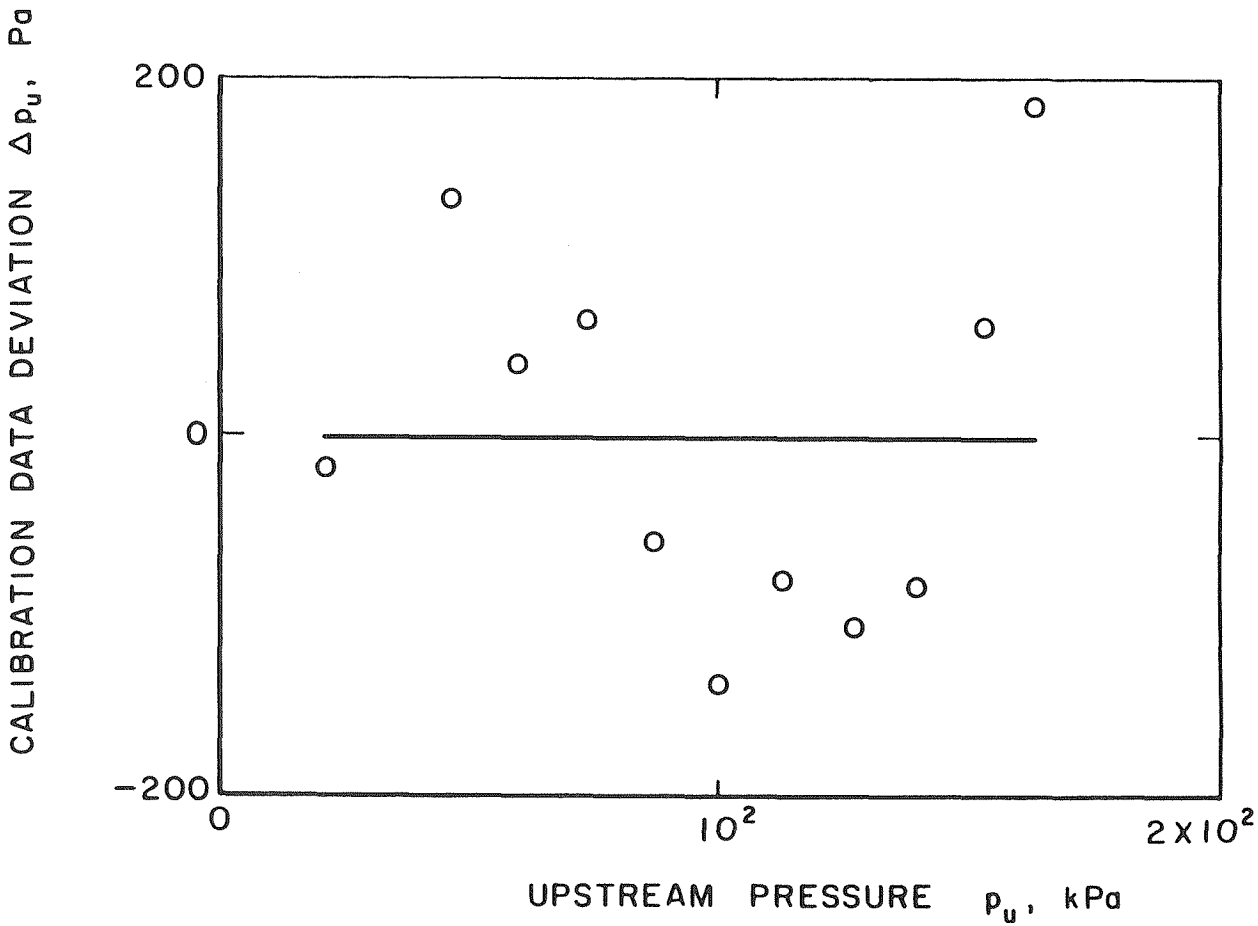

Figure 6.2. Deviation of the upstream pressure transducer calibration points from the linear regression line. The deviation has been expressed in equivalent pressure error using the slope of the calibration line and plotted v/s the input pressure.

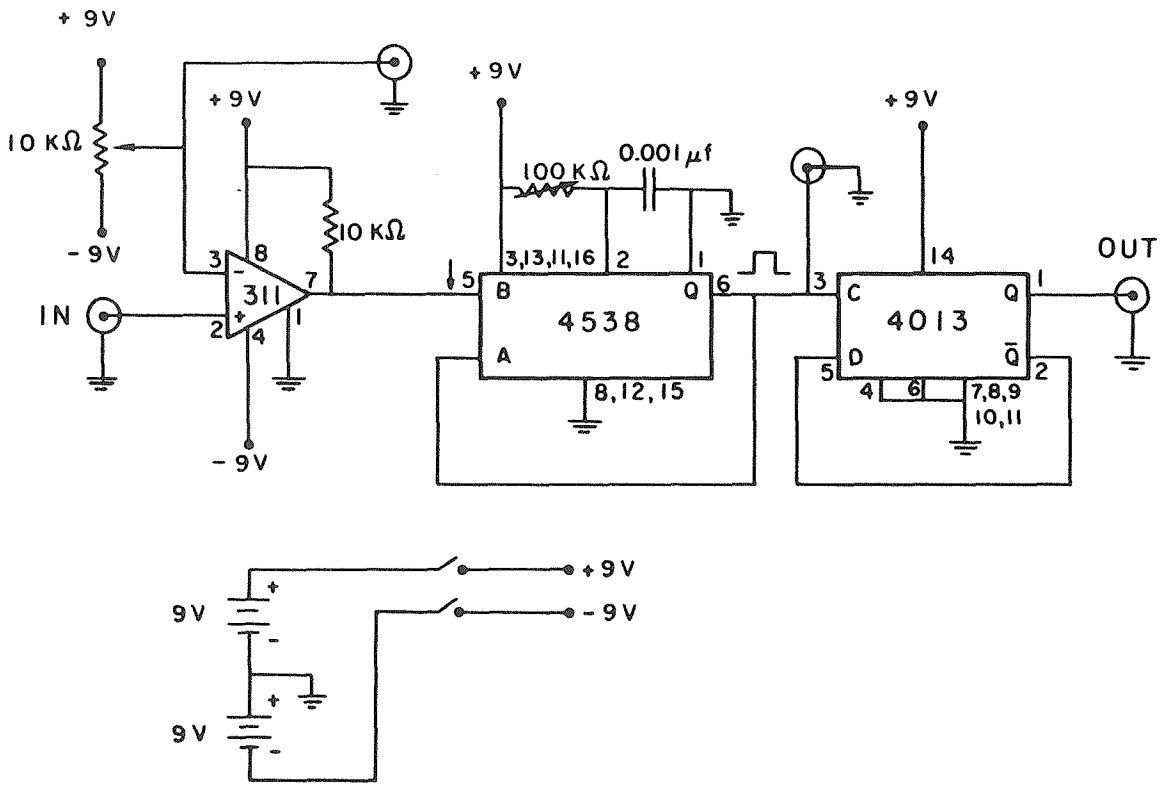

Figure 6.3. Electronic schematic of the LDV calibration unit. It converts the electrical pulses generated by the traces on the calibration disk into an alternating rectangular signal used for triggering a counter. The unit includes a comparator (311), a square pulse generator (4538) a flip-flop (4013) and two variable resistances (10 kΩ and 100 kΩ).

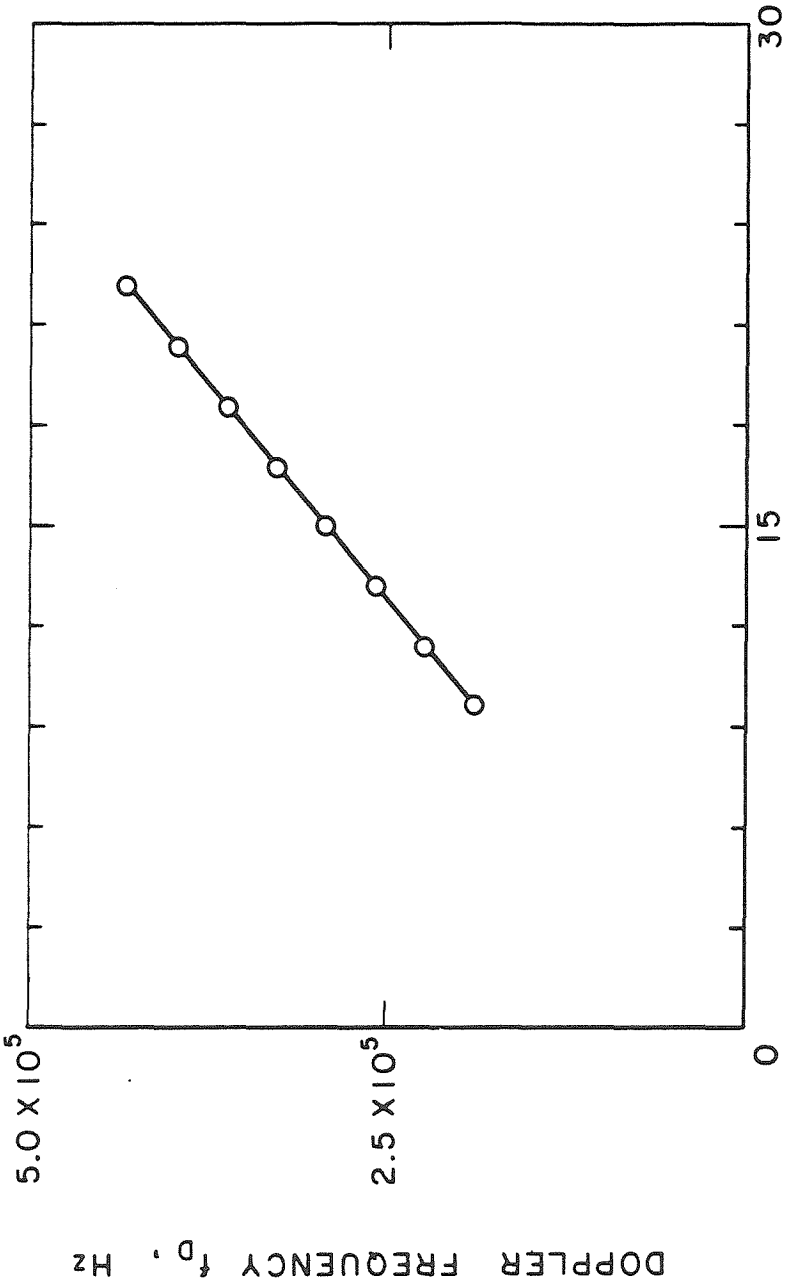

Figure 6.4. LDV calibration points and linear regression line. The Doppler frequency read by CSM Signal Processor is plotted v/s the velocity. Eight groups of four calibration points have been used (they overlap in the drawing).

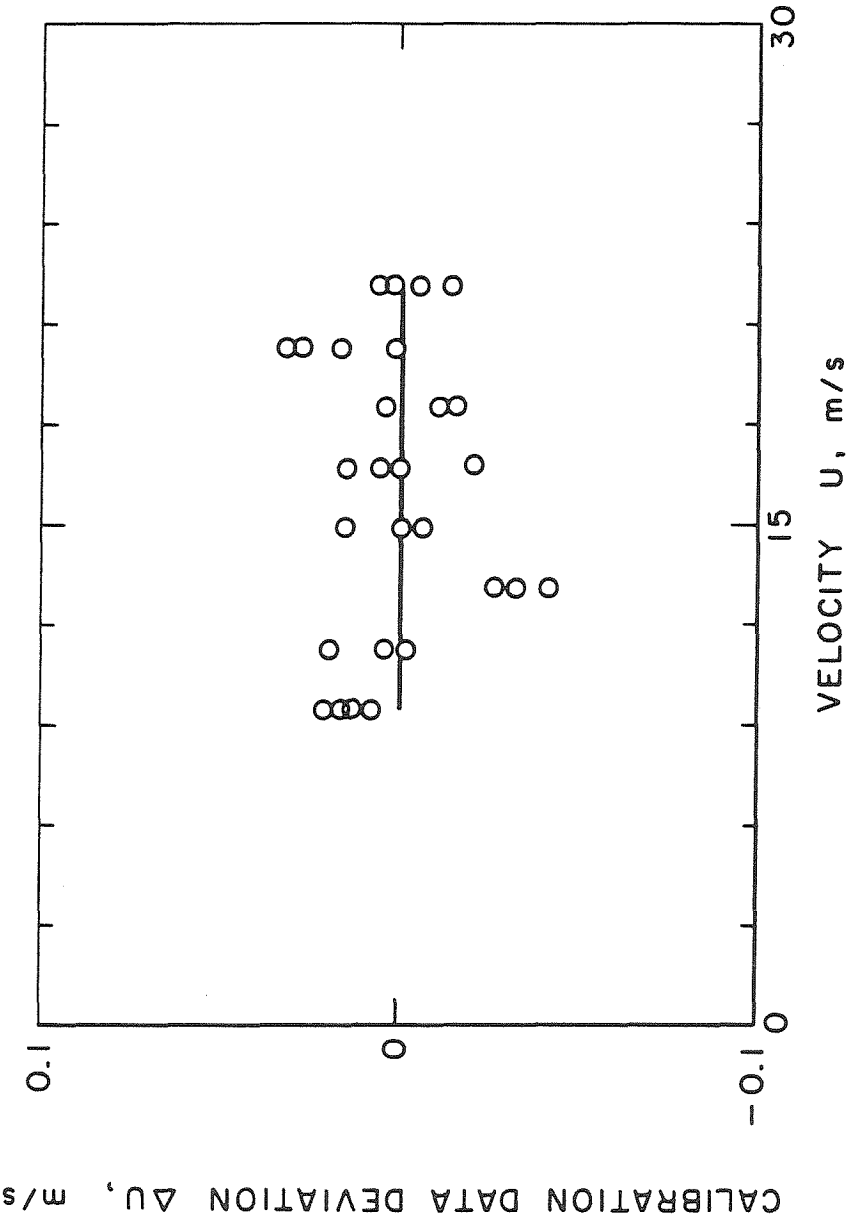

Figure 6.5. Deviation of the LDV calibration points from the linear regression line. The deviation has been expressed in equivalent velocity error using the slope of the calibration line and plotted v/s the input velocity.

Chapter 7. CSM OPERATION RESULTS AND DISCUSSION

7.1. Experimental Procedure

The experimental procedure for measuring the water quality with the CSM is relatively simple. The water source is connected to the inlet using the shortest possible tubing and taking care to avoid abrupt changes of the duct internal diameter. The system is turned on and the temperature of the electronics is allowed to stabilize for about fifteen minutes. Care must be taken to prevent the specular reflections of the laser beams generated by the inner and outer surfaces of the venturi from reaching the photomultiplier, in order to avoid saturation problems. At the same time a good vacuum (say a few thousand Pascals) is created in the exhaust tank using the vacuum pump in conjunction with the cryogenic moisture trap. With the ball valve at the exhaust of the venturi tube closed, the water lines to the upstream pressure transducer are then carefully bled of all air and the pressure transducer itself is connected to the upstream section of the venturi. The data acquisition and reduction program is loaded and run in order to make the computer ready to receive the data from the CSM Signal Processor.

Each set of raw data from a CSM run can be written in a magnetic disk file with the general information about the instrument settings and the optional comments of the operator. The data acquisition can be controlled step by step by the operator. However, when multiple runs in rapid sequence are to be made, it is more convenient to use the semi-automated sequence executed by the computer under the control of the data acquisition and reduction program. In this case the operator specifies the root of a family of data files and the range of two-digit intergers that the computer will append to the root in order to generate a sequence of file names for storing the raw data from successive runs of the CSM. At the end of the transfer of the raw data from the CSM Signal Processor the computer briefly displays the plot of the Doppler frequency readings and asks whether the raw data currently loaded should be saved on a

disk file or not. Then the computer gets ready for accepting the raw data from the next run.

The temperature of the sampled water is measured with a thermometer and its air content with a manometric van Slyke meter. Finally, the inlet line is purged using the by-pass line, the venturi is connected to the water inlet and the exhaust valve is opened. The exhaust pressure tends to remain very nearly constant even when, for simplicity, the exhaust pressure regulator is not used and the needle valve is closed. Only during the longer runs and when the exhaust pressure is higher has an increase of the exhaust pressure been detected.

The location of the LDV focal point is very important for obtaining reproducible results of good quality from the operation of the CSM. Experience showed that the best location is at the end of the venturi throat section. When the LDV focal point is moved upstream (where the cavities are smaller) the number of cavitation events recorded by the CSM Signal Processor decreases. On the other hand, if the LDV beams are focused inside the diffuser the quality of the Doppler signal drops and the dispersion of the velocity data increases. The deterioration of the Doppler signal is likely to be a consequence of the bigger size of the cavities, whose dimensions become significantly larger than the fringe spacing in the LDV focal volume. The increase of the dispersion of velocity data is probably due to two combined factors: the presence of thicker boundary layers and of a significant pressure gradient in the diffuser. As a consequence of the former factor a larger portion of the velocity readings can possibly be coming from scatterers convected inside the boundary layers. In addition, the pressure gradient in the diffuser generates slip velocities between each cavity and the sorrounding liquid which depend, among other things, on the size of the cavities themselves. Since the size of the cavities varies greatly, the resulting differences in their slip velocities have the consequence of increasing the dispersion of the Doppler frequency data. Furthermore, the minimum pressure experienced by the cavitation nuclei in the venturi tube is most likely to occur at the end of the throat section because of the displacement effect associated with the boundary

layer growth. Therefore, positioning the LDV focal point at this location is also consistent with the aim of directly measuring, if possible, the minimum pressure in the venturi. In practice the location of the pressure minimum can be easily determined from the velocity profile obtained using the transversal translation stage to move the LDV focal point along the venturi's centerline.

The electronic settings also are of crucial importance for the operation of the CSM since they determine the number of cavitation events recognized and counted in given flow conditions. The choice of "proper" values for these electronic settings is linked to the definition of a general criterion for discriminating in dynamic conditions unstable cavitating nuclei from stable ones and to the existence of a firm relation linking the size of the scatterers to the intensity of the LDV signals they produce. The second aspect of the problem can be partially resolved by calibrating the LDV signal from cavities of measurable sizes, for example by monitoring the sampled water with holographic methods. However, the definition of criterion for the discrimination of the unstable cavities is essentially equivalent to the precise definition of the cavitation inception conditions which is still an open problem in cavitation research. Until these two problems are satisfactorily solved the selection of the electronic settings of the CSM remains, at least to some extent, arbitrary. In the present case it has been carried out empirically, trying to optimize the operation of the electronics and to ensure the applicability of the same settings to the full range of the expected operational conditions.

In establishing the most convenient combination for the electronic settings it must be born in mind that the CSM Signal Processor only counts Doppler bursts exceeding the particle thresholds but not the bubble ones. Therefore Doppler frequency data become insufficient in number when the two couples of thresholds are set too close to each other, or tend to be adversely affected by the electronic noise when the reverse is the case. In general one should try to obtain the highest possible number of velocity data over the full duration of the CSM run. When the acquisition rate of Doppler frequency data is much higher than

the one of cavitation events the velocity information tends to be concentrated only on the final part of the run because Doppler frequency data are stored cyclically on the available 1024 memory locations, deleting pre-recorded data when necessary. In order to avoid this problem without having to change the particle thresholds the CSM Signal Processor incorporates the Particle Sample Time circuits (see Appendix 2) which generate the Enable Particle Stuff (EPS) signal used to limit the sampling of particle bursts from the LDV signal to an adjustable fraction of the total run time. However, in the present set-up the EPS signal has not yet been synchronized with the occurrence of zero crossings. Therefore it interferes with the correct counting of the Doppler frequency and has not been used so far.

In view of the above considerations the photomultiplier excitation was chosen to be 830 VDC, which seemed a good compromise for ensuring adequate sensitivity without incurring in saturation problems. The electronic thresholds have been set as explained in Appendix 2 using a simulated LDV signal. The value of the threshold is determined by the amplitude of the simulated signal (measured at the test point TP 15 on Board 3 of the CSM Signal Processor) which marginally triggers the corresponding comparator. With the above definition the particle thresholds have been set at 100 mV and the bubble thresholds at 160 mV, which experience showed to give good results in conjunction with the above photomultiplier excitation over a wide range of operating conditions.

7.2. CSM Flow Regimes

The cavitation observations and results of the CSM operation reported in this chapter have been obtained testing tap water in the venturi tubes No. 1 and No. 2 briefly described in Sec. 4.3 and respectively shown in Fig. 4.6 and Fig. 4.7. These two venturi tubes differ significantly in the interface to the inlet and outlet water lines, but are very similar in their fluid mechanical characteristics. They both have about the same throat section length (5 mm ca.) and the same geometrical contraction and expansion ratios ($C_c \simeq 1/100$ and $C_e \simeq 1.44$,

respectively). Besides, they are both made of blown glass, which seems to be the only material providing at the same time all the necessary properties: optical transparency for LDV operation, surface quality for flow stability and mechanical resistance to cavitation damage. The velocity profile determined from fully wetted flow measurements with artificial seeding using the LDV is also very similar in the two venturi and the corresponding minimum pressure developed in both cases is about $-35\,kPa$. This result is consistent with the throat pressure measurements independently obtained from the CSM in flows with very sporadic cavitation. The most important difference between the two venturi tubes under the fluid mechanical point of view consists in the different length of the exit section, which is much shorter in the venturi No. 1 (only a few diameters) than in the venturi No. 2, where it is about 3 cm long. As a consequence, the flow in the second venturi is considerably more stable with respect to the insurgence of cavitation-separation and of other undesired phenomena, as shown later in this chapter.

Three different flow regimes have been observed in the venturi tubes:

- travelling bubble cavitation;
- cavitation-separation;
- resonant cavitation.

Clearly only the first one is the nominal operational regime of the CSM where meaningful water quality measurements can be made. The others involve unwanted phenomena, which perturb the flow conditions in an incontrollable way and thereby prevent the possibility of reliably measuring the active cavitation nuclei concentration in the sampled water. They are, however, important because of the limitations they impose on the operation of CSM's in general and because some of the phenomena they involve can also occur sporadically in the normal operation of the CSM in the travelling bubble cavitation regime. They will be examined first in view of their usefulness for understanding some aspects of CSM normal operation results.

7.3. Cavitation-Separation

The cavitation-separation flow regime is characterized by the presence of an attached cavity originating in the upstream part of the diffuser and has been observed in both venturi tubes No. 1 (see Fig. 7.1) and No. 2 (see Fig. 7.2). Most likely the occurrence of this cavity is related to the insurgence of laminar separation in the early portion of the diffuser, as mentioned in Sec. 2.8. This phenomenon has also been reported by previous investigators [Oldenziel, 1982a], [Shen et al., 1986], [Ito and Oba, 1980]. When laminar separation takes place, cavitation nuclei from the main flow may, in the long run, be trapped in the recirculation region, where they eventually grow and possibly develop into an attached cavity.

The cavity can extend downstream to the exhaust section when the flow conditions are favourable (high velocity) and the exit section of the tube is relatively short, as in the venturi tube No. 1. In this case the exhaust pressure is established throughout the cavity and the useful portion of the diffuser is proportionally shortened. Therefore the pressure recovery in the diffuser is greatly reduced and the throat pressure increases to a value slightly lower than the exhaust pressure. On the other hand, when the exit section of the venturi is longer as in the venturi tube No. 2, the cavity usually terminates before reaching the exhaust section. The length of the separation-cavitation cavity changes greatly in response to the flow conditions, ranging in general from 0 to about 15 mm. Since the pressure inside the cavity (and consequently in the surrounding liquid) is about constant, when a cavity of significant length is established the flow in the venturi is greatly perturbed and the operation of the CSM is compromised.

The cavitation-separation cavity can be permanent or intermittent, steady or unsteady depending on the flow conditions: in general it is more likely to occur at higher flow velocity. In the venturi tube No. 1 the cavity first appears intermittently when the exhaust pressure is gradually reduced and always extends to the exhaust section. At lower downstream pressures the cavity tends to

become increasingly stable and its behaviour is usually steady, although in some instances it has been observed to rotate rapidly around the diffuser. However, when the exhaust pressure drops below a few thousand Pascals approaching the water vapor pressure, the cavity tends again to behave intermittently. It appears therefore that the presence of a non-condensable gas pressure has a stabilizing effect on cavitation-separation bubbles communicating with the exhaust.

This conclusion is also supported by the observation of the flow in the venturi tube No. 2, where the conditions for the occurrence of laminar separation are similar, but the presence of a much longer exit section prevents the cavitation-separation bubble from reaching the exhaust. In this tube the formation of a long attached cavity in the upstream part of the diffuser is usually intermittent and has been observed only occasionally, in most cases when the tube had been left dry and unused for some time. The last observation seems to indicate that surface nuclei on the inner wall of the venturi tube can play a role in stabilizing and possibly even in originating attached cavities during CSM operation. Evidence supporting this conclusion is also independently provided by the observation of phenomena attributed to surface nuclei in the resonant cavitation regime.

The occurrence of cavitation-separation causes a sudden drop of the arrival rate of cavitation events recorded by the CSM Signal Processor, due to the increase of the pressure at the venturi throat. When the cavity is unsteady, the above drop of the cavitation rate is also accompanied by a significant increase of the dispersion of the Doppler frequency readings from the remaining scatterers. If the cavity is steady and reaches the exhaust section its effect is limited to a sharp decrease of the achievable tension applied to the liquid at the throat section, as observed in the venturi tube No. 1. In most cases, however, the occurrence of cavitation-separation in the venturi produces large perturbations in the flow and compromises the operation of the CSM.

7.4. Resonant Cavitation

The resonant cavitation flow regime is characterized by the periodic occurrence of cavitation bubbles accompanied by a very distinct low frequency noise (ringing). It has only been observed in the venturi tube No. 1, usually in water samples with relatively low content of free stream nuclei. Resonant cavitation is a very stable phenomenon: the only way to eliminate it once it had established itself was to shut off the flow completely and to start it anew. Even in this case the probability of observing again, soon or within a short time, the occurrence of resonant cavitation was very high.

The bubbles originate in the initial part of venturi throat section, travel downstream and reach the exhaust section of the tube before collapsing. Their occurrence is extremely regular. When observed under stroboscopic light at a frequency commensurable with the bubble arrival frequency (synchronous frequency was not achievable with the available equipment) it is almost possible to freeze the appearance of the flow. A regular sequence of individual, isolated cavities can clearly be seen slowly moving either upstream or downstream, according to the sign of the instantaneous time phase difference between the illuminating light and the passage of the cavities. All cavitation bubbles appear to have very nearly the same size at the same location in the venturi tube. At the early stages of their growth the cavities have a distinct droplike shape, with a pronounced cusp facing upstream and always tilted towards the same side of the venturi wall, as if they originated from one specific spot on the internal surface of the tube. This situation is also confirmed by the observation that the velocity of the cavities in resonant cavitating flows is generally lower than recorded at the same location and under the same conditions in the absence of resonance and exhibits a marked decrease when the LDV focal point is moved upstream of its normal location in the CSM venturi tube.

Resonant cavitation disappeared after repeated cleaning of the venturi's internal surface, unfortunately before photographic records could be taken, and

stubbornly eluded all further attempts to reproduce it. However, all available evidence suggests that it is initiated by the presence of a microscopic cavitation nucleus at the surface of the venturi throat section, which sequentially generates tiny attached cavities. These cavities are then released in the venturi flow when they grow large enough to be swept away by the incoming stream. The shearing action of the deeper region of the boundary layer on the cavitation bubbles explains their observed shape and the orientation of their cusp. As mentioned earlier, the internal surface of the venturi tube No. 1 is made of blown glass and is extremely smooth. In no case it has been possible to observe visually any imperfection which could be identified as the nucleation agent.

The resulting two-phase compressible mixture in the diffuser is likely to be able to sustain resonant fluid mechanical oscillations when excited at suitable frequencies. Treating this mixture as an homogeneous compressible flow in a straight duct shows that an infinite set of natural acoustical frequencies exists, which depend on the boundary conditions. In the present situation the most realistic boundary conditions require constant exhaust pressure and no velocity perturbation at the inlet, where the flow is clearly dominated by the effects of the venturi's large contraction. The resulting expression of the resonant frequencies is:

$$f_n = (n + 1/2)\frac{c^2 - u^2}{2Lc}; \qquad n = 1, 2, \ldots \tag{7.1}$$

where n is the wave number, L the duct length, u the unperturbed velocity and c the sonic speed of the flow.

Admittedly the actual situation in the CSM venturi is considerably different in many ways. For example, the observed time interval between neighbouring bubbles and their velocity indicate that only one or possibly two bubbles are simultaneously present in the venturi at any time and that therefore the flow can hardly be considered an homogeneous mixture. The observation of a larger number of cavities in the venturi under stroboscopic light is clearly an artifact due to the fact that the frequency of the illuminating light pulses is not an integer

multiple of the bubble transit frequency. Furthermore, dynamic effects in the growth of the bubbles are likely to be important and would undermine another implicit assumption of the above compressible flow analysis: the existence of a barotropic relation between the pressure and the average mixture density.

Nevertheless it still seems certain that the diffuser flow can develop fluid mechanical oscillations when exposed to adequate excitation. Most likely the excitation is provided by the release of the cavities from the original surface nucleus in the stream, a phenomenon which is intrinsically periodic in nature. If the frequency of this excitation source happens to be sufficiently close to one of the natural frequencies of the flow, the whole system can be set into oscillation and a stationary pressure wave of relatively large amplitude can be induced. In turn the pressure and, to a lesser extent, the velocity fluctuations associated with this wave would interact with the mechanism controlling the release of the cavities in the flow stream, thus making the oscillation self sustained and extremely stable as long as the surface nucleus remains active.

The occurrence of resonant cavitation produces an LDV signal with Doppler bursts regularly spaced in time. Apart from this feature, which is only apparent when the signal is monitored on the oscilloscope at relatively slow sweep rate, there is no other immediately evident indication of irregular operation. The observed density distribution of the bubble delay times of a typical CSM run in resonant cavitation regime is shown in Fig. 7.3. For this run the bubble thresholds have been set almost equal to the amplitude of the Doppler bursts produced by the periodic passage of the cavities. This amplitude is very nearly constant from one cavity to the next, but sometimes shows some small, slow fluctuations. Therefore the great majority of the bubble counts have been recorded with a constant time delay corresponding to the large histogram in Fig. 7.3. A few other cavities following some missing counts have time delays which are integer multiples of the fundamental one and are represented in the figure by the smaller histograms regularly spaced along the time axis. The period of occurrence of the bursts in the above run is about 1 ms. This value is the also the most commonly

observed period of oscillation in resonant cavitation conditions and corresponds to a separation between the cavities of about 1.5 cm.

In few other cases shorter periods of about 350 μs have been recorded, with constant amplitude of the Doppler bursts, in agreement with the about equal size and shape displayed by the cavities at the same location in the tube. In one instance, however, a more complex resonance phenomenon has been observed where the time delay between bursts remained constant but two bursts of about equal size where followed by a larger one. In this case two surface nuclei were probably active since the cavities seemed to originate from both sides of the venturi's internal surface. The bubble occurrence frequency in resonant cavitation conditions has also been found to increase with the flow speed as suggested by equation (7.1), but no quantitative data have been recorded to document this phenomenon.

In the case of resonant cavitation the nature and the extent of the perturbations induced in the flow are so significant as to preclude the possibility of carrying out meaningful measurements of the concentration of unstable cavitation nuclei in the sampled water.

7.5. Travelling Bubble Cavitation

The travelling bubble flow regime is characterized by the random occurrence of cavitation bubbles in the CSM venturi and has been observed in both venturi tubes No. 1 (see Fig. 7.4) and No. 2 (see Fig. 7.5). The bubbles start to develop in the bulk of the liquid in the upstream region of the venturi's throat section, travel downstream reaching their maximum size somewhere in the diffuser or sometimes in the exit section and later collapse.

Under stroboscopic light the bubbles appear approximately spherical, at least during their growth phase. The length of the region where cavitation bubbles can be observed in the CSM venturi, their maximum size and occurrence rate depend on the flow conditions, clearly increasing with the throat tension and the velocity of the flow. In the venturi tube No. 2 (the only one where the entire

life cycle of the cavitation bubbles can be observed) the length of the cavitation region ranges from about 5 to 25 mm. The maximum size of the bubbles varies greatly from one bubble to the next and can even be comparable to the local diameter of the venturi. Optical observation also seems to indicate that larger bubbles occur when the cavitation event rate is relatively low. This behaviour suggests the possible presence of significant interactive effects among the bubbles at higher concentrations and is directly related to the general problem of flow saturation, which will be discussed later in detail.

The physical raw data and the reduced data of a typical CSM run in travelling bubble cavitation regime are shown in Fig. 7.6 through Fig. 7.13 as they are displayed and generated by the data acquisition and reduction program. They specifically refer to a tap water sample with an air content of 20.5 ppm at 21 °C, but are generally representative of the results obtained in other similar cases. The water sample, initially at atmospheric pressure, was tested in the venturi tube No. 2 at a throat pressure of −15 kPa corresponding to a velocity of 14.8 m/s. These data illustrate at the same time some of the most important aspects of the travelling bubble cavitation flow regime, the general operation of the CSM in a practical case and the main features of the data acquisition and reduction program.

The first three plots display the physical raw data relative to the counted Doppler bursts (particles) originally collected by the CSM Signal Processor. They respectively show the number of zero crossings (Fig. 7.6), the Doppler frequency readings (Fig. 7.7) and the corresponding upstream pressure readings (Fig. 7.8) as a function of the data index for the 1024 Doppler bursts recorded during the run.

The number of zero crossings depends on the size, shape and optical properties of the scatterer, on the location of its trajectory in the LDV probe volume, on the general characteristics of the LDV system and on the setting of the electronic thresholds in the CSM Signal Processor. In consideration of the many uncertainties involved, the measured numbers of zero crossings agree surpris-

ingly well with the estimated maximum number of fringes obtained from the LDV optical analysis, $N_{fr} = 17$ (see Sec. 3.3).

The Doppler frequency data are centered about the average value indicated on the scale. The dispersion of the data in this case is a bit larger than normally recorded in similar conditions due to the particularly heavy cavitation occurring during the run. Part of the data deviation from the average value can be attributed to the intrinsic slightly unsteady nature of the flow, to the non-uniformity of the velocity profile in the venturi or to imperfections in the measuring process. However, this data set also contains a small but significant number of low frequency readings which cannot be safely considered artifacts. Some of these readings do not appear to be randomly distributed during the run but rather seem to occur sequentially in small groups. Experience with the sensitivity of the LDV and the fact that the above low frequency scatterers have not been recorded in many other runs from water with similar particulate content indicate that they are probably coming from cavities in the flow rather than, for example, from small particles normally present in the boundary layer. Most likely they are due to bubbles originating from the disintegration of small attached cavities from surface nuclei under the action of the incoming flow and later swept downstream through the LDV probe volume before they had time to accelerate to the surrounding flow velocity. This conclusion is supported by the observation that cavitation events also occasionally occur in clusters corresponding to the short, almost horizontal stretches in the plot of the bubble arrival time data (see Fig. 7.11). On a much larger scale the same phenomenon is also produced by the disintegration of relatively large air bubbles naturally contained in the sampled water during their passage through the steep contraction of the venturi. This point is clearly illustrated for example by the large concentration of low frequency readings in the plot of Fig. 7.14 which refers to a different run.

The pressure data set is a very uneventful one, showing that the venturi upstream pressure stays indeed very nearly constant throughout the run at a

value slightly lower than the atmospheric pressure (from which the sample was drawn) due to the hydrostatic and frictional losses in the inlet duct to the CSM.

The next two plots show the filtered Doppler frequency and velocity data after all readings deviating from the mean more than three standard deviations have been eliminated. In the first plot (Fig. 7.9) the Doppler frequency data are again displayed as a function of their index. In the second plot (Fig. 7.10) a histogram chart representing the velocity distribution has been constructed and compared to the Gaussian curve derived from the average value and standard deviation of the velocity data. Note that in this case the observed distribution of velocity data seems to follow rather closely a normal distribution and does not display any appreciable skewness which could be attributed for example to the effects of the boundary layers, as previously mentioned in Sec. 5.2. Therefore the boundary layer thickness has been assumed to be zero and the theoretical distribution curve of equation (5.4) has not been fitted to the observed data. An example of a negatively skewed velocity distribution is shown in Fig. 7.15 for a different CSM run. The solid curve in the plot represents the theoretical velocity distribution (5.4) which minimizes the quadratic error expressed by the equation (5.5). In this case the estimated ratio of the boundary layer thickness to the local duct radius is 0.10.

Experience from other runs showed that the skewness of velocity distributions is usually small and that it occurs with about the same frequency in either direction, as if the biasing effects of the boundary layer were unimportant or masked by some other phenomenon. In addition, the shape of the velocity distributions does not seem to be correlated with any measured property of the venturi flow. The above discrepancy could be the consequence of the non-uniform distribution of the scatterers on the cross-sectional area of the venturi. High velocity readings from the core of the flow may indeed occur more frequently because most of the velocity tracers consist of small cavities which cannot be deeply contained in the boundary layer owing to their relatively large size. One can speculate that this effect may at times prevail on the opposite

influence of the boundary layer in determining the shape of the velocity data distribution. Alternatively, the skewness of the velocity data distribution could simply be the consequence of a slow drift of the flow velocity during the CSM run or of statistically insignificant fluctuations of the data. At the moment the available evidence is inconclusive in this respect. Therefore the estimates of the ratio of the boundary layer thickness computed from the observed negative skewness of the velocity data distribution should be regarded with some skepticism, despite the fact that they never gave unrealistic results.

The arrival times of the particle data are shown in Fig. 7.11. The stepwise nature of the data is due to the rather coarse resolution (204.8 ms) of the digital representation of the particle arrival time in the CSM Signal Processor. The discontinuity on the right-end side is the consequence of the cyclical storage sequence followed by the CSM Signal Processor when the number of recorded data exceeds the 1024 available memory locations.

Similarly, the occurrence times of the cavitation bubbles are shown in the next plot (Fig. 7.12) as a funtion of their arrival index. The resolution of the bubble time data (50 μs) is much higher than the one of the particle time data. The data have already been validated as explained in Sec. 5.2 in order to eliminate outliers. This presentation of the bubble time data is particularly useful to assess whether the flow conditions remained roughly constant during the entire run, as required for proper operation of the CSM. In this case the mean arrival rate of cavitation bubbles is constant and therefore the above plot is, in the average, a straight line. On the other hand, this is no longer the case when the exhaust pressure or the water quality change appreciably during the run. In particular, the above plot would exhibit a positive (upward) curvature when the exhaust pressure raises during the run. In general non-constant conditions tend to occur more frequently during the longest CSM runs, mostly as a consequence of a slow change of the exhaust pressure. Note that the order of magnitude of the average cavitation rate ($\overline{\nu}_b = 388.6$ Hz) is in good agreement with the expected range deduced from the CSM operational analysis of Sec. 2.5. As mentioned

earlier, the occurrence of the brief periods of faster arrival rate corresponding to the short, almost horizontal stretches of the bubble time plot are probably due to the disintegration of small attached cavities from surface nuclei under the action of the incoming flow.

In the last plot (Fig. 7.13) the histogram chart representing the distribution of the observed time intervals between cavitation events obtained from the validated bubble arrival times is compared with the theoretical exponential distribution calculated from equation (5.2) under the hypothesis of Poissonian cavitation occurrence. As mentioned in Sec. 2.5, the occurrence of cavitation in the CSM venturi is expected to be described by a Poisson process when the flow conditions are steady and the cavitation events are uncorrelated. Therefore the agreement of the observed distribution of the time intervals between the transit of cavitation bubbles with the theoretical exponential distribution provides a way to assess the importance of mutual interference effects between the cavities at the throat of the CSM venturi.

Cavitation bubbles in the CSM venturi flow can interfere with each others according to various mechanisms. In the most common and important type of mutual interaction the growth of a cavitation bubble increses the pressure in the surrounding liquid and therefore may reduce or prevent the growth of neighbouring cavities. The pressure perturbations associated to the volume changes of any individual bubble decrease with the distance and therefore their effects tend to be localized in space and time. This kind of interaction would therefore penalize the occurrence of the shortest delay times between the observation of cavitation events with respect to the theoretical exponential distribution. The deviation of the observed frequency of cavitation bubbles from the expected one at low time delays compared to the total number of recorded data provides a quantitative estimate of the likelihood of short range interference effects among cavities in the venturi flow and a rational way to introduce appropriate corrections to the CSM results when necessary.

However, the effects of short range bubble interference in CSM flows are

never large. At most they affect a few percent of the total number of cavities and only tend to appear at heavier cavitation rates when the separation between cavitating nuclei is proportionally reduced. This is not surprising when considering that the average separation of the cavitation bubbles computed from the measured flow velocity (15 m/s) at the highest mean cavitation rate (from 500 to 1000 events per second) is larger than 1.5 cm and therefore comparable to the length of the CSM venturi tube. Clearly more cavities are actually present in the flow whose LDV signatures are not large enough for them to be recognized as cavitation events by the CSM Signal Processor. However, their size and consequently their dynamic effects are proportionally smaller. The data from the present run do not show any evidence of important short range bubble interference. An example of a distribution of the observed time intervals between cavitation events deviating from the theoretical exponential distribution as a consequence of the above bubble interference effects is shown in Fig. 7.16 for a different CSM run.

When a large number of cavities is continuously present in the cavitation region of the CSM venturi the collective effects of the bubble volume changes produce a global, permanent increase of the pressure throughout the venturi test section. In this situation the tube is saturated and the maximum tension that venturi tube can develop at any given flow rate is reduced, as it will be shown later in this chapter. However, the pressure experienced by any one bubble is not appreciably modified by the presence of the neighbouring ones, since saturation is a large scale effect due to the collective contribution of many cavities widely distributed in the flow. Therefore this kind of bubble interference will affect the average cavitation rate but will not be reflected in an anomalous distortion of the observed distribution of the time intervals between cavitation events. Clearly saturation phenomena tend to increase with the concentration of unstable cavitation nuclei in the water sample and with the tension they are exposed to and impose limitations to the range of liquid quality measurements which can be carried out with the CSM.

Long range bubble interference mechanisms are also possible when a more organized large scale motion is excited in the flow, as we have seen in the case of resonant cavitation. Also in this case the distribution of the observed time intervals between cavitation events would be affected, most likely displaying peaks at one or more particular values of the time delay between the transit of cavitation bubbles.

The standard statistical method used to test the hypothesis that a distribution of M observed frequencies O_i fits the corresponding distribution of expected frequencies E_i consists in computing the variable:

$$\chi^2 = \sum_{i=1}^{M} \frac{(O_i - E_i)^2}{E_i} \tag{7.2}$$

Provided that the majority of the expected frequencies E_i are not smaller than 2 the above variable approximately follows a χ^2 distribution with $M-1$ degrees of freedom, mean value $M-1$ and standard deviation $\sqrt{2(M-1)}$. The value of χ^2 clearly decreases when the agreement of the observed distribution to the expected one increases and can be used to assess the likelihood that the observed statistical data come from a population following the expected distribution.

For the above distribution of time intervals between cavitation events the computed value of $\chi^2 = 52.6$ is not significantly large compared to the expected value $\overline{\chi^2} = 31$ and standard deviation $\sigma_{\chi^2} = 7.87$. This result confirms that the observed data are well represented by the expected distribution and that bubble interference effects, except possibly saturation, did not play an important role during the run.

The final reduced data and parameters for the CSM run of Fig. 7.6 are:

Minimun number of zero crossings:	$N_{zc_{min}} = 4$
Outlier filtering criterion in standard deviations:	$F_c = 3$
Number of data groups:	$M = 32$
Number of validated particle data:	$N_p = 878$
Average Doppler frequency:	$\overline{f}_D = 290.92\,\text{kHz}$

Doppler frequency data standard deviation:	$\sigma_{f_D} = 15.06\,\text{kHz}$
Average Doppler frequency standard deviation:	$\sigma_{\overline{f}_D} = 0.508\,\text{kHz}$
Average upstream pressure:	$\overline{p}_u = 95.43\,\text{kPa}$
Upstream pressure data standard deviation:	$\sigma_{p_u} = 0.202\,\text{kPa}$
Average upstream pressure standard deviation:	$\sigma_{\overline{p}_u} = 6.83\,\text{Pa}$
Average throat velocity:	$\overline{u}_t = 14.84\,\text{m/s}$
Throat velocity data standard deviation:	$\sigma_{u_t} = 0.7766\,\text{m/s}$
Average throat velocity standard deviation:	$\sigma_{\overline{u}_t} = 0.0262\,\text{m/s}$
Boundary layer thickness ratio:	$\delta_{BL}/R = 0$
Average throat pressure:	$\overline{p}_t = -15.021\,\text{kPa}$
Throat pressure data standard deviation:	$\sigma_{p_t} = 11.54\,\text{kPa}$
Average throat pressure standard deviation:	$\sigma_{\overline{p}_t} = 0.3896\,\text{kPa}$
Cavitation nuclei concentration:	$n(p_t) = 20.79\,\text{cm}^{-3}$
Cavitation nuclei concentration standard deviation:	$\sigma_n = 0.6499\,\text{cm}^{-3}$
Number of cavitation events:	$N_b = 1024$
Sample volume:	$V_s = 49.24\,\text{cm}^3$
Sample time:	$t_s = 2.633\,\text{s}$
Average time between cavitation events:	$\overline{\tau}_b = 2.573\,\text{s}$
Computed value of χ^2:	$\chi^2 = 52.61$
Expected value of χ^2:	$\overline{\chi^2} = 31$
Standard deviation of χ^2:	$\sigma_{\chi^2} = 7.874$

At given settings of the CSM the accuracy in the determination of the water quality is due to the errors in the measurement of the cavitating nuclei concentration and of the average throat pressure. Both these errors are inversely proportional to the square root of the size of the data sample and therefore can be significantly reduced by averaging the measured quantities on a sufficiently large number of data, provided that the flow conditions are constant during the run. Since the number of filtered data is usually close to 900, the relative error of the measurement of the cavitating nuclei concentration is rather small, of

the order of a few percent. As expected the standard deviation of the throat pressure data is quite large in relative sense due to the dispersion of the throat velocity data and to the small value of the pressure at the CSM venturi throat. Values of about 5 to 10 kPa for the standard deviation of the throat pressure data, as in the above case, are representative of the results usually obtained from CSM runs. This value must be divided by the square root of the sample size in order to obtain the standard deviation of the average throat pressure. With the same size of data sample as previously assumed the corresponding error in the determination of the average throat pressure is therefore of the order of a few hundred Pascals.

The above expected errors are both relatively small, but it should be born in mind that they strictly refer to the measuring process alone. In a broader sense the indetermination in the measurement of the water quality also includes the effects of the uncertainties in the relationship between the LDV signal intensity and the size of cavitating bubbles and in the discrimination of unstable nuclei from the stable ones. The former of these effects is related to the specific nuclei detection technique used in the CSM and could presumably be resolved to a large extent by calibrating the instrument response with cavities of known sizes, as previously suggested. The latter is instead shared by all currently devised techniques of cavitation nuclei detection. The inclusion of all error sources involved makes the measurement of the liquid quality with CSM's (and with other alternative methods) considerably more uncertain than it would first appear from the above considerations.

7.6. Water Quality Measurements

The results of repeated CSM runs on the same water sample at different flow conditions can be used to determine the change of the concentration of unstable cavitation nuclei as a function of the throat pressure in the venturi tube. In this process care must be taken to ensure the maximum possible uniformity of the sample. In particular the inlet line to the CSM test section must be filled with

water whose characteristics are as similar as possible to the water to be sampled and the test runs should be executed quickly to prevent the errors due to changes of the characteristics of the sample. The acquisition rate is presently limited by the speed of the computer to about one run per minute plus, of course, the time needed to execute the run.

Several tap water samples have been tested in this way using the venturi tube No. 2, whose operation is usually free from undesired phenomena. The water was sampled from the tap using an overflow line open to the atmosphere in order to continously resupply the inlet line to CSM. The total distance from the tap to the CSM test section was about three meters and the water transit time at the operational flow rate ranged from about five to ten seconds depending on the flow conditions. At visual observation the water appeared to contain a large number of microbubbles in suspension. The dissolved air content of the water was monitored with the manometric van Slyke device and its temperature with a thermometer just before the beginning of the test. A series of about ten runs was recorded at increasing values of the throat pressure. The flow was regulated by increasing the exhaust pressure in roughly equal steps from the lowest achievable value almost to the desinent cavitation conditions in the venturi tube. In this process the exhaust pressure ranged from a lower value close to the vapor pressure of the water sample (about 2000 Pa at the room temperature) to an upper value in the neighborhood of 30 kPa.

Some examples of the application of the CSM to the measurement of the concentration of cavitation nuclei as a function of the minimum pressure in the venturi throat in samples of tap water are shown in Fig. 7.17 through Fig. 7.19. The water quality measurements have been recorded on different days, but the characteristics of the water samples are quite similar. The first measurement (Fig. 7.17) refers to a tap water sample with a temperature of 21 °C and a dissolved air content of 20.5 ppm. In the second measurement (Fig. 7.18) the water temperature is 21.3 °C and the dissolved air content is 21.3 ppm. Finally, the third set of data (Fig. 7.19) has been obtained from a sample of tap water

at 21 °C with a dissolved air content of 20.8 ppm.

In consideration of the uncertainties involved and of the inherent differences among the various samples the agreement of the above results is satisfactory. In all cases the concentration of cavitation nuclei seems to follow the same pattern when the throat pressure is lowered. At first it increases roughly in an exponential way until the throat pressure reaches a certain value. A similar behaviour has also been reported by other investigators [Oldenziel, 1982], [Shen and Gowing, 1984], [Shen et al., 1986]. When the throat pressure is further reduced the concentration of cavitation nuclei reaches a maximum and then remains about constant. The value of the maximum measured concentration of cavitation nuclei varies from 20 to 40 cm^{-3} and the throat pressure corresponding to the transition in the nuclei concentration diagrams is in the range of -7 kPa. Both the maximum value of the unstable nuclei concentration and of the throat pressure where the above transition occurs seem to depend on the characteristics of the sample. The occurrence of some sort of transition in the flow conditions when the throat pressure decreases is also strongly suggested by the behaviour of the dispersion of the throat velocity data. The standard deviation of the throat velocity readings for the last water sample of Fig. 7.19 is plotted in Fig. 7.20 as a function of the throat pressure. The dispersion of the velocity data is initially low and about constant and later increases quickly when the throat pressure is further reduced.

The most likely explanation of this situation is that the observed behaviour of the concentration of cavitation nuclei really reflects the lack of cavitation nuclei which become active when the throat pressure is lowered below about -7 kPa. In this case a further decrease of the throat pressure would simply produce a more violent growth and collapse of the available population of active nuclei. Hence larger perturbations would be induced in the flow, with the consequence of generating the steady increase in the dispersion of the throat velocity readings observed in Fig. 7.20. According to equation (2.2) the equilibrium radius of a gas bubble which becomes unstable at about -7 kPa is of the

order of 4 μm. Since most of the cavitation nuclei in the above water samples consist of suspended microbubbles, one can for example speculate that bubbles with radius smaller than about 4 μm quickly dissolved in the surrounding water due to the high internal pressure (about 140 kPa) generated by surface tension effects. Alternatively, the absence of smaller bubbles could be the result of the specific nature of the original mechanism of bubble formation in the water sample. In both these cases the concentration of cavitation nuclei would stop increasing with the applied tension simply because practically all existing nuclei have already been excited to cavitate and relatively few are left which would react to even lower pressures. Although the above interpretation of the observed behaviour of the concentration of the cavitation nuclei seems plausible, the evidence available at the moment is not fully conclusive in this respect. This explanation could, however, be tested by examining the CSM results obtained from water samples of known nuclei concentration density distribution.

Assuming that the throat pressure is correctly measured also in the presence of heavy cavitation, the minimum pressure generated by the CSM venturi is of the order of -15 kPa for all the runs except the first. Clearly this pressure was obtained when the exhaust pressure of the venturi approached its minimum possible value corresponding to the vapor pressure of the sampled water at the exhaust conditions, about 2 kPa. Since the venturi used in the test can develop considerably lower pressures at the throat in the absence of extensive cavitation, it appears that saturation phenomena are responsible for the observed decrease of the maximum achievable tension in the venturi. The average arrival time interval of cavitation events measured in the last water sample is plotted in Fig. 7.21. The same data from the other samples are quite similar and have been omitted. This plot shows that the average time delay between cavitation bubbles at the minimum value of the throat pressure is of the order of 2 ms, and even lower in some cases. The corresponding cavitation rate is very high, about 500 events per second, and supports the above conclusion that saturation effects may be the cause of the observed limitations of the CSM venturi performance.

The concentrations of cavitation nuclei in Fig. 7.17, Fig. 7.18 and Fig. 7.19 also display a slight decline at the lowest values of the throat pressure, which correspond to the fastest flows. It is clearly impossible that this situation reflects a real state of affairs because each nucleus which cavitates at a certain pressure level will also cavitate at any other lower level of the pressure. The most likely explanation of this effect is that the increase of the flow velocity allows the cavities less time to grow in the throat section of the venturi before they reach the LDV focal point and that the number of cavities recorded by the CSM Signal Processor decreases only as a consequence of the parallel decrease of their size. The velocity change from the location of the maximum of the cavitating nuclei concentration to the conditions corresponding to the lowest throat pressure is relatively small and its effect is also countered by the increase of the tension driving the growth of the cavitation bubbles. Therefore one would expect that the combined influence of these two mechanisms should not be large and indeed the observed decrease of the unstable nuclei concentration in the above figures is relatively small. Clearly, this effect could also be a contributing factor in the stabilization of the concentration of cavitating nuclei when the pressure is reduced.

7.7. Future Work

The available operational experience with the present CSM venturi configuration suggests that the immediate areas of further work and development of the system can be identified as follows:

- improvement of the control of cavitation-separation, possibly by inducing turbulent transition at some intermediate location in the diffuser in order to promote the stability of the boundary layer. Previous attempts of inducing transition using small backward-facing steps in the diffuser have failed because of the occurrence of cavitation-separation in the transition region. Unfortunately the problem may be extremely difficult or maybe impossible

to solve if it turns out that even the perturbations due to spontaneous transition are capable to induce again the insurgence of cavitation-separation in flows exposed to negative pressures.

- increase of the maximum value of the tension at the venturi throat. The solution of this problem is strictly connected to the control of cavitation-separation because the minimum pressure in the venturi clearly depends on the maximum pressure recovery achieved in the diffuser.
- improvement of the control of the effects due to surface nuclei such as sheet cavitation and resonant cavitation which interfere with the normal operation of the CSM.
- calibration and comparison of the CSM with a different and reliable nuclei detection method (holography) in order to "properly" choose the thresholds for the discrimination of cavitation events and in order to correctly interpret of some of the observed results.
- synchronized photographic observation of the occurrence of cavitation in order to measure the average size of the cavities recognized by the CSM at given settings of the discrimination thresholds.

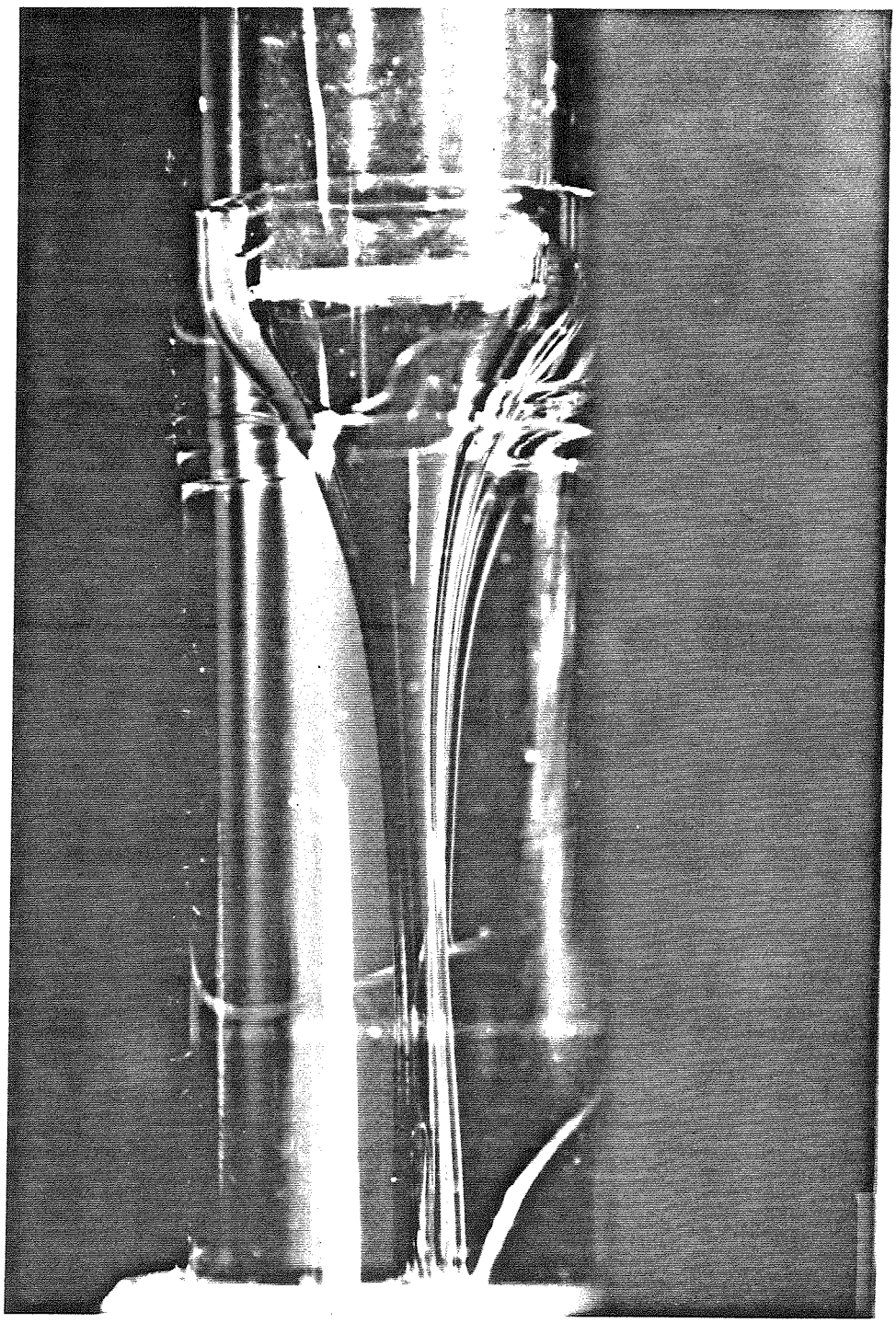

Figure 7.1. Cavitation-separation of a tap water sample initially at atmospheric pressure in the CSM venturi tube No. 1. The flow is from right to left. Cavitation-separation originates the small parabolic bubble visible in the terminal section of the diffuser. The exhaust pressure is about 5000 Pa and the throat velocity about 13.5 m/s.

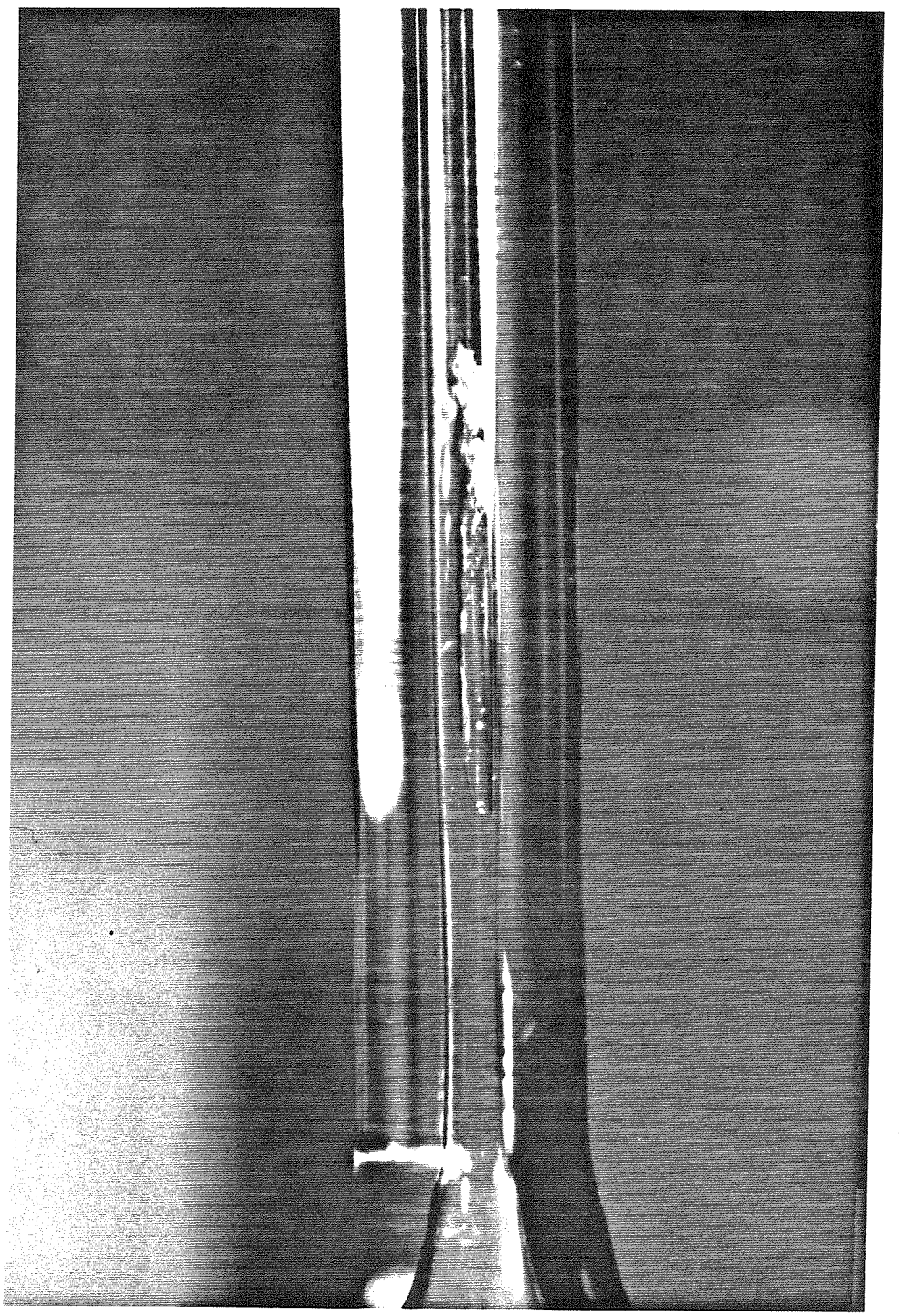

Figure 7.2. Cavitation-separation of a tap water sample initially at atmospheric pressure in the CSM venturi tube No. 2. The flow is from left to right. The cavitation-separation bubble originates in the diffuser and terminates in the exit section without reaching the exhaust. The exhaust pressure is about 5000 Pa and the throat velocity about 13.5 m/s.

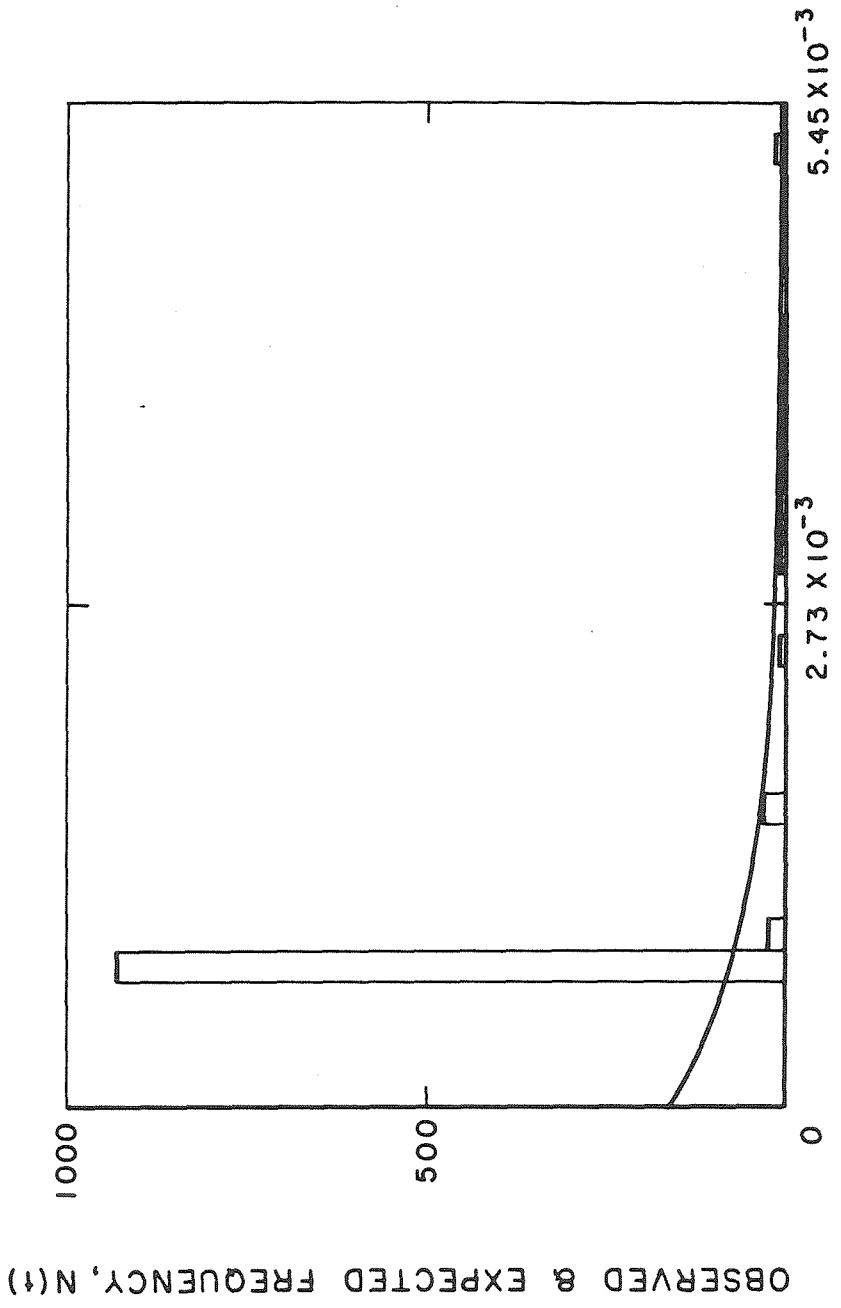

Figure 7.3. Histogram chart of the observed density distribution of time intervals between cavitation events in resonant cavitation conditions in the CSM venturi tube No. 1. The continuous line indicates the expected (Poissonian) distribution corresponding to the observed value of the average arrival rate.

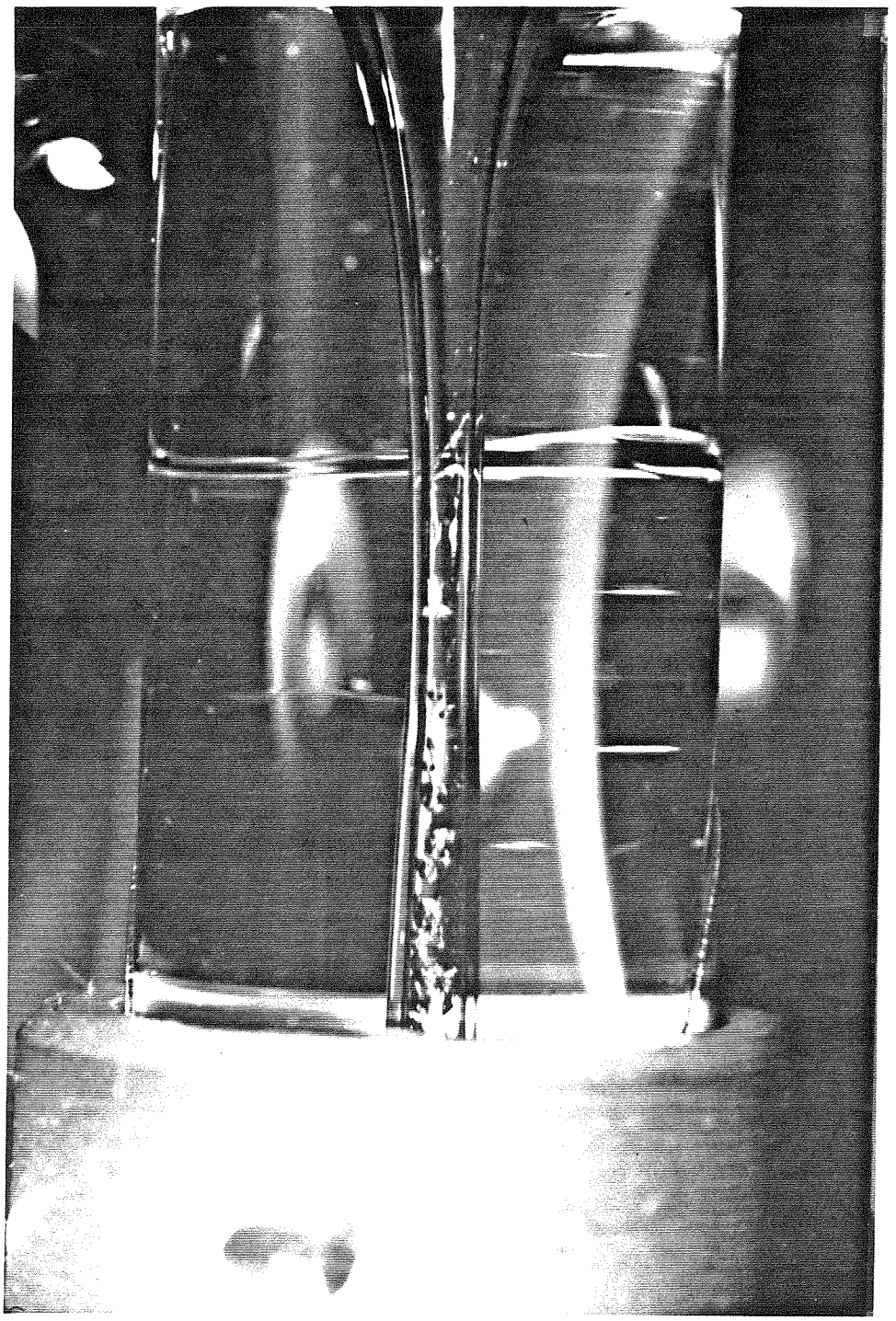

Figure 7.4. Travelling bubble cavitation of a tap water sample initially at atmospheric pressure in the CSM venturi tube No. 1. The flow is from right to left. The throat pressure is about −15 kPa and the throat velocity about 14.8 m/s.

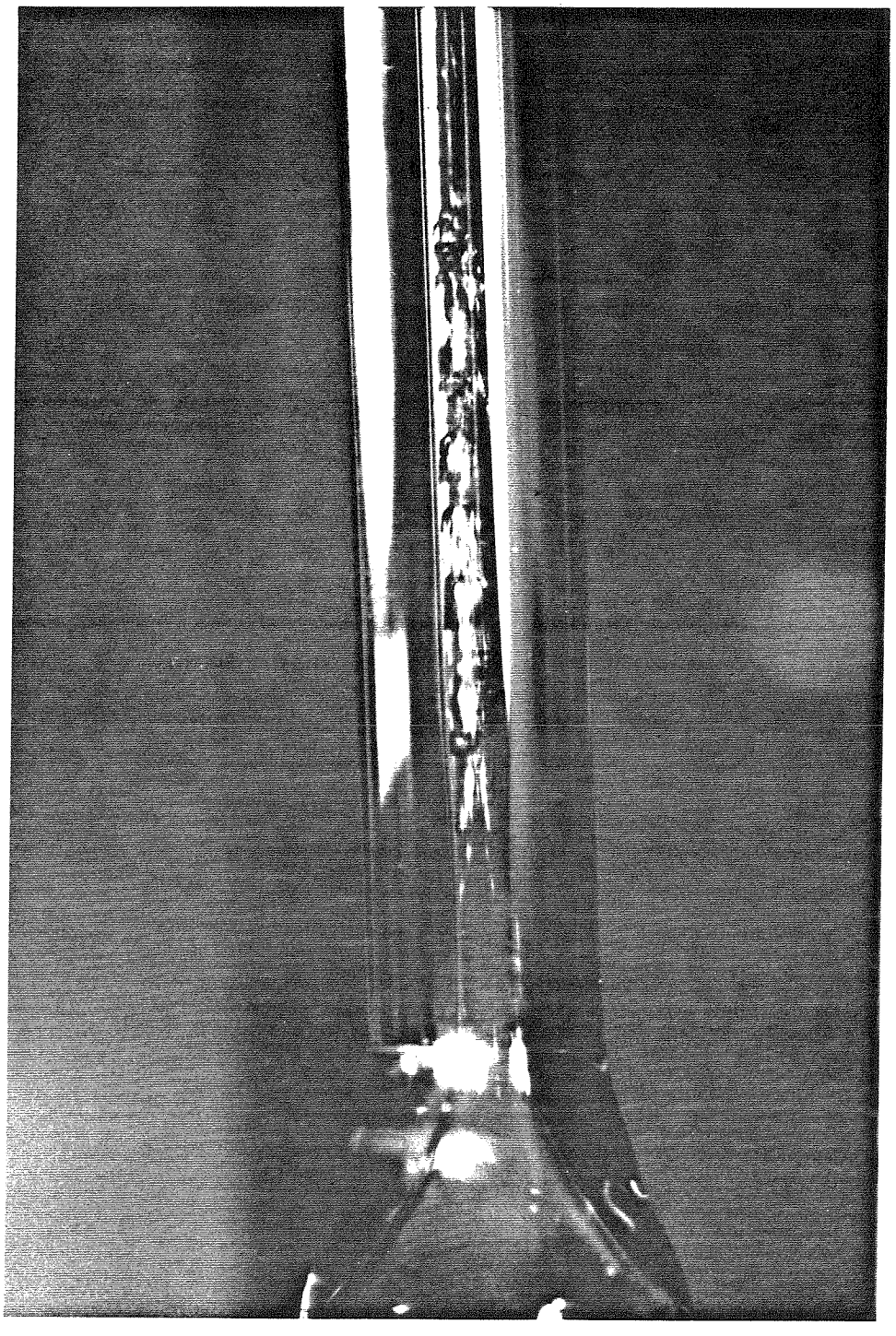

Figure 7.5. Travelling bubble cavitation of a tap water sample initially at atmospheric pressure in the CSM venturi tube No. 2. The flow is from left ot right. The throat pressure is about −15 kPa and the throat velocity about 14.8 m/s.

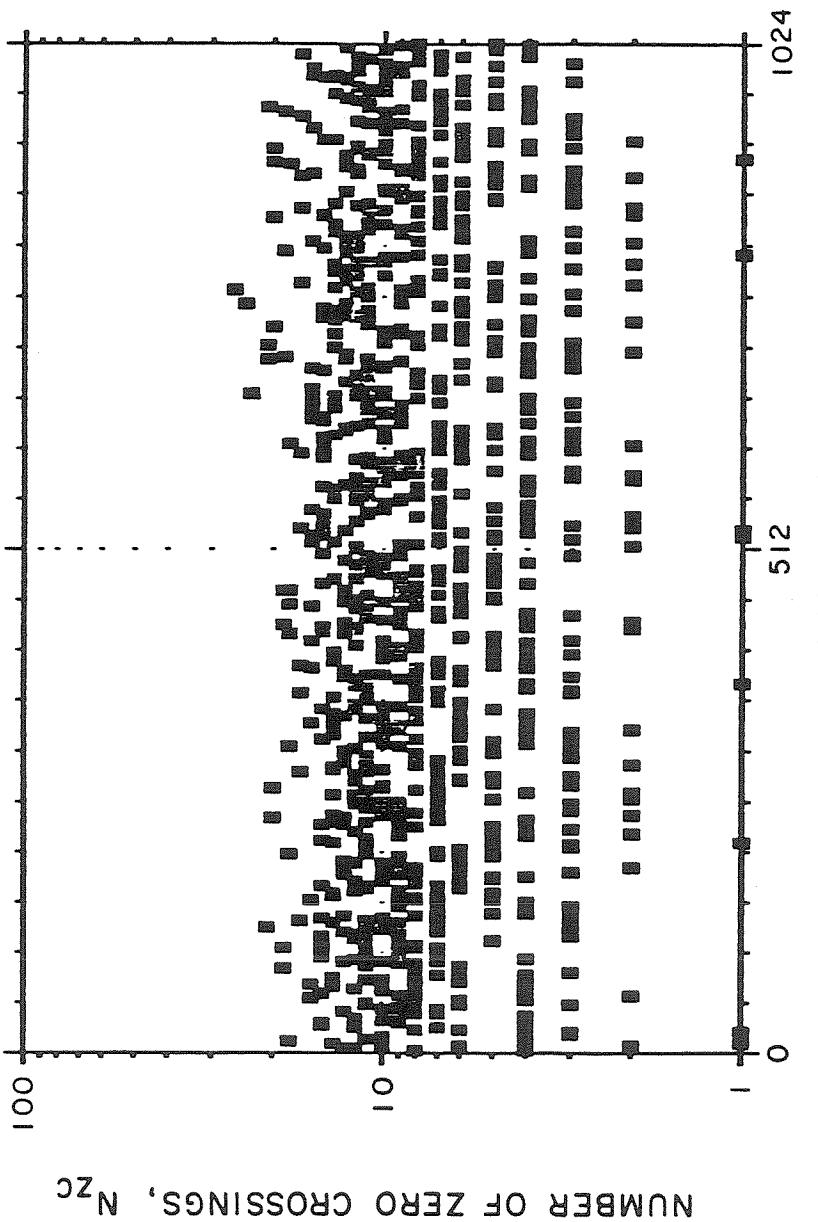

Figure 7.6. Zero crossing data N_{zc} as a function of the data index I in a typical CSM run. The data refer to a tap water sample with the following initial properties: initial pressure $p_o = 1\,\text{atm}$, temperature $T = 21\,^\circ\text{C}$ and air content $\alpha = 20.5\,\text{ppm}$. The throat pressure and velocity are: $p_t = -15\,\text{kPa}$, $u_t = 14.8\,\text{m/s}$.

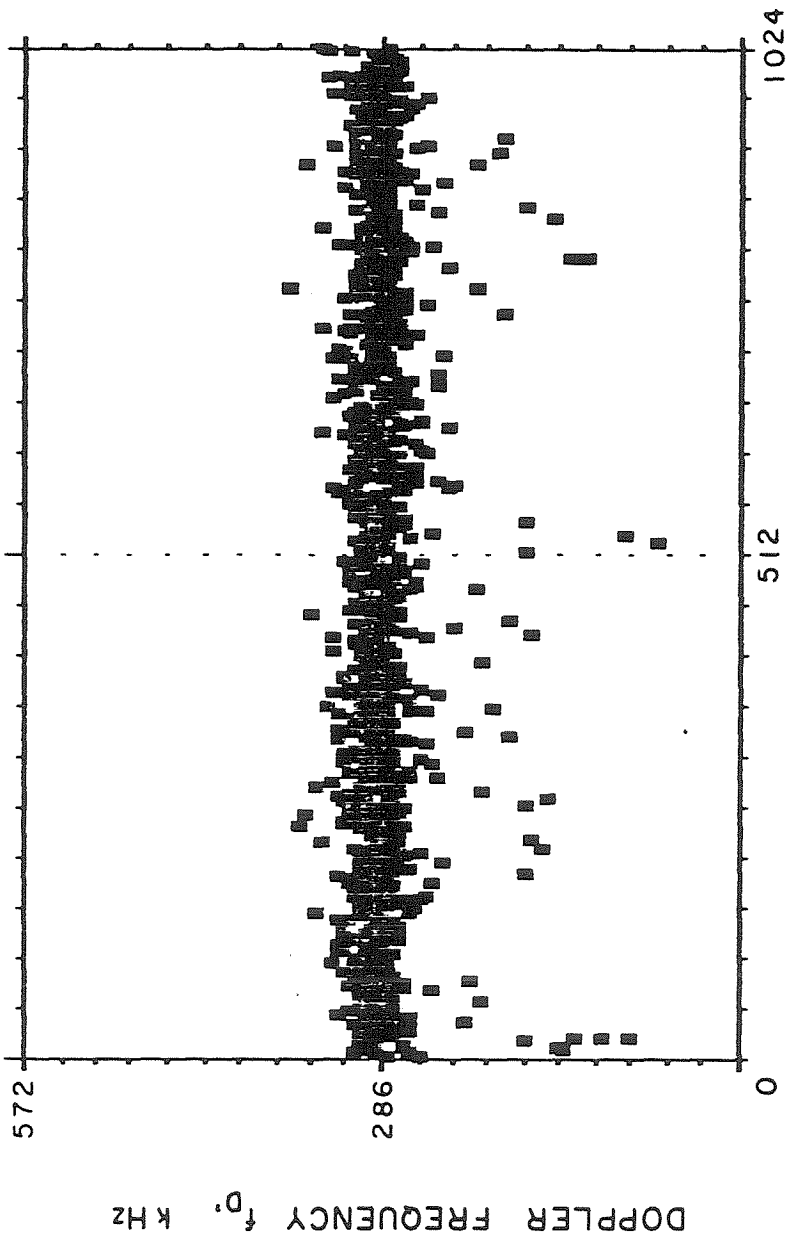

Figure 7.7. Doppler frequency data f_D as a function of the data index I in a typical CSM run. The data refer to the tap water sample of Fig. 7.6: initial pressure $p_o = 1\,\text{atm}$, temperature $T = 21\,^\circ\text{C}$, air content $\alpha = 20.5\,\text{ppm}$, throat pressure $p_t = -15\,\text{kPa}$ and throat velocity $u_t = 14.8\,\text{m/s}$.

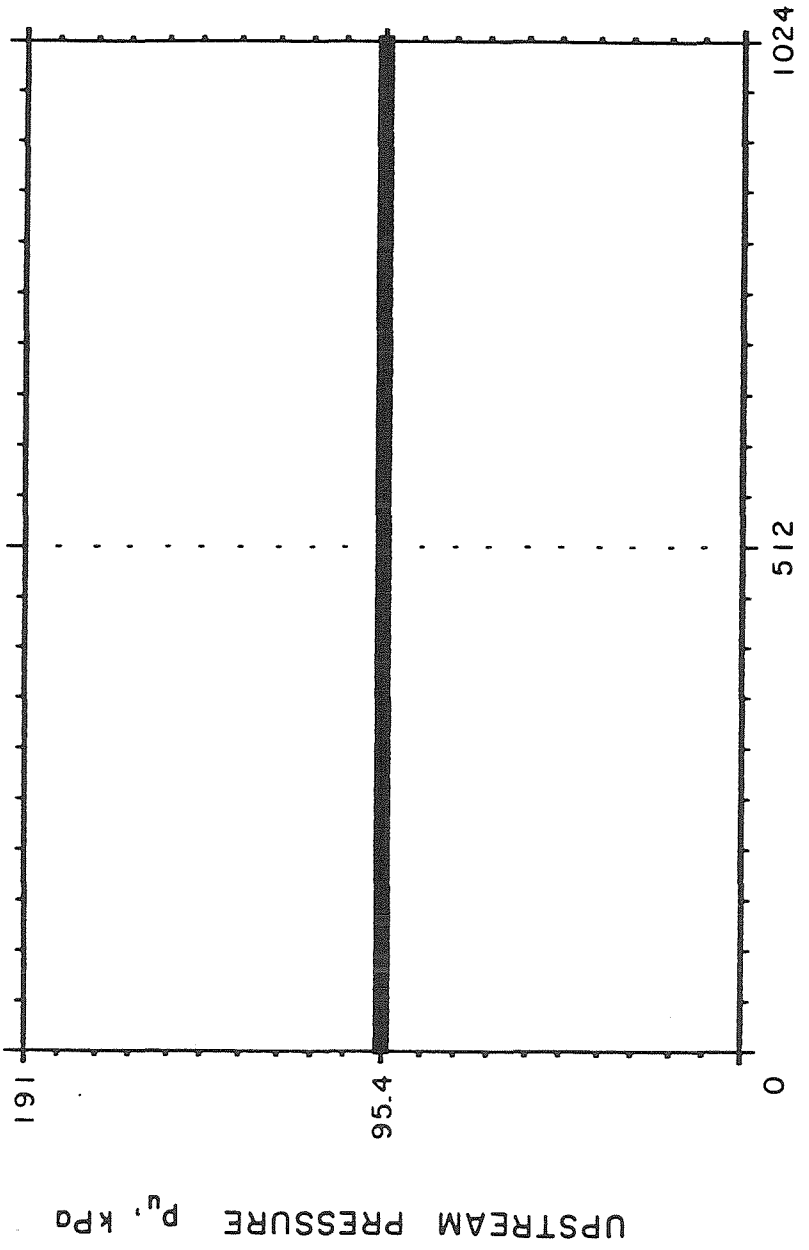

Figure 7.8. Upstream pressure data p_u as a function of the data index I in a typical CSM run. The data refer to the tap water sample of Fig. 7.6: initial pressure $p_o = 1$ atm, temperature $T = 21\,^{\circ}\mathrm{C}$, air content $\alpha = 20.5$ ppm, throat pressure $p_t = -15$ kPa and throat velocity $u_t = 14.8$ m/s.

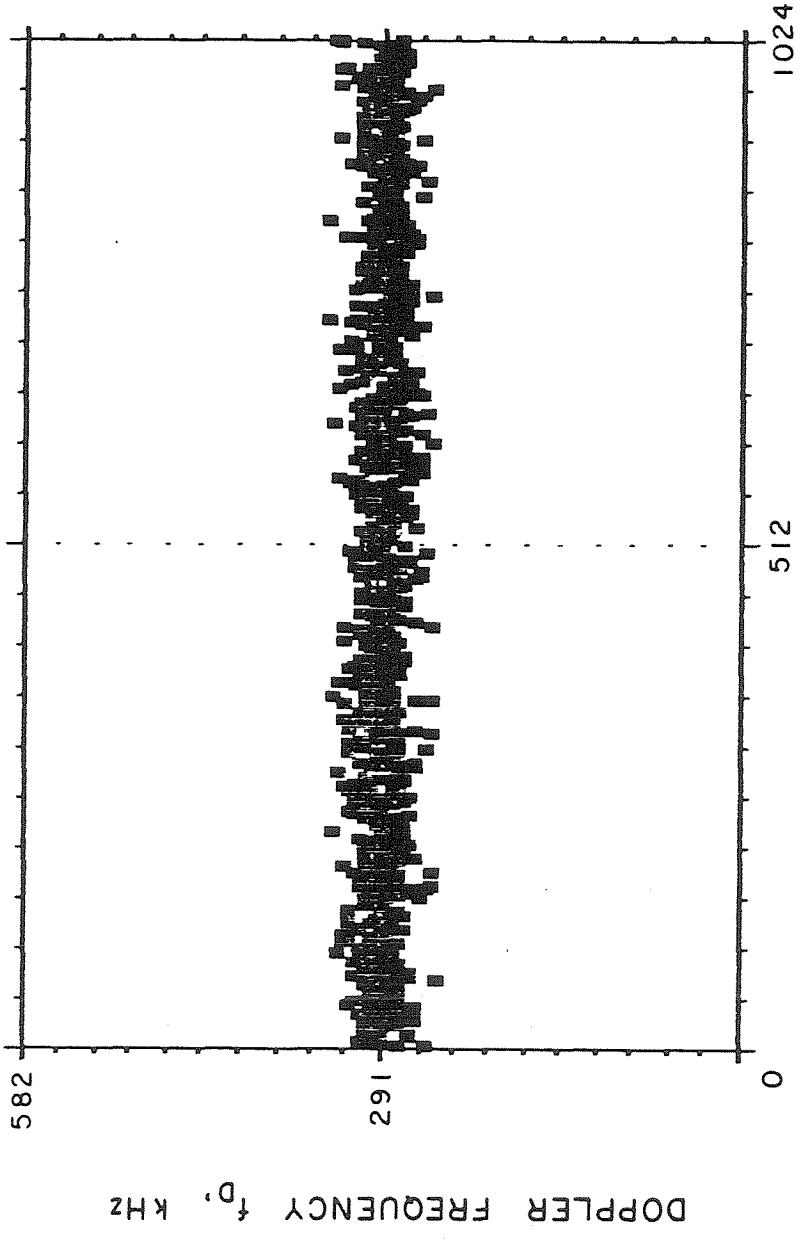

Figure 7.9. Filtered Doppler frequency data f_D as a function of the data index I in a typical CSM run. The data refer to the tap water sample of Fig. 7.6: initial pressure $p_o = 1$ atm, temperature $T = 21\,^{\circ}$C, air content $\alpha = 20.5$ ppm, throat pressure $p_t = -15$ kPa and throat velocity $u_t = 14.8$ m/s. Readings deviating from the mean more than three standard deviations have been eliminated.

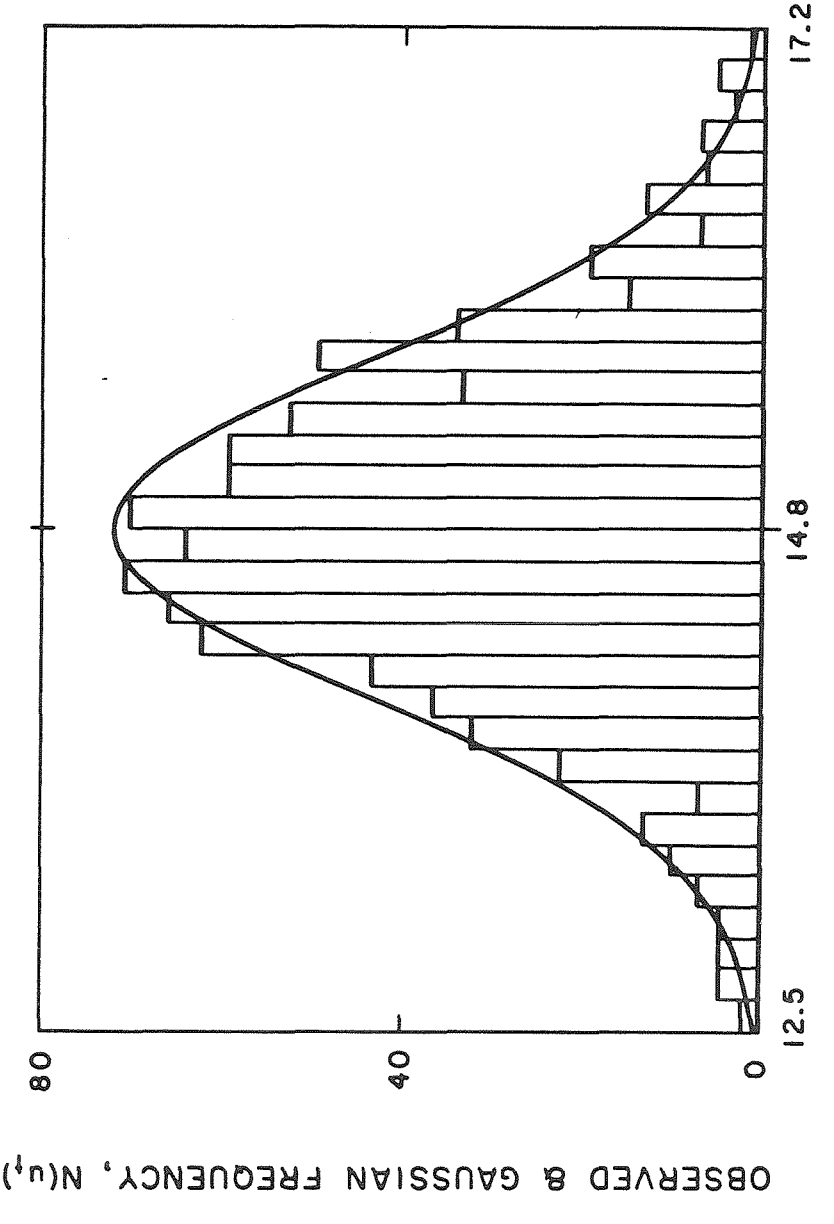

Figure 7.10. Histogram chart of the observed distribution of filtered throat velocity data compared to the Gaussian distribution (solid line) of equal mean and standard deviation in a typical CSM run. The data refer to the tap water sample of Fig. 7.6: initial pressure $p_o = 1$ atm, temperature $T = 21\,^{\circ}$C, air content $\alpha = 20.5$ ppm, throat pressure $p_t = -15$ kPa and throat velocity $u_t = 14.8$ m/s. Readings deviating from the mean more than three standard deviations have been eliminated.

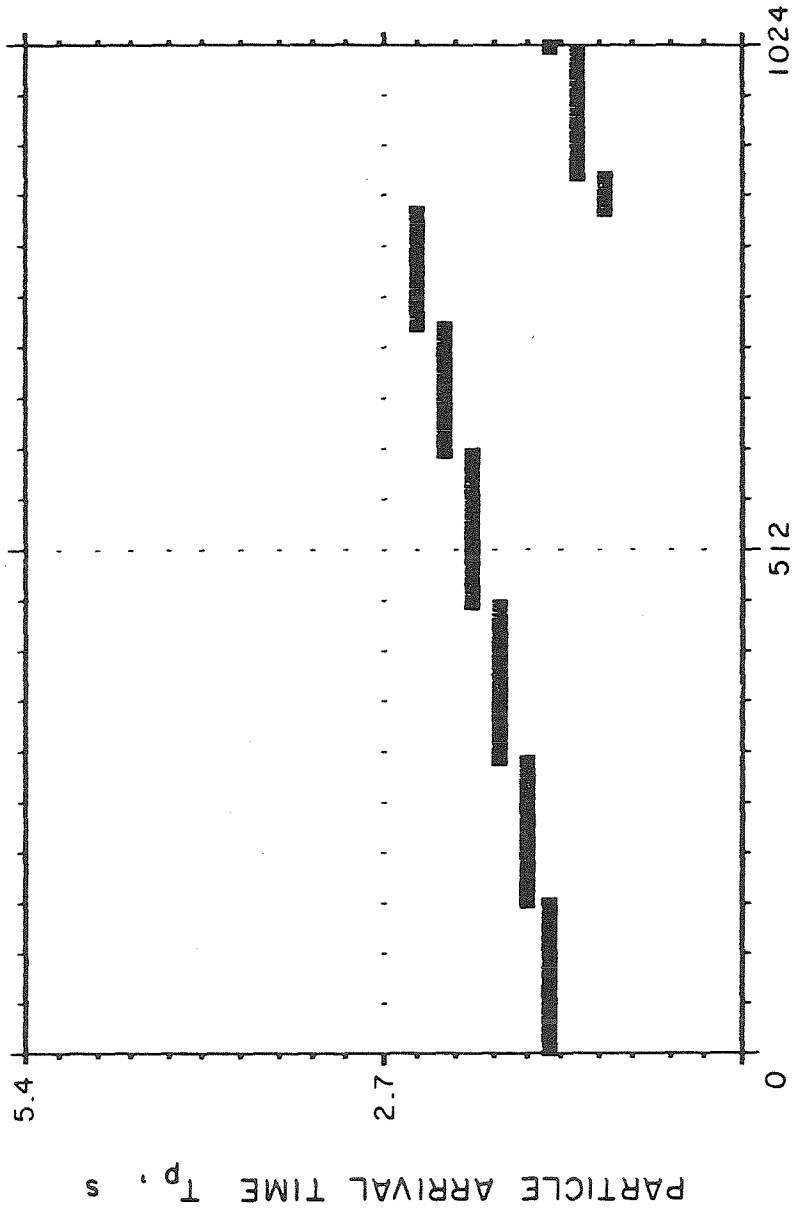

Figure 7.11. Arrival time data T_p of velocity tracers (particles) as a function of the data index I in a typical CSM run. The data refer to the tap water sample of Fig. 7.6: initial pressure $p_o = 1$ atm, temperature $T = 21\,^{\circ}$C, air content $\alpha = 20.5$ ppm, throat pressure $p_t = -15$ kPa and throat velocity $u_t = 14.8$ m/s.

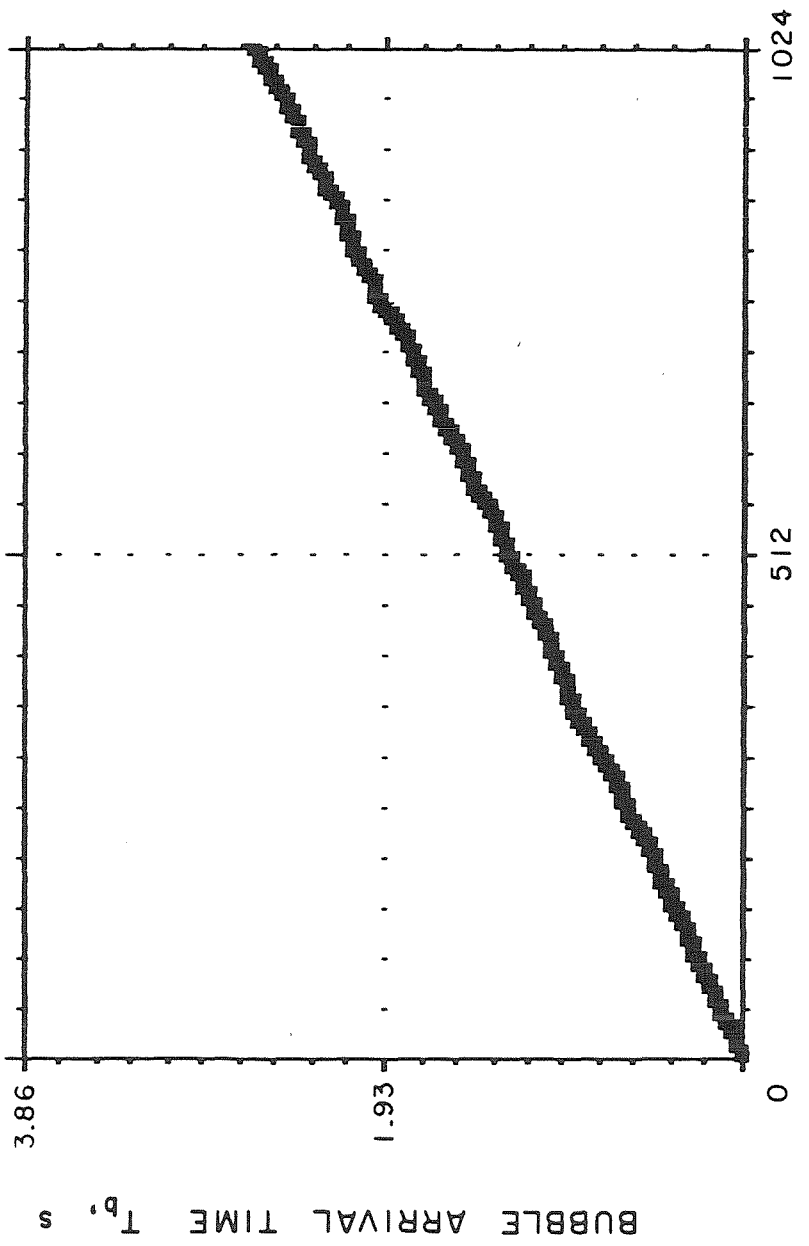

Figure 7.12. Arrival time data T_b of cavitation events (bubbles) as a function of the data index I in a typical CSM run. The data refer to the tap water sample of Fig. 7.6: initial pressure $p_o = 1\,\text{atm}$, temperature $T = 21\,^\circ\text{C}$, air content $\alpha = 20.5\,\text{ppm}$, throat pressure $p_t = -15\,\text{kPa}$ and throat velocity $u_t = 14.8\,\text{m/s}$.

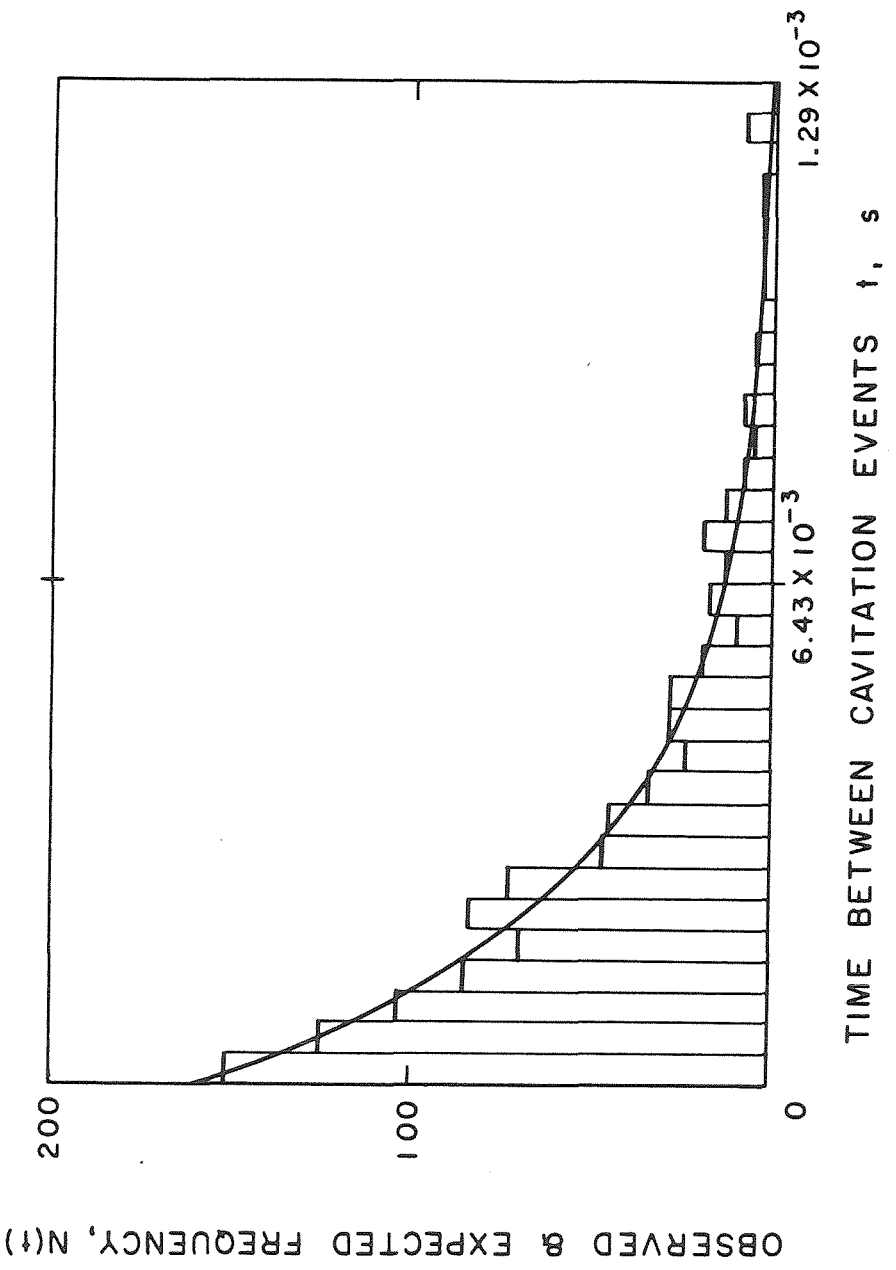

Figure 7.13. Observed distribution of time intervals between cavitation events (histograms) compared to the theoretical Poissonian distribution (solid line) of equal average arrival rate in a typical CSM run. The data refer to the tap water sample of Fig. 7.6: initial pressure $p_o = 1$ atm, temperature $T = 21\,^{\circ}\mathrm{C}$, air content $\alpha = 20.5$ ppm, throat pressure $p_t = -15$ kPa and throat velocity $u_t = 14.8$ m/s.

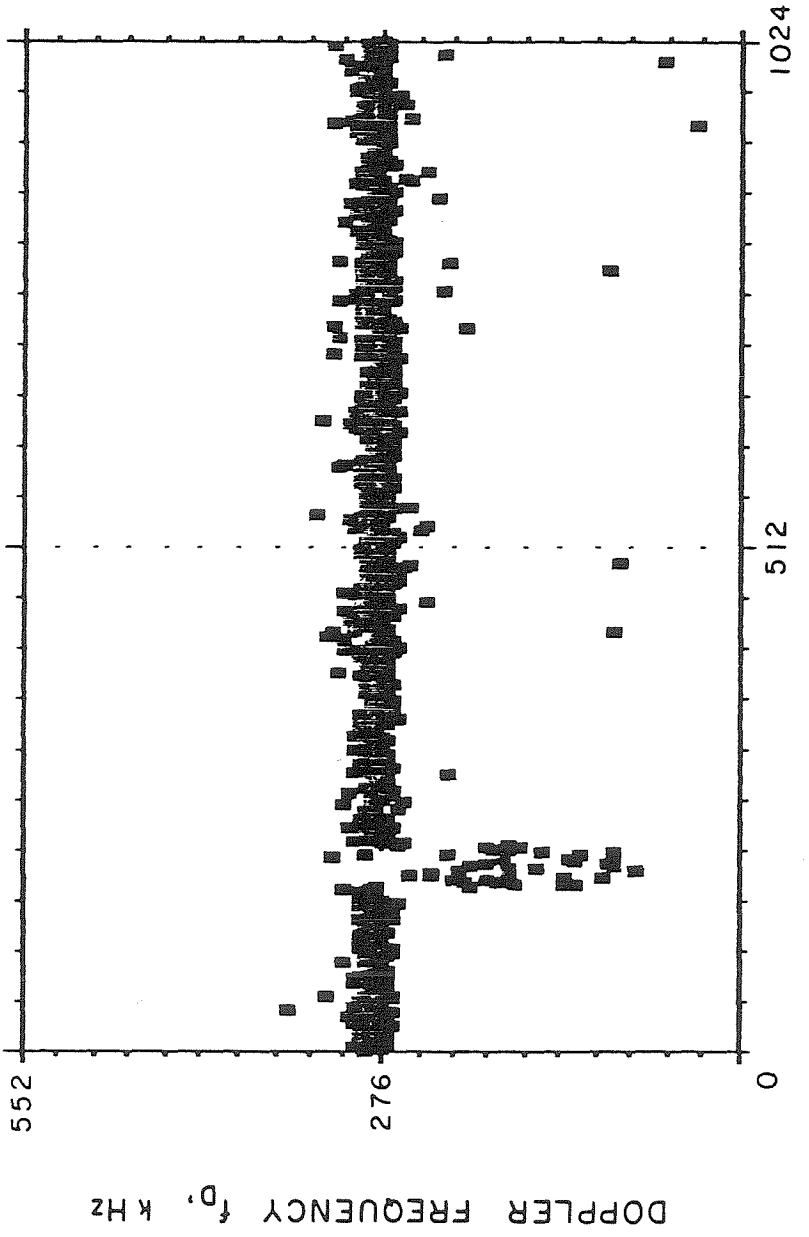

Figure 7.14. Example of Doppler frequency data f_D as a function of the data index I showing a large concentration of low frequency readings due to the disintegration of an air bubble during its transit through the venturi throat.

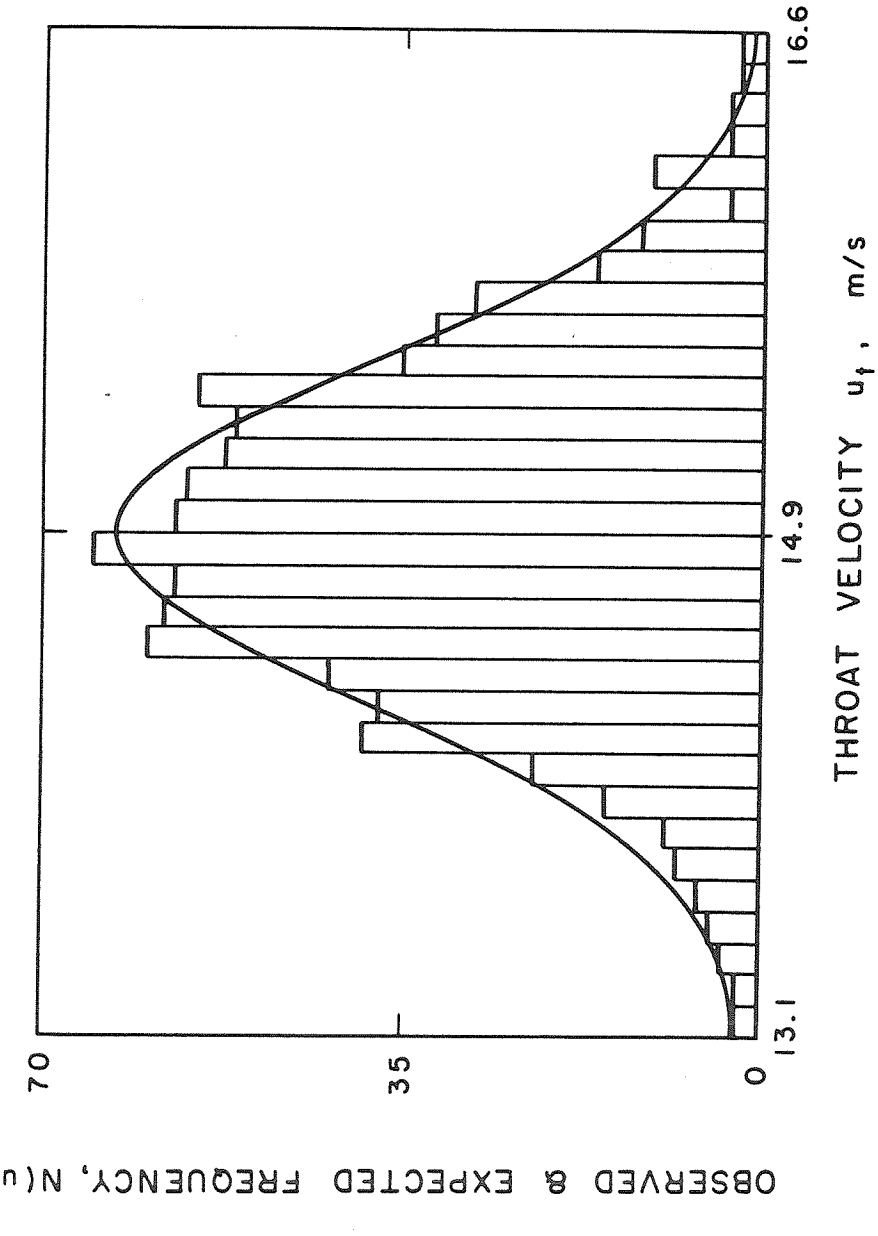

Figure 7.15. Example of negatively skewed observed distribution of throat velocity data compared to the fitted theoretical distribution in a typical CSM run. Readings deviating from the mean more than three standard deviations have been eliminated.

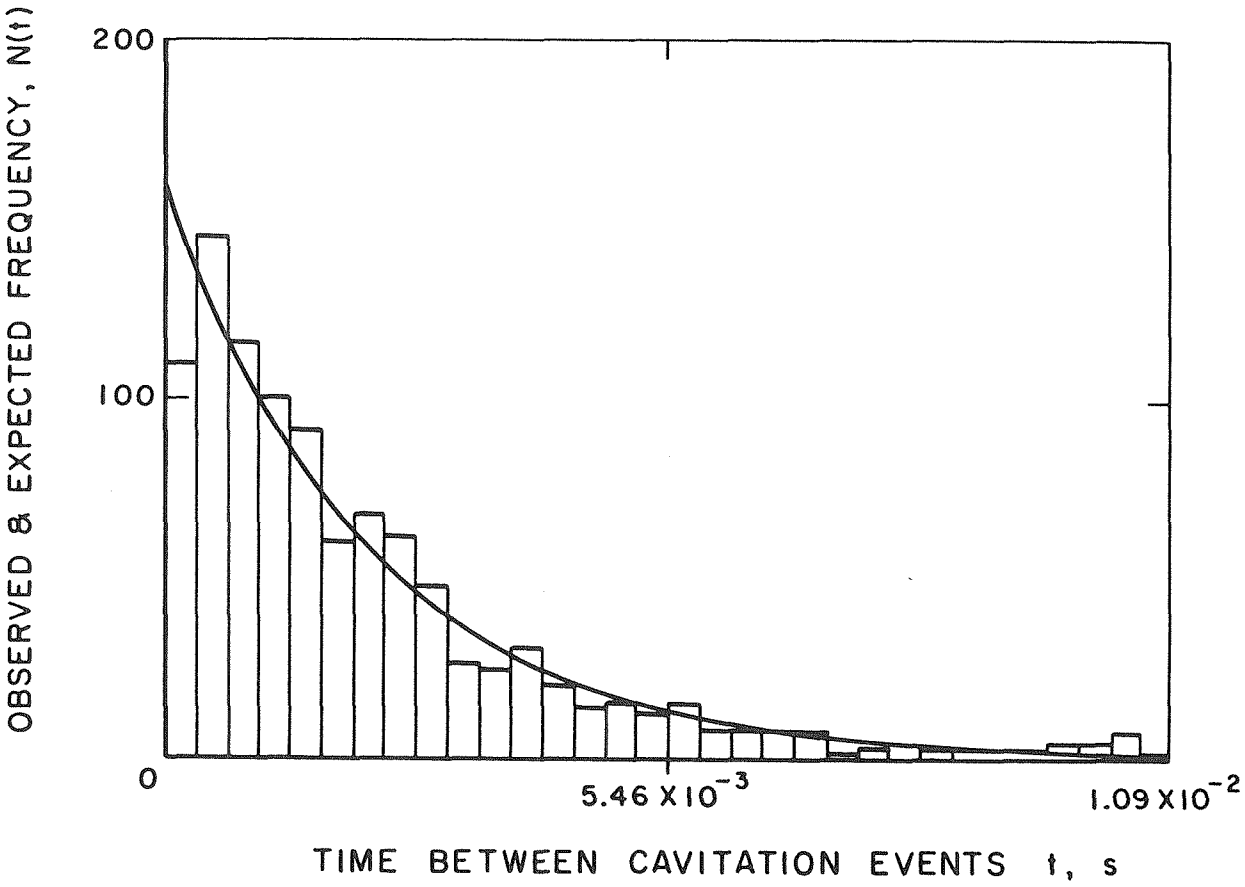

Figure 7.16. Observed distribution of time intervals between cavitation events (histograms) slightly deviating close to the origin from the theoretical exponential distribution (solid line) as a consequence of short range bubble interference effects.

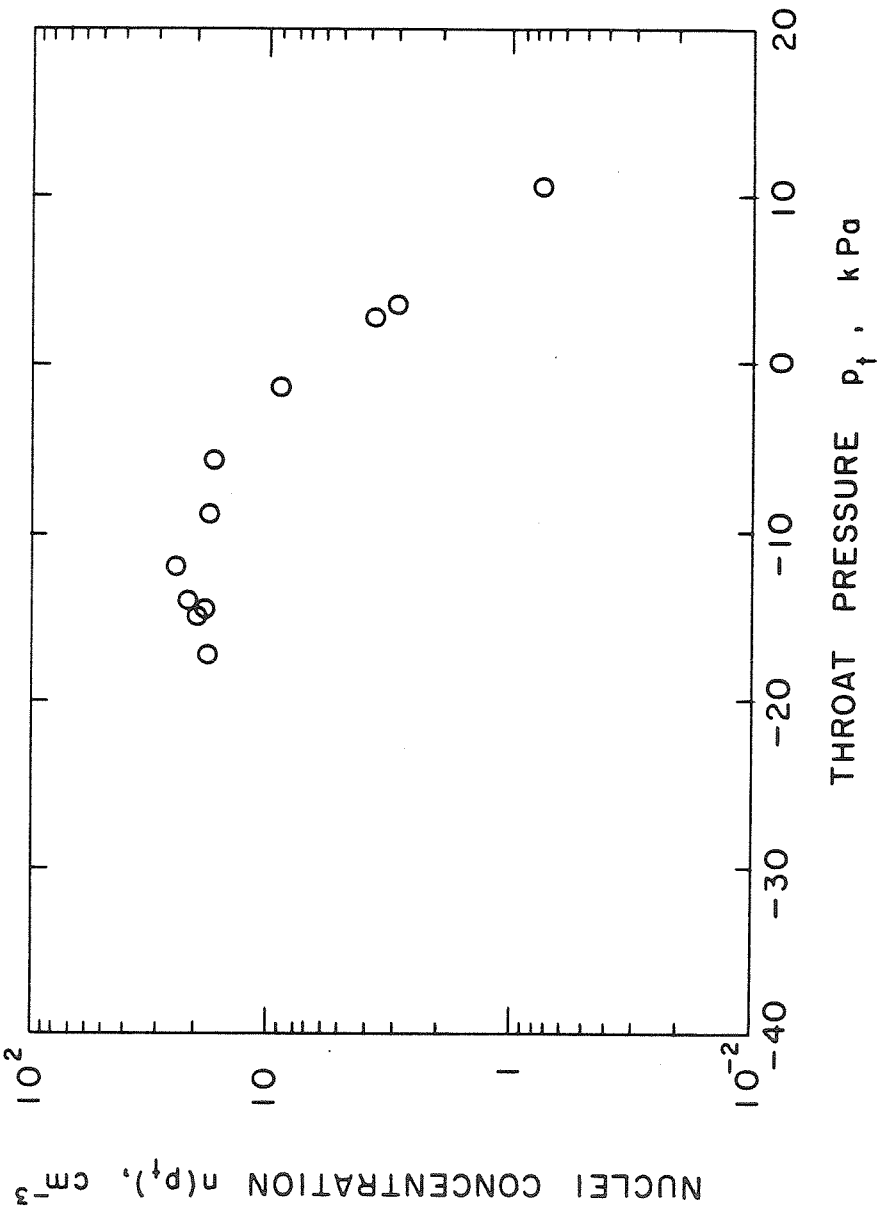

Figure 7.17. Cavitating nuclei concentration $n(p_t)$ measured by the CSM as a function of the venturi throat pressure p_t in a sample of tap water with temperature $T = 21\,^{\circ}\mathrm{C}$ and air content $\alpha = 20.5\,\mathrm{ppm}$.

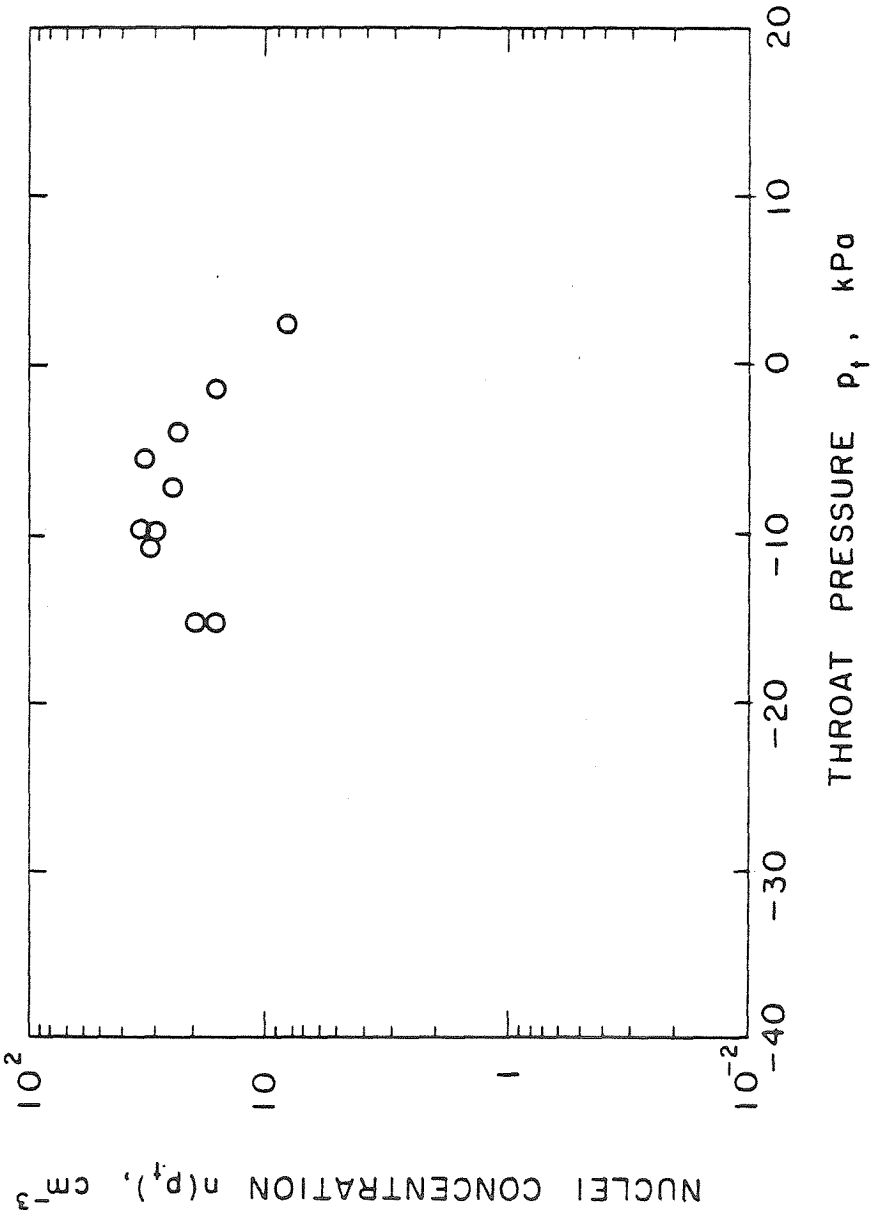

Figure 7.18. Cavitating nuclei concentration $n(p_t)$ measured by the CSM as a function of the venturi throat pressure p_t in a sample of tap water with temperature $T = 21.3\,^{\circ}\mathrm{C}$ and air content $\alpha = 21.3\,\mathrm{ppm}$.

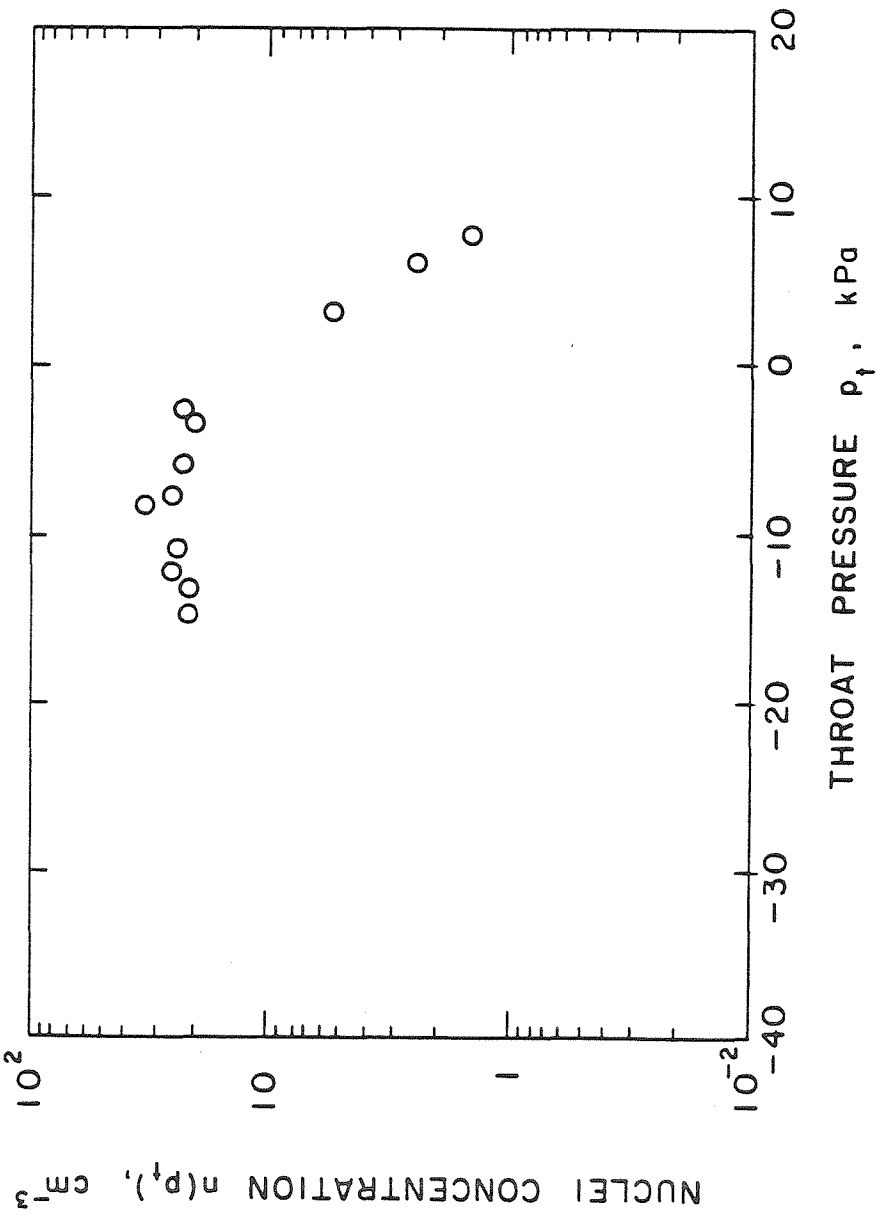

Figure 7.19. Cavitating nuclei concentration $n(p_t)$ measured by the CSM as a function of the venturi throat pressure p_t in a sample of tap water with temperature $T = 21\,^{\circ}\mathrm{C}$ and air content $\alpha = 20.8$ ppm.

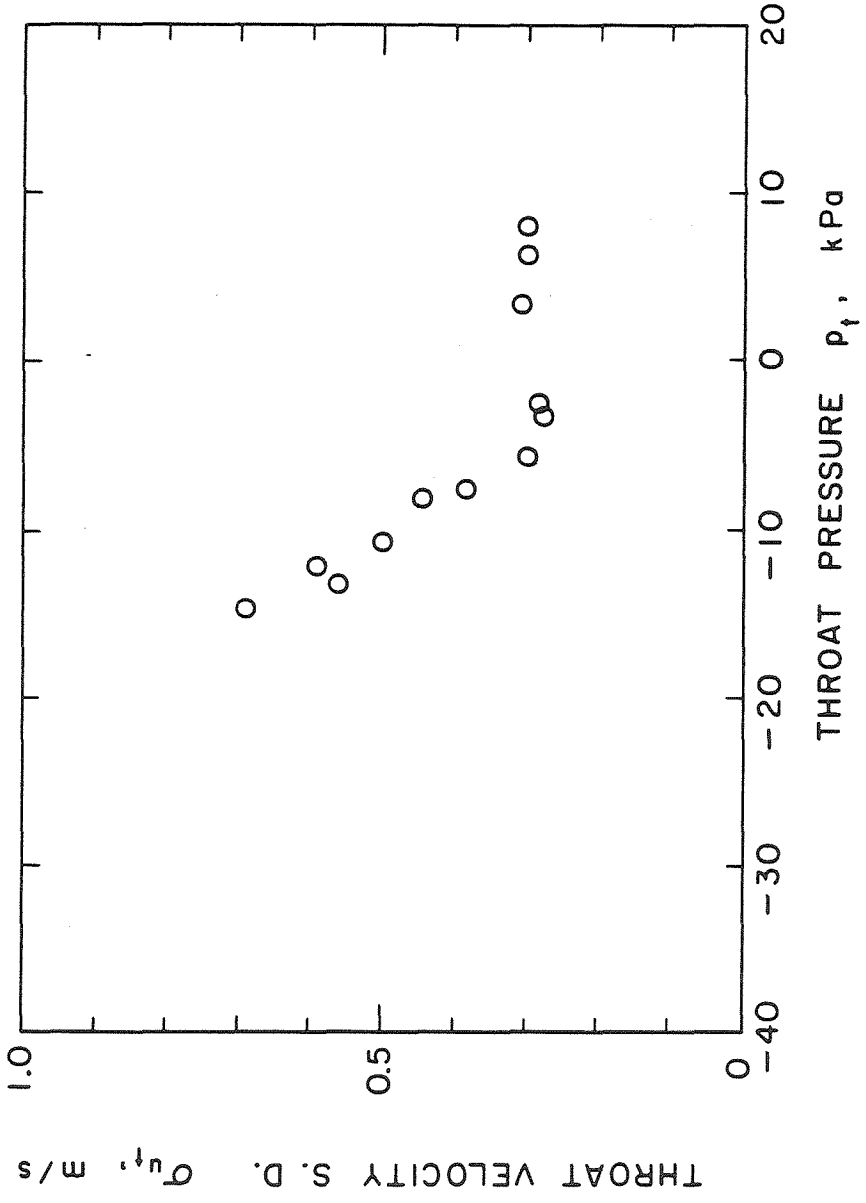

Figure 7.20. Standard deviation of the throat velocity data σ_{u_t} as a function of the throat pressure p_t in the tap water sample of Fig. 7.17 with temperature $T = 21\,^{\circ}\mathrm{C}$ and air content $\alpha = 20.8\,\mathrm{ppm}$.

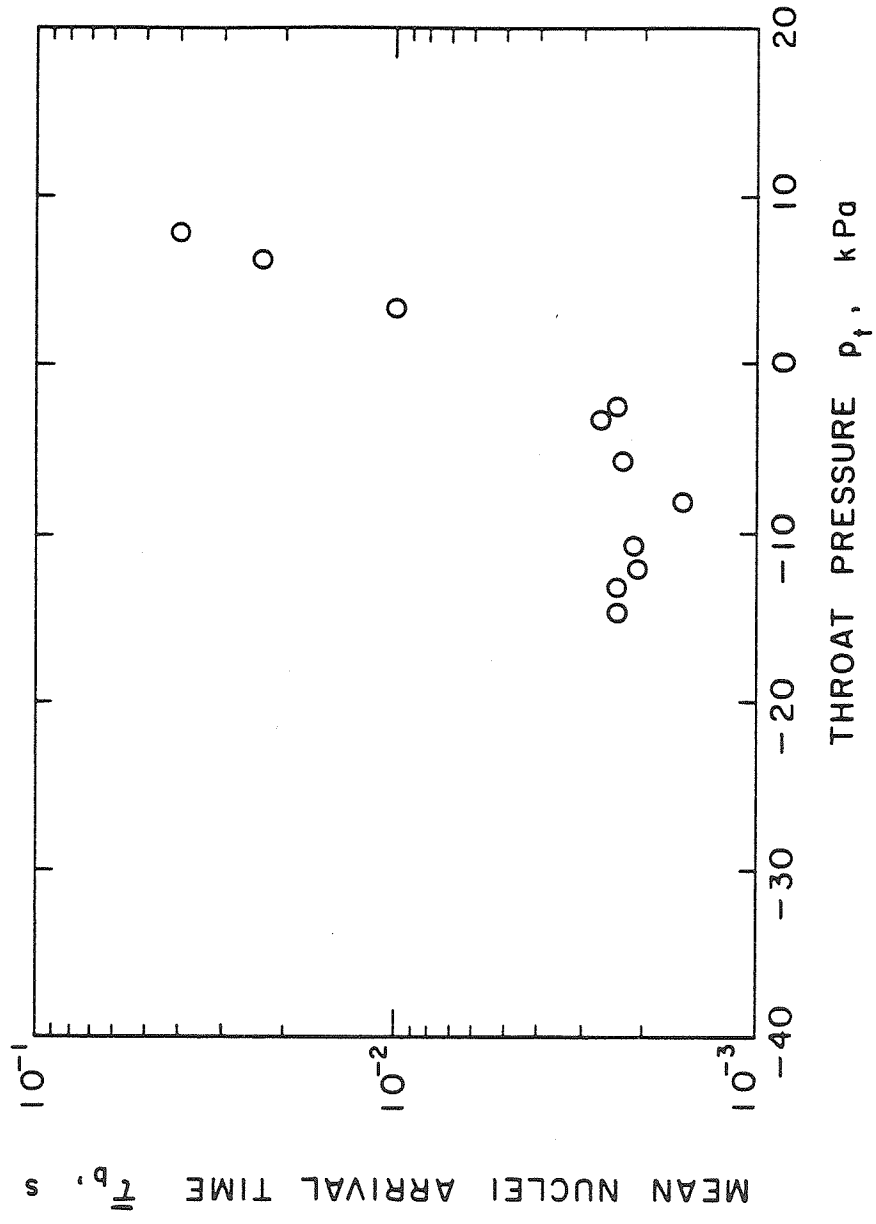

Figure 7.21. Average arrival time interval between cavitating nuclei $\overline{\tau}_b$ as a function of the throat pressure p_t in the tap water sample of Fig. 7.17: temperature $T = 21\,^{\circ}\mathrm{C}$ and air content $\alpha = 20.8$ ppm.

Chapter 8. SUMMARY AND CONCLUSIONS

8.1. Summary

The present work reports the latest research effort at Caltech for the development and implementation of a CSM based on original concepts. The operation of CSM's has been analyzed in order to clarify the most relevant factors affecting their design. By means of various assumptions and approximations a simplified model has been derived which describes the operation of CSM's in terms of a limited number of parameters. This analysis led to a CSM design based on the following functional characteristics:

- the throat pressure is deduced indirectly from the local flow velocity measured with a dual-beam back-scattering LDV and from the absolute pressure upstream of the venturi's contraction;
- cavitation is detected optically at the end of the venturi throat from the intensity of the LDV signal and optical access to the cavitation region is preserved using glass venturi tubes;
- the generation and temporary collection of the data is carried out in real time by a custom-made Signal Processor;
- the frequency of the LDV bursts is measured in the time domain by the CSM Signal Processor with a digital counting technique using adjustable threshold levels for noise rejection, signal discrimination and validation;
- the final acquisition and reduction of the data is performed by a microcomputer;
- the flow in the venturi is laminar throughout the throat section, with the presence of a potential core in all operational conditions;
- the throat section is longer than about 5 mm in order to allow the cavities enough time to reach observable sizes;
- the volume of the throat section is minimized (1 mm diameter) in order to limit saturation effects;

- the expansion in the diffuser is extremely slow to avoid flow separation.

The various steps and considerations leading to the final design concept are discussed in detail and the implementation of the whole system is described in order to provide the all the necessary information for its calibration and operation. The results of application of the CSM to the measurement of the water quality of tap water samples are finally presented and critically discussed with reference to other similar or alternative methods of cavitation nuclei detection.

8.2. Conclusions

The following conclusions can be drawn from the available experience on the CSM system at the present stage of the project:

- three different flow regimes have been observed in the CSM venturi tube:
  a) travelling bubble cavitation, during normal operation;
  b) cavitation-separation in the diffuser;
  c) resonant cavitation, due to the periodic release of cavities in the flow from surface nuclei under the effect of self-sustained flow oscillations.
- the proposed design concept has been successfully demonstrated in all its components;
- the CSM is able to measure the concentration of active cavitation nuclei as a function of the throat pressure over an extended range of applied tensions;
- the maximum value of the tension currently attainable ($-35\,kPa$) is often insufficient for cavitating waters with relatively low nuclei content;
- flow saturation produces a generalized increase of the pressure and a parallel decrease of the velocity throughout the venturi throat section and therefore limits the performance of the CSM by reducing the maximum value of the tension exerted on the liquid;
- contrary to the preliminary expectations, the arrival of cavitation events remains nearly Poissonian also at high cavitation rates. Therefore satura-

tion does not produce important short range interference effects between cavitating nuclei nor, consequently, poses limitations to the measurement of the concentration of active cavitation nuclei other than the ones due to the reduction of the maximum tension applied to the liquid;

- the maximum measurable concentration of active cavitation nuclei in the water samples tested so far appears to be limited by the available supply of nuclei in the samples rather than by the occurrence of saturation;
- there is evidence of some sort of transition in the occurrence of cavitation when the throat pressure is lowered. This transition probably takes place when the throat pressure is reduced after all available active nuclei in the sample have been excited;
- active cavitation nuclei concentrations up to about $40\,cm^{-3}$ have been recorded with little evidence of short range interference effects between cavitating bubbles;
- the flow is very sensitive to laminar separation in the diffuser, which limits the minimum throat pressure currently attainable to about $-35\,kPa$;
- cavitation-separation in the diffuser and sheet cavitation at the venturi throat frequently interfere with the normal operation of the CSM;
- the possibility of measuring the velocity of individual cavities at the venturi throat represents a powerful and unique mean for discriminating the cavities produced by free-stream nuclei from the ones originated from surface nuclei and for introducing corrections to the CSM measurements when necessary;
- the possibility of recording the correct transit time of cavitating bubbles is extremely useful to assess the importance of short range saturation effects from the statistical characteristics of the cavitation process;
- the measurements of the cavitation nuclei number concentration density distributions in tap water samples obtained using the CSM show little dispersion and good repeatability;

- calibration of the CSM with a different and reliable nuclei detection method (holography) is indispensable in order to "properly" choose the thresholds for the discrimination of cavitation events and in order to correctly interpret of some of the observed results.

REFERENCES

Apfel R.E., 1984, "Acoustic Cavitation Inception", Ultrasonics, pp. 167-173.

Akulichev V.A. and Ilychev V.I., 1986, "Acoustic Cavitation in Sea Water", Proceedings of the International Symposium on Propeller and Cavitation, Wuxi, China, pp. 201-205.

Arakeri V.H. and Acosta A.J., 1973, "Viscous Effects in the Inception of Cavitation on Axisymmetric Bodies", ASME J. Fluid Eng., Vol. 95, pp. 519-527.

Arakeri V.H. and Acosta A.J., 1979, "Viscous Effects in the Inception of Cavitation", International Symposium on Cavitation Inception, ASME, New York, New York, pp. 1-9.

Arakeri V.H. and Shanmuganathan V., 1985, "On the Evidence for the Effect of Bubble Interference on Cavitation Noise", J. Fluid Mech., Vol. 159, pp. 131-150.

Arndt R., 1981, "Cavitation in Fluid Machinery and Hydraulic Structures", Ann. Rev. Fluid Mech., 13, pp. 273-328.

Bader H., 1970, "The Hyperbolic Distribution of Particle Sizes", J. of Geophysical Research, Vol. 75, No. 15, pp. 2822-2830.

Billet M., 1986 a, "The Importance and Measurement of Cavitation Nuclei", Advancements in Aerodynamics, Fluid Mechamics and Hydraulics, Minneapolis, Minnesota, pp. 967-989.

Billet M., 1986 b. Personal communication.

Billet M., 1985, "Cavitation Nuclei Measurement – A Review", ASME Cavitation and Multiphase Flow Forum, Albuquerque, New Mexico, pp. 31-38.

Browlee K.A., 1960, "Statistical Theory and Methodology in Science and Engineering", John Wiley & Sons.

Carder K.L., Beardsley G.F. and Pak H., 1971, "Particle Size Distributions in the Eastern Equatorial Pacific", J. of Geophysical Research, Vol. 76, No. 21, pp. 5070-5077.

Carsternsen E.L., and Foldy, L. L., 1947, "Propagation of Sound through a Liquid Containing Bubbles", J. Acoust. Soc. Am., Vol. 19, pp. 481-501.

Chaine G.L. and Shen, Y.T., 1986, "Bubble Dynamics and Cavitation Inception in Cavitation Susceptibility Meters", ASME Journal of Fluids Engineering, Vol. 108, pp. 444-452.

Chmielewski G.E., 1974, "Boundary Layer Consideration in the Design of Aerodynamic Contractions", J. of Aircraft, Vol. 11, No. 8, pp. 435-438.

d'Agostino L. and Acosta A.J., 1983, "On the design of cavitation susceptibility meters", 1983 American Towing Tank Conference, Hoboken, New Jersey, U.S.A.

d'Agostino L. Brennen C.E. and Acosta A.J., 1984, "On the Linearized Dynamics of Two-Dimensional Bubbly Flows over Wave-Shaped Surfaces", ASME Cavitation and Multiphase Flow Forum, pp. 8-13.

Dickson L.D., 1970, "Characteristics of a Propagating Gaussian Beam", Applied Physics, Vol. 9, No. 8, pp. 1854-1861.

Durst F., Melling A. and Whitelaw J.H., 1981, "Principles and Practice of Laser-Doppler Anemometry", Academic Press, 2nd edition.

Feldberg L.A. and Shlemonson K.T., 1973, "The Holographic Study of Cavitation Nuclei", Discussion to Proc. IUTAM Symposium of Non-Steady Flow of Water at High Speeds, Leningrad, USSR.

Foldy L.L. 1945, "The Multiple Scattering of Waves", Phys. Rev., Vol. 67, pp. 107-119.

Fox S.E., Curley S.R. and Larson G.S., May 1955, "Phase Velocity and Absorption Measurements in Water Containing Air Bubbles", J. Acoust. Soc. Am., Vol. 27, No. 3, pp. 534-539.

Gates E.M., 1977, "The Influence of Free Stream Turbulence, Free Stream Nuclei Population and a Drag Reducing Polymer on Cavitation Inception on Two Axisymmetric Bodies", Ph. D. thesis, Calif. Inst. of Tech., Pasadena, California.

Gates E.M. and Bacon J., 1978, "Determination of Cavitation Nuclei Distributions by Holography", J. Ship Res., Vol. 22, No. 1, pp. 29-31.

Godefroy H.W.H.E., Jansen R.H.J., Keller A.P., and van Renesse R.L., 1981, "Comparison of Measuring and Control Methods of the Water Quality with Respect to Cavitation Behaviour", Delft Hydraulics Laboartory Publication.

Harvey E.N., McElroy W.D. and Whiteley A.H., 1947, "On Cavity Formation in Water", Journal of Applied Physics, Vol. 18.

Hentschel W., Lauterborn W. Zarschinzky H. and Tanger H., 1984, "Nuclei Seeding and their Measurements by Means of Automatically Scanned Off-Axis Holography", International Symposium on Cavitation Inception, ASME, New Orleans, Louisiana.

Holl J.W., 1970, "Nuclei and Cavitation", J. of Basic Engineering, ASMe, pp. 681-688.

Ito Y. and Oba R., 1980, "Cavitation Observations through a Fine Laser-Beam Technique", Report No. 337, Institute of High Speed Mechanics, Tohoku University.

Keller A.P., 1972, "The Influence of the Cavitation Nuclei Spectrum on Cavitation Inception Investigated with a Scattered Light Counting Method", J. of Basic Engineering, pp. 917-925.

Knapp R.T., Daily J.W. and Hammitt F.G., 1970, "Cavitation", McGraw Hill.

Kogelnik H. and Li T., 1966, "Laser Beams and Resonators", Applied Optics, Vol. 5, No. 10, pp. 1550-1567.

Lecoffre Y. and Bonnin J., 1979, "Cavitation tests and nucleation control", International Symposium on Cavitation Inception, New York, New York, pp. 141-145.

Le Goff J.P. and Lecoffre Y., 1983, "Nuclei and Cavitation", 14th Symposium on Naval Hydrodynamics, National Academy Press, pp. 215-242.

Macpherson J.D., 1957, "The Effect of Gas Bubbles on Sound Propagation in Water", Proc. Phys. Soc. London, Vol. 70 B, pp. 85-92.

Medwin H., 1970, "In Situ Acoustic Measurements of Bubble Populations in Coastal Ocean Waters", J. Geophysical Research, 75, 3, pp. 599-611.

Medwin H., 1977, "Acoustical Determinations of Bubble-Size Spectra", J. Acoust. Soc. Am., Vol. 62, No. 4, pp. 1041-1044.

Mikhail M.N., 1978, "Optimum Design of Wind Tunnel Contractions", AIAA Journal, Vol. 17, No. 5, pp. 471-477.

Muir J.F. and Eichhorn 1963, "Compressible Flow of an Air-Water Mixture through a Vertical Two-Dimensional Converging-Diverging Nozzle", Proc. Heat Trans., Fluid Mech. Inst., Standford, Standford University Press.

Noorddzij L., 1973, "Shock Waves in Mixtures of Liquids and Air Bubbles, Doctoral thesis", Technische Hogeschool, Twente, Netherlands.

Noorddzij L. and van Wijngaärden L., 1974, "Relaxation Effects, Caused by Relative Motion, on Shock Waves in Gas-Bubble/Liquid Mixtures", J. Fluid Mech., vol. 66, part 1, pp. 115-143.

Oba R. et al., 1980, "Cavitation-Nuclei Measurements by a Newly Made Coulter Counter without Adding Salt in Water", Report No. 340, Institute of High Speed Mechanics, Tohoku University.

Oba R., Ikohagi T. and Kim K.T., 1979, "Cavitation in an Extremely Limited Flow through Very Small Orifices", International Symposium on Cavitation Inception, ASME, New York, New York, pp. 147-152.

Oldenziel D.M., 1982a, "A New Instrument in Cavitation Research: the Cavitation Susceptibility Meter", ASME Journal of Fluids Engineering, Vol. 104, pp. 136-142.

Oldenziel D.M., Jansen R.H.J., Keller A.P. Lecoffre Y., and van Renesse R.L., 1982b, "Comparison of Instruments for Detection of Particles and Bubbles in Water during Cavitation Studies", Proceedings of Symposium on Operating Problems of Pump Stations and Power Plants, IAHR, Amsterdam.

Oldenziel D.M., 1982c, "Utility of Available Instruments during Cavitation Tests", Proceedings of Symposium on Operating Problems of Pump Stations and Power Plants, IAHR, Amsterdam.

Oldenziel D.M., 1979, "New Instruments in Cavitation Research", International Symposium on Cavitation Inception, New York, New York, pp. 111-124.

Plesset M.S., 1969, "The Tensile Strength of Liquids", ASME Fluids Engineering and Applied Mechanics Conference, Evanston, Illinois, pp. 15-25.

Plesset M.S. and Prosperetti A., 1977, "Bubble Dynamics and Cavitation", Ann. Rev. Fluid Mech., Vol. 9, pp 145-85.

Prosperetti A., 1984, "Bubble Phenomena in Sound Fields: Part One", Ultrasonics, March 1984, pp. 69-78.

Sheldon R.W., Prakash A. and Sutcliffe Jr. W.H., 1972, "The Size Distribution of Particles in the Ocean", Limnology and Oceanography, Vol. XVII, No. 3, pp. 327-340.

Shen Y.T., Gowing S. and Pierce R., 1984, "Cavitation Susceptibility Meters by a Venturi", International Symposium on Cavitation Inception, ASME Winter Annual Meeting, pp. 9-18.

Shen Y.T. and Gowing S., 1985, "Scale Effects on Bubble Growth and Cavitation Inception in Cavitation Susceptibility Meters", ASME Cavitation and Multiphase Flow Forum, Albuquerque, Mew Mexico, pp. 14-16.

Shen Y.T., Gowing S. and Eckstein B., 1986, "Cavitation Susceptibility Measurements of Ocean Lake and Laboratory Waters", David W. Taylor Naval Ship Research and Development Center, Report DTNSRDC-86/D19.

Silberman E., 1957, "Sound Velocity and Attenuation in Bubbly Mixtures Measured in Standing Wave Tubes", J. Acoust. Soc. Am., Vol. 18, No. 8, August, pp. 925-933.

Stratford B.S., 1954, "Flow in Laminar Boundary Layer near Separation", Aeronautical Research Council, R&M 3002.

Tangren R.F., Dodge C.H., and Seifert H.S., 1949. "Compressibility Effects in Two-Phase Flows", J. Appl. Phys., vol 20, pp. 637-645.

Thorpe S.A., 1982, "On the Clouds of Bubbles Formed by the Breaking Wind-Waves in Deep Waters and their Role in Air-Sea Gas Transfer", Phil. Trans. R. Soc. Lond. A, Vol. 304, pp. 155-210.

van Wijngaärden L., 1964, "On the Collective Collapse of a Large Number of Gas Bubbles in Water", Proc. 11th Int. Congr. Appl. Mech., Springer-Verlag, Berlin, pp. 854-861.

van Wijngaärden L., 1968, "On the Equations of Motion of Mixtures of Liquid and Gas Bubbles", J. Fluid Mech., Vol. 33, part 3, pp. 465-474.

van Wijngaärden L., 1972, "One-Dimensional Flow of Liquids Containing Small Gas Bubbles", Ann. Rev. Fluid. Mech., Vol. 4, pp. 369-396.

Voinov O.V., 1973, "Force Acting on a Sphere in an Inhomogeneous Flow of an Ideal Incompressible Fluid", Plenum Publishing Coorp., transl. from Zhurnal Prikladnoi Mekhaniki i Tekhnicheskoi Fiziki, No. 4, pp. 182-184, July-August 1973.

White F.M., 1974, "Viscous Fluid Flow", McGraw Hill.

Appendix 1

CSM SIGNAL PROCESSOR

1. Introduction

The following brief description of the CSM Signal Processor is intended to give the "unaware" reader an introduction to the concepts of its operation and a general overview of its most important components. Since from the user's point of view it is mostly important to understand the meaning and possible limitations of the collected information, more emphasis is given on the way data are generated than on the way they are handled by the control logic. The various circuits are introduced and discussed in the order that made the functional description of the entire system easier to follow.

2. Drawing List

1. Control Stuff
2. Particle Duration Counter
3. Bubble Count Comparator
4. Dividers
5. Particle Sample Time
6. Memory and Buffers
7. Memory and Buffers
8. Elapsed Time Counter
9. Zero Crossing Counter
10. RS232 Data Interface
11. Threshold Circuits
12. LDV Amplifier
13. More Memory and Buffers

14. Analog to Digital Converter
15. Power Supply Capacitors for Boards 1, 2 and 3
16. LDV Comparators
17. Chassis Wiring Diagram
18. Board Interconnect 1 and 2
19. Chassis Layout
20. Board 1 Lay-out
21. Board 2 Lay-out
22. Board 3 Lay-out

3. Nomenclature

The electronic boards are identified by their number, which is also written on each of them. The individual electronic components of the CSM Signal Processor are indicated with the symbols used in the relevant drawings. Thus, for example:

U23A-3	identifies pin 3 of the unit No. 23A
TP15	identifies test point No. 15 and the corresponding signal
R60	identifies resistor No. 60
C12	identifies capacitor No. 12
[78]	identifies point No. 78 and the corresponding signal
Q7	identifies transistor No. 7

Furthermore, the main subsystems are indicated as follows:

ETC	Elapsed Time Counter (from the beginning of the run)
PDC	Particle Duration Counter
ZCC	Zero Crossing Counter
BAC	Bubble Address Counter (also counts bubbles)
PAC	Particle Address Counter (also counts particles)

Additional notations for commonly occurring signals are:

EPS	Enable Particle Stuff (gates particle sampling)
GT	particle Gate Time
ZC	gated Zero Crossing pulse train
A	memory reset at run start
RUN	run under way
UL	data unloading under way
Inh	data storage under way
RST	system reset

Overlines indicate complementary signals.

4. Functional Description of Main Circuits

LDV Amplifiers

Sheet 12 - Board 3

The LDV signal from the photomultiplier tube, after optional external pre-amplification, enters the board through TP13 and goes to a first medium gain amplifier (transistors Q1, Q3, Q4) which in turn drives in parallel a high gain amplifier (transistors Q5, Q6) with output at TP14 for particle detection and a low gain amplifier (transistors Q8, Q9) with output at TP15 for bubble detection. The inputs to the threshold comparators are high-pass filtered immediately after TP14 and TP15. The band width of the amplifiers is adjusted by changing the capacitors C3, C10 and C14. Its current value is about 2 MHz. The gain of the amplifiers can be adjusted by changing the resistors R4, R11, R17 and R77.

LDV Comparators

Sheet 16 - Board 3

The outputs TP14 and TP15 of the LDV signal amplifiers go to the comparators:

U25	positive bubble threshold
U26	positive particle threshold

U27 zero crossing particle threshold

U28 negative particle threshold

U29 negative bubble threshold

For proper noise rejection and bubble/particle discrimination the zero threshold and each couple of particle and bubble thresholds must be set precisely symmetric with respect to the zero level of the input signal to the corresponding comparators. This zero level does not exactly correspond to the ground level due to the voltage drop in the input circuits of the comparators which have a non zero bias current (about $10\,\mu A$). Therefore the thresholds are best set by observing the output of the comparators in the presence of a simulated DC filtered LDV signal from a signal generator. The zero crossing level is correctly set when the duty cycle of the comparator output is balanced, i.e. the zero crossings are equally spaced in time, which corresponds to a threshold level of about $-120\,mV$. This setting is a rather critical because relatively small changes ($\pm 50\,mV$) can induce errors up to 5-10% in the Doppler frequency measurement (especially if the threshold is set higher than its due value). Similarly, bubble and particle thresholds are properly adjusted when they count equal number of fringes within one count tolerance. These settings are less critical in terms of the errors they induce in the Doppler frequency measurement. However, the bubble and particle thresholds should be chosen in such a way to avoid as much as possible the occurrence of a particle with a delay shorter than 10 to $15\,\mu s$ with respect to the previous bubble, in order to allow the writing of the bubble data to the memory without interference with the counting of the next particle, whose gate time is otherwise proportionally reduced. The variable resistors for adjusting the comparator thresholds are located close to the top edge of the board. From right to left they are:

R60 for TP3, positive bubble threshold

R63 for TP4, positive particle threshold

R66 for TP5, zero crossing threshold

R69 for TP6, negative particle threshold

R72 for TP7, negative bubble threshold

The comparators generate the following digital outputs:

U26 with output at TP9 and feed-back at TP17

U27 with output at TP10 and no feed-back

U28 with output at TP11 and feed-back at TP18

U25 with output at TP8 and feed-back at TP16

U29 with output at TP12 and feed-back at TP19

for the threshold circuits (sheet 11). The output of each comparator is also used to provide a DC filtered feed-back in order reduce the occurrence of multiple transitions due to electronic noise. The feed-backs at TP17, TP18 from the particle Gate Time signal and TP18, TP19 from the bubble occurrence signal have been currently disconnected.

Threshold Circuits

Sheet 11 - Board 3

The threshold circuits operate on the output of the LDV comparators to generate the following signals for the Control Stuff:

[33] validated bubble signal

[32] bubble Doppler fringe signal

[31] particle Gate Time signal (GT)

[72] particle Zero Crossing pulse train signal (ZC)

[78] Enable Particle Stuff signal (EPS)

The output TP10 of the zero crossing comparator U27 goes to the system of units U34, U35A, U36A, U36D, U36B, U94A which generate a short pulse in response to: a negative zero crossing (U36B-4), a positive zero crossing (U94A-3) or to any zero crossing either positive or negative (U35A-3 and U36D-13).

The flip-flops U30A (positive bubble threshold), U31A (positive particle threshold), U31B (negative particle threshold) and U95A (negative bubble

threshold) receive their clock signals TP8, TP9, TP11, TP12 from the corresponding threshold comparators U25, U26, U28, U29 and their reset signals form the zero crossing pulse generators of opposite sign. Thus their outputs reflect the presence of LDV signal from bubbles or particles which has exceeded the corresponding positive or negative thresholds but has not yet reached zero (positive and negative fringe signals).

The signals from the positive and negative bubble threshold flip-flops U30A-5 and U95A-5 are then logically added in U35B, whose output [33] therefore reflects the presence of LDV signal which has exceeded either the positive or negative bubble threshold but that has not yet reached zero. This signal indicates the occurrence of a Doppler fringe from a cavitation event or bubble. The main signals generated by the bubble threshold circuits are shown in Fig. 1.

In the same way, the signals from the positive and negative particle threshold flip-flops U31A and U31B are logically added in U35C, whose output thus reflects the presence of LDV signal which has exceeded either the positive or negative particle threshold but that has not yet reached zero. This signal indicates the occurrence of a Doppler fringe from a velocity tracer or particle.

The unit U30B uses the signals from U35B (bubble Doppler fringe signal) and from the zero crossing pulse generator U35A to produce a short pulse to reset the counter U33 only when a bubble fringe is not present at the time of a zero crossing. The delayed feed-back from pin 9 to pin 10 through R74 and C41 is used to adjust the duration of the pulse.

The unit U33 counts the positive transitions of the bubble Doppler fringe signal from U35B until it is stopped by the feed-back 13 when the minimum count number set by the jump S5 is reached. The number of fringes corresponds to the value Q0, Q1, Q2,... shown in the drawing. The unit is reset by the signal from U30B, i.e. by the first zero crossing occurring when no bubble Doppler fringe is present. The signal [33] is therefore used for bubble signal validation.

The unit U32B generates short pulses set by the presence of particle Doppler

fringe signal from U35C at the time of a zero crossing from U35A (zero crossing pulse generator) and reset by the time delayed feed-back (pin 8 and 13) if signal [78] (Enable Particle Stuff) is present. The resulting signal [72] is therefore the particle validated zero crossing pulse train ZC.

The unit U32A generates two complementary signals TP17 and TP18 [31] which are set by the occurrence of particle validated zero crossing [72] and reset either by the occurrence of a non-validated zero crossing indicated by the input 3 from the zero crossing pulse generator U35A in the absence of input 4. The unit is also reset by the signal [78] (Enable Particle Stuff). Therefore the outputs 5 and 6 signal [31] represent the particle Gate Time signal GT.

The unit U95B gates the Inh signal [46] (data storage under way) with the clock input 11 in order to generate the signal [69] synchronous with the occurrence of zero crossings for controlling the Zero Crossing Counter (ZCC) and the Particle Duration Counter (PDC).

The main signals generated by the particle threshold circuits are shown in Fig. 2.

Control Stuff

Sheet 1 - Board 1

The Control Stuff activates and synchronizes the components of the CSM Signal Processor in response to the external commands from the operator and to the internal status of the system in order to perform operations such as: reset, run start and data unload sequences, pressure data A/D conversion, memory data address incrementation, data writing to the memory and run termination. The following system status signals and their complements are generated and used by the Control Stuff to pilot other components of the Signal Processor:

A	or [71]	memory reset at run start
RUN	or [54]	run under way
UL	or [98]	data unloading under way
Inh	or [46]	data storage under way

The flip-flop U114A is triggered by the run start command to generate the signal [71] and its complement (pin 2) for memory clearing at the beginning of each run and for control of other components. At the conclusion of the memory reset the second flip-flop U2A generates the signal [54] and its complement (pin 1) indicating that a run is under way until it is terminated by overtime [47], stop command [64], bubble count conclusion from U22-13, power-on reset from U9A, reset command [65] or unload signal [98] from U13B-13.

The unit U13A responds to the unload command [66] generating the start load reset signal [50] and synchronizing the unload flip-flop U13B with the unload clock frequency [99] to produce the signal [98] and its complement [53], which indicate that the data unloading to the computer is under way.

The units U3A, U3B and U4 use the validated bubble signal [33], the 1 MHz and 20 kHz clock frequencies to generate the Bubble Time Write Enable signal [29] for the memory and the clock signal (pin 7) for the Bubble Address Counter (BAC), U12.

The unit U21A responds to the bubble fringe signal [32] generating the signal [46] and its complement (pin 2), which therefore indicate the presence (or the absence) of a bubble. They are used to carry out the sequence of operations corresponding to either bubbles or particles by selectively enabling or disabling the proper components of the CSM Signal Processor.

The units U115, U21B and U22A use the particle Gate Time signal [31] and the 2 MHz clock frequency from U82-1 to produce the synchronized clock enable signal (pin 1). Units U23 uses this signal together with the 2 MHz clock frequency to generate the the Particle Time Write Enable signal [30] for the memory when pressure data conversion has taken place (signal from U108). Similarly, unit U23 uses the same signal to generate the Pressure Data Write Enable signal [49] for the memory and the clock signal (pin Q6) for the Particle Address Counter (PAC), U16.

The unit U17 is activated during the reset or unload sequences and generates the control signals [1] through [8], [56], [57] for sequentially enabling of the

output buffers. Finally, the output pulse of unit U2B-13 resets the unload sequences at the end of each data unloading to the computer.

A/D Converter

Sheet 14 - Board 1

The A/D Converter U108 digitizes the analog signal [83] from the pressure transducer. The input scaling of the A/D Converter can be adjusted to the input signal range by establishing proper connections among pins 22, 23, 24, 25, 26 and 29, as indicated in the enclosed instructions for the use of the AD5240 (U108). The current setting is 0 to 5 V. The variable resistor R4 is used for resetting the unit and the input from U110-2 or U23-2 for initiating the conversion. The buffers U112 and U113 interface the A/D converter output with the pressure data bus and are gated by the signal [71] (memory clearing at run start).

Dividers

Sheet 4 - Board 1

The dividers are used to generate the clock signals of different frequencies needed for the operation and synchronization of the CSM Signal Porcessor. The first divider comprises units U82, U83 and U100A connected to the 20 MHz oscillator and produces the following outputs:

U82-11	at 4 MHz,	not used
U82-12	at 2 MHz,	for particle time writing synchronization
U100-1	at 1 MHz,	for bubble time writing synchronization
U83-6	at 200 kHz,	for particle sample time circuits
[70]	at 20 kHz,	for elapsed time measurement (to ETC)

The output from the 20 MHz oscillator is also directly used by the Particle Duration Counter (PDC) for the measurement of the particle Gate Time. The second divider, unit U99, is connected to the 1.8432 MHz oscillator and generated the proper frequency for data output to the RS232C serial port at 9600 baud.

Zero Crossing Counter (ZCC)

Sheet 9 - Board 2

The Zero Crossing Counter U67 is activated by the logical addition of the signal [72] (particle zero crossing pulse train) and [31] (particle Gate Time). The unit U114A is used to reverse the polarity of the pulse train to the counter in order to slightly delay the counting which occurs at the negative edges of the pulses. The slight delay is necessary in order to have consistent number of counts even when the bubble data writing to the memory partially overlaps with the occurrence of the next valid particle. The unit is also reset through pin 11 by any of the following signals:

[69] synchronized Inh signal (data storage under way)

[33] validated bubble signal

[71] memory clearing at run start

[81] reset after writing particle data

Elapsed Time Counter (ETC)

Sheet 8 - Board 2

The Elapsed Time Counter measures the time from the beginning of the run. The counters U68 and U69 are incremented by the signal [70] from the 20 kHz clock U83-14 and are reset by either the signal [54] (run not under way) or [71] (memory clearing at run start). The full 24 bits output is used to record the time of occurrence of cavitation events (bubbles). However, only the 12 most significant bits are used for recording the time of occurrence of velocity tracers (particles), whose resolution is therefore reduced by a factor of 2^{12}. The most significant bit signal [47] is also used to terminate the run when the counter has been used to full capacity (run overtime).

Particle Duration Counter (PDC)

Sheet 2 - Board 1

The Particle Duration Counter measures the time duration of LDV signals

from velocity tracers or particles. The counter U70 is incremented by the 20 MHz clock signal only during the particle gate time interval indicated by the signal from U32-2 and it is reset by any of the following signals:

U21-1	bubble occurrence
U6-9	system reset signal
U11-6	reset after writing data to the memory
[71]	memory clearing at run start

Bubble Count Comparator

Sheet 3 - Board 1

The Bubble Count Comparator generates the signal for run termination when a preset number of bubbles has been counted. The chained comparators U72, U73, U74 are connected with the Bubble Address Counter (BAC) and with the multiple switch S1, where the maximum number of bubbles to be counted is coded in binary form by properly setting its 10 individual switches. The output 13 of U72 carries the information whether or not the preset number of bubbles has been reached. The flip-flop U22, with the connections to U111-10, to U114-1 (memory clearing signal run start) and the delayed feed-back between pin 13 and 10, is used to transform the output of the comparator into a brief pulse signal to unit U8-2 of the Control Stuff for run termination.

Particle Sample Time

Sheet 5 - Board 1

The Particle Sample Time circuits are used to generate the Enable Particle Stuff (EPS) signal [78] which gates the sampling of particles from the LDV signal to an adjustable fraction of the total run time. The 200 kHz input from U83-6 is divided by unit U88 into eight outputs of different frequencies. The comparator U89 selects one of these frequencies according to the status of contacts C, B and A of the multiple switch S4 as summarized in the following table:

CBA	Frequency [Hz]
0 0 0	391
0 0 1	195
0 1 0	98
0 1 1	49
1 0 0	24
1 0 1	12
1 1 0	6
1 1 1	3

The selected signal provides the duty cycle frequency at which the time gate for particle sampling is open by the output signal [78] (Enable Particle Stuff). It also drives the 8-bit counter U90. The comparators U91, U93 and the flip-flop U100B keep open the time gate for particle sampling (signal [78]) synchronous with the 200 kHz clock frequency as long as the count in U90 reaches the number selected by the status of the contacts B0, B1, ... B7 of multiple switches S2 and S3. Setting a binary number N = B7 B6 ... B0 ($0 \leq N < 256$) in S2 and S3 results into opening the time gate for particle sampling for $N/256$th of the duty cycle period. The reset signal from unit U6-9 of the Control Stuff clears the counter U90 for a new count.

Memory and Buffers

Sheet 6 - Board 2

The input buffers U37, U38, U39 transfer data from the Elapsed Time Counter (ETC) to the memories U43 through U48. The signal [29] (Bubble Time Write Enable) from unit U11-11 of the Control Stuff directs the buffers to send the data and the memory to receive them.

The output buffers U40, U41, U42 are activated sequentially by the signals [1], [2], [3] generated by the counter U17 of the Control Stuff and transfer the data from the memories to the output bus under the control of the signal from

the Bubble Address Counter (BAC) U12. When inactive they remain in a high impedance state in order not to affect the output bus.

Memory and Buffers

Sheet 7 - Board 2

The input buffers U49, U50, U51, U61B, U62 transfer data from the Particle Duration Counter (PDC), the Elapsed Time Counter (ETC) and the Zero Crossing Counter (ZCC) to the memories U55 through U60, U61B, U62. The signal [30] (Particle Time Write Enable) from the Control Stuff directs the buffers to send the data and the memory to receive them. Only the 12 most significant bits of the ETC are recorded as particle time data, therefore the time resolution of such measurement is reduced by a factor 2^{12} with respect to the resolution of the recorded bubble time data.

The output buffers U52, U53, U54, U63, U102B are activated sequentially by the signals [4], [5], [6], [7], [8] generated by the counter U17 of the Control Stuff and transfer the data from the memories to the output bus under the control of the signal from the Particle Address Counter (PAC) U16. When inactive they remain in a high impedance state in order not to affect the output bus.

More Memory and Buffers

Sheet 13 - Board 2

The input buffers U101, U102A transfer pressure data from the A/D Converter to the memories U104, U105, U106. The signal [49] (Pressure Data Write Enable) from the Control Stuff directs the buffers to send the data and the memory to receive them.

The output buffers U103, U61A are activated sequentially by the signals [56], [8] generated by the counter U17 of the Control Stuff and transfer the data from the memories to the output bus under the control of the signal from the

Particle Address Counter (PAC) U16. When inactive they remain in a high impedance state in order not to affect the output bus.

RS232C Data Interface

Sheet 10 - Board 2

The RS232C data interface accepts 8-bit parallel data from the memory output bus and converts them into RS232C serial format. It is activated by the unload signal [98] synchronized with the 9.6 kHz control clock signal [99] by the gate U77 and is reset by the start load reset signal [50]. The read clock signal [48] increments the Bubble Address Counter (BAC) or the Particle Address Counter (PAC) after each datum has been sent to the RS232C serial port. The auxiliary signals [71] (memory reset at run start) and [53] (data unload not under way) prevent accidental data output when not required.

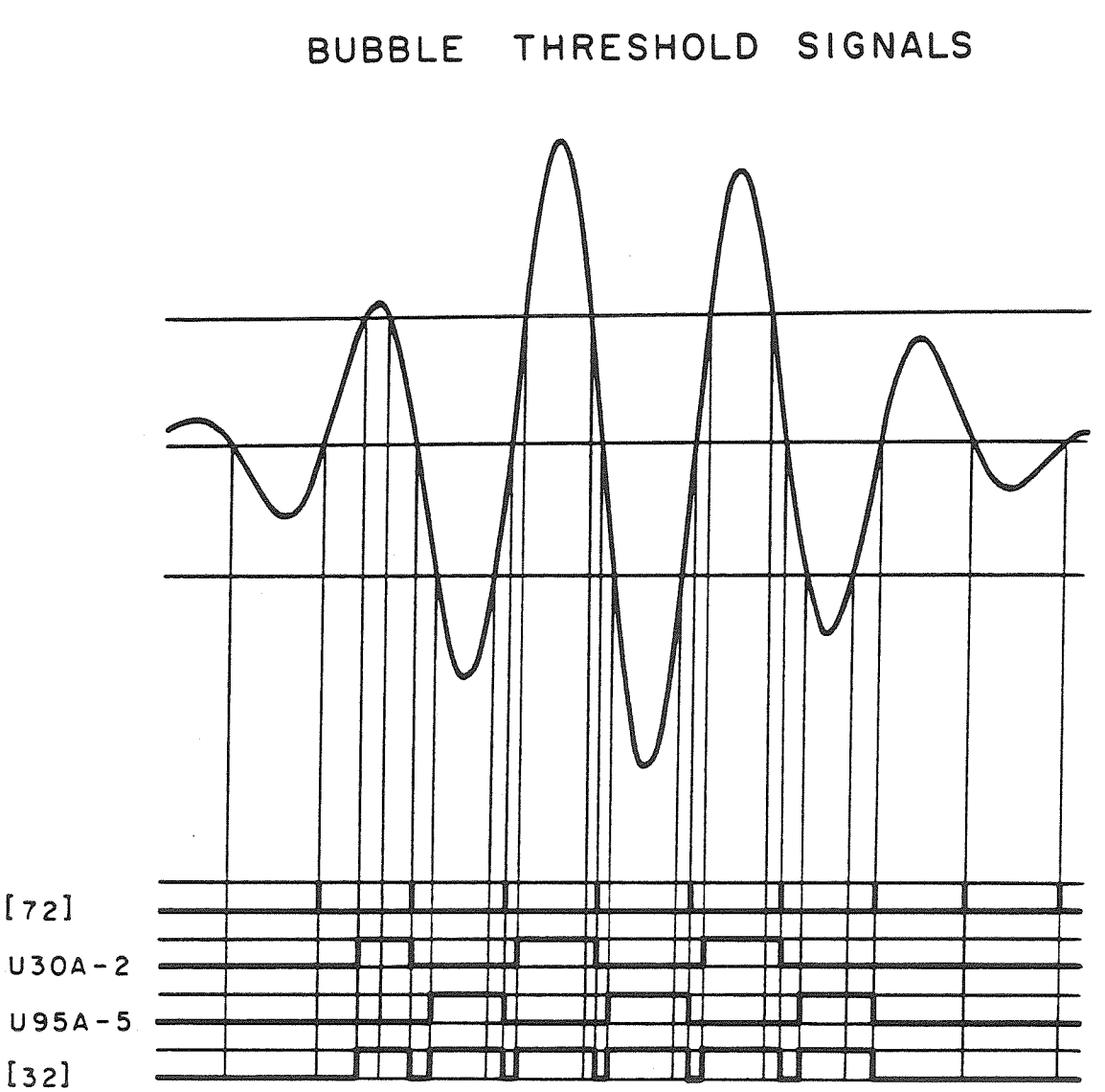

Figure 1. Main signals (bottom) generated by the bubble threshold circuits in response to a typical filtered LDV burst (top) shown with reference to the zero and the bubble threshold levels: the zero crossing pulse train [72], the positive bubble fringe U30A-2, the negative bubble fringe U95A-5 and their logic sum, the bubble fringe signal [32].

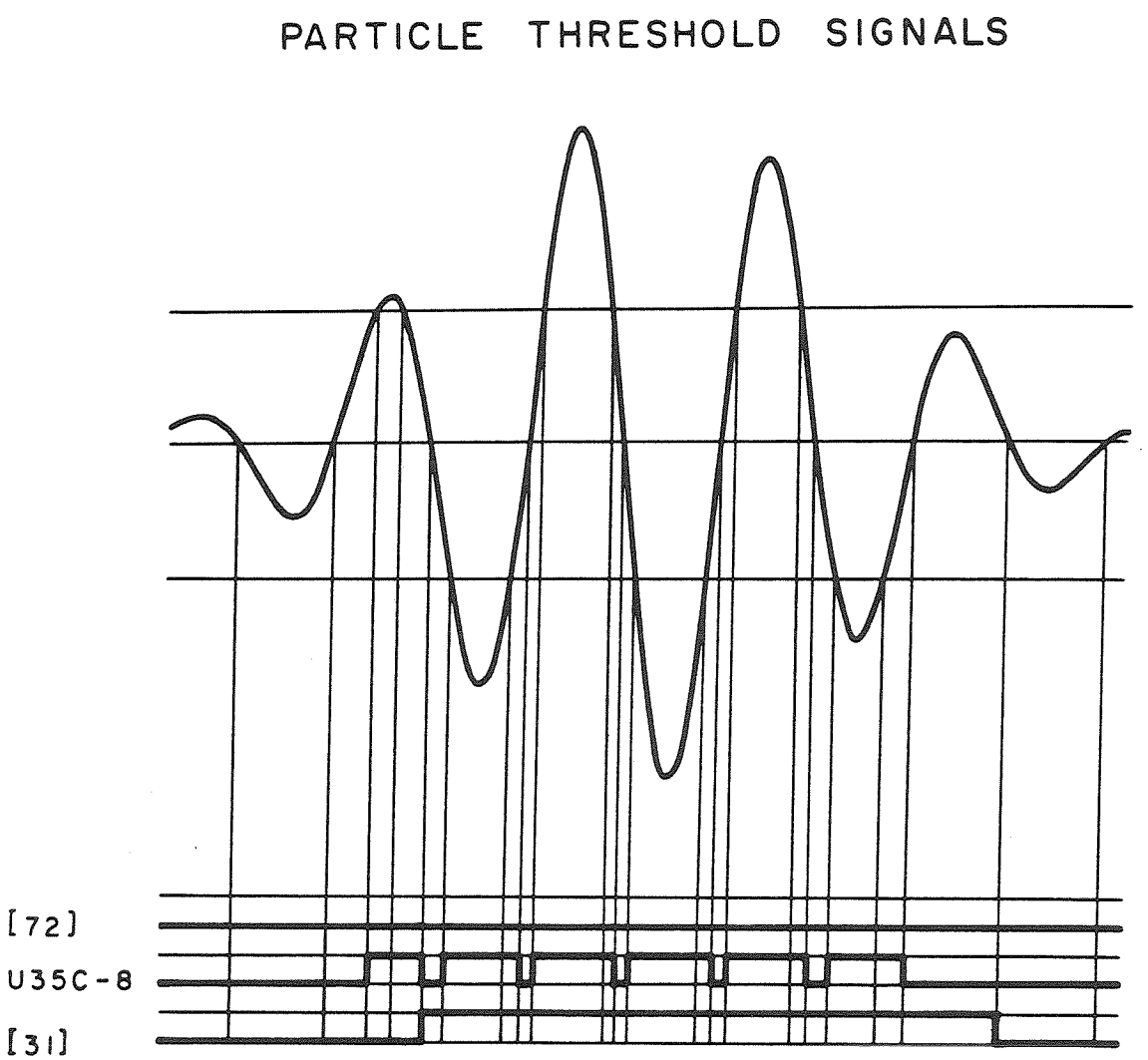

Figure 2. Main signals (bottom) generated by the particle threshold circuits in response to a typical filtered LDV burst (top) shown with reference to the zero and the particle threshold levels: the zero crossing pulse train [72], the particle fringe signal U35C-8 (obtained as the corresponding bubble fringe signal of Fig. 1) and the particle gate time signal [31].

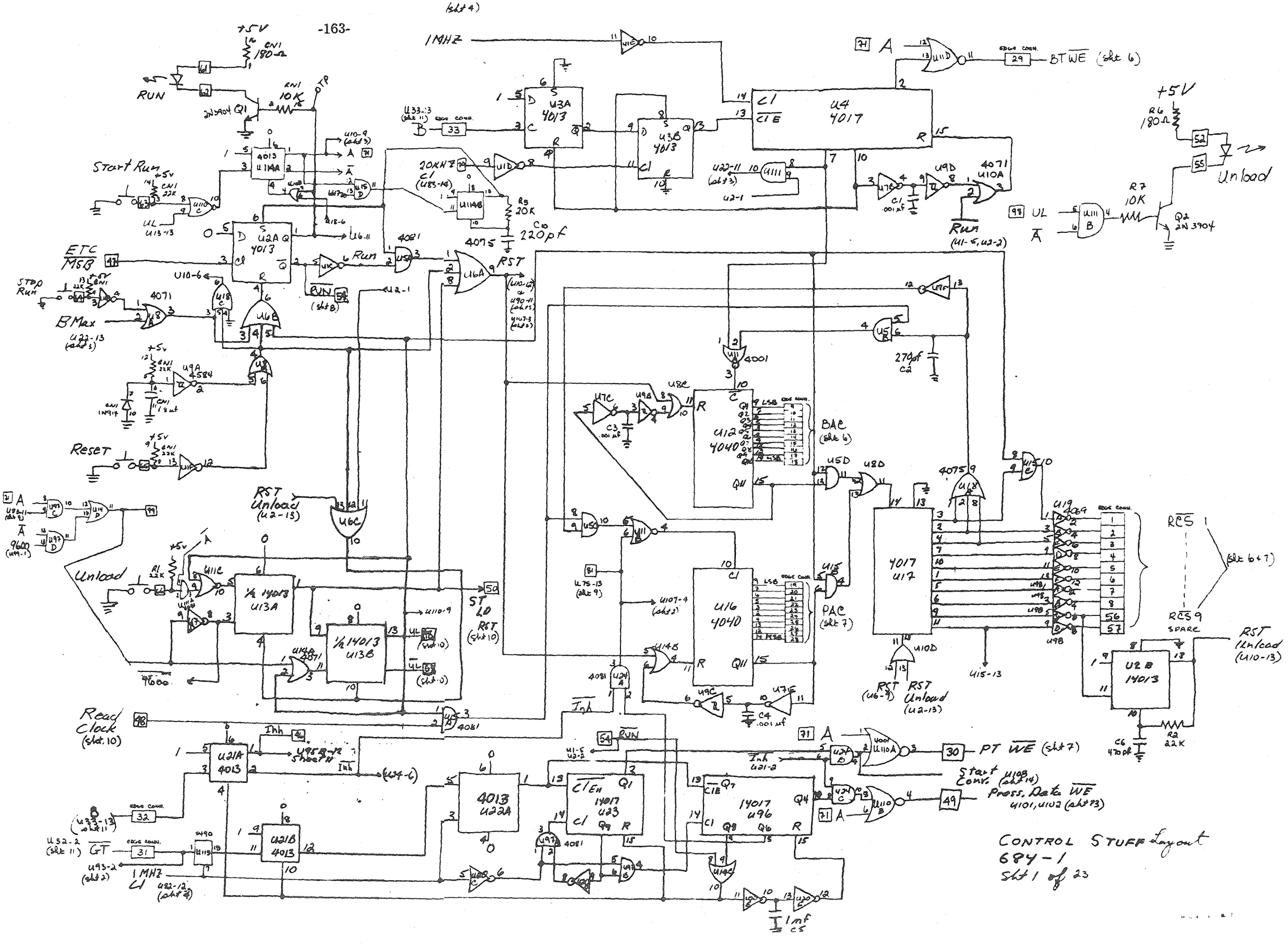
(sht 4)
1MHZ
+5V
CN1 180Ω
RUN
2N3904 Q1
RN1 10K
TP
4013 U11AA
U10-9 (sht 3)
A
Ā
Start Run
UL U13-13
U10 C
U2A 4013
ETC MSB
47
STOP Run
BMax
U22-13 (sht 3)
4071 U8 A
U1B C
U6B
U9A 4584
CN1 1N914
Reset
U1F
A
U93-11 (sht 2)
U14 D
99
9600 (U99-1)
U97 D
Unload
R1 22K
U11C
1/2 14013 U13A
1/2 14013 U13B
U14A 4071
9600
ST LD
RST (sht 10)
50
UL
U110-9
RST Unload (U2-13)
U6C
U6A
RST
U10-12 & U90-11 (sht 5) U107-3 (sht 2)
U2-1
4081
U5B
Run
RUN 53 (sht 8)
20KHZ C1 (U83-14)
U1D
U114B
R5 20K
C10 220pf
4075
U33-3 (sht 11) B
33
U3A 4013
U3B 4013
U4 4017
U22-11 (sht 3)
U111
U2-1
U7B
U9D
4071 U10A
Run (U1-5, U2-2)
C1 .001µf
A
U11D
29
BT WE (sht 6)
+5V
R6 180Ω
52
55
Unload
R7 10K
UL
Ā
98
U111 B
Q2 2N3904
U7F
U5B
270pf C2
U1 4001
U8C
U7C
U9B
C3 .001µf
U12 4040
BAC (sht 6)
U5D
U8D
4075 U18
U15 C
U19 4069
RCS 1
RCS 9 SPARE
(sht 6+7)
4017 U17
U10D
RST (U6-9)
RST Unload (U2-13)
U15-13
U2B 14013
RST Unload (U10-13)
C6 470pf
R2 22K
U5C
U11
81
U75-13 (sht 9)
U107-4 (sht 2)
U16 4040
PAC (sht 7)
U15
U14B
U24 A 4081
U9C
C4 .001µf
U7E
Read Clock (sht 10)
48
U5 A 4081
U21A 4013
Inh
U95 8-12 Sheet 11
U34-6
U22A 4013
54 RUN
U1-5 U2-2
14017 U23
14017 U96
71 A
U110A 4001
30
PT WE (sht 7)
Inh U21-2
Start Conv. U108 (sht 14)
U34 C
U110 B
49
Press. Data WE U101, U102 (sht 13)
U33-13 (sht 11)
32
U32-2 (sht 11) GT
31
U93-2 (sht 2)
U21B 4013
1 MHZ Cl U82-12 (sht 8)
U90 U11
U20 C
U97
U14C
U20 U20
1nf C5
CONTROL STUFF Layout
684-1
Sht 1 of 23

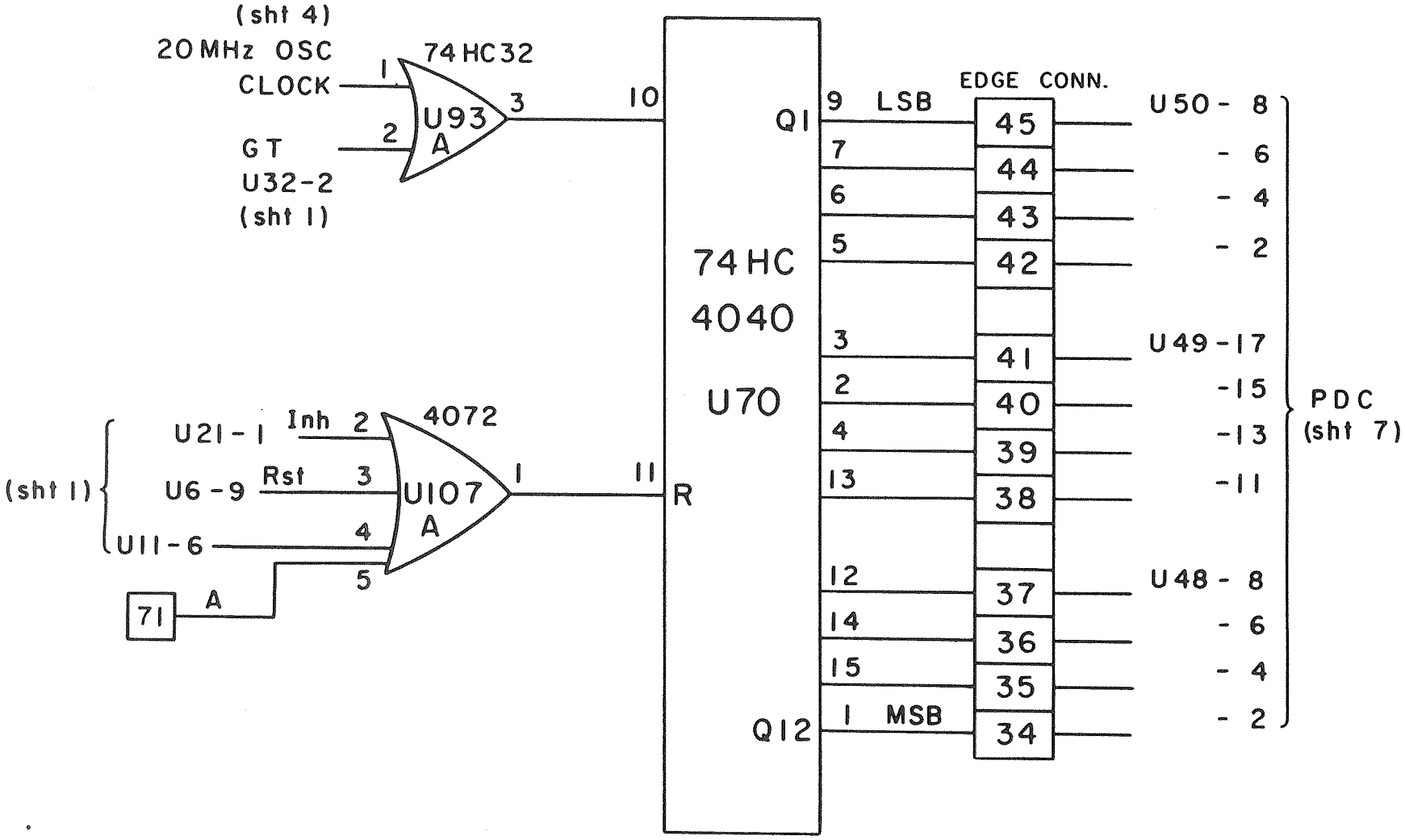

PARTICLE DURATION COUNTER
684
sht 2 of 22

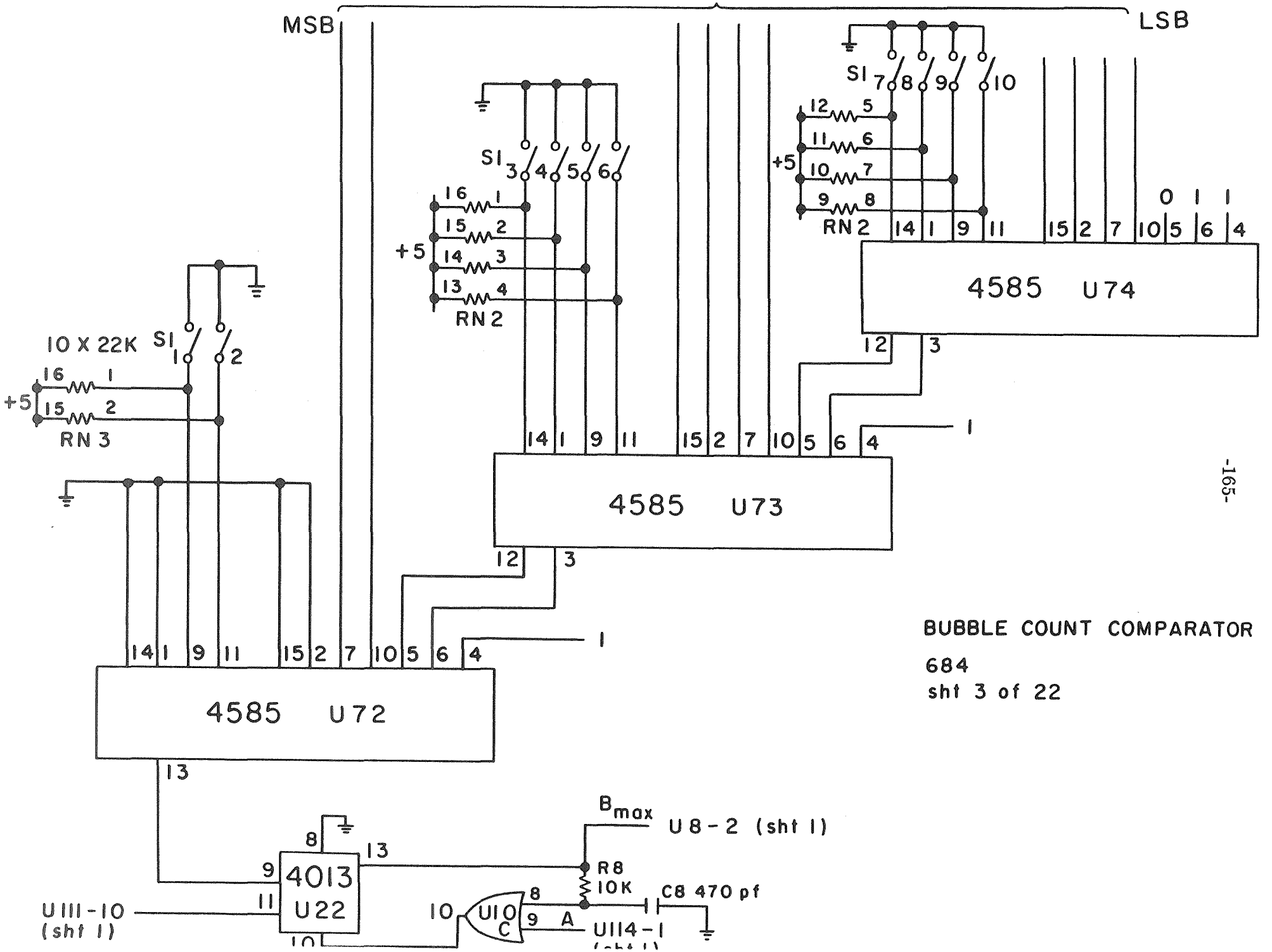
MSB
LSB
SI
10 X 22K
+5
RN 3
RN 2
4585 U72
4585 U73
4585 U74
4013 U22
U111-10 (sht 1)
U114-1
U10 C
A
R8 10K
C8 470 pf
Bmax U8-2 (sht 1)
BUBBLE COUNT COMPARATOR
684
sht 3 of 22
-165-

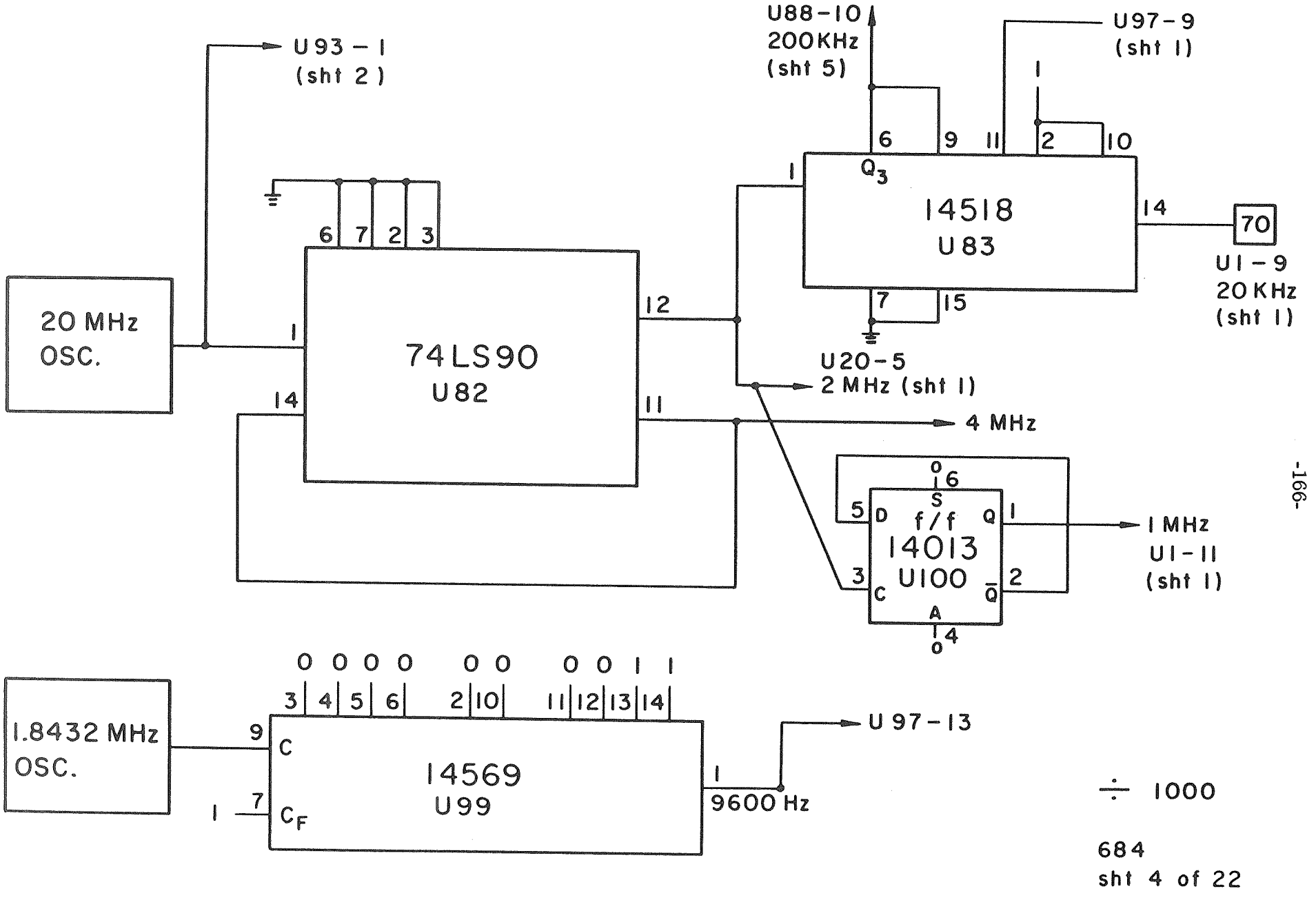
U88-10
200KHz
(sht 5)
U97-9
(sht 1)
U93-1
(sht 2)
6
9
11
1
2
10
Q3
14518
U83
14
70
U1-9
20KHz
(sht 1)
7
15
U20-5
6
7
2
3
20 MHz
OSC.
1
74LS90
U82
12
2 MHz (sht 1)
14
11
4 MHz
0
6
S
5
D
f/f
Q
1
14013
U100
3
C
Q
2
A
0
4
1 MHz
U1-11
(sht 1)
0 0 0 0 0 0 0 0 1 1
3
4
5
6
2
10
11
12
13
14
1.8432 MHz
OSC.
9
C
14569
U99
1
7
CF
1
9600 Hz
U97-13
÷ 1000
684
sht 4 of 22

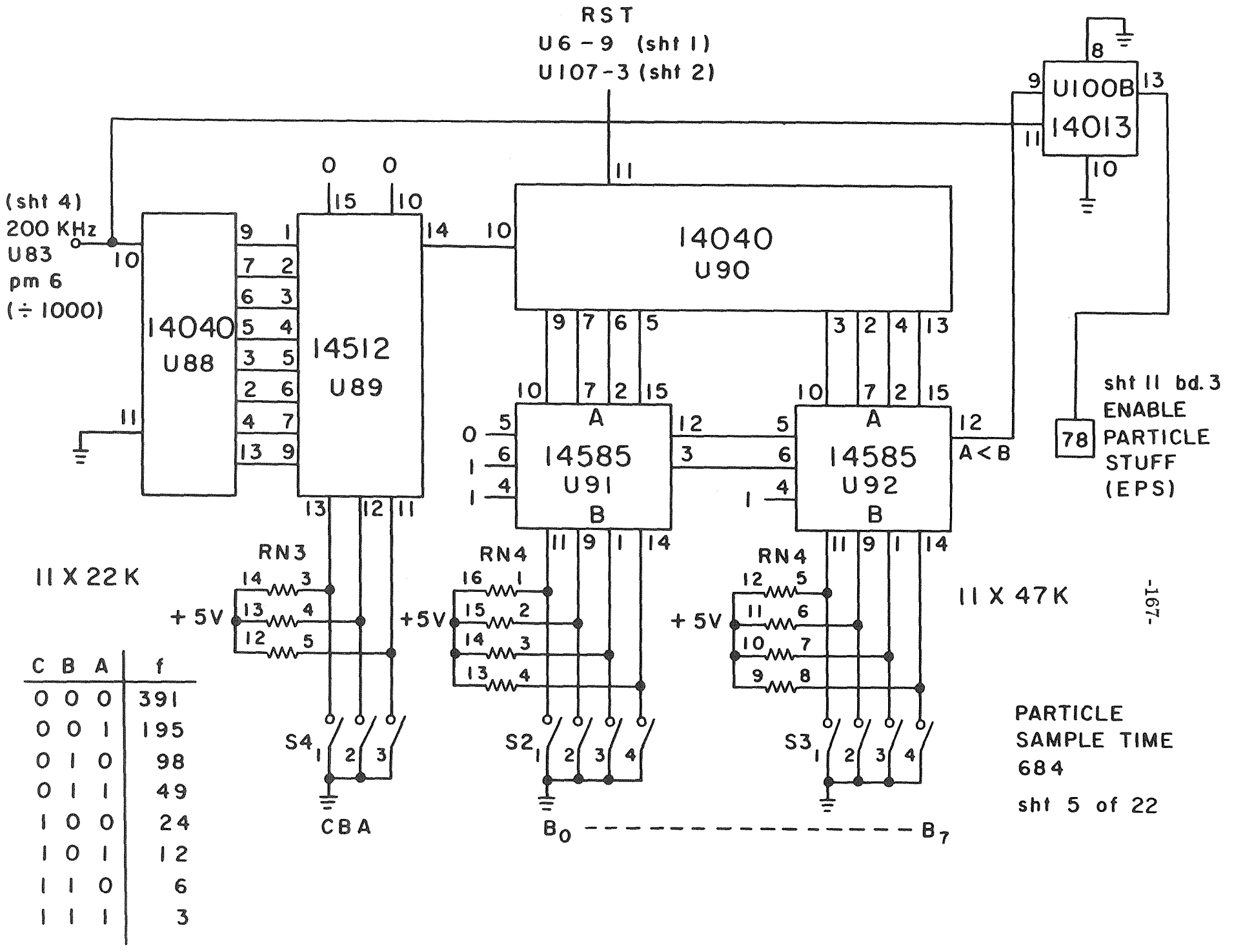

C	B	A	f
0	0	0	391
0	0	1	195
0	1	0	98
0	1	1	49
1	0	0	24
1	0	1	12
1	1	0	6
1	1	1	3

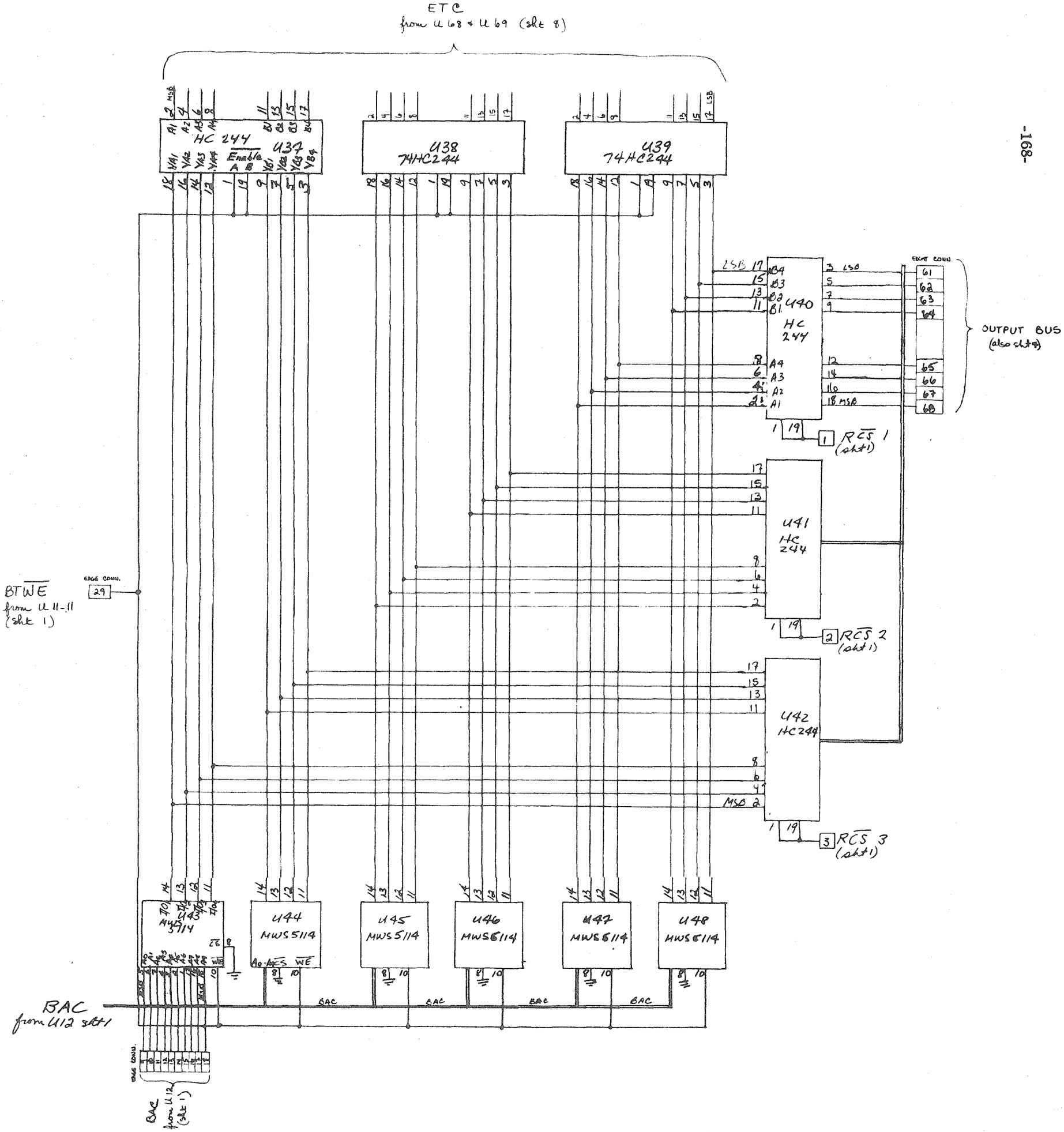

MEMORY + BUFFERS
684-6
Sheet 6 of 23

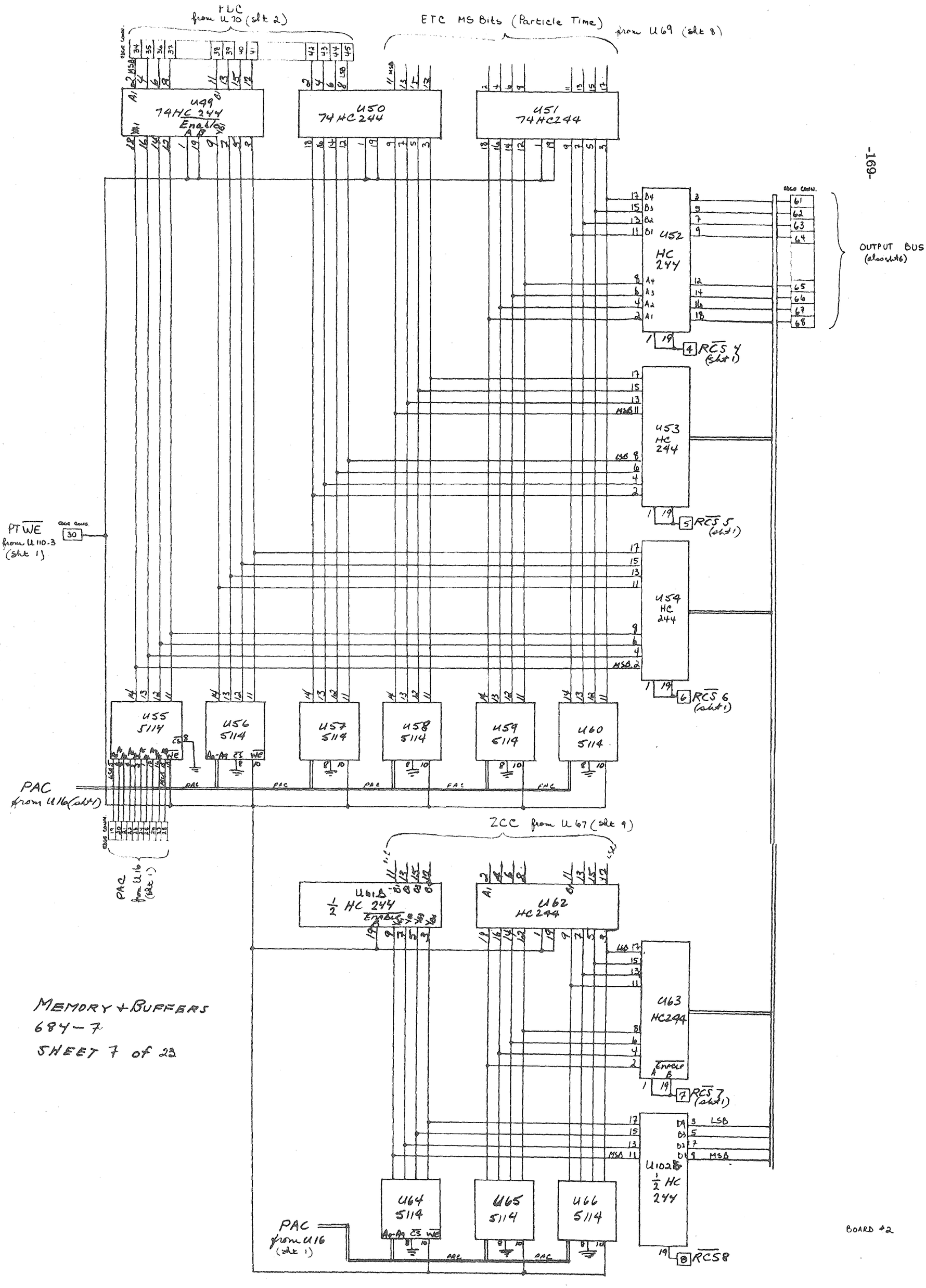
PLC from U70 (sht 2)
ETC MS Bits (Particle Time) from U69 (sht 8)
U49 74HC 244 Enable A B
U50 74HC244
U51 74HC244
U52 HC 244
U53 HC 244
U54 HC 244
U55 5114
U56 5114
U57 5114
U58 5114
U59 5114
U60 5114
OUTPUT BUS (also sht 6)
RCS 4 (sht 1)
RCS 5 (sht 1)
RCS 6 (sht 1)
PTWE from U110-3 (sht 1)
PAC from U16 (sht 1)
ZCC from U67 (sht 9)
U61 1/2 HC 244
U62 HC244
U63 HC244
U102 1/2 HC 244
U64 5114
U65 5114
U66 5114
RCS 7 (sht 1)
RCS 8
MEMORY + BUFFERS
684-7
SHEET 7 of 23
BOARD #2

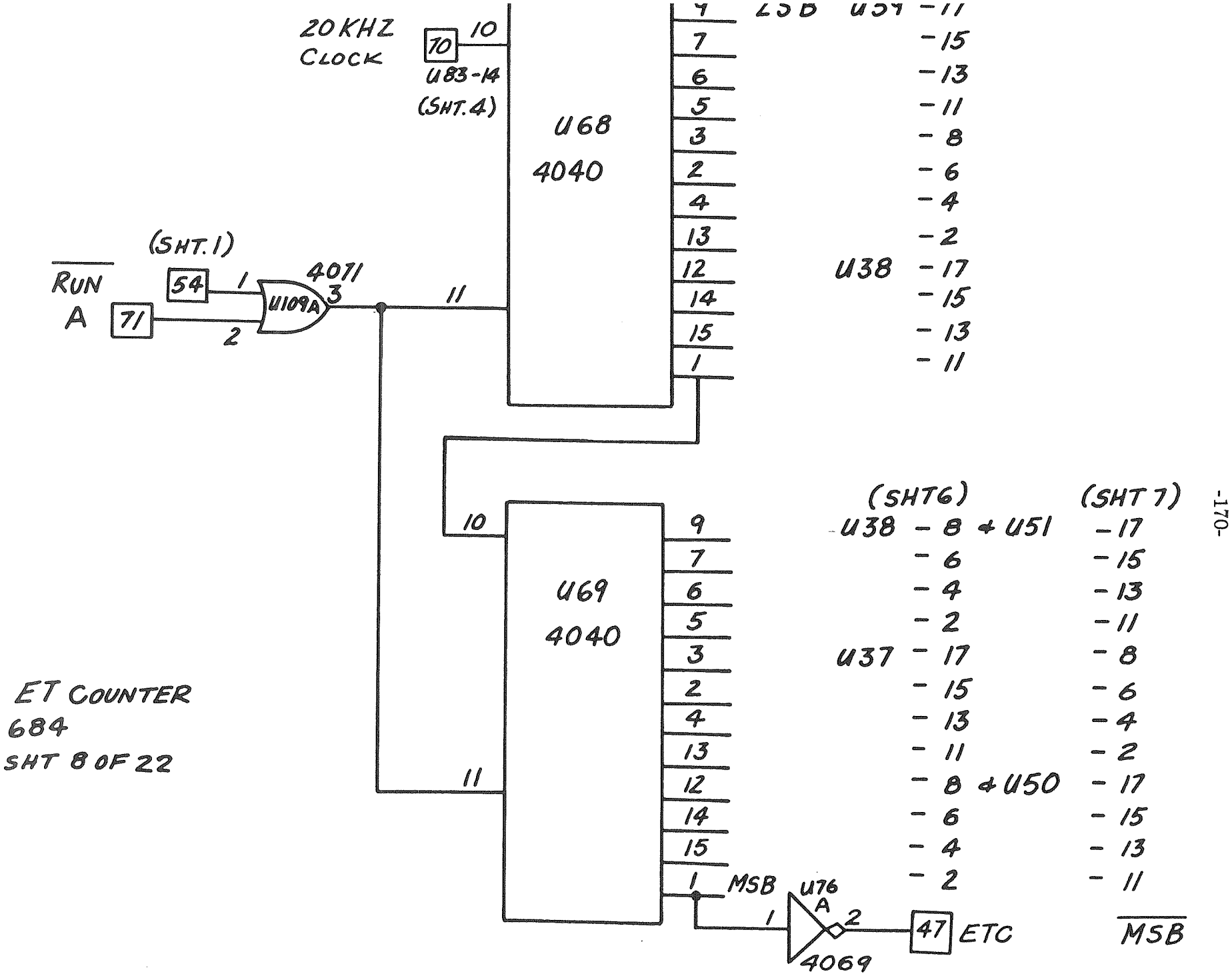
20 KHZ CLOCK
70
10
U83-14 (SHT. 4)
U68 4040
7
6
5
3
2
4
13
12
14
15
1
(SHT. 1)
RUN A
54
71
1
2
4071
U109A
3
11
10
U69 4040
9
7
6
5
3
2
4
13
12
14
15
1
11
MSB
U76 A
1
2
4069
47
ETC
(SHT 6)
U38 - 8 & U51
- 6
- 4
- 2
U37 - 17
- 15
- 13
- 11
- 8 & U50
- 6
- 4
- 2
(SHT 7)
- 17
- 15
- 13
- 11
- 8
- 6
- 4
- 2
- 17
- 15
- 13
- 11
U38 - 17
- 15
- 13
- 11
MSB
ET COUNTER
684
SHT 8 OF 22
BOARD #2

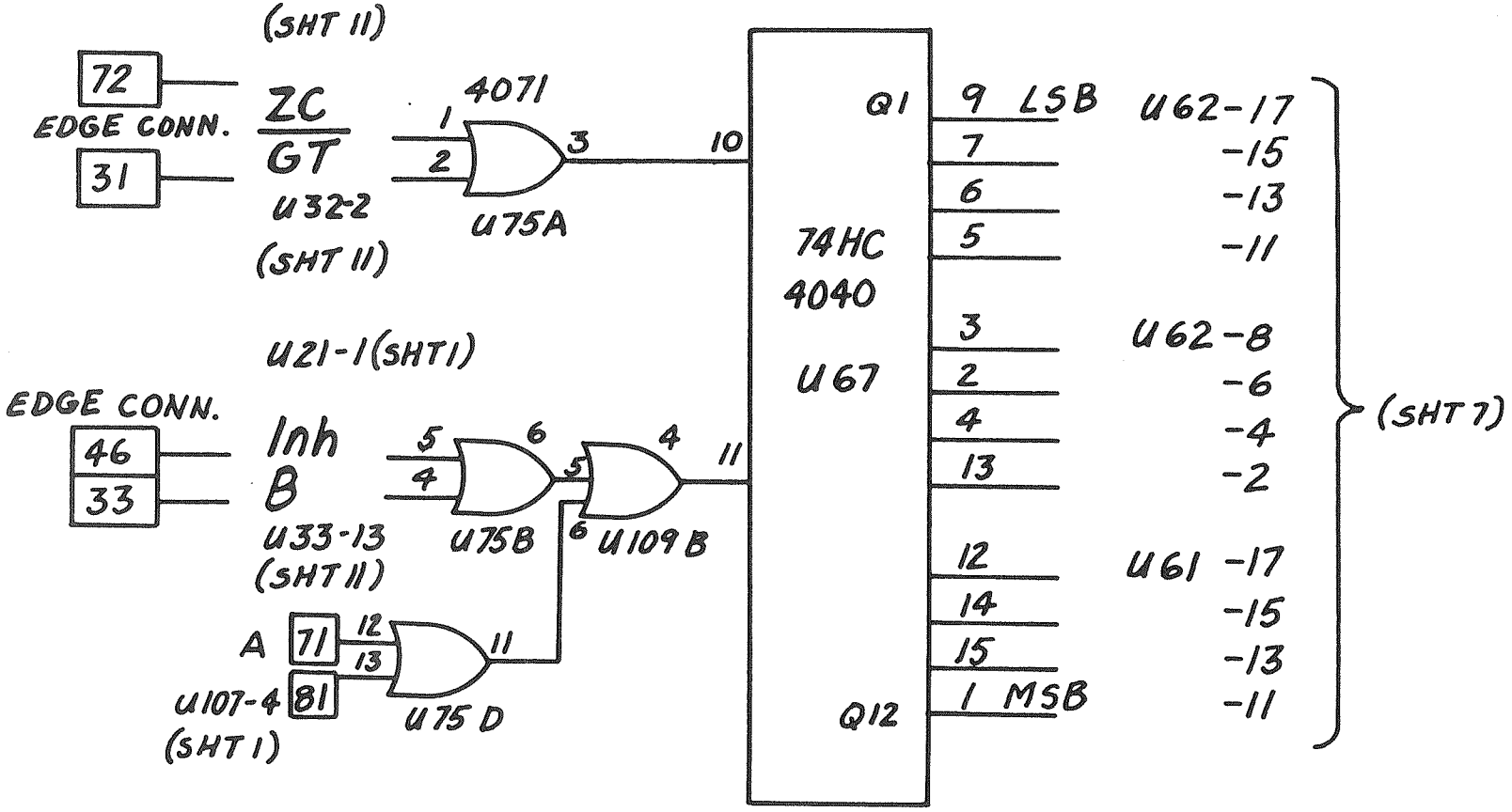

ZERO CROSSING COUNTER

684

SHT 9 OF 22

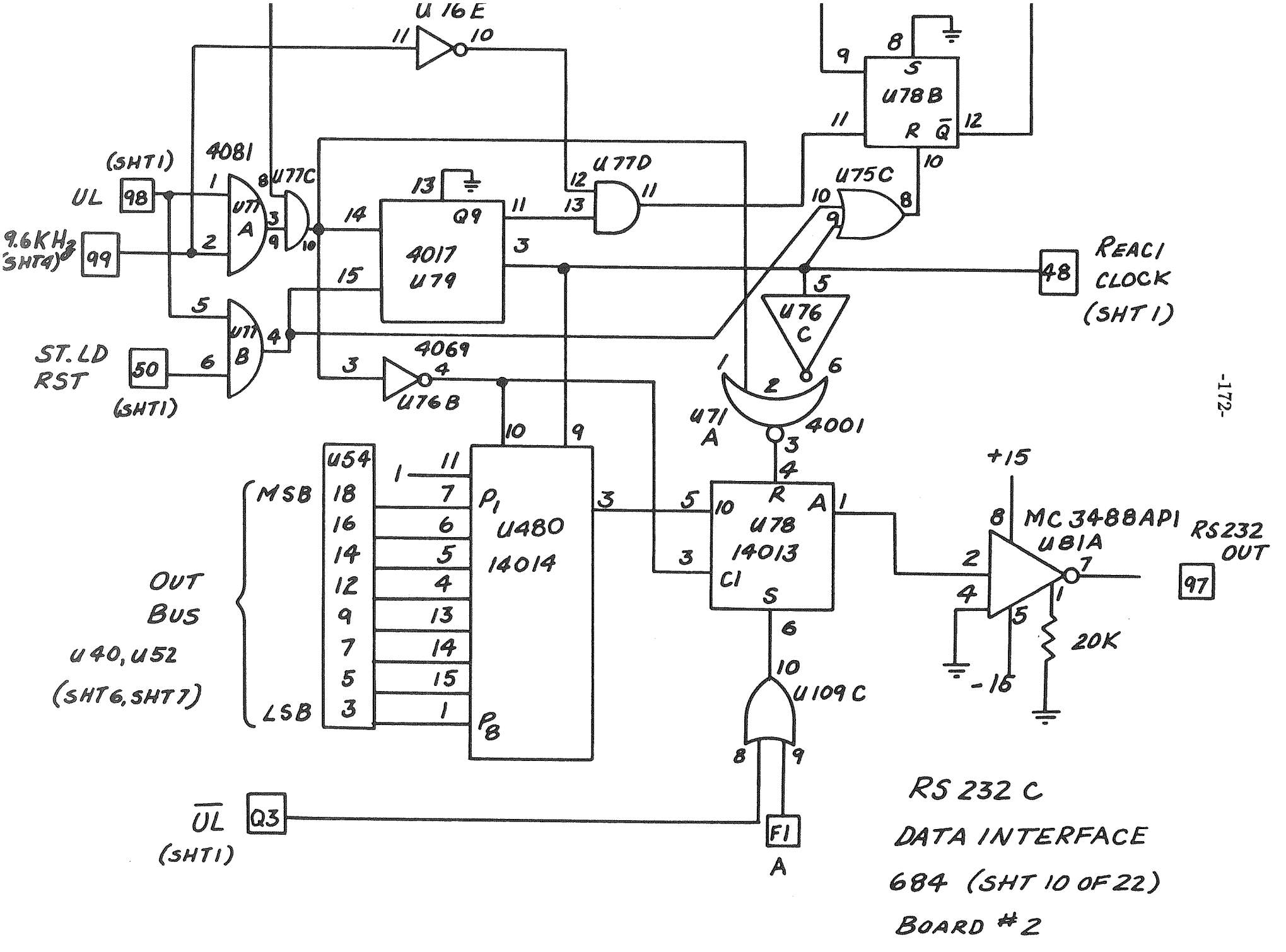
U 16 E
U78 B
R Q
U75C
U77D
U77C
4081
(SHT1)
UL
98
9.6KHz
(SHT4)
99
U71 A
U71 B
4017
U79
Q9
4069
U76B
U76 C
ST. LD
RST
50
(SHT1)
REACI
CLOCK
(SHT 1)
48
U71 A
4001
U54
MSB
LSB
OUT
BUS
U40, U52
(SHT6, SHT7)
P1
U480
14014
P8
U78
14013
R
A
CI
S
+15
MC 3488API
U81A
RS232
OUT
97
20K
-16
U109 C
UL
(SHT1)
Q3
F1
A
RS 232 C
DATA INTERFACE
684 (SHT 10 OF 22)
BOARD # 2
-172-

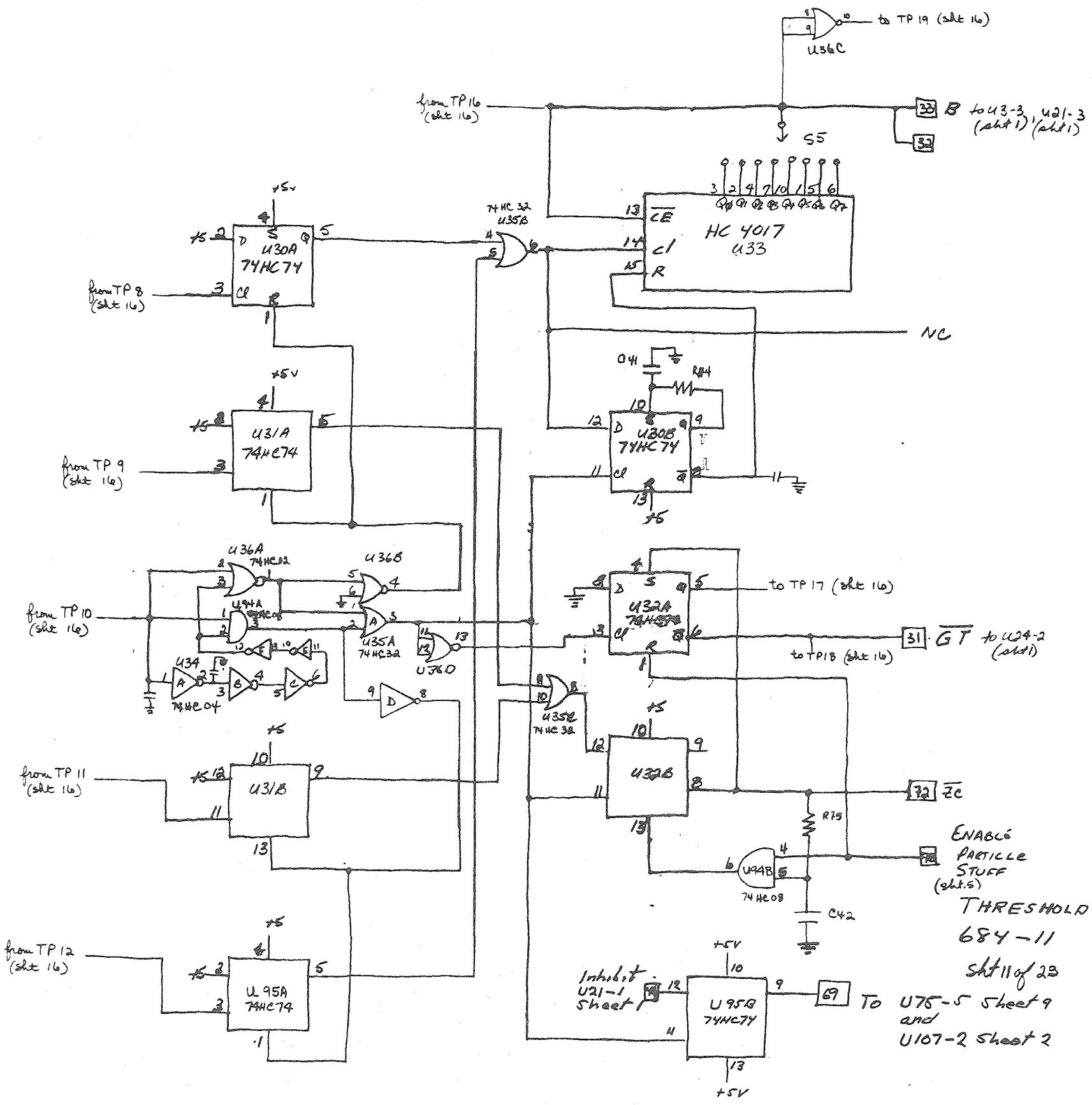

THRESHOLD CIRCUITS
684-11
Sht 11 of 23

BOARD # 3

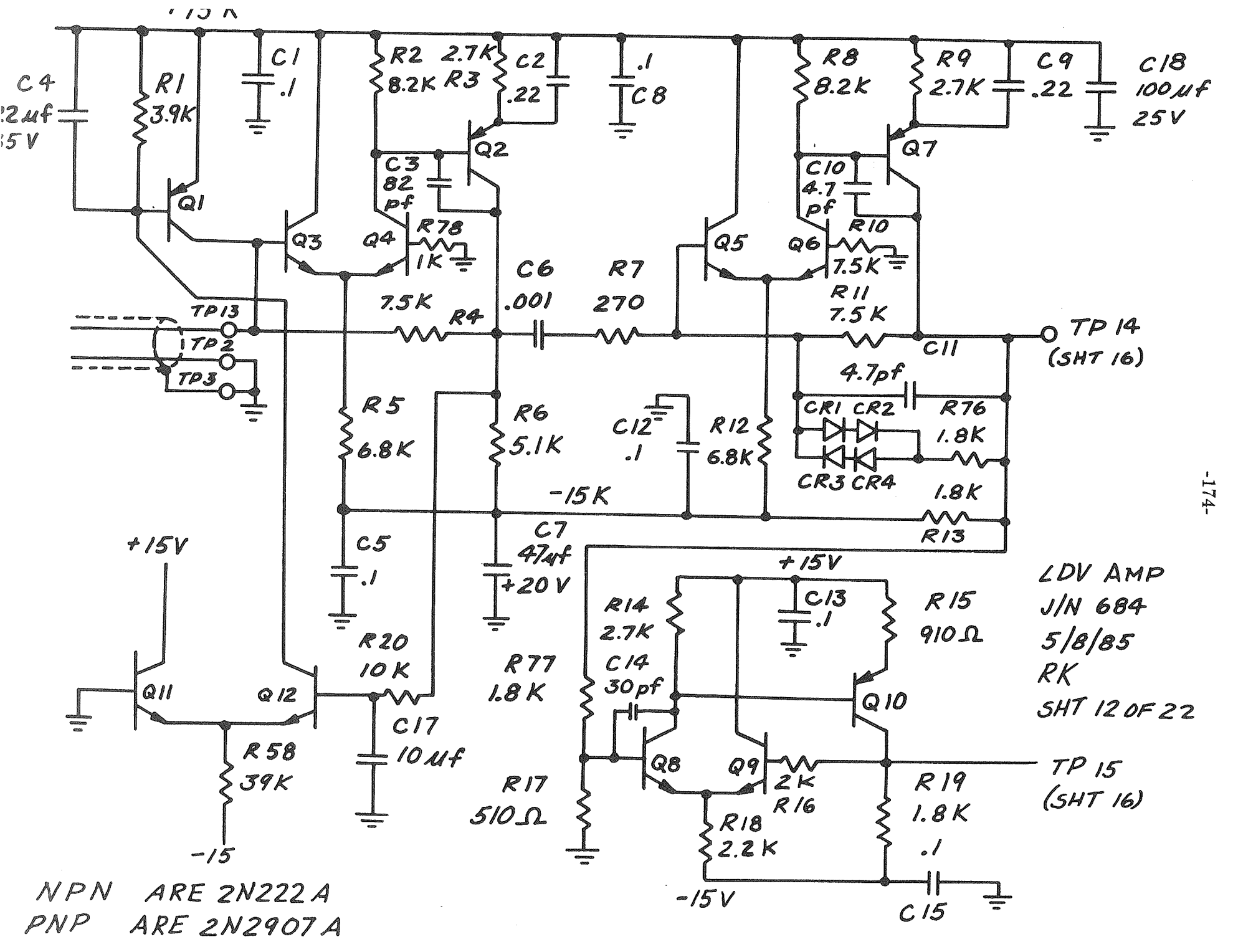
+15 K
C4
2 µf
5 V
R1
3.9K
C1
.1
R2
8.2K
2.7K
R3
C2
.22
.1
C8
R8
8.2K
R9
2.7K
C9
.22
C18
100 µf
25 V
Q1
Q2
Q7
C3
82
pf
C10
4.7
pf
R10
Q3
Q4
R78
1K
Q5
Q6
7.5K
R11
7.5K
C6
.001
R7
270
7.5K
R4
TP13
TP2
TP3
TP 14
(SHT 16)
C11
4.7pf
R5
6.8K
R6
5.1K
C12
.1
R12
6.8K
CR1
CR2
R76
1.8K
CR3
CR4
-15K
1.8K
R13
C7
47µf
+20 V
C5
.1
+15V
+15V
C13
.1
R14
2.7K
R15
910Ω
R20
10K
R77
1.8K
C14
30pf
Q10
Q11
Q12
C17
10 µf
R58
39K
Q8
Q9
2K
R16
TP 15
(SHT 16)
R17
510Ω
R18
2.2K
R19
1.8K
.1
-15
-15V
C15
LDV AMP
J/N 684
5/8/85
RK
SHT 12 OF 22
NPN ARE 2N222A
PNP ARE 2N2907A

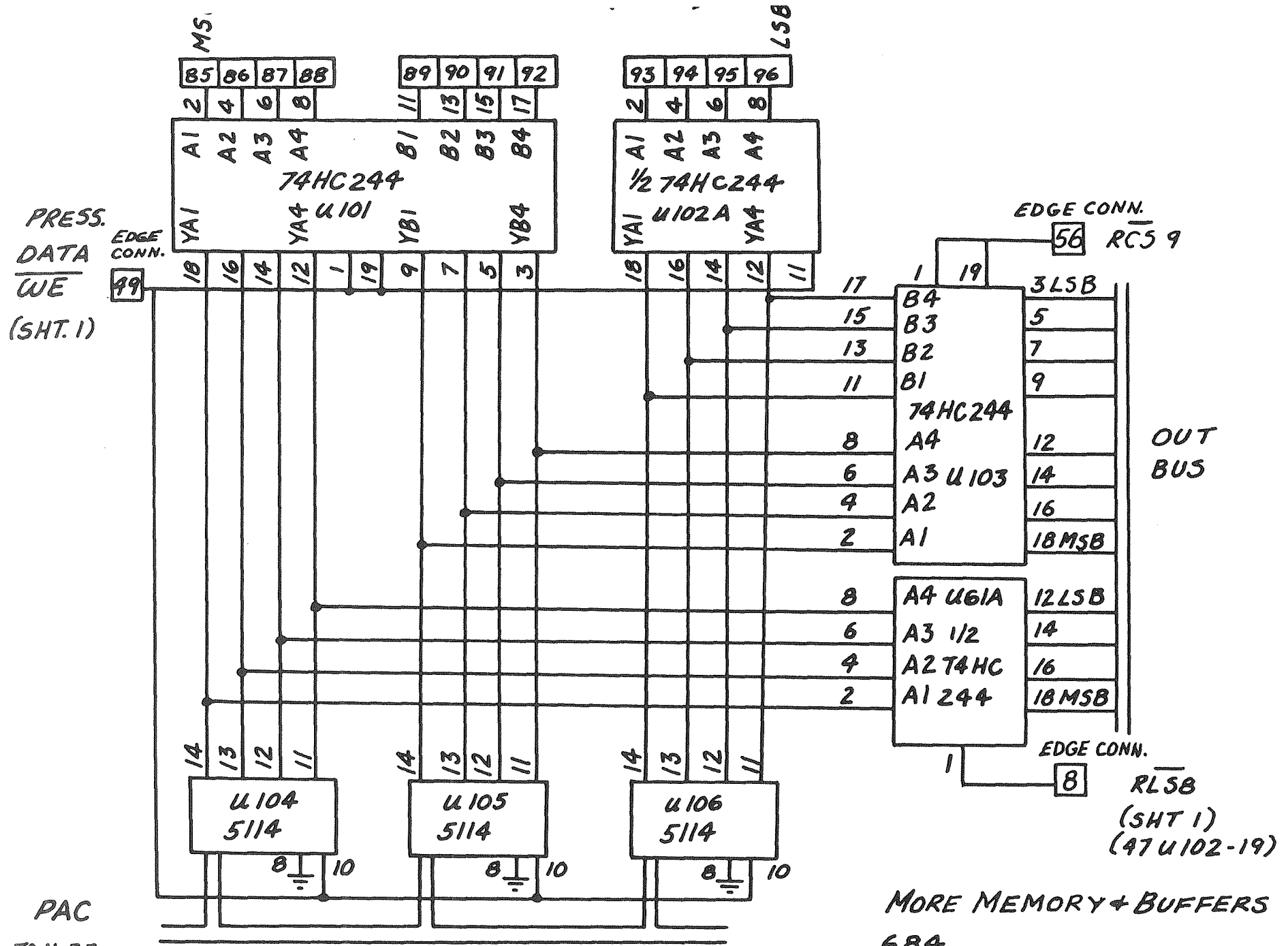
MSB
85 86 87 88
89 90 91 92
93 94 95 96
LSB
2 4 6 8
11 13 15 17
A1 A2 A3 A4
B1 B2 B3 B4
74HC244
YA1 YA4 U101
YB1 YB4
1/2 74HC244
U102A
PRESS. DATA WE
(SHT. 1)
EDGE CONN.
99
18 16 14 12 1 19 9 7 5 3
18 16 14 12 11
EDGE CONN.
56
RCS 9
1 19
3 LSB
5
7
9
OUT BUS
12
14
16
18 MSB
17 15 13 11
8 6 4 2
B4 B3 B2 B1
74HC244
A4 A3 A2 A1
U103
A4 U61A
A3 1/2
A2 T4HC
A1 244
12 LSB
14
16
18 MSB
EDGE CONN.
1
8
RLSB
(SHT 1)
(47 U102-19)
14 13 12 11
U104 5114
U105 5114
U106 5114
8
10
PAC
TO U55
(SHT. 7)
MORE MEMORY + BUFFERS
684
SHT 13 OF 22

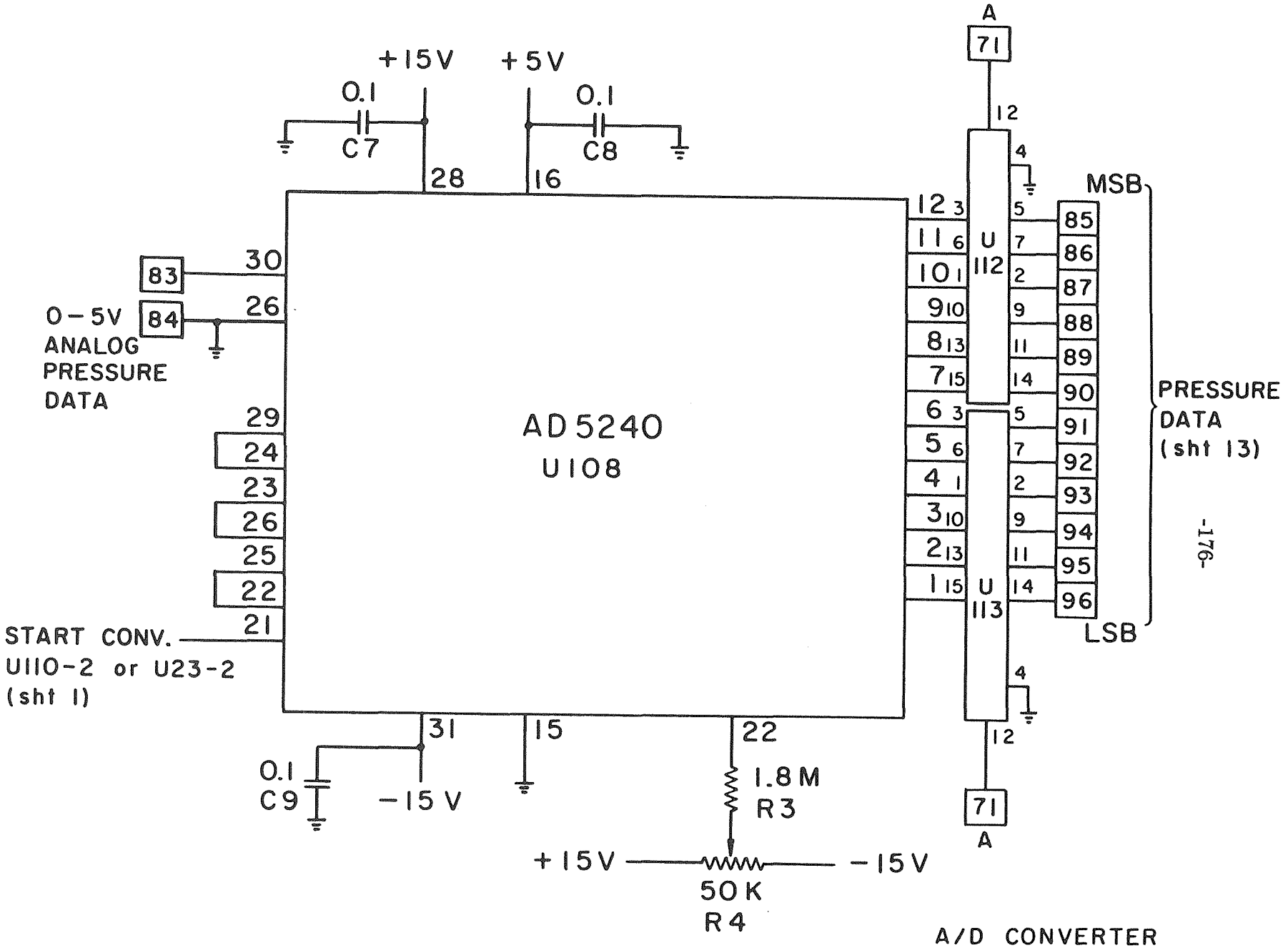
+15V
+5V
0.1
C7
0.1
C8
28
16
30
26
29
24
23
26
25
22
21
31
15
22
83
84
0-5V
ANALOG
PRESSURE
DATA
AD5240
U108
START CONV.
U110-2 or U23-2
(sht 1)
0.1
C9
-15V
1.8M
R3
+15V
-15V
50K
R4
A
71
12
4
12 3
11 6
10 1
9 10
8 13
7 15
6 3
5 6
4 1
3 10
2 13
1 15
U
112
U
113
5
7
2
9
11
14
5
7
2
9
11
14
4
12
71
A
MSB
85
86
87
88
89
90
91
92
93
94
95
96
LSB
PRESSURE
DATA
(sht 13)
A/D CONVERTER
684
sht 14 of 22

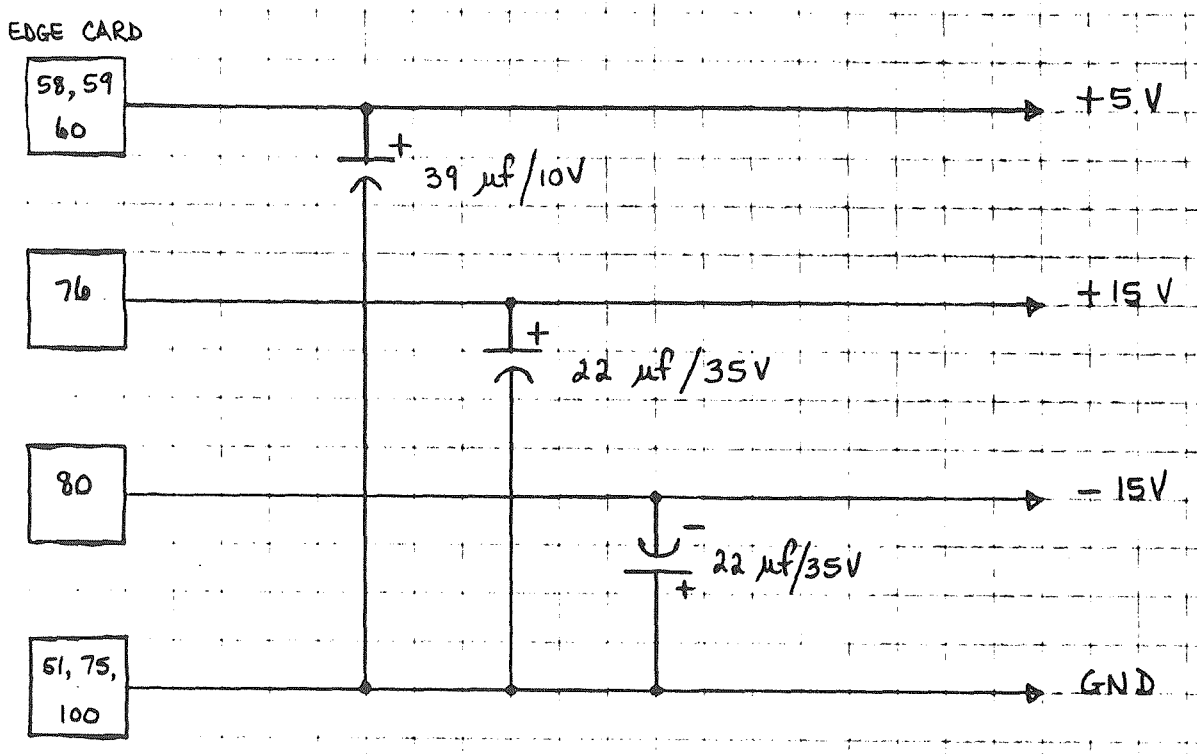

Power Supply Capacitors for Boards 1, 2 & 3

6884-15

Sheet 15 of 22

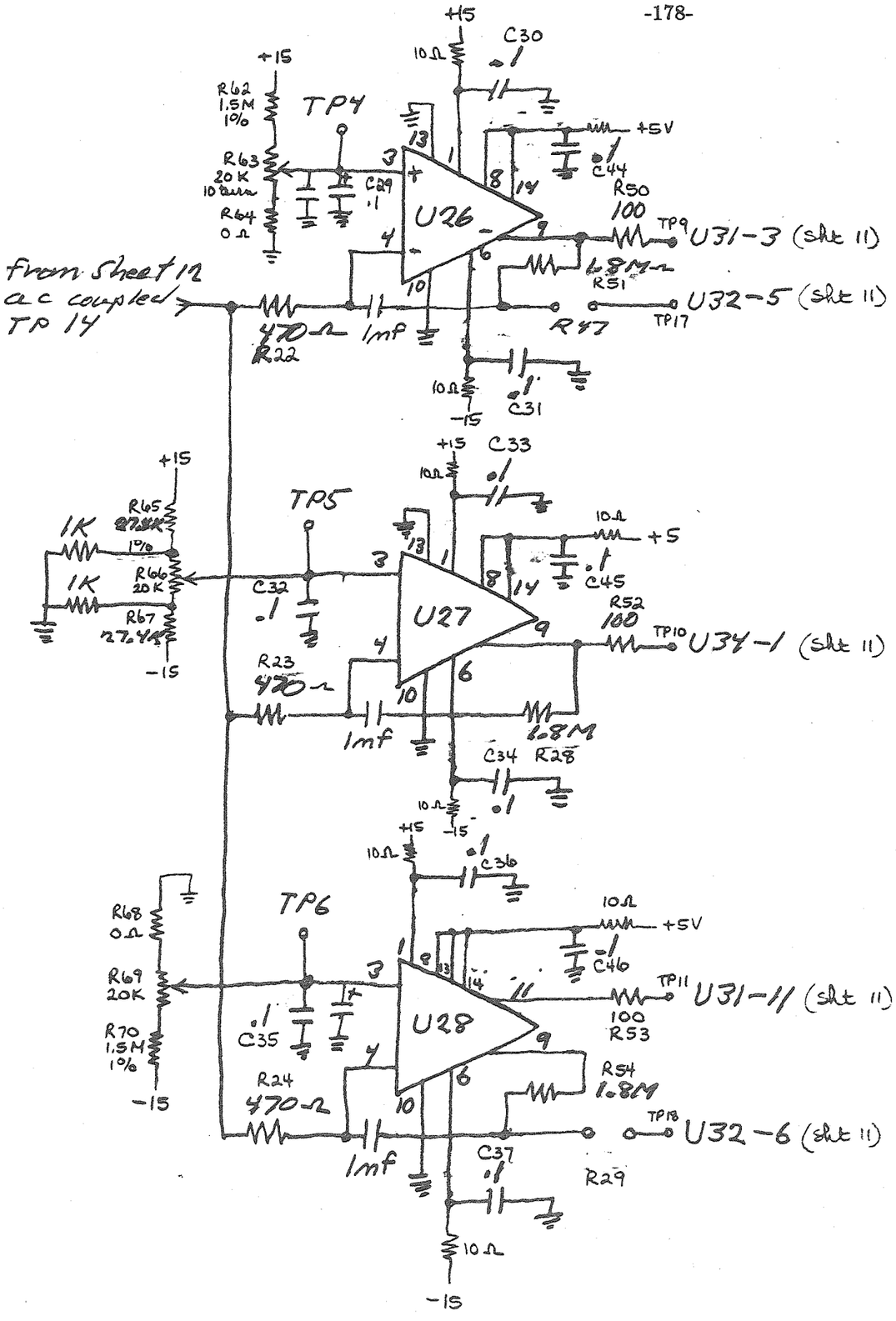

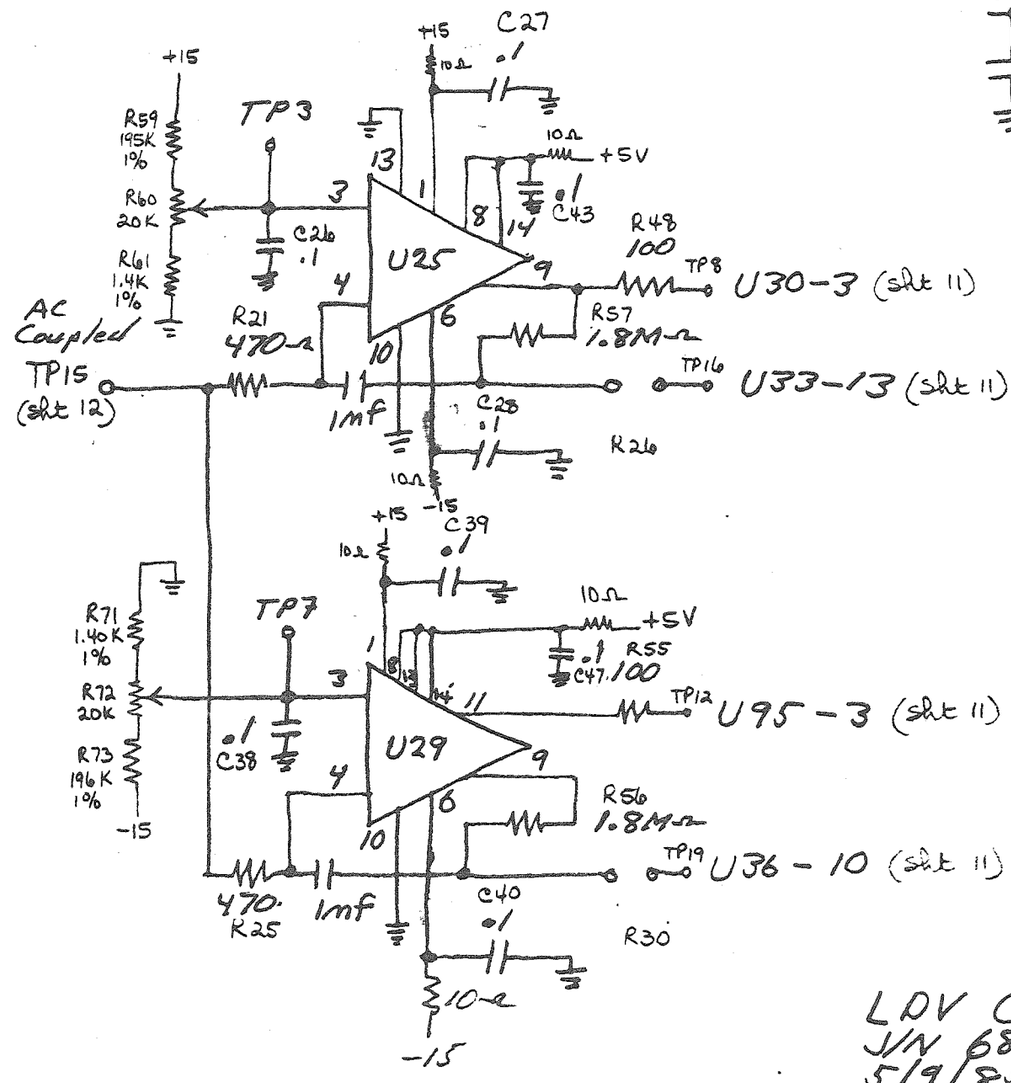

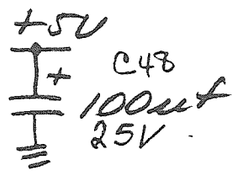

U25 – U29 are LM361

LDV Comparators
J/N 684
5/9/85
RK

Sheet 16 of 23

Revised 10/85 KSB – Add 10Ω decoupling resistors to +5V, +15V & –15V

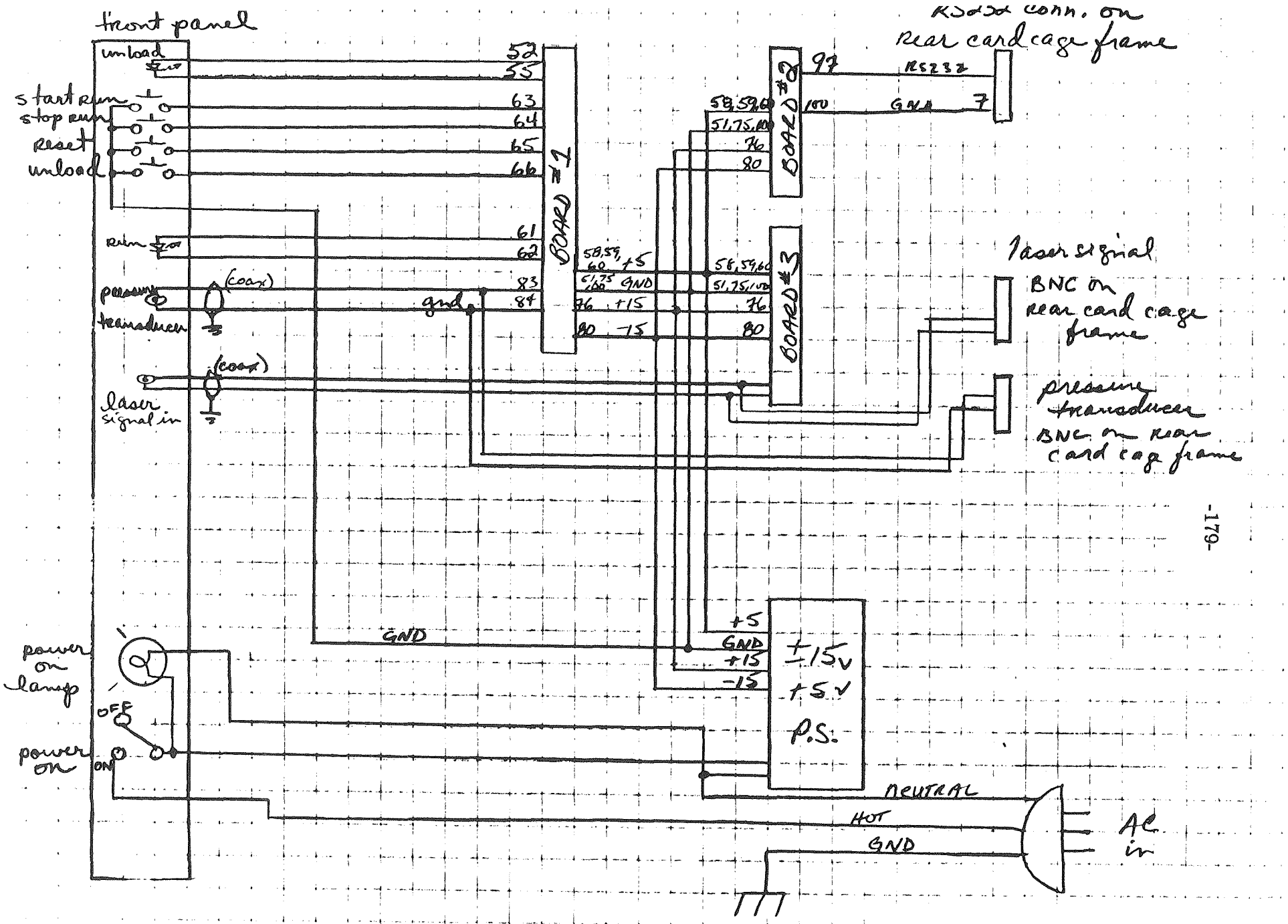

-179-

Cal Tech LDV
Chassis wiring diagram
KR 2/5/84 Sheet 17

Cal Tech Board Interconnect Sheet 8 2/5/85

Board #1

Board #2

Board #3

	Board #1	Board #2	Board #3
1	RCS 1	1	
2	RCS 2	2	
3	RCS 3	3	
4	RCS 4	4	
5	RCS 5	5	
6	RCS 6	6	
7	RCS 7	7	
8	RCS 8	8	
9	BAC LSB	9	
10	BAC	10	10 — laser signal
11	BAC	11	
12	BAC	12	
13	BAC	13	
14	BAC	14	
15	BAC	15	
16	BAC	16	
17	BAC	17	
18	BAC MSB	18	
19	PAC LSB	19	
20	PAC	20	
21	PAC	21	
22	PAC	22	
23	PAC	23	
24	PAC	24	
25	PAC	25	
26	PAC	26	
27	PAC	27	
28	PAC MSB	28	
29	BT WE	29	
30	PT WE	30	
31	GT	31	GT 31
32	BP		BP 32
33	B	33	B 33
34	PDC LSB	34	
35	PDC	35	
36	PDC	36	
37	PDC	37	
38	PDC	38	
39	PDC	39	
40	PDC	40	
41	PDC	41	
42	PDC	42	
43	PDC	43	
44	PDC	44	
45	PDC	45	
46	Enh		46
47		ETC MSB	47
48	READ CLOCK		48
49	PRES DATA WE		49
50	ST. LD RST		50
51	GND	51	GND 51
52	unload	52	
53	UL	53	
54	RUN	54	
55			
56	RES 9	56	
57	SPARE		
58		58	58
59	+5V	59	+5V 59
60		60	60

18 SHT 1 OF 2

Board #1

Board #2

Board #3

	Board #1	Board #2	Board #3
61	arm	61	OUTPUT BUS LSB
62		62	OUT BUS
63	start arm	63	OUT BUS
64	stop arm	64	OUT BUS
65	reset	66	OUT BUS
66	unload	66	OUT BUS
67		67	OUT BUS
68		68	OUT BUS
69	SYNC INH	69	69
70	20KHz	90	
71	A	91	
72		92	FC 72
73		73	
74		74	
75	GND	75	75
76	+15V	76	76
77			
78			FAARS PARTICLE STUFF 78
79			
80	-15V	80	80
81		81	
82			
83	PRESS TRANSDUCER		
84	GND		
85	PRESSURE DATA	85	
86	P DATA	86	
87	P DATA	87	
88	P DATA	88	
89	P DATA	89	
90	P DATA	90	
91	P DATA	91	
92	P DATA	92	
93	P DATA	93	
94	P DATA	94	
95	P DATA	95	
96	P DATA	96	
97			
98	UL	98	RS232 DB Con
99	9600 Hz	99	
100	GND	100	GND 7

SPARE

-180-

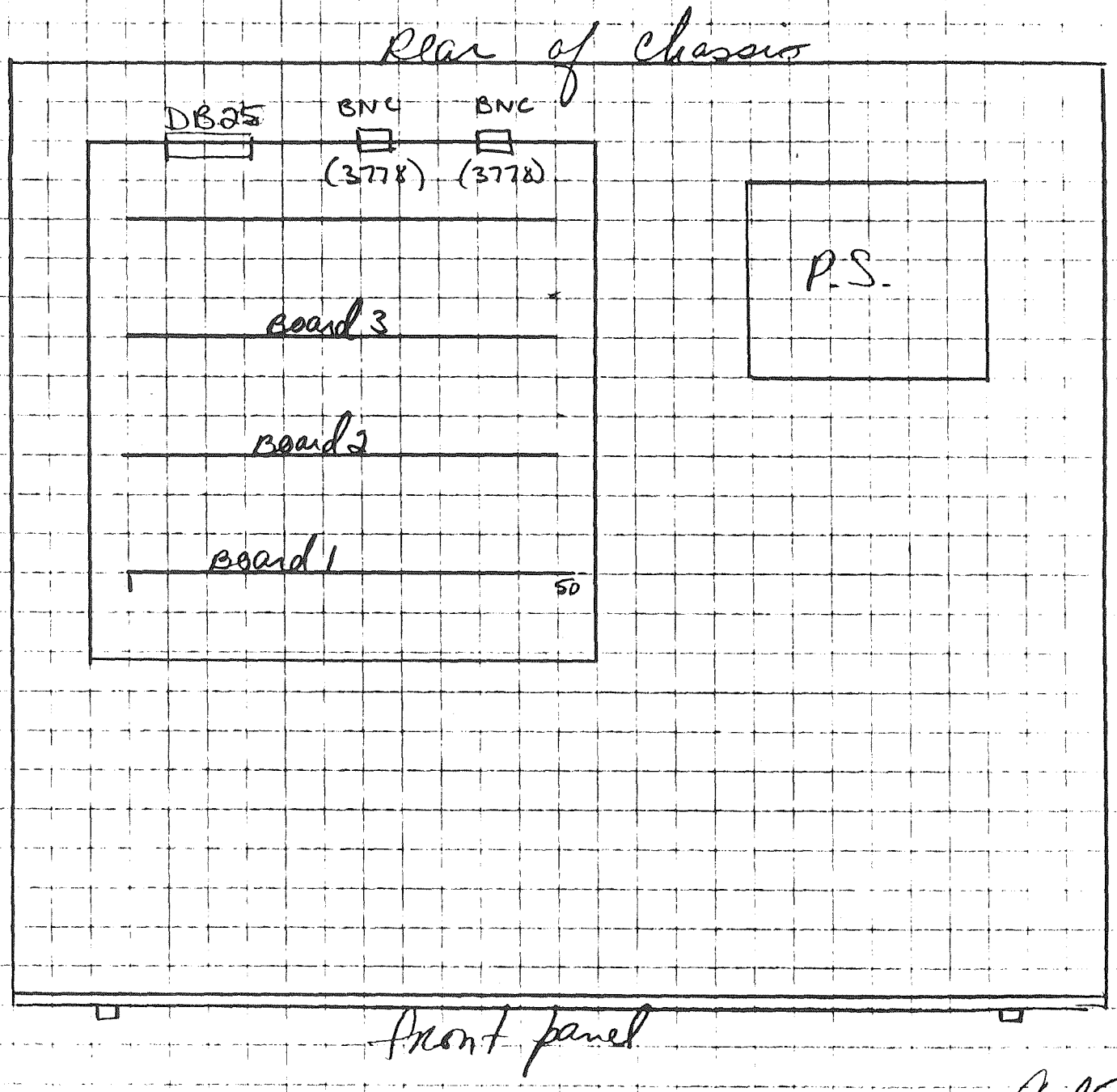

Cal Tech
Chassis layout
F/N684 Sheet 19

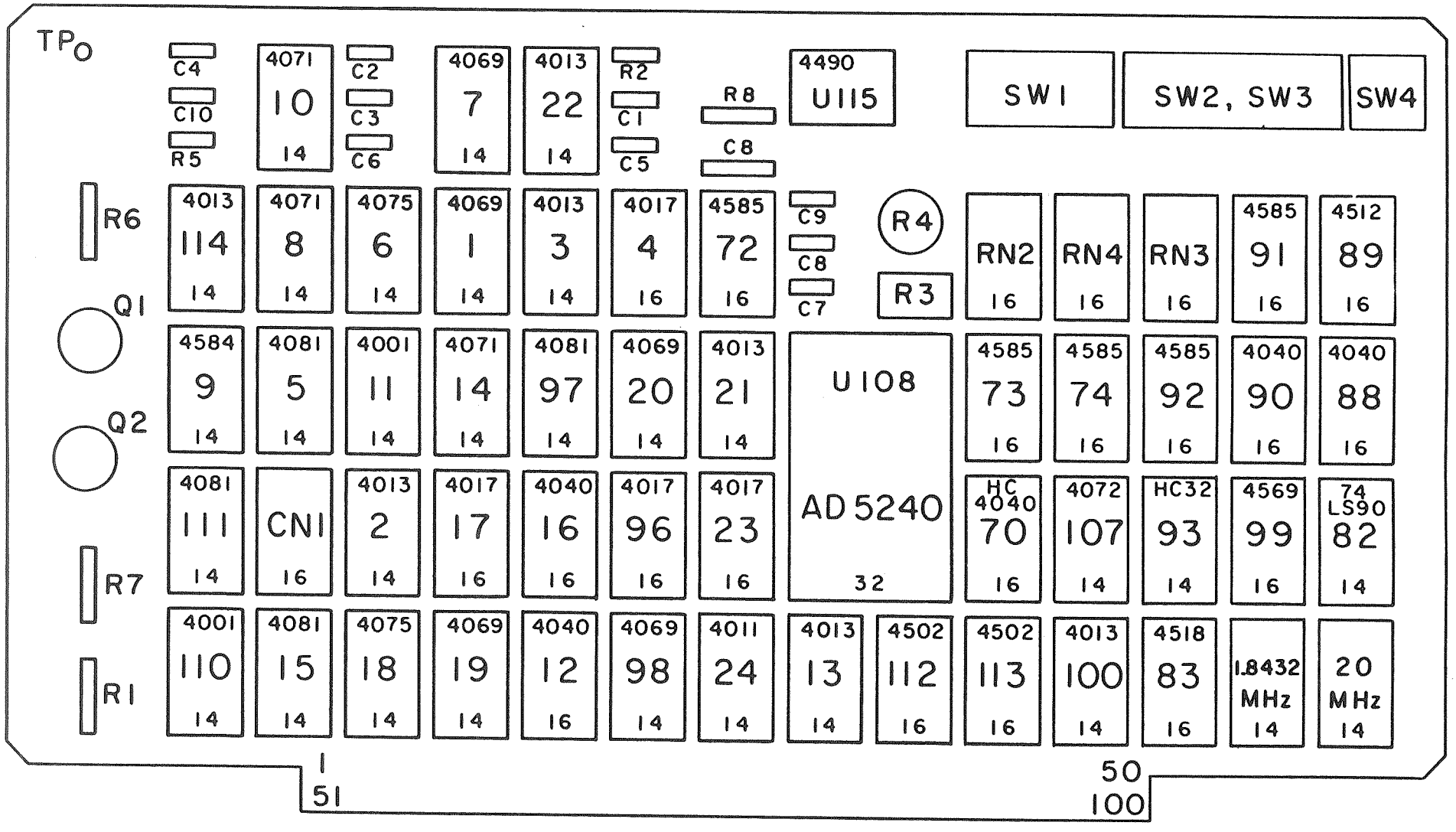

+5V → 58, 59, 60
GND → 51, 75, 100
+15V → 76
−15V → 80

LAYOUT sht 20

LAYOUT
SHEET 21

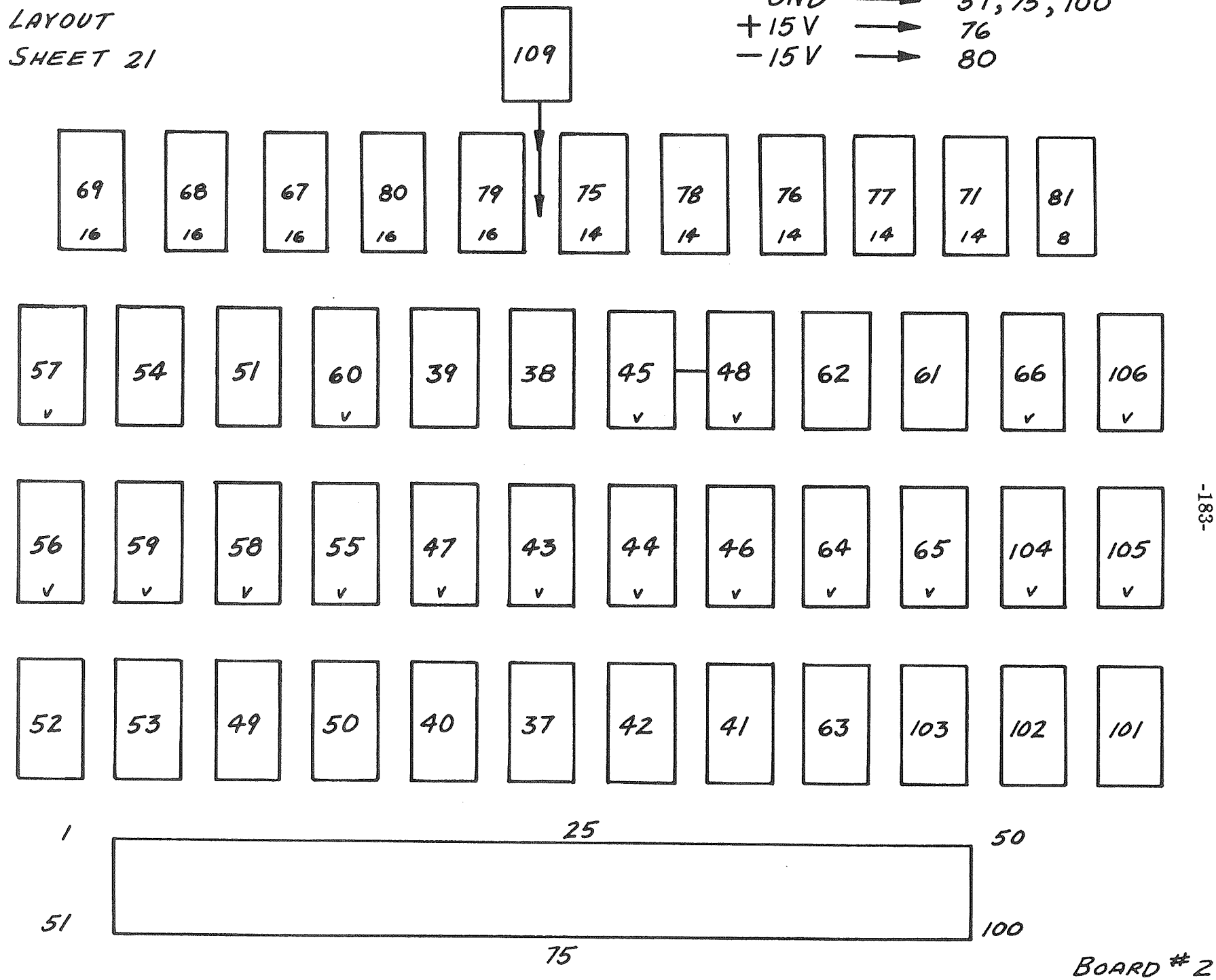

BOARD #2

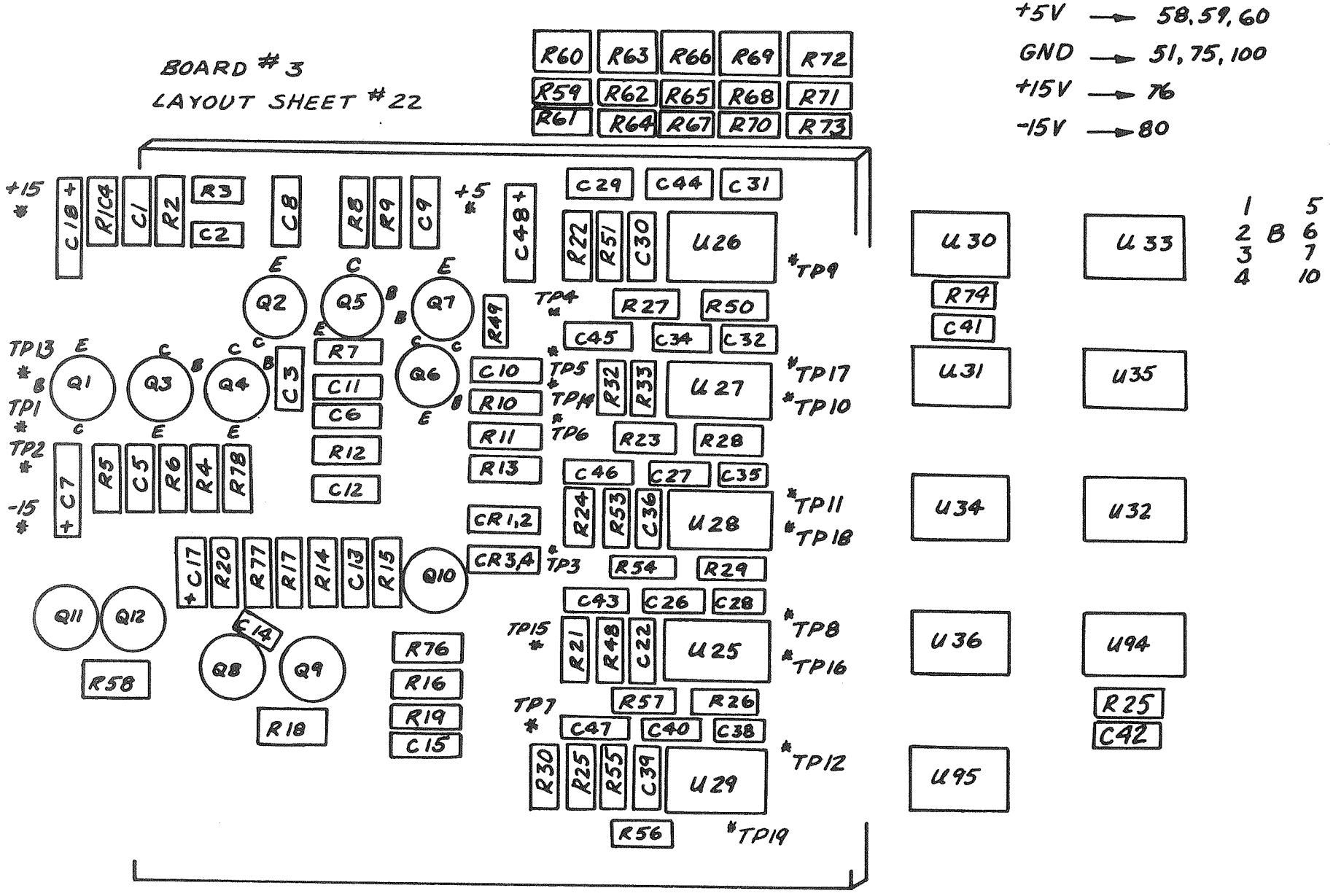
BOARD #3
LAYOUT SHEET #22
+5V → 58, 59, 60
GND → 51, 75, 100
+15V → 76
-15V → 80
R60 R63 R66 R69 R72
R59 R62 R65 R68 R71
R61 R64 R67 R70 R73
+15
C18 +
R1C4
C1
R2
R3
C2
C8
R8
R9
C9
+5
C48 +
C29 C44 C31
R22 R51 C30
U26
TP9
U30
U33
1 5
2 B 6
3 7
4 10
R74
C41
TP4
R27 R50
C45 C34 C32
R49
TP13
TP1
TP2
-15
Q1 Q3 Q4 Q2 Q5 Q7 Q6
C3
R7
C11
C6
R12
C12
C10
R10
R11
R13
TP5
TP14
TP6
R32 R33
U27
TP17
TP10
U31
U35
R23 R28
C7 +
R5 C5 R6 R4 R7B
C46 C27 C35
R24 R53 C36
U28
TP11
TP18
U34
U32
CR1,2
CR3,4
TP3
R54 R29
C17 + R20 R77 R17 R14 C13 R15
Q10
Q11 Q12
C14
Q8 Q9
R58
R18
R76
R16
R19
C15
C43 C26 C28
TP15
R21 R48 C22
U25
TP8
TP16
U36
U94
R57 R26
TP7
C47 C40 C38
R25
C42
R30 R25 R55 C39
U29
TP12
U95
R56
TP19

BOARD #3

Appendix 2

CSM DATA ACQUISITION AND REDUCTION PROGRAM

```
10 OPTION BASE 1: DIM COMMENT$(10)
20 COMMENT$(1)="CSM Data Reduction Program REDUCE9.BAS"
30 COMMENT$(2)="Luca d'Agostino 11.18.1986 - Revised on: 02.07.1987"
40 CLS: PRINT COMMENT$(1): PRINT COMMENT$(2): PRINT
50 INPUT"Enter Date: ", RESP$: COMMENT$(3)="Date: "+RESP$
60 '
70 ' Machine Language Subroutines, Constants & Functions
80 GOSUB 6000: PG=3.14159: RTCF=20000: GTCF=2E+07: B0=.2316419
90 B1=.3193815: B2=-.3565638: B3=1.781478: B4=-1.821256: B5=1.330274
100 PNTMAX%=1024: SET%=2: GDAT%=22: RDAT%=22: GRP%=32: GRPMAX%=128: RTHR=0:NSR=2
110 DIM GDAT$(22), GDAT(22), RDAT$(22), RDAT(22), OF%(128), SAVEX%(128,2)
120 DIM XX(1024,2), YY(1024,2), PNT%(2), SYMBMAP%(2), INCSET%(2), EXPNT%(1024,2)
130 NPX%=440: NSX%=130: NPY%=130: NSY%=60: GOSUB 5040
140 DEF FNX%(I%,K%)=PEEK((K%-1)*PNTMAX%+I%-1)
150 DEF FNRD$(I%,K%)=HEX$(INT(FNX%(I%,K%)/16))+HEX$(FNX%(I%,K%) MOD 16)
160 DEF FNTB(I%)=(FNX%(I%,1)+256!*(FNX%(I%,2)+256!*FNX%(I%,3)))/RTCF
170 DEF FNTP(I%)=(FNX%(I%,4)+(FNX%(I%,5) MOD 16)*256!)*4096/RTCF
180 DEF FNTG(I%)=(INT(FNX%(I%,5)/16)+FNX%(I%,6)*16!)/GTCF
190 DEF FNZC%(I%)=FNX%(I%,7)+(FNX%(I%,8) MOD 16)*256!
200 DEF FNPU(I%)=GDAT(1)+GDAT(2)*(INT(FNX%(I%,8)/16)*256!+FNX%(I%,9))
210 DEF FNFD(I%)=FNZC%(I%)/2/FNTG(I%)
220 DEF FNU(I%)=GDAT(3)+GDAT(4)*FNFD(I%)
230 DEF FNCPT=.5*GDAT(19)*GDAT(6)^2*(1/GDAT(7)^2-1/GDAT(8)^2)
240 DEF FNPT(I%)=FNPU(I%)-FNCPT*(FNU(I%))^2
250 DEF FNYHAT(X)=A0+A1*X
260 DEF FNFT(T)=EXP(-T/RDAT(19))/RDAT(19)
270 DEF FNFTC(T)=1-EXP(-T/RDAT(19))
280 DEF FNT(X)=1/(1+B0*ABS(X))
290 DEF FNSBT(X)=((((B5*FNT(X)+B4)*FNT(X)+B3)*FNT(X)+B2)*FNT(X)+B1)*FNT(X)
300 DEF FNERF(X)=SGN(X)*(1-SQR(2/PG)*EXP(-X*X/2)*FNSBT(X))
310 DEF FNND(X,S)=EXP(-X*X/2/S/S)/S/SQR(2*PG)
320 DEF FNTM(T$)=60*VAL(MID$(T$,4,2))+VAL(RIGHT$(T$,2))
330 DEF FNLINIX%(X)=INT(NPX%*(X-XXMIN)/XNORM+.5)
340 DEF FNLINJY%(Y)=INT(NPY%*(Y-YYMIN)/YNORM+.5)
350 DEF FNLOGIX%(X)=INT(NPX%*LOG(X/XXMIN)/XNORM+.5)
360 DEF FNLOGJY%(Y)=INT(NPY%*LOG(Y/YYMIN)/YNORM+.5)
370 GDAT$(1)="PT Calibration Off-Set Constant [Pa]: "
380 GDAT$(2)="PT Calibration Slope Constant [Pa/bit]: "
390 GDAT$(3)="LDV Calibration Off-Set Constant [m/s]: "
400 GDAT$(4)="LDV Calibration Slope Constant [m/s Hz]: "
410 GDAT$(5)="Venturi Tube No.: "
420 GDAT$(6)="Venturi Section at LDV Focal Point [m^2]: "
430 GDAT$(7)="Venturi Section at the Throat Section [m^2]: "
440 GDAT$(8)="Upstream Station Duct Section [m^2]: "
450 GDAT$(9)="Maximum No. of Cavitation Events: "
460 GDAT$(10)="No. of Bubble Validation Fringes (0 if disabled): "
470 GDAT$(11)="EPS Frequency (0 if disabled): "
480 GDAT$(12)="EPS Duty Cycle Figure (0 if disabled): "
```

```
490 GDAT$(13)="Low-Pass Frequency [kHz]: "
500 GDAT$(14)="High-Pass Frequency [kHz]: "
510 GDAT$(15)="Bubble Threshold [mV]: "
520 GDAT$(16)="Particle Threshold [mV]: "
530 GDAT$(17)="Liquid Temperature [Celsius]: "
540 GDAT$(18)="Liquid Air Content [ppm]: "
550 GDAT$(19)="Liquid Density [kg/m^3]: "
560 GDAT$(20)="Focal Point Distance from C.S.M. Exit Section [mm]:"
570 GDAT$(21)="Photomultiplier Supply Voltage [V]: "
580 GDAT$(22)="Photomultiplier Field Stop Diameter [mm]: "
590 RDAT$(1)="Minimum No. of Zero Crossing for Data Validation: "
600 RDAT$(2)="Outlier Filtering Criterion in S.D.'s: "
610 RDAT$(3)="No. of Data Groups: "
620 RDAT$(4)="Doppler Frequency [Hz]: "
630 RDAT$(5)="Doppler Frequency S.D. [Hz]: "
640 RDAT$(6)="No. of Validated Particle Data: "
650 RDAT$(7)="Upstream Pressure [Pa]: "
660 RDAT$(8)="Upstream Pressure S.D. [Pa]: "
670 RDAT$(9)="Throat Velocity [m/s]: "
680 RDAT$(10)="Throat Velocity S.D. [m/s]: "
690 RDAT$(11)="B.L. Thickness Ratio: "
700 RDAT$(12)="Throat Pressure [Pa]: "
710 RDAT$(13)="Throat Pressure S.D. [Pa]: "
720 RDAT$(14)="Nuclei Concentration [1/m^3]: "
730 RDAT$(15)="Nuclei Concentration S.D. [1/m^3]: "
740 RDAT$(16)="No. of Cavitation Events: "
750 RDAT$(17)="Sample Volume [m^3]: "
760 RDAT$(18)="Sample Time [s]: "
770 RDAT$(19)="Mean Nuclei Arrival Time [s]: "
780 RDAT$(20)="Computed Value of CHI^2: "
790 RDAT$(21)="Expected Value of CHI^2: "
800 RDAT$(22)="CHI^2 Standard Deviation: "
810 '
820 ' Option Display
830 GOSUB 1070: FLROOT$="": FLNAME$="": DEF SEG=&H3000: ZCN%=1: FC=3
840 FOR K%=1 TO 9: FOR I%=1 TO PNTMAX%: POKE (K%-1)*PNTMAX%+I%-1,0: NEXT: NEXT
850 PRINT: PRINT"Select:"
860 PRINT" 0. Quit"
870 PRINT" 1. Load, Check & Store Raw Data from CSM Signal Processor"
880 PRINT" 2. Input & Reduce Raw Data from Disk Files, Store Reduced Data"
890 PRINT" 3. Input & Plot Reduced Data from Disk Files"
900 PRINT" 4. Generate Simulated Data"
910 PRINT" 5. List Disk Directory"
920 INPUT"Selection"; SEL%: IF SEL%=0 THEN 820
930 ON SEL% GOSUB 5710, 1110, 7630, 5070, 7260
940 '
950 PRINT: PRINT"Select:"
960 PRINT" 0. Quit"
970 PRINT" 1. Display Raw Data"
980 PRINT" 2. Store Raw Data on a Disk File"
990 PRINT" 3. Display Physical Data"
1000 PRINT" 4. Plot Physical Data"
1010 PRINT" 5. Reduce Data"
1020 PRINT" 6. Display Reduced Data"
1030 PRINT" 7. List Disk Directory"
```

```
1040 INPUT"Selection"; SEL%: IF SEL%=0 THEN 820
1050 ON SEL% GOSUB 1380, 1530, 1700, 5500, 1850, 2940, 7260: GOTO 950
1060 '
1070 ' Data Array Clearing
1080 FOR N%=4 TO RDAT%: RDAT(N%)=0: NEXT: FOR J%=1 TO SET%: FOR I%=1 TO PNTMAX%
1090 EXPNT%(I%,J%)=0: XX(I%,J%)=0: YY(I%,J%)=0: NEXT: NEXT: RETURN
1100 '
1110 ' Raw Data Input & Reduction, Reduced Data Storage from/to Disk Files
1120 CLS: PRINT"* Raw Data Input & Reduction, Reduced Data Storage": PRINT
1130 INPUT"Source Disk Drive <A/B>"; DRIVE$
1140 INPUT"File Name Root (null for single file input only)"; FLROOT$
1150 IF FLROOT$<>"" THEN 1200
1160 INPUT"Source File Name"; FLNAME$: GOSUB 1240
1170 INPUT;"Null to Continue, Any Key to Quit: ", RESP$
1180 IF RESP$<>"" THEN CLOSE: PRINT ELSE GOSUB 1330
1190 RETURN
1200 INPUT"Initial & Final File Number"; FN%, FX%: GOSUB 7430
1210 FOR F%=FN% TO FX%: GOSUB 7480: FLNAME$=FLNAME$+".DAT": GOSUB 1240
1220 GOSUB 7360: GOSUB 1330: GOSUB 1850: NEXT: FLROOT$="": RETURN
1230 '
1240 ' Input Title, Comments & General Run Data from Disk Files
1250 CLS: PRINT"* Input Data from File: "; FLNAME$
1260 OPEN"I",1,DRIVE$+":"+FLNAME$: INPUT#1, TITLE$, COMM%
1270 PRINT: PRINT TITLE$: IF COMM%=0 THEN 1300
1280 PRINT: FOR N%=1 TO COMM%: INPUT#1, COMMENT$(N%): PRINT COMMENT$(N%): NEXT
1290 PRINT: GOSUB 7360
1300 PRINT: PRINT" General Run Data from File: ";: PRINT FLNAME$
1310 FOR N%=1 TO GDAT%:INPUT#1,GDAT(N%):PRINT GDAT$(N%);GDAT(N%):NEXT:RETURN
1320 '
1330 ' Input Raw Data from Disk Files
1340 FOR K%=1 TO 9: FOR J%=1 TO PNTMAX%/64: INPUT#1, X$: FOR L%=1 TO 64
1350 POKE (K%-1)*PNTMAX%+(J%-1)*64+L%-1,VAL("&H"+MID$(X$,2*L%-1,2)): NEXT: NEXT
1360 NEXT: CLOSE: PRINT: PRINT"Raw Data Input from Disk File Completed": RETURN
1370 '
1380 ' Raw Data Display
1390 CLS: PRINT"* Raw Data Display": PRINT
1400 SCR%=0: INPUT"kbyte No.: (zero to exit)"; K%: IF K%=0 THEN CLS: RETURN
1410 PRINT: FOR I%=1 TO PNTMAX%
1420 RD$=HEX$(INT(FNX%(I%,K%)/16))+HEX$(FNX%(I%,K%) MOD 16)
1430 IF (I% MOD 16)<>0 THEN PRINT USING"""; FNRD$(I%,K%); " ";
1440 IF (I% MOD 16)=0 THEN PRINT USING"""; FNRD$(I%,K%)
1450 IF (I% MOD 256)=0 OR I%=PNTMAX% THEN 1460 ELSE 1510
1460 SCR%=SCR%+1: PRINT: PRINT"Kbyte No.:"; K%, "Screen No.:"; SCR%;
1470 PRINT" (256 Data per Screen) Last Data Index:"; I%
1480 INPUT"Null to Continue, Any Key to Quit: ", RESP$
1490 IF RESP$<>"" THEN CLS: RETURN
1500 CLS: IF I%=PNTMAX% THEN 1400
1510 NEXT: CLS: RETURN
1520 '
1530 ' Raw Data Storage in a Disk File
1540 CLS: PRINT"* Raw Data Storage in a Disk File": PRINT
1550 INPUT"Storage File Name"; FLNAME$: INPUT"Storage Disk Drive <A/B>"; DRIVE$
1560 GOSUB 7290: GOSUB 7310: GOSUB 7170
1570 OPEN "O",1,DRIVE$+":"+FLNAME$: GOSUB 1600: GOSUB 1650: CLOSE
1580 PRINT"Raw Data Storage in a Disk File Completed": RETURN
```

```
1590 '
1600 ' Title, Comments & General Run Data Writing on a Disk File
1610 PRINT #1, TITLE$; ",";  COMM%;
1620 IF COMM%<>0 THEN FOR N%=1 TO COMM%: PRINT#1, COMMENT$(N%); ",";: NEXT
1630 FOR N%=1 TO GDAT%: PRINT#1, GDAT(N%);: NEXT: RETURN
1640 '
1650 ' Raw Data Writing on a Disk File
1660 FOR K%=1 TO 9: FOR J%=1 TO PNTMAX%/64: X$="": FOR L%=1 TO 64
1670 I%=(J%-1)*64+L%: X$=X$+HEX$(INT(FNX%(I%,K%)/16))+HEX$(FNX%(I%,K%) MOD 16)
1680 NEXT: PRINT#1, X$; ",";: NEXT: NEXT: RETURN
1690 '
1700 ' Physical Data Display
1710 CLS: PRINT"* Physical Data Display": PRINT: PG%=PNTMAX%/16: FOR P%=1 TO PG%
1720 PRINT" Tb [s] Pu [Pa] Tp [s] Tg [s] ZC";
1730 PRINT" I": PRINT: FOR Q%=1 TO 16: I%=(P%-1)*16+Q%
1740 IF EXPNT%(I%,2)<>0 THEN PRINT "*"; ELSE PRINT " ";
1750 PRINT USING"##.######^^^^"; FNTB(I%);
1760 IF EXPNT%(I%,1)<>0 THEN PRINT " *"; ELSE PRINT " ";
1770 PRINT USING"##.######^^^^"; FNPU(I%); FNTP(I%); FNTG(I%);
1780 PRINT USING"#### "; FNZC%(I%);: PRINT USING"####"; I%
1790 NEXT: PRINT: PRINT"Page No."; P%; "of"; PG%; " (16 x 5 Data per Page) ";
1800 PRINT"Stars mark excluded data"
1810 INPUT"Null to Continue, Any Key to Quit: ", RESP$
1820 CLS: IF RESP$<>"" THEN RETURN
1830 NEXT: PRINT"Physical Data Display Completed": RETURN
1840 '
1850 ' Data Reduction
1860 CLS: PRINT"* Data Reduction": PRINT: IF FLROOT$="" THEN GOSUB 7430
1870 GOSUB 1070: ZCN%=1: FC=10: DAT%=1: GOSUB 4960: GOSUB 6070
1880 PRINT"* Zero Crossing Validation and Data Filtering": FOR I%=1 TO PNTMAX%
1890 IF FNZC%(I%)<ZCN% OR FNTG(I%)=0 THEN EXPNT%(I%,1)=1 ELSE EXPNT%(I%,1)=0
1900 NEXT: DAT%=3: GOSUB 4960: RDAT(4)=YBAR:RDAT(5)=YSD:RDAT(6)=NY%: GOSUB 6070
1910 DAT%=4: GOSUB 4960: RDAT(6)=NY%: RDAT(7)=YBAR: RDAT(8)=YSD: GOSUB 6070
1920 IF ZCN%<>RDAT(1) OR FC<>RDAT(2) THEN ZCN%=RDAT(1): FC=RDAT(2): GOTO 1880
1930 IF FLROOT$="" THEN 1940 ELSE 2020
1940 PRINT: PRINT"Current Minimum No. of Zero Crossings: "; ZCN%
1950 PRINT"Current Outlier Filtering Criterion in S.D.'s: "; FC
1960 PRINT: INPUT"Minimum No. of Zero Crossings (0 to exit): ", ZCN%
1970 IF ZCN%=0 THEN 2020 ELSE RDAT(1)=ZCN%
1980 INPUT"Outlier Filtering Criterion in S.D.'s: ", FC
1990 IF FC=0 THEN FC=3
2000 RDAT(2)=FC: CLS: GOTO 1880
2010 '
2020 ' Filtered Data Distribution Plotting & Statistics Display
2030 GRP%=RDAT(3): FOR DAT%=3 TO 5: GOSUB 6600: PRINT: GOSUB 7360: NEXT
2040 '
2050 ' Computation of Potential Core Velocity, S.D. & B.L. Thickness Ratio
2060 CLS: PRINT"* Fitting of the Velocity Probability Density Distribution"
2070 RDAT(21)=GRP%-1: RDAT(22)=SQR(2*(GRP%-1))
2080 T1=-.01: T=0: V0=YBAR: S0=YSD: D0=0: SF=NY%*(XX(2,1)-XX(1,1))
2090 GOSUB 2190: RMSE0=RMSE: GM0=GM: IF YSF1>=0 OR S0/V0<.01 THEN 2330
2100 PRINT: PRINT" RMSE"," -grad RMSE-"," V [m/s]"," Sv [m/s]"," delta/R"
2110 FOR I%=1 TO 20: T=0: GOSUB 2190
2120 PRINT USING"##.######^^^^"; RMSE, GM/GRP%/RMSE, V, S, D
2130 IF ABS(RMSE-RMSE0)<.0001 AND GM<.01*GM0 THEN 2330 ELSE RMSE0=RMSE
```

```
2140 R1=G1/GM: R2=G2/GM: R3=G3/GM: F0=G1*R1+G2*R2+G3*R3: T=T1: GOSUB 2190
2150 F=G1*R1+G2*R2+G3*R3: T1=-T*(F+F0)/2/(F-F0): T=T+T1: V0=V0+T*R1: S0=S0+T*R2
2160 D0=D0+T*R3: T1=-ABS(T1/2)
2170 NEXT: PRINT: GOSUB 7360: GOTO 2100
2180 '
2190 ' Computation of Quadratic Error Sum and Gradients
2200 G1=0: G2=0: G3=0: QE=0: RDAT(20)=0: V=V0+T*R1: S=S0+T*R2: D=D0+T*R3
2210 FOR N%=1 TO GRP%: U=(XX(N%+1,1)+XX(N%,1))/2: GOSUB 2260
2220 DEV=SF*FU-YY(N%+1,1): G1=G1+DEV*SF*FUV: G2=G2+DEV*SF*FUS: G3=G3+DEV*SF*FUD
2230 IF T=0 THEN QE=QE+DEV*DEV: RDAT(20)=RDAT(20)+DEV*DEV/SF/FU
2240 NEXT: RMSE=SQR(QE/GRP%): GM=SQR(G1*G1+G2*G2+G3*G3): RETURN
2250 '
2260 ' Computation of Velocity Probability Density and Gradients
2270 NDU=FNND(U,S): NDUV=FNND(U-V,S): ERFU=FNERF(U/S): ERFUV=FNERF((U-V)/S)
2280 TMP=3/V/V/V*((U*U+S*S)/2*(ERFU-ERFUV)-S*S*(V+U)*NDUV+U*S*NDU): FUD=TMP-NDUV
2290 FU=D*TMP+(1-D)*NDUV: FUV=3*D/V*(NDUV-TMP)-(1-D)*(V-U)/S/S*NDUV
2300 FUS=3*D/V/V/V*(S*(ERFU-ERFUV)-V*(2*S*S+V*(V-U))/S*NDUV)
2310 FUS=FUS+(1-D)/S*(((V-U)/S)^2-1)*NDUV: RETURN
2320 '
2330 ' Computation of Throat Pressure Average & S.D.
2340 RDAT(9)=V0: RDAT(10)=S0: RDAT(11)=D0
2350 RDAT(12)=RDAT(7)-FNCPT*(RDAT(9)^2+RDAT(10)^2)
2360 RDAT(13)=SQR(RDAT(8)^2+2*(FNCPT*RDAT(10))^2*(2*RDAT(9)^2+RDAT(10)^2))
2370 '
2380 ' Plotting of Observed and Expected Velocity Density Distributions
2390 TITLE$="Observed & Expected Velocity Density Distributions"
2400 YNAME$="n(U) ": YUNIT$="": XNAME$="U ": XUNIT$=" [m/s]"
2410 FOR N%=1 TO GRPMAX%+1
2420 XX(N%,2)=XX(1,1)+(N%-1)*(XX(GRP%+1,1)-XX(1,1))/GRPMAX%
2430 U=XX(N%,2): V=V0: S=S0: D=D0: GOSUB 2260: YY(N%,2)=SF*FU: NEXT:INCSET%(1)=1
2440 INCSET%(2)=1: PNT%(2)=GRPMAX%+1: SYMBMAP%(2)=2: GOSUB 6760: PRINT
2450 FOR N%=8 TO 10:PRINT RDAT$(N%);:PRINT USING"##.######^^^^";RDAT(N%):NEXT
2460 FOR N%=19 TO 22:PRINT RDAT$(N%);:PRINT USING"##.######^^^^";RDAT(N%):NEXT
2470 PRINT: GOSUB 7360
2480 '
2490 ' Plotting of Particle, Bubble & Validated Bubble Time Data
2500 DAT%=7: GOSUB 6070: DAT%=8: GOSUB 6960: GOSUB 6350: GOSUB 6070
2510 '
2520 ' Computation of Intervals between Cavitation Events
2530 T1=0: FOR I%=1 TO PNTMAX%: IF EXPNT%(I%,2)<>0 THEN 2550
2540 TAU=YY(I%,2)-T1: T1=YY(I%,2): YY(I%,2)=TAU: XX(I%,2)=I%
2550 NEXT: RDAT(18)=T1: K%=2: GOSUB 4810
2560 '
2570 ' Computation of the Unstable Nuclei Concentration
2580 RDAT(16)=NY%+1: RDAT(19)=YBAR: RDAT(17)=GDAT(6)*RDAT(9)*RDAT(18)
2590 RDAT(14)=RDAT(16)/RDAT(17): RDAT(15)=SQR(RDAT(16))/RDAT(17)
2600 '
2610 ' Computation of Observed and Expected Cavitation Occurrence Frequencies
2620 TAUMAX=5*RDAT(19): XX(1,2)=0: XX(GRP%+1,2)=TAUMAX: K%=2: GOSUB 6860
2630 FOR N%=1 TO GRP%: YY(N%+1,1)=NY%*(FNFTC(XX(N%+1,2))-FNFTC(XX(N%,2))): NEXT
2640 '
2650 ' Computation of CHI^2 Variable for Test of Agreement
2660 RDAT(20)=0: RDAT(21)=GRP%-1: RDAT(22)=SQR(2*(GRP%-1)): RDAT(3)=GRP%
2670 FOR N%=2 TO GRP%+1: RDAT(20)=RDAT(20)+(YY(N%,2)-YY(N%,1))^2/YY(N%,1): NEXT
2680 '
```

```
2690 ' Plotting Observed & Expected Cavitation Delay Time Density Distributions
2700 TITLE$="Observed & Expected Cavitation Delay Time Density Distributions"
2710 YNAME$=" N(t)": YUNIT$="": XNAME$="t ": XUNIT$=" [s]"
2720 INCSET%(1)=1: PNT%(1)=GRPMAX%+1: SYMBMAP%(1)=2: FOR N%=1 TO GRPMAX%+1
2730 XX(N%,1)=XX(1,2)+(N%-1)*(XX(GRP%+1,2)-XX(1,2))/GRPMAX%
2740 YY(N%,1)=NY%*FNFT(XX(N%,1))*TAUMAX/GRP%: NEXT
2750 XXMIN=XX(1,2): XXMAX=XX(GRP%+1,2): YYMIN=0: YYMAX=0: GOSUB 6760
2760 PRINT: GOSUB 7360
2770 '
2780 ' Display & Optional Storage of Reduced Data
2790 GOSUB 2940: IF FLROOT$<>"" THEN GOSUB 7530: GOTO 2820
2800 PRINT: INPUT"Null to Store Data on a Disk File, Any Key to Exit: ", RESP$
2810 IF RESP$="" THEN GOSUB 7530
2820 FC=3: PRINT: RETURN
2830 '
2840 ' General Run Data Input
2850 CLS: PRINT"* Enter General Run Data:": PRINT
2860 PRINT"Null to Accept Current Value, Any Key to Change It: "
2870 FOR N%=1 TO GDAT%: PRINT GDAT$(N%); GDAT(N%);: INPUT"", RESP$
2880 IF RESP$="" THEN 2890 ELSE INPUT"Enter New Value: ", GDAT(N%)
2890 NEXT: INPUT"Null to Exit, Any Key to Save General Data: ", RESP$
2900 IF RESP$="" THEN RETURN
2910 OPEN"O",1,"GDFILE.DAT": FOR N%=1 TO GDAT%: PRINT#1, GDAT(N%);: NEXT
2920 CLOSE: PRINT"General Data Storage in a Disk File Completed": RETURN
2930 '
2940 ' Display of Reduced Data & General Run Data
2950 CLS: PRINT"* Reduced Data from File: ";: PRINT FLNAME$
2960 FOR N%=1 TO RDAT%: PRINT RDAT$(N%); RDAT(N%): NEXT: GOSUB 7360: RETURN
2970 CLS: PRINT"* General Run Data from File: ";: PRINT FLNAME$
2980 FOR N%=1 TO GDAT%: PRINT GDAT$(N%); GDAT(N%): NEXT: RETURN
2990 '
3000 ' Diagram Display
3010 IF XXMIN<>XXMAX THEN 3020 ELSE AUTOXMINMAX%=1: GOSUB 4250
3020 IF YYMIN<>YYMAX THEN 3110 ELSE AUTOYMINMAX%=1
3030 SWAP AUTOXMINMAX%, AUTOYMINMAX%: SWAP LINX%, LINY%
3040 SWAP XXMIN, YYMIN: SWAP XXMAX, YYMAX
3050 FOR J%=1 TO SET%:FOR I%=1 TO PNT%(J%): SWAP XX(I%,J%),YY(I%,J%): NEXT:NEXT
3060 GOSUB 4250
3070 SWAP AUTOXMINMAX%, AUTOYMINMAX%: SWAP LINX%, LINY%
3080 SWAP XXMIN, YYMIN: SWAP XXMAX, YYMAX
3090 FOR J%=1 TO SET%:FOR I%=1 TO PNT%(J%): SWAP XX(I%,J%),YY(I%,J%): NEXT:NEXT
3100 '
3110 ' Definition of Plotting Coordinate Transformations
3120 IF LINX%=1 THEN XNORM=XXMAX-XXMIN ELSE XNORM=LOG(XXMAX/XXMIN)
3130 IF LINY%=1 THEN YNORM=YYMAX-YYMIN ELSE YNORM=LOG(YYMAX/YYMIN)
3140 '
3150 ' Drawing of Diagram Axes
3160 KEY OFF: SCREEN 2: CLS: LINE (NSX%,200-NSY%)-(NSX%+NPX%,200-NSY%-NPY%), , B
3170 '
3180 ' Drawing of Scale Points on the Axes
3190 IF LINX%=1 AND DLTX=0 THEN AUTODLTX%=1: DLTX=XNORM/2: DLTPX=DLTX: DOTX%=10
3200 IF LINX%<>1 AND DLTX=0 THEN AUTODLTX%=1:DLTX=10: DLTPX=DLTX: DOTX%=10
3210 IF LINY%=1 AND DLTY=0 THEN AUTODLTY%=1: DLTY=YNORM/2: DLTPY=DLTY: DOTY%=10
3220 IF LINY%<>1 AND DLTY=0 THEN AUTODLTY%=1:DLTY=10: DLTPY=DLTY: DOTY%=10
3230 IF LINX%=1 THEN IMAX%=INT(XNORM/DLTPX+.5): GOTO 3250
```

```
3240 SGNX%=SGN(XXMIN): IMAX%=INT(SGNX%*XNORM/LOG(DLTPX)+.5)
3250 FOR I%=0 TO IMAX%
3260 IF LINX%=1 THEN IX%=FNLINIX%(XXMIN+I%*DLTPX): GOTO 3290
3270 IF SGNX%>0 THEN IX%=FNLOGIX%(XXMIN*DLTPX^I%): GOTO 3290
3280 IX%=FNLOGIX%(XXMAX*DLTPX^I%)
3290 LINE (NSX%+IX%,200-NSY%)-(NSX%+IX%,200-NSY%+3)
3300 LINE (NSX%+IX%,200-NSY%-NPY%)-(NSX%+IX%,200-NSY%-NPY%-3): NEXT
3310 IF LINY%=1 THEN JMAX%=INT(YNORM/DLTPY+.5): GOTO 3330
3320 SIGNY%=SGN(YYMIN): JMAX%=INT(SIGNY%*YNORM/LOG(DLTPY)+.5)
3330 FOR J%=0 TO JMAX%
3340 IF LINY%=1 THEN JY%=FNLINJY%(YYMIN+J%*DLTPY): GOTO 3370
3350 IF SIGNY%>0 THEN JY%=FNLOGJY%(YYMIN*DLTPY^J%): GOTO 3370
3360 JY%=FNLOGJY%(YYMAX*DLTPY^J%)
3370 LINE (NSX%,200-NSY%-JY%)-(NSX%-5,200-NSY%-JY%)
3380 LINE (NSX%+NPX%,200-NSY%-JY%)-(NSX%+NPX%+5,200-NSY%-JY%): NEXT
3390 '
3400 ' Writing of Scale Values on the Axes
3410 IF LINX%=1 THEN IMAX%=INT(XNORM/DLTX+.5): GOTO 3430
3420 IMAX%=INT(SGNX%*XNORM/LOG(DLTX)+.5)
3430 FOR I%=0 TO IMAX%
3440 IF LINX%=1 THEN XXVAL=XXMIN+I%*DLTX: IX%=FNLINIX%(XXVAL): GOTO 3470
3450 IF SGNX%>0 THEN XXVAL=XXMIN*DLTX^I%: IX%=FNLOGIX%(XXVAL): GOTO 3470
3460 XXVAL=XXMAX*DLTX^I%: IX%=FNLOGIX%(XXVAL)
3470 LOCATE INT((200-NSY%)/8+1.5), INT((NSX%+IX%)/8-1.5)
3480 IF LINX%=1 THEN PRINT USING "##.##^^^^"; XXVAL;: GOTO 3500
3490 PRINT USING "##^^^^"; XXVAL;
3500 NEXT
3510 IF LINY%=1 THEN JMAX%=INT(YNORM/DLTY+.5): GOTO 3530
3520 JMAX%=INT(SIGNY%*YNORM/LOG(DLTY)+.5)
3530 FOR J%=0 TO JMAX%
3540 IF LINY%=1 THEN YYVAL=YYMIN+J%*DLTY: JY%=FNLINJY%(YYVAL): GOTO 3570
3550 IF SIGNY%>0 THEN YYVAL=YYMIN*DLTY^J%: JY%=FNLOGJY%(YYVAL): GOTO 3570
3560 YYVAL=YYMAX*DLTY^J%: JY%=FNLOGJY%(YYVAL)
3570 LOCATE INT((200-NSY%-JY%)/8+1), 1+INT(NSX%/8-10)
3580 IF LINY%=1 THEN PRINT USING "##.##^^^^"; YYVAL;: GOTO 3600
3590 PRINT USING "##^^^^"; YYVAL;
3600 NEXT
3610 '
3620 ' Drawing of Scale Dots in the Diagram
3630 FOR J%=0 TO JMAX%
3640 IF LINY%=1 THEN JY%=FNLINJY%(YYMIN+J%*DLTPY): GOTO 3670
3650 IF SIGNY%>0 THEN JY%=FNLOGJY%(YYMIN*DLTPY^J%): GOTO 3670
3660 JY%=FNLOGJY%(YYMAX*DLTPY^J%)
3670 FOR I%=0 TO IMAX%-1
3680 FOR IH%=1 TO DOTX%
3690 IF LINX%=1 THEN IX%=FNLINIX%(XXMIN+(I%+IH%/DOTX%)*DLTPX): GOTO 3720
3700 IF SGNX%>0 THEN IX%=FNLOGIX%(XXMIN*IH%*DLTPX^I%): GOTO 3720
3710 IX%=FNLOGIX%(XXMAX*IH%*DLTPX^I%)
3720 PSET (NSX%+IX%,200-NSY%-JY%): NEXT: NEXT: NEXT
3730 FOR I%=0 TO IMAX%
3740 IF LINX%=1 THEN IX%=FNLINIX%(XXMIN+I%*DLTPX): GOTO 3770
3750 IF SGNX%>0 THEN IX%=FNLOGIX%(XXMIN*DLTPX^I%): GOTO 3770
3760 IX%=FNLOGIX%(XXMAX*DLTPX^I%)
3770 FOR J%=0 TO JMAX%-1
3780 FOR JK%=1 TO DOTY%
```

```
3790 IF LINY%=1 THEN JY%=FNLINJY%(YYMIN+(J%+JK%/DOTY%)*DLTPY): GOTO 3820
3800 IF SIGNY%>0 THEN JY%=FNLOGJY%(YYMIN*JK%*DLTPY^J%): GOTO 3820
3810 JY%=FNLOGJY%(YYMAX*JK%*DLTPY^J%)
3820 PSET (NSX%+IX%,200-NSY%-JY%): NEXT: NEXT: NEXT
3830 '
3840 ' Drawing of Scale Dots along the Axes
3850 FOR I%=0 TO IMAX%-1
3860 FOR IH%=1 TO DOTX%
3870 IF LINX%=1 THEN IX%=FNLINIX%(XXMIN+(I%+IH%/DOTX%)*DLTPX): GOTO 3900
3880 IF SGNX%>0 THEN IX%=FNLOGIX%(XXMIN*IH%*DLTPX^I%): GOTO 3900
3890 IX%=FNLOGIX%(XXMAX*IH%*DLTPX^I%)
3900 PSET (NSX%+IX%,200-NSY%+1): PSET (NSX%+IX%,200-NSY%-NPY%-1): NEXT: NEXT
3910 FOR J%=0 TO JMAX%-1
3920 FOR JK%=1 TO DOTY%
3930 IF LINY%=1 THEN JY%=FNLINJY%(YYMIN+(J%+JK%/DOTY%)*DLTPY): GOTO 3960
3940 IF SIGNY%>0 THEN JY%=FNLOGJY%(YYMIN*JK%*DLTPY^J%): GOTO 3960
3950 JY%=FNLOGJY%(YYMAX*JK%*DLTPY^J%)
3960 LINE (NSX%-2,200-NSY%-JY%)-(NSX%-1,200-NSY%-JY%)
3970 LINE (NSX%+NPX%+2,200-NSY%-JY%)-(NSX%+NPX%+1,200-NSY%-JY%): NEXT: NEXT
3980 '
3990 ' Writing of Title & Variable Names
4000 LOCATE 22,10: PRINT TITLE$;
4010 LOCATE INT((200-NSY%)/8+2.5), INT((NSX%+NPX%*.8)/8+.5)
4020 PRINT XNAME$; " "; XUNIT$
4030 LOCATE INT((200-NSY%-NPY%)/8+3),1: PRINT YNAME$
4040 LOCATE INT((200-NSY%-NPY%)/8+3+2),1: PRINT YUNIT$
4050 '
4060 ' Diagram Drawing
4070 FOR J%=1 TO SET%: IF INCSET%(J%)=0 THEN 4130
4080 FOR I%=1 TO PNT%(J%): IF EXPNT%(I%,J%)<>0 THEN 4120
4090 IF LINX%=1 THEN IX%=FNLINIX%(XX(I%,J%)) ELSE IX%=FNLOGIX%(XX(I%,J%))
4100 IF LINY%=1 THEN JY%=FNLINJY%(YY(I%,J%)) ELSE JY%=FNLOGJY%(YY(I%,J%))
4110 ON SYMBMAP%(J%) GOSUB 4580, 4640, 4690
4120 NEXT
4130 NEXT
4140 '
4150 ' Reset of Automatically Selected Quantities
4160 IF AUTOXMINMAX%=1 THEN AUTOXMINMAX%=0: XXMIN=0: XXMAX=0
4170 IF AUTOYMINMAX%=1 THEN AUTOYMINMAX%=0: YYMIN=0: YYMAX=0
4180 IF AUTODLTX%=1 THEN AUTODLTX%=0: DLTX=0: DLTPX=0: DOTX%=0
4190 IF AUTODLTY%=1 THEN AUTODLTY%=0: DLTY=0: DLTPY=0: DOTY%=0
4200 '
4210 LOCATE 23,1
4220 PRINT" "
4230 GOSUB 7360: SCREEN 0: RETURN
4240 '
4250 ' Computation of XXMAX & XXMIN or YYMAX & YYMIN
4260 FOR J%=1 TO SET%: FOR I%=1 TO PNT%(J%)
4270 IF INCSET%(J%)=1 AND EXPNT%(I%,J%)=0 THEN 4290
4280 NEXT: NEXT
4290 XXMIN=XX(I%,J%): XXMAX=XX(I%,J%)
4300 FOR J%=1 TO SET%: IF INCSET%(J%)=0 THEN 4350
4310 FOR I%=1 TO PNT%(J%): IF EXPNT%(I%,J%)<>0 THEN 4340
4320 IF XX(I%,J%)<XXMIN THEN XXMIN=XX(I%,J%)
4330 IF XX(I%,J%)>XXMAX THEN XXMAX=XX(I%,J%)
```

```
4340 NEXT
4350 NEXT
4360 IF (XXMAX-XXMIN)>XXMIN*.0000001 AND (XXMAX-XXMIN)>XXMAX*.0000001 THEN 4390
4370 XXMIN=XXMIN-1: XXMAX=XXMAX+1
4380 '
4390 ' Round-off of XXMIN & XXMAX or YYMIN & YYMAX
4400 IF LINX%<>1 THEN 4470
4410 TEMPX=LOG(XXMAX-XXMIN)/LOG(10): RPOW=10^INT(TEMPX)
4420 IF INT(TEMPX)=TEMPX THEN RPOW=10^INT(TEMPX-1)
4430 XXMIN=RPOW*INT(XXMIN/RPOW)
4440 IF INT(XXMAX/RPOW)<>XXMAX/RPOW THEN XXMAX=RPOW*INT(XXMAX/RPOW+1)
4450 IF INT(XXMAX/RPOW)=XXMAX/RPOW THEN XXMAX=RPOW*INT(XXMAX/RPOW): RETURN
4460 '
4470 IF XXMIN*XXMAX<=0 THEN PRINT "Non Plottable Points: both >0 & <0": STOP
4480 IF XXMIN>0 THEN XXMIN=10^(INT(LOG(XXMIN)/LOG(10)))
4490 IF XXMAX>0 THEN 4500 ELSE 4520
4500 TEMPX=LOG(XXMAX)/LOG(10): XXMAX=10^(INT(TEMPX)+1)
4510 IF INT(TEMPX)=TEMPX THEN XXMAX=10^(INT(TEMPX))
4520 IF XXMIN<0 THEN 4530 ELSE 4550
4530 TEMPX=LOG(ABS(XXMIN))/LOG(10): XXMIN=-10^(INT(TEMPX)+1)
4540 IF INT(TEMPX)=TEMPX THEN XXMIN=-10^(INT(TEMPX))
4550 IF XXMAX<0 THEN XXMAX=-10^(INT(LOG(ABS(XXMAX))/LOG(10)))
4560 RETURN
4570 '
4580 ' Drawing of Points in the Diagram
4590 IF IX%<0 OR IX%>NPX% OR JY%<0 OR JY%>NPY% THEN 4620
4600 PRESET(NSX%+IX%,200-NSY%-JY%)
4610 DRAW "S4A0C1M-2,-1M+4,+0M-4,+1M+4,+0M-4,+1M+4,+0M-2,-1"
4620 RETURN
4630 '
4640 ' Draw of Curves in the Diagram
4650 IF ABS(JY%)>30000 THEN JY%=SGN(JY%)*30000
4660 IF I%<>1 THEN LINE (NSX%+IX%,200-NSY%-JY%)-(NSX%+IXO%,200-NSY%-JYO%)
4670 IXO%=IX%: JYO%=JY%: RETURN
4680 '
4690 ' Draw of Histograms in the Diagram
4700 IF ABS(JY%)>30000 THEN JY%=SGN(JY%)*30000
4710 IF I%=1 THEN IXO%=IX%: JYO%=JY%: GOTO 4790
4720 IF IXO%<0 AND IX%<=0 OR IXO%>=NPX% AND IX%>NPX% THEN 4790
4730 IF IXO%<0 AND IX%>0 AND IX%<=NPX% THEN IXO%=0: GOTO 4760
4740 IF IXO%<NPX% AND IXO%>=0 AND IX%>NPX% THEN IX%=NPX%: GOTO 4760
4750 IF IXO%<0 AND IX%>NPX% THEN IXO%=0: IX%=NPX%: GOTO 4760
4760 IF JY%>NPY% THEN JY%=NPY%
4770 IF JY%<0 THEN JY%=0
4780 LINE (NSX%+IXO%,200-NSY%-JYO%)-(NSX%+IX%,200-NSY%-JY%), , B: IXO%=IX%
4790 RETURN
4800 '
4810 ' Statistical Analysis
4820 NY%=0: SUMY#=0: SUMY2#=0: FOR I%=1 TO PNTMAX%
4830 IF EXPNT%(I%,K%)=0 THEN YMIN=YY(I%,K%): YMAX=YMIN: GOTO 4850
4840 NEXT: INPUT"All Data Excluded! Hit RETURN to Continue: ", RESP$: RETURN
4850 FOR I%=1 TO PNTMAX%: IF EXPNT%(I%,K%)<>0 THEN 4890
4860 IF YY(I%,K%)<YMIN THEN YMIN=YY(I%,K%)
4870 IF YY(I%,K%)>YMAX THEN YMAX=YY(I%,K%)
4880 NY%=NY%+1: SUMY#=SUMY#+YY(I%,K%): SUMY2#=SUMY2#+YY(I%,K%)*YY(I%,K%)
```

```
4890 NEXT: GOSUB 4900: GOSUB 4920: RETURN
4900 YBAR#=SUMY#/NY%: YSD#=SQR(ABS((SUMY2#-NY%*YBAR#*YBAR#)/(NY%-1)))
4910 YBAR=YBAR#: YSD=YSD#: RETURN
4920 YSF1=0: YSF2=0: FOR I%=1 TO PNTMAX%: IF EXPNT%(I%,K%)<>0 THEN 4940
4930 DEV=YY(I%,K%)-YBAR: YSF1=YSF1+DEV*DEV*DEV: YSF2=YSF2+DEV*DEV*DEV*DEV
4940 NEXT: YSF1=YSF1/YSD/YSD/YSD/NY%: YSF2=YSF2/YSD/YSD/YSD/YSD/NY%: RETURN
4950 '
4960 ' Data Filtering
4970 GOSUB 6960: GOSUB 4810: IF NY%=3 THEN RETURN
4980 DEV0=0: FOR I%=1 TO PNTMAX%: IF EXPNT%(I%,K%)<>0 THEN 5000
4990 DEV=ABS(YBAR-YY(I%,K%)): IF DEV>DEV0 THEN DEV0=DEV: I0%=I%
5000 NEXT: IF DEV0<=YSD*FC THEN GOSUB 4920: RETURN
5010 EXPNT%(I0%,K%)=1: NY%=NY%-1: SUMY#=SUMY#-YY(I0%,K%)
5020 SUMY2#=SUMY2#-YY(I0%,K%)*YY(I0%,K%): GOSUB 4900: GOTO 4980
5030 '
5040 ' General Data Input
5050 OPEN"I",1,"GDFILE.DAT":FOR N%=1 TO GDAT%:INPUT#1,GDAT(N%):NEXT:CLOSE:RETURN
5060 '
5070 ' Simulated Raw Data Generation & Testing
5080 CLS: PRINT" * Simulated Raw Data Generation and Testing": PRINT
5090 PRINT"Generate Original Physical Data and Derive Raw Data"
5100 RANDOMIZE TIMER: TB0=.00025: PU0=100000!: PU1=1000
5110 TP0=.001: FD0=500000!: FD1=400000!: ZC0%=0: ZC1%=20: TB=TB0: TP=TP0
5120 FOR I%=1 TO PNTMAX%: TB=TB-TB0*LOG(1-RND): TP=TP-TP0*LOG(1-RND): PU=0:FD=0
5130 N%=16: FOR J%=1 TO N%: PU=PU+RND: FD=FD+RND: NEXT: PU=PU0+PU1*PU/SQR(N%)
5140 FD=FD0-FD1*(FD/N%)^2: ZC%=ZC0%+ZC1%*RND: TG=ZC%/FD/2: TBB=0: TPP=0
5150 IF RND<RTHR THEN TBB=TB: TB=TB*NSR*RND
5160 IF RND<RTHR THEN PU=PU*NSR*RND
5170 IF RND<RTHR THEN TPP=TP: TP=TP*NSR*RND
5180 IF RND<RTHR THEN FD=FD*NSR*RND
5190 IF RND<RTHR THEN TG=TG*NSR*RND
5200 TTB=INT(TB*RTCF+.5): IF TTB>=2^24 THEN PRINT"Tb too large": STOP
5210 PPU=INT((PU-GDAT(1))/GDAT(2)+.5):IF PPU>2^12 THEN PRINT"Pu too large": STOP
5220 TTP=INT(TP*RTCF/4096+.5): IF TTP>=2^12 THEN PRINT"Tp too large": STOP
5230 TTG=INT(TG*GTCF+.5): IF TTG>=2^12 THEN PRINT"Tg too large": STOP
5240 ZZC%=ZC%: IF ZZC%>=2^12 THEN PRINT"ZC too large": STOP
5250 '
5260 ' Raw Data Storage in High Memory
5270 FOR K%=1 TO 9
5280 ON K% GOTO 5290, 5300, 5310, 5320, 5330, 5340, 5350, 5360, 5370
5290 X%=TTB MOD 256: GOTO 5380
5300 X%=INT(TTB/256) MOD 256: GOTO 5380
5310 X%=INT(TTB/256^2) MOD 256: GOTO 5380
5320 X%=TTP MOD 256: GOTO 5380
5330 X%=INT(TTP/256) MOD 16+(TTG MOD 16)*16: GOTO 5380
5340 X%=INT(TTG/16) MOD 256: GOTO 5380
5350 X%=ZZC% MOD 256: GOTO 5380
5360 X%=INT(ZZC%/256) MOD 16+(INT(PPU/256) MOD 16)*16: GOTO 5380
5370 X%=PPU MOD 256
5380 POKE (K%-1)*PNTMAX%+I%-1, X%: NEXT
5390 '
5400 ' Comparison of Original Test Data to Physical Data
5410 IF ABS(TB-FNTB(I%))>1/RTCF THEN PRINT"Tb inaccurate?": STOP
5420 IF ABS(PU-FNPU(I%))>1*GDAT(2) THEN PRINT"Pu inaccurate?": STOP
5430 IF ABS(TP-FNTP(I%))>4096/RTCF THEN PRINT"Tp inaccurate?": STOP
```

```
5440 IF ABS(TG-FNTG(I%))>1/GTCF THEN PRINT"Tg inaccurate?": STOP
5450 IF ABS(ZC%-FNZC%(I%))>1 THEN PRINT"ZC inaccurate?": STOP
5460 IF TBB<>0 THEN TB=TBB
5470 IF TPP<>0 THEN TP=TPP
5480 NEXT: PRINT"Physical Data Conform to Original Test Data": RETURN
5490 '
5500 ' Physical Data Plotting
5510 CLS: PRINT"* Physical Data Plotting"
5520 PRINT: PRINT"Select:"
5530 PRINT" 0. Exit"
5540 PRINT" 1. Plot Data v/s Data Index"
5550 PRINT" 2. Plot Data Frequency Distribution"
5560 INPUT"Selection"; SEL%: IF SEL%=0 THEN RETURN
5570 GOSUB 5600: IF SEL%=1 THEN GOSUB 5680
5580 INPUT"Selection"; DAT%: IF DAT%=0 THEN RETURN
5590 ON SEL% GOSUB 6070, 6600: GOTO 5570
5600 PRINT: PRINT"Select:"
5610 PRINT" 0. Exit"
5620 PRINT" 1. Particle Zero Crossing"
5630 PRINT" 2. Particle Gate Time"
5640 PRINT" 3. Particle Doppler Frequency"
5650 PRINT" 4. Upstream Pressure"
5660 PRINT" 5. Velocity"
5670 PRINT" 6. Throat Pressure": RETURN
5680 PRINT" 7. Particle Occurrence Time"
5690 PRINT" 8. Bubble Occurrence Time": RETURN
5700 '
5710 ' Sequential Loading, Checking & Storage of Raw Data
5720 CLS: PRINT"* Sequential Loading, Checking & Storage of Raw Data": PRINT
5730 INPUT"File Name Root (null for single data set loading only)"; FLROOT$
5740 IF FLROOT$="" THEN 5770
5750 INPUT"Initial & Maximum Final File Number"; FN%, FX%
5760 INPUT"Storage Disk Drive <A/B>"; DRIVE$
5770 GOSUB 7170: IF FLROOT$="" THEN GOSUB 5860: RETURN ELSE GOSUB 7310
5780 FOR F%=FN% TO FX%: GOSUB 7480: FLNAME$=FLNAME$+".TDT"
5790 PRINT: PRINT"File: "; FLNAME$: GOSUB 5860
5800 SEL%=1: DAT%=3: GOSUB 6070: GOSUB 7290
5810 INPUT"Null to Accept Data for Storage, Any Key to Reject: ", RESP$
5820 IF RESP$<>"" THEN F%=F%-1 ELSE GOSUB 1570
5830 PRINT: INPUT"Null to Recycle, Any Key to Exit: ", RESP$
5840 IF RESP$<>"" THEN RETURN
5850 NEXT: PRINT"File Numbering Capacity Exeeded": RETURN
5860 DEF SEG: GOSUB 5900: PRINT"UNLOAD Raw Data from CSM Signal Processor"
5870 DEF SEG=&H2F00: DEF USR0=0: A=USR0(0): DEF SEG=&H3000: B=0
5880 PRINT"Raw Data Input from LDV Signal Processor Completed": RETURN
5890 '
5900 ' Initializing the 8250
5910 OUT 1019,128 'Set line control register(3FBH) bit 7 high(80H)
5920 OUT 1016,12 'Set baud rate to 9600 3F8H=0CH
5930 OUT 1017,0 '3F9H=00H
5940 OUT 1019,3 'Set line control register parity disabled,
5950 ' 1 stop bit and 8-bit word
5960 OUT 1020,3 'Set modem control (Probably not needed but safe)
5970 OUT 1017,0 'Disable interrupt generation by 8250(3F9H)
5980 RETURN
```

```
5990 '
6000 ' Machine Language Subroutine for Data Input
6010 DEF SEG=&H2F00: FOR I%=0 TO 46: READ J%: POKE I%, J%: NEXT
6020 DATA 252,30,6,184,0,48,142,192,186,253,3,191,0,0,185
6030 DATA 255,35,236,168,1,116,251,186,248,3,236,144,144,144,144
6040 DATA 144,144,144,170,73,227,5,186,253,3,235,231,7,31,251,203,0
6050 RETURN
6060 '
6070 ' Data Plotting
6080 FOR J%=1 TO SET%: INCSET%(J%)=0: PNT%(J%)=PNTMAX%
6090 FOR I%=1 TO PNTMAX%: XX(I%,J%)=I%: NEXT: NEXT: XXMIN=0: XXMAX=PNTMAX%
6100 GOSUB 6960: INCSET%(K%)=1: SYMBMAP%(K%)=1
6110 ON DAT% GOTO 6120, 6140, 6170, 6190, 6210, 6250, 6280, 6310
6120 TITLE$="Number of Zero Crossings v/s Data Index"
6130 YNAME$=" ZC ": YUNIT$=" ": XNAME$="I": XUNIT$="": GOTO 6160
6140 TITLE$="Particle Gate Time Data v/s Data Index"
6150 YNAME$=" Tg ": YUNIT$=" [s] ": XNAME$="I": XUNIT$=""
6160 YYMIN=0: YYMAX=0: LINX%=1: LINY%=0: GOTO 6330
6170 TITLE$="Doppler Frequency v/s Data Index"
6180 YNAME$=" Fd": YUNIT$=" [Hz]": XNAME$="I": XUNIT$="": GOSUB 4810: GOTO 6230
6190 TITLE$="Upstream Pressure v/s Data Index"
6200 YNAME$=" Pu": YUNIT$=" [Pa]": XNAME$="I": XUNIT$="": GOSUB 4810: GOTO 6230
6210 TITLE$="Velocity v/s Data Index"
6220 YNAME$=" U": YUNIT$=" [m/s]": XNAME$="I": XUNIT$="": GOSUB 4810
6230 YYMIN=0: YYMAX=2*YBAR
6240 LINX%=1: LINY%=1: GOTO 6330
6250 TITLE$="Throat Pressure v/s Data Index"
6260 YNAME$=" Pt": YUNIT$=" [Pa] ": XNAME$="I": XUNIT$="": GOSUB 4810
6270 YYMIN=YBAR-5*YSD: YYMAX=YBAR+5*YSD: GOTO 6240
6280 TITLE$="Particle Time Data v/s Data Index"
6290 YNAME$=" Tp": YUNIT$=" [s]": XNAME$="I": XUNIT$=""
6300 GOSUB 4810: YYMIN=0: YYMAX=3*YBAR: GOTO 6240
6310 TITLE$="Bubble Time Data v/s Data Index"
6320 YNAME$=" Tb": YUNIT$=" [s]": XNAME$="I": XUNIT$="": GOTO 6300
6330 GOSUB 3000: RETURN
6340 '
6350 ' Bubble Time Data Validation
6360 CLS: PRINT"* Bubble Time Data Validation"
6370 NY%=0: SUMX#=0: SUMY#=0: SUMX2#=0: SUMY2#=0: SUMXY#=0
6380 FOR I%=1 TO PNTMAX%: IF EXPNT%(I%,K%)<>0 THEN 6410
6390 SUMX#=SUMX#+XX(I%,K%): SUMY#=SUMY#+YY(I%,K%): SUMX2#=SUMX2#+XX(I%,K%)^2
6400 SUMY2#=SUMY2#+YY(I%,K%)^2: SUMXY#=SUMXY#+XX(I%,K%)*YY(I%,K%): NY%=NY%+1
6410 NEXT
6420 A1=(SUMXY#-SUMX#*SUMY#/NY%)/(SUMX2#-SUMX#*SUMX#/NY%)
6430 XBAR=SUMX#/NY%: YBAR=SUMY#/NY%: A0=YBAR-A1*XBAR
6440 SIGMA=(SUMY2#+NY%*A0^2+SUMX2#*A1^2-2*(A0*SUMY#+A1*SUMXY#-A0*A1*SUMX#))/NY%
6450 SIGMA=SQR(SIGMA): DEV0=0: YYL=0: YYU=2*FNYHAT(XX(PNTMAX%,K%))
6460 FOR I%=1 TO PNTMAX%: IF EXPNT%(I%,K%)<>0 THEN 6550
6470 IF I%=1 THEN YYL=0: GOTO 6500
6480 FOR IL%=I%-1 TO 1 STEP -1:IF EXPNT%(IL%,K%)=0 THEN YYL=YY(IL%,K%):GOTO 6500
6490 NEXT IL%: YYL=0
6500 IF I%=PNTMAX% THEN YYU=2*FNYHAT(XX(PNTMAX%,K%)): GOTO 6530
6510 FOR IU%=I%+1 TO PNTMAX%: IF EXPNT%(IU%,K%)=0 THEN YYU=YY(IU%,K%): GOTO 6530
6520 NEXT IU%: YYU=2*FNYHAT(XX(PNTMAX%,K%))
6530 IF YY(I%,K%)>=YYL AND YY(I%,K%)<=YYU THEN 6550
```

```
6540 DEV=ABS(FNYHAT(XX(I%,K%))-YY(I%,K%)):IF DEV>DEV0 THEN DEV0=DEV:I0%=I%
6550 NEXT I%: IF DEV0=0 OR NY%=3 THEN RETURN
6560 EXPNT%(I0%,K%)=1: SUMX#=SUMX#-XX(I0%,K%): SUMY#=SUMY#-YY(I0%,K%)
6570 SUMX2#=SUMX2#-XX(I0%,K%)^2: SUMY2#=SUMY2#-YY(I0%,K%)^2
6580 SUMXY#=SUMXY#-XX(I0%,K%)*YY(I0%,K%): NY%=NY%-1: GOTO 6420
6590 '
6600 ' Plotting of Frequency Density Distributions
6610 ON DAT% GOTO 6620, 6640, 6660, 6680, 6700, 6720
6620 TITLE$="Zero Crossing Density Distribution"
6630 YNAME$="n(ZC)": YUNIT$="": XNAME$="ZC": XUNIT$="": GOTO 6740
6640 TITLE$="Particle Gate Time Density Distribution"
6650 YNAME$="n(Tg)": YUNIT$="": XNAME$="Tg ": XUNIT$="[s]": GOTO 6740
6660 TITLE$="Doppler Frequency Density Distribution"
6670 YNAME$="n(Fd)": YUNIT$="": XNAME$="Fd ": XUNIT$="[Hz]": GOTO 6740
6680 TITLE$="Upstream Pressure Density Distribution"
6690 YNAME$="n(Pu)": YUNIT$="": XNAME$="Pu ": XUNIT$="[Pa]": GOTO 6740
6700 TITLE$="Measured Velocity Density Distribution"
6710 YNAME$="n(U)": YUNIT$="": XNAME$="U ": XUNIT$="[m/s]": GOTO 6740
6720 TITLE$="Throat Pressure Density Distribution"
6730 YNAME$="n(Pt)": YUNIT$="": XNAME$="Pt ": XUNIT$="[Pa]"
6740 GOSUB 4960: XX(1,K%)=YBAR-FC*YSD: XX(GRP%+1,K%)=YBAR+FC*YSD
6750 XXMIN=XX(1,K%): XXMAX=XX(GRP%+1,K%): GOSUB 6860: YYMIN=0: YYMAX=0
6760 FOR J%=1 TO SET%: FOR N%=1 TO GRPMAX%+1: SAVEX%(N%,J%)=EXPNT%(N%,J%)
6770 EXPNT%(N%,J%)=0: NEXT: NEXT: LINX%=1: LINY%=1: GOSUB 3000
6780 FOR J%=1 TO SET%: INCSET%(J%)=0: FOR N%=1 TO GRPMAX%+1
6790 EXPNT%(N%,J%)=SAVEX%(N%,J%): NEXT: NEXT
6800 CLS: PRINT"* Statistical Parameters:": PRINT:
6810 PRINT"Mean Value: ";: PRINT USING"##.######^^^^"; YBAR
6820 PRINT"Standard Deviation: ";: PRINT USING"##.######^^^^"; YSD
6830 PRINT"Number of Data: "; NY%: PRINT"1st Shape Factor: "; YSF1
6840 PRINT"2nd Shape Factor: "; YSF2: RETURN
6850 '
6860 ' Frequency Density Distribution Computation
6870 FOR N%=1 TO GRP%: OF%(N%)=0
6880 XX(N%,K%)=XX(1,K%)+(XX(GRP%+1,K%)-XX(1,K%))*(N%-1)/GRP%: NEXT
6890 FOR I%=1 TO PNTMAX%: IF EXPNT%(I%,K%)<>0 THEN 6930
6900 NM%=1: NX%=GRP%+1: IF YY(I%,K%)=XX(1,K%) THEN OF%(1)=OF%(1)+1
6910 N%=INT((NM%+NX%)/2): IF YY(I%,K%)>XX(N%,K%) THEN NM%=N% ELSE NX%=N%
6920 IF NX%<>NM%+1 THEN 6910 ELSE OF%(NM%)=OF%(NM%)+1
6930 NEXT: YY(1,K%)=0: PNT%(K%)=GRP%+1: INCSET%(K%)=1: SYMBMAP%(K%)=3
6940 FOR N%=1 TO GRP%: YY(N%+1,K%)=OF%(N%): NEXT: RETURN
6950 '
6960 ' Data Loading from High Memory in Auxiliary Arrays
6970 IF DAT%=8 THEN K%=2 ELSE K%=1
6980 FOR I%=1 TO PNTMAX%
6990 ON DAT% GOTO 7010, 7030, 7050, 7070, 7080, 7100, 7120, 7140
7000 XX(I%,K%)=I%: NEXT: RETURN
7010 YY(I%,K%)=FNZC%(I%): IF FNZC%(I%)<1 OR FNTG(I%)=0 THEN EXPNT%(I%,K%)=1
7020 GOTO 7000
7030 YY(I%,K%)=FNTG(I%): IF YY(I%,K%)¡=0 THEN EXPNT%(I%,K%)=1
7040 GOTO 7000
7050 IF FNTG(I%)<>0 THEN YY(I%,K%)=FNFD(I%) ELSE EXPNT%(I%,K%)=1
7060 GOTO 7000
7070 XX(I%,K%)=I%: YY(I%,K%)=FNPU(I%): GOTO 7000
7080 IF FNTG(I%)<>0 THEN YY(I%,K%)=FNU(I%) ELSE EXPNT%(I%,K%)=1
```

```
7090 GOTO 7000
7100 IF FNTG(I%)<>0 THEN YY(I%,K%)=FNPT(I%) ELSE EXPNT%(I%,K%)=1
7110 GOTO 7000
7120 YY(I%,K%)=FNTP(I%): IF YY(I%,K%)¡=0 THEN EXPNT%(I%,K%)=1
7130 GOTO 7000
7140 YY(I%,K%)=FNTB(I%): IF YY(I%,K%)¡=0 THEN EXPNT%(I%,K%)=1
7150 GOTO 7000
7160 '
7170 ' General Data Management
7180 PRINT: PRINT"Select:"
7190 PRINT" 0. Use General Run Data Previously Loaded"
7200 PRINT" 1. Read General Run Data from Disk File"
7210 PRINT" 2. Enter General Run Data"
7220 INPUT"Selection"; SSEL%: IF SSEL%<>0 THEN ON SSEL% GOSUB 5040, 2840
7230 GOSUB 2970: INPUT"Null to Continue, Any Key to Recycle: ", RESP$
7240 IF RESP$="" THEN RETURN ELSE CLS: GOTO 7170
7250 '
7260 ' Disk Directory Display
7270 PRINT: FILES: RETURN
7280 '
7290 ' File Title & Comment Input
7300 TITLE$="Cavitation Susceptibility Meter Data": RETURN
7310 PRINT: FOR COMM%=4 TO 10
7320 PRINT"Comment: (one line only; null to exit)": INPUT RESP$
7330 IF RESP$<>"" THEN COMMENT$(COMM%)=RESP$ ELSE COMM%=COMM%-1: RETURN
7340 NEXT
7350 '
7360 ' Program Execution Pause & Stop/Restart (if required)
7370 PRINT"Hit F1 to Stop ";: ON KEY (1) GOSUB 7390: KEY (1) ON
7380 TM0=FNTM(TIME$): WHILE FNTM(TIME$)-TM0¡3: WEND: GOTO 7400
7390 INPUT;"& RETURN to Restart: ", RESP$
7400 KEY (1) OFF: LOCATE ,1: PRINT" ";
7410 LOCATE ,1: RETURN
7420 '
7430 ' Input of Data Reduction Parameters
7440 CLS: PRINT"*Enter Data Reduction Parameters:": PRINT: GOSUB 1070
7450 FOR N%=1 TO 3: PRINT RDAT$(N%);: INPUT"", RDAT(N%): NEXT
7460 GRP%=RDAT(3): RETURN
7470 '
7480 ' File Name Generation
7490 RESP$=RIGHT$(STR$(F%),LEN(STR$(F%))-1)
7500 IF LEN(RESP$)=1 THEN RESP$=RIGHT$(STR$(0),1)+RESP$
7510 FLNAME$=FLROOT$+RESP$: RETURN
7520 '
7530 ' Reduced Data Storage in a Disk File
7540 CLS: PRINT: PRINT"*Reduced Data Storage in a Disk File": PRINT
7550 TITLE$="Reduced Data from File: "+FLNAME$
7560 IF FLNAME$<>"" THEN FLNAME$=LEFT$(FLNAME$,LEN(FLNAME$)-4)+".RDT": GOTO 7590
7570 INPUT"Storage File Name (null to skip storage)"; FLNAME$
7580 IF FLNAME$="" THEN RETURN
7590 PRINT"Storage File: "; FLNAME$: OPEN"O",1,DRIVE$+":"+FLNAME$: GOSUB 1600
7600 FOR N%=1 TO RDAT%: PRINT#1, RDAT(N%);: NEXT
7610 CLOSE: PRINT"Reduced Data Storage in a Disk File Completed": RETURN
7620 '
7630 ' Reduced Data Input & Plotting
```

```
7640 CLS: PRINT"*Reduced Data Input & Plotting": PRINT
7650 PRINT"Select y & x Plotting Variables:"
7660 FOR N%=4 TO RDAT%: PRINT" "; STR$(N%); ". "; RDAT$(N%): NEXT
7670 INPUT"Enter y & x Variable Index: ", YY%, XX%
7680 PRINT: INPUT"Source Disk Drive ¡A/B¿"; DRIVE$
7690 INPUT"File Name Root"; FLROOT$
7700 INPUT"Initial & Final File Number"; FN%, FX%
7710 C%=0: FOR F%=FN% TO FX%: C%=C%+1: GOSUB 7480: FLNAME$=FLNAME$+".RDT"
7720 GOSUB 1240: GOSUB 7360: FOR N%=1 TO RDAT%: INPUT#1, RDAT(N%): NEXT: CLOSE
7730 GOSUB 2940: XX(C%,1)=RDAT(XX%): YY(C%,1)=RDAT(YY%): EXPNT%(C%,1)=0
7740 INPUT"Enter 1 to Exclude Data, 0 to Accept: ", EXPNT%(C%,1): NEXT
7750 PRINT: PRINT"Reduced Data Input from Disk File Completed"
7760 INCSET%(1)=1: INCSET%(2)=0: SYMBMAP%(1)=1: PNT%(1)=C%
7770 X$=RDAT$(XX%): Y$=RDAT$(YY%): XNAME$="": XUNIT$="": YNAME$="": YUNIT$=""
7780 IF RIGHT$(X$,1)<>":" THEN X$=LEFT$(X$,LEN(X$)-1): GOTO 7780
7790 IF RIGHT$(Y$,1)<>":" THEN Y$=LEFT$(Y$,LEN(Y$)-1): GOTO 7790
7800 TITLE$=LEFT$(Y$,LEN(Y$)-1)+" v/s "+LEFT$(X$,LEN(X$)-1)
7810 PRINT: INPUT"Select Y-Axis Scale (0. Logarithmic, 1. Linear): ", LINY%
7820 INPUT"Enter Minimum, Maximum Y Values: ", YYMIN, YYMAX
7830 INPUT"Select X-Axis Scale (0. Logarithmic, 1. Linear): ", LINX%
7840 INPUT"Enter Minimum, Maximum X Values: ", XXMIN, XXMAX
7850 GOSUB 3000: INPUT"Null to exit, Any Key to Replot: ", RESP$
7860 IF RESP$<>"" THEN 7810 ELSE FLROOT$="": RETURN
```

Appendix 3

COMPARISON OF HOLOGRAPHIC AND COULTER COUNTER MEASUREMENTS OF CAVITATION NUCLEI IN THE OCEAN *

by Tim J. O'Hern, Luca d'Agostino and Allan J. Acosta
Department of Engineering and Applied Sciences
California Institute of Technology
Pasadena, California, 91125

1. ABSTRACT

Holographic and Coulter Counter detection techniques were jointly used to measure the concentration density distribution of cavitation nuclei in the ocean. Comparison of the two techniques indicates that Coulter Counter analysis underestimates the particulate content by up to an order of magnitude and may produce a distorted number concentration distribution. Several possible explanations of the observed discrepancies are proposed and discussed, including fundamental differences between the in situ holographic samples and the collected samples examined with the Coulter Counter, differences between the unknown electrical conductivity of the measured particles in the sea water samples and the non-conductive particles used to calibrate the Coulter Counter, the rupture of aggregate particles in the flow through the Coulter Counter orifice, the effect of electronic noise on the Coulter Counter signal, and the effect of statistical sampling error. The particle number concentration distributions decrease ap-

* submitted to the ASME Journal of Fluids Engineering on February 12, 1987.

proximately with the fourth power of the particle radius in the observed size range of 10 to 50 μm radius. Both sets of data indicate an increase in particle concentration near the bottom of the thermocline, and the holographic bubble concentrations also indicate a similar behavior. Much higher concentrations of particles were detected in the ocean, according to the holographic analysis, than in typical cavitation test facilities. Consideration of the static equilibrium of individual bubbles indicates that the average tensile strength of the ocean waters examined in this study is on the order of a few thousand Pascals, with a minimum expected value of about one hundred Pascals.

2. NOMENCLATURE

a	particle cross-sectional area
A	Coulter Counter orifice cross-sectional area
c	MCA channel index corresponding to calibration radius R_c
i, j	MCA channel index
l	particle length
L	Coulter Counter orifice length
$n(R)$	nuclei number concentration density distribution function
$N(R)$	concentration of nuclei with radius smaller than R
N_g	number of nuclei counts in each radius group
N_{tot}	total particle concentration in the measured radius range
ΔN	nuclei concentration in the radius range ΔR
p_o	bubble equilibrium external pressure
p_v	liquid vapor pressure
$(p_v - p)_{cr}$	bubble critical tension
R	particle radius
$\overline{R}$	nominal radius of each data group
R_c	radius of Coulter Counter calibration particles
R_i, R_j	particle radius corresponding to channel i, j of MCA
R_o	bubble equilibrium radius

ΔR	nuclei radius range about R
ΔR_{or}	change of Coulter Counter orifice electrical resistance
S	bubble surface tension
T	liquid temperature
V_p	particle volume
V_s	liquid sample volume
α, β	PSA calibration constants
σ	liquid electrical conductivity
σ'	particle electrical conductivity

3. INTRODUCTION

The maximum tensile stress of liquids is considerably reduced by the presence of weak spots, generically called nuclei, which act as preferential sites for the occurrence of liquid rupture. These nuclei have been the subject of considerable research effort, yet their exact nature and origin have not been firmly established. However, it has been recognized that bubbles, some kinds of solid particles and gas pockets inside crevices and cracks on the surface of particulates suspended in the liquid can act as cavitation nuclei and that their effect usually dominates that of the nuclei located at the liquid boundaries.

The presence of nuclei is particularly important in technical applications because they control the onset and the development of cavitation, which is a generally undesirable phenomenon due to the severe limitations it imposes on the overall performance of hydraulic operating machinery. The liquid characteristics which affect the occurrence of cavitation through their influence on the nuclei population are collectively called liquid quality. For the purpose of cavitation research the concentration of nuclei in the liquid and their dynamic behaviour when exposed to a change of pressure are thought to be of special importance in trying to predict cavitation inception and to deduce scaling laws capable of correlating the results from model test to full-scale operation. Not all the nuclei respond in the same way to a change of the surrounding pressure.

The dynamic properties of gas bubbles in mechanical equilibrium can be directly related to their size, so in this case the liquid quality is adequately described by the nuclei number concentration distribution as a function of bubble size. Traditionally the nuclei number concentration distribution has also been used in the literature to characterize the liquid quality even when the main source of nuclei is represented by particles, whose dynamic behaviour cannot be directly related to their geometry. In this case the size measurements of particulates contained in liquids still provides an upper limit for the concentration of potentially active cavitation nuclei. Significant efforts have been made to develop suitable methods of nuclei detection in liquids, based on various physical principles. In general the results obtained using these methods are in substantial qualitative agreement, but they often differ significantly under the quantitative point of view.

Ocean waters are known to contain the above nucleation agents as well as many others of organic origin. These waters represent a very interesting environment for cavitation research because of their great technical importance in various fields of applied sciences such as, for example, naval hydrodynamics, ship propulsion, underwater acoustics and optics. Detailed knowledge of the sea water liquid quality is essential for the simulation of marine conditions in the laboratory and for the scaling of model tests to prototype operation. However, relatively little is known about nuclei in marine environments because, due to the inherent experimental difficulties, there are not many reported studies in the literature on this subject. The various types of nuclei found in the ocean are of interdisciplinary interest far beyond cavitation, leading previous researchers to separately explore bubbles [see for example: Medwin, 1977; Thorpe, 1982], particles [Carder et al., 1982] and organisms [Pieper and Holliday, 1984]. A review of the work on nuclei detection in ocean waters pertaining to cavitation is included in Billet, 1985. In this paper we report the application and compare the results of two of these methods, namely holographic and Coulter Counter detection, to the monitoring and sizing of cavitation nuclei in the ocean.

4. HOLOGRAPHIC EXPERIMENTAL APPARATUS

The holographic investigation involves in situ optical recording of ocean water samples for later analysis and derivation of the size and concentration of both microbubbles and particulate matter. A sketch of the system used for recording Fraunhofer holograms of ocean water samples is depicted in Fig. 1, which shows a modified version of the system first described by Katz et al., 1984. Detailed descriptions of the Fraunhofer holographic process are available in several texts and articles (see for example Collier et al., 1971 and DeVelis et al., 1966) so only an elementary description will be given here. A pulsed ruby laser is used as the coherent light source for hologram recording. The laser is mounted inside a submersible hull with windows through which the expanded laser beam passes to illuminate an external water sample. Particles in the illuminated sample scatter a portion of the laser beam, while the remaining portion passes through the sample undiffracted. The hologram is a record of the pattern formed by interference of the diffracted and undiffracted laser light on a high resolution roll film (Agfa 10E75). Maximum submersion is presently limited to 33.5 m by the electrical cables controlling and monitoring the laser and associated equipment.

Holographic reconstruction is accomplished by illuminating the developed hologram with a collimated continuous wave He-Ne laser beam. The hologram acts as a diffraction grating to produce three-dimensional real and virtual images of the original volume. Measurements are made by using a closed circuit vidicon system to examine a highly magnified portion of the real image. The resolution is approximately 5 μm. Discrimination of bubbles from solid particulates is important in monitoring cavitation nuclei and is made by visually examining the focused bubble image for roundness, brightness, and presence of a dark central spot due to the focusing effect of the bubble geometry. No attempt is made to establish the nature of nuclei with radii smaller than 10 μm.

Holographic determination of nuclei size is made by focusing a 220X magni-

fied image of each nucleus on the reconstruction system monitor. At the focused plane, a major and minor diameter can be directly measured for non-circular objects. For purposes of comparison with the Coulter Counter results, the volume of the holographically detected particles is computed by assuming an ellipsoidal shape with the length of the third axis taken as the geometric mean of the two measured values, or, in cases of long thin objects, by assuming a cylindrical shape. The radius of a sphere of equal volume is then calculated.

5. COULTER COUNTER EXPERIMENTAL APPARATUS

The measurement of particulate matter in the sea water was carried out using the particle sizing and counting instrumentation of the Department of Environmental Engineering of the California Institute of Technology. This system includes a Model B Coulter Counter in conjunction with a Hewlett Packard 1208B oscilloscope, a Nuclear Data Particle Sizing Amplifier (PSA), a Multi-Channel Analyzer (MCA) for sorting of the signal amplitudes and a Teletype for output of the data. The apparatus is described in detail by Hunt, 1980. Here the principles of operation of the system and the procedure used for computing the particle size distributions are briefly reviewed to the extent needed for the interpretation of the results presented in this paper.

In the Coulter Counter a known volume of the sampled liquid is forced through a small orifice of known diameter in an electrically insulating medium. When an electric field is established in the conducting liquid across the orifice, inhomogeneities (here generally called particles regardless of their true nature) whose electrical resistivity is different from that of the surrounding liquid can be detected, counted and sized by the perturbation they induce in the electrical resistance across the orifice. The amplitude of the electrical signal is approximately proportional to the volume of the particle as long as its dimensions are less than about 40% of the orifice diameter. The signal amplitude also depends on the orifice diameter, electrical excitation, signal amplification and on the conductivities of the liquid and of the particle. Due to finite lower resolu-

tion, different electronic settings and orifice diameters are needed to measure relatively wide size distributions.

In the present apparatus the Coulter Counter pulse signal is amplified by the PSA, whose output is proportional to the logarithm of the volume of the sampled particle through two adjustable gain constants. The MCA then sizes the incoming pulses according to their amplitude and stores the corresponding counts in 128 separate channels. At the same time the MCA data are also displayed on the oscilloscope. During each run a preset volume of liquid is sampled. Data from multiple consecutive runs can be summed in the MCA in order to reach the required number of counts for a statistically significant measurement of the particle population. Because of the logarithmic response of the PSA, particles of radius R are counted in the channel of index $i = \alpha + \log_\beta R^3$. The calibration constants α and β depend in general on the instrument settings (excitation, amplification, orifice size and electrical conductivities of the liquid and of the particle) and are determined by sampling two or more suspensions of monodisperse particles of known size and electrical conductivity. Ideally in this case all the counts should be concentrated in just one channel, but in practice the distribution is broader and the channel corresponding to the mode of the distribution is used for calibration purposes. In this process care must be taken to correctly isolate the mode, since aggregation of two or more particles is possible and can cause misleading results. Then, if R_c is the radius of the calibration particles and c the corresponding channel index, the radius corresponding to any channel i is:

$$R_i = R_c \beta^{(i-c)/3} \tag{1}$$

At high amplification levels electronic noise determines the maximum useful sensitivity and, together with the characteristics of the MCA, limits the measurement range to a maximum to minimum radius ratio of about 4.

The system was initially calibrated with monodisperse suspensions of electrically non-conductive polystyrene latex spheres (Duke Scientific Corporation)

in filtered sea water at room temperature for given electronic settings (current excitation and signal amplification) and orifice diameter. The size distribution of the calibration particles was very nearly Gaussian, with modal diameters of 19.1 μm, 49.4 μm and 99.1 μm and standard deviations 1.4 μm, 2.5 μm and 4.8 μm respectively. Only one orifice of 140 μm diameter was used with two different electronic settings to cover the particle radius range from about 10 μm to about 50 μm. The calculated logarithmic bases of the PSA agreed within the achievable experimental accuracy with the values obtained with the same apparatus by previous investigators.

6. DATA REDUCTION

In cavitation research literature the liquid quality is usually expressed in terms of the nuclei number concentration density distribution function:

$$n(R) = \frac{dN}{dR} \simeq \frac{\Delta N}{\Delta R} \tag{2}$$

where $N(R)$ is the concentration of nuclei with radius smaller than R and ΔN is the observed concentration of particles with radius in the range ΔR containing the nominal radius R. From this definition it follows that the total concentration of particles in the liquid is:

$$N_{tot} = \int_0^{+\infty} n(R)\, dR \tag{3}$$

The nuclei number concentration density distribution $n(\overline{R})$ is measured by grouping together adjacent radii counts until a predetermined number of counts N_g is reached. This value is then divided by the corresponding radius range and sampled volume, V_s. Thus, if the nuclei radii are ordered by decreasing size and R_j is the maximum radius of the group:

$$n(\overline{R}) \simeq \frac{N_g}{V_s(R_j - R_{j+N_g})} \tag{4}$$

The statistical error associated with this procedure is uniform and depends only on the size of the groups, N_g. Assuming that the occurrence of nuclei in the liquid

sample volume is a Poisson process, as it should be if the nuclei were spatially uncorrelated, the best estimate of the relative r.m.s. error in the computation of the number concentration density distribution is equal to the reciprocal of the square root of the group size, $1/\sqrt{N_g}$. The nominal radius $\overline{R}$ of each group is defined as the geometric mean of the minimum and maximum values of the radii of the group. This choice usually minimizes the difference between the observed total concentration of particles and the value calculated by integrating the measured nuclei number distribution.

The above reduction procedure differs slightly from the more common way of computing the number concentration distribution density based on the number of counts observed in each prefixed interval subdividing the size range. First, it assures that the statistical error due to the finite number of counts of the sampled population is uniform for all the computed data points. Furthermore, by adjusting the size interval to the occurrence of the observed data, it avoids the upward bias which occurs when sparse data are assigned to fixed size intervals and zero counts are neglected, instead of being averaged with the neighbouring ones over a wider size range. Finally, it preserves the information on the relative density of the distribution of the available data as a function of size, which would otherwise be lost.

7. OCEAN TESTS

Field tests were performed in late August 1985 at two locations near Santa Catalina Island, southwest of Los Angeles (see Fig. 2) using the 65 foot R/V Seawatch operated by the Institute for Marine and Coastal Studies of the University of Southern California. At each site holograms were recorded at various depths and sea water samples were collected with Nansen bottles for later Coulter Counter analysis. At approximately the same time standard oceanographic measurements were made including Secchi disk casts together with transmissometer and salinity-temperature-depth (STD) profiles. Holographic data were collected only while anchored or drifting to avoid recording of artifact boat-

generated bubbles. The water samples for Coulter Counter analysis were transferred to opaque polyethylene bottles, kept refrigerated while on board in order to reduce alteration as much as possible, stored overnight at ambient conditions to reach room temperature and processed within 24 hours. Just before the analysis each water sample was stirred with a magnetic agitator to resuspend those particles that settled to the bottom of the container, taking care not to entrain new bubbles in the process.

The first test location was off Long Point, Santa Catalina Island. The boat drifted in waters ranging from 132 to 228 m depth during the two hours while holograms were being recorded. The water was quite clear, with the Secchi disk visible to 17 m depth. Sea state was 0 to 1, with less than 0.3 m swells, and no wind. Temperature and transmissivity profiles are presented in Fig. 3. Thirty holograms were recorded, sampling the water column from the surface to 32 m. The second test location was off the eastern point of Santa Catalina Island and was not as well protected from winds as the first station. The sea floor depth was 92.7 m, Secchi disk visibility was 19 m, with sea state and wave activity the same as at the first test location. Temperature and transmissivity profiles are presented in Fig. 4. Fourteen holograms were recorded at this station, all at either 27.4 or 32 m.

8. EXPERIMENTAL RESULTS AND DISCUSSION

For the purpose of cavitation research the most important nuclei are the largest ones which usually have smaller critical tensions and whose effects in cavitating flows therefore tend to dominate those of the smaller, generally less susceptible nuclei. For this reason the present paper focuses on nuclei of relatively large radius (more than 10 μm), unlike most previous investigations of particulate content of the ocean which used similar optical or electrical detection techniques.

Some results of particulate concentrations in the ocean obtained by holographic and Coulter Counter analysis of sea water from the same locations and

at comparable depths and time are shown in Fig. 5 through Fig. 8. Data are expressed in terms of the number concentration density distribution, $n(R)$, as a function of the particle radius, R, obtained as explained in Sec. 6. Here the number of radius counts per group is chosen as $N_g = 4$ and the corresponding estimate of the relative r.m.s. error of the data is 50%. The Coulter Counter analysis was carried out on 20 ml water samples using two electronic settings of different sensitivity in order to extend as much as possible the radius range of the measurement. In the computation of the number concentration density distribution from holographic records the sample volumes examined were on the order of 1 ml for nuclei from 10 to 25 μm radius and 100 ml for larger sizes. Since the sea water samples rested for about 24 hours before being processed with the Coulter Counter, no bubbles with radii larger than 10μm, were expected nor observed at the time of examination. Therefore, for better comparison of the data obtained with the two methods, the bubble population determined holographically has not been included in the data of Fig. 5 through Fig. 8, but will be discussed separately below.

The holographic results are consistently higher than the ones deduced using the Coulter Counter by as much as one order of magnitude. Since the holographic number concentration density distributions were determined by visual inspection of a magnified image recorded in situ, there is little reason to doubt their validity. The fact that the Coulter Counter consistently indicated fewer nuclei is not surprising in view of the following considerations. First, some of the particles may have permanently settled during the relatively long time (about 24 hours) from water sample collection to the actual processing of the sample, despite the efforts to resuspend them by agitation prior to the analysis. Second, the sampling of the Nansen bottles for Coulter Counter analysis differs from the recording of holographic data in both depth (within one meter), horizontal location (within five meters, neglecting drift) and time (less than one hour). Fluctuations of the particle population over relatively small distances are known to exist in ocean waters [Pieper and Holliday, 1984]. These fluctuations

do not introduce a systematic error, yet they may have contributed to some of the observed differences between the Coulter Counter and holographic data. However, in our opinion the most likely and important reason for the observed discrepancy in the results of the two detection techniques is the fundamental difference between the unknown electrical conductivity of the measured particles in the sea water samples and the non-conductive particles used to calibrate the Coulter Counter. In order to estimate the importance of this effect, let us consider a small cylindrical particle of cross-sectional area a, length l and electrical conductivity σ' suspended in a liquid of electrical conductivity σ at the center of a cylindrical orifice of cross-sectional area $A \gg a$ and length $L \gg l$. Then, from a simplified one-dimensional electrical model where the resistance of the particle, $l/a\sigma'$, is in parallel with that of the surrounding liquid, $l/(A-a)\sigma$, the total change of the electrical resistance across the orifice due to the presence of the particle can be expressed by:

$$\Delta R_{or} = \frac{\frac{V_p}{A^2\sigma}\left(\frac{\sigma'}{\sigma} - 1\right)}{1 + \frac{a}{A}\left(\frac{\sigma'}{\sigma} - 1\right)} \tag{5}$$

where $V_p = al$ is the particle volume. For small particles the denominator of equation (5) can be approximated to unity, the above change in the electrical resistance of the orifice is small with respect to the unperturbed value and the Coulter Counter signal is therefore proportional to $V_p(\sigma'/\sigma - 1)$. Then, for example, the size of particles whose electrical conductivity is equal to 90% of the conductivity of the suspending liquid would be underestimated by one order of magnitude. Indeed relatively high values of the electrical conductivity are not unrealistic in our case since most of the particles suspended in unpolluted oceans are of organic origin [Sheldon et al., 1972] and therefore their electrical conductivity is likely to be of the same order of magnitude as that of the surrounding waters.

The number concentration density distributions determined using the Coulter Counter are steeper than those determined holographically, as indicated by Fig. 5 through Fig. 8. A possible reason for this difference is the rupture of

the aggregate particles due to the shearing and elongational strains in the flow of the sampled liquid through the Coulter Counter orifice. The rupture of aggregate particles would increase the number of counts at smaller size ranges and therefore steepen the number concentration density distribution. Aggregate particles were indeed observed in the holographic images of the sample. Since recognition could only be made for relatively large aggregate particles, we cannot estimate their total concentration and therefore the importance of their potential contribution to this effect.

The Coulter Counter also displays the general tendency to produce slightly concave number concentration density distribution curves, unlike the holographic data. We believe that this is the result of the change of relative importance of the electronic noise with particle size, which was found to be significant only for the higher radius range where the number of spurious, noise induced counts becomes comparable to the original particle signal. However, no correction could be made due to the extreme sparsity of the data in this region of the size spectrum.

The particle number concentration density distributions deduced from holographic data decrease approximately with the fourth power of the particle radius in the observed size range. Similar dependence has been reported in the literature for the population of particles in many natural environments including sea waters [Bader, 1970], as well as for the population of comparable size bubbles in the ocean [Mulhearn, 1981; Medwin, 1977].

The holographic and Coulter Counter determinations of total concentration of particles for various depths at the two test sites are presented in Fig. 9 and Fig. 10. Only particles in the 10 to 50 μm radius range are used in the calculation of the total concentration, as the holographic and Coulter Counter data directly overlap only over this radius range. Results are based on the analysis of eight holograms (six from the Long Point site and two from off east Santa Catalina Island) and eight Coulter Counter water samples (four from each site). The holographic data in Fig. 9 and Fig. 10 indicate higher total particulate con-

centrations in the 10 to 50 μm radius range than those reported in the literature for either ocean or laboratory waters. They also clearly reflect the previously noted discrepancy between the concentrations measured using the two methods. Both sets of data in Fig. 9 from the Long Point test site seem to indicate an increase in particle concentration near the bottom of the thermocline and to correlate well with the transmissometer trace of Fig. 3, which shows a drop in transmissivity near the thermocline depth. Similar behavior at the test site off east Santa Catalina Island is displayed by the Coulter Counter data of Fig. 10, as well as by the transmissometer trace of Fig. 4. The holographic results at this site are too sparse to indicate any trend with depth.

The observation of particle concentration increase near the bottom of the thermocline is supported by the data of Pieper and Holliday, 1984, who present zooplankton concentrations determined by microscopic examination of organisms deposited on filters as sea water samples were pumped through from various depths. This testing was done in May, 1978, at a location and at depths very similar to the Long Point test site examined in this study. The thermoclines were similar in each test, with the top at about 18 m and the bottom at about 30 m, although that in Pieper and Holliday, 1984, was stronger (5 °C) and the surface temperature was lower (17 °C). Their results show peak zooplankton concentrations near the bottom of the thermocline. The present holographic results support this finding, clearly showing that a large percentage of the "particles" observed, especially below the thermocline, are living organisms. The finding of high zooplankton counts in deeper waters should be of interest in cavitation studies since zooplankton, with their metabolic gases, can presumably act as cavitation nuclei.

Although the Coulter Counter can be used, with some limitations, for detection of bubbles [Oba et al., 1981 for example] such an investigation was not undertaken in the present study since, as mentioned earlier, the sea water samples used for Coulter Counter analysis were handled in such a way that no bubbles were expected nor observed at the time of analysis. However, since

bubbles are known to be primary cavitation nuclei, results of the holographic study of bubbles will be included and briefly discussed here. Table 1 presents bubble concentrations, and total number of bubbles counted, in various radius ranges for several depths at the two test sites. No bubbles larger than 50 μm radius were seen in any of the holographic samples. Recall that no attempt was made to distinguish bubbles from particulates in the smallest size range, about 2.5 to 10 μm radius, so these data are not presented here.

Several observations can be made based on the small number of bubbles seen in the holographic images. The concentration of small bubbles (10 to 25 μm radius) at the test site off Long Point seems to be very high near the surface, then to decrease with depth until the thermocline is reached, at which point the concentration increases. Larger bubbles (25 to 50 μm radius) are found only below the thermocline. The bubble data for the test site off east Santa Catalina Island are sparse and represent water below the thermocline only, indicating a fairly high concentration of larger bubbles at the 32 m depth. The relative r.m.s. error for each bubble size interval is expected to be equal to $1/\sqrt{N_g}$, where N_g is the corresponding number of counts, shown in brackets in Table 1. This error is often large, especially for those size ranges with sparse bubble observations. The overall high bubble concentrations, particularly near the surface at the Long Point site, are surprising in view of the calm windless conditions at the time these holograms were recorded, as well as for several days earlier. Strong dependence of ocean bubble concentrations on wind speed have been reported by Medwin, 1977 and Thorpe, 1982. The existence of microbubbles down to 32 m and the apparent population inversion below the thermocline are also surprising. Shen et al., 1984, detected microbubbles to 25 m depth at both stations reported, with decreasing bubble concentration as a function of depth, although sampling below the deep thermocline at their subtropical test sites was not reported [Zsolnay et al., 1986]. Medwin, 1977, observed bubbles as deep as 36 m, and under a windrow observed peak bubble concentrations at that depth. He speculates that the Langmuir cells under the windrow acted to deplete the upper waters

without affecting the deep water bubbles, which are postulated to be of biological origin. Windrows were not present at the stations holographically examined in the present study but, as discussed above, there seemed to be a peak in biological activity below the thermocline, so bubbles of organic origin may play a role here. Several hypotheses have been formulated to explain the presence of bubbles at depth [Johnson and Cooke, 1981; Medwin, 1977; Mulhearn, 1981].

The relationship between the nuclei number concentration density distribution and the tensile strength of the suspending liquid is still an elusive problem in cavitation research due to the many complexities and uncertainties involved. Little can be said about the role of particulates as cavitation nuclei from their holographic observation or from the Coulter Counter sizing, apart from the obvious consideration that larger concentrations of particulates are likely to lead to higher active cavitation nuclei populations. This difficulty can only be overcome by direct observation of cavitation induced by the liquid particulates under controlled circumstances, for example by means of cavitation susceptibility meters [Oldenziel, 1982]. On the other hand, the dynamic properties of gas bubbles are indirectly related to their size by the Rayleigh-Plesset equation [Knapp et al., 1970]. However, even in this case cavitation results from the combination of the dynamic and interference effects among developing cavities with the statistical occurrence of bubble nuclei and depends significantly on the specific flow conditions. Therefore a constant relation between the tensile strength of liquids and their bubble population can only be established in the idealized situation where dynamic and interference effects are neglected, i.e. by considering the static equilibrium of individual bubbles. Then a lower bound for the tension required to cause cavitation is given by the critical tension of a spherical gas bubble which, in the absence of viscosity, mass diffusion and thermal effects, is expressed by [Knapp et al., 1970]:

$$(p_v - p)_{cr} = \frac{4S}{3R_o}\left[3\left(1 + \frac{p_o - p_v}{2S/R_o}\right)\right]^{-1/2} \tag{6}$$

where R_o and p_o are the equilibrium radius and external pressure of the bubble

and S is the surface tension. This relation is plotted in Fig. 11 for the case of an air bubble in water at a temperature of 20 °C and for several equilibrium pressures. The sparse bubble measurements are insufficient to determine a statistically significant value of the tensile strength for each water sample examined, but several important points can still be made. A single bubble with 50 μm radius was seen at 23 m submergence at the site off Long Point (see Table 1), so Fig. 11 indicates that this water would be expected to cavitate at least occasionally under an applied tension of about 100 Pa. In general Table 1 shows that all samples contained some bubbles larger than 10 μm radius, so Fig. 11 can be used to show that each of these would be expected to cavitate under an applied tension of about 2000 Pa.

9. CONCLUSIONS

Holographic detection clearly is the more reliable of the two methods considered in this paper for measuring the nuclei number concentration density distributions. The unique capability of holography to provide discrimination between bubbles, particles and organisms is also of great value for in situ sea water analysis. However, the reconstruction and detailed visual analysis of holographic images is extremely time-consuming.

The comparison of representative data obtained using the two techniques indicates that Coulter Counter analysis tends to underestimate the particulate content by up to an order of magnitude as a probable consequence of the combined effects of particle settling and of the assumption of electrically nonconducting particles implicit in the calibration procedure. It is conceivably possible to introduce empirical corrections to compensate for the latter phenomenon when the general nature of the major portion of the particulate population in the sampled water is known. The apparent distortions of the number concentration density distributions obtained from the Coulter Counter also suggest that rupture of particle aggregates might take place during the analysis of the sample due to the strain produced by the flow of the liquid through the orifice, and that

electronic noise is likely to be important only in the upper radius range where particle counts tend to become very sparse. These problems can be limited by using large aperture orifices and increasing the signal to noise ratio of the Coulter Counter electronics.

The observation that the Coulter Counter may consistently underestimate the size of organic particles could be an important one, as this device is commonly used for sea water analysis (see for example Carder et al., 1971, and Sheldon et al., 1972). Despite these limitations, in our opinion the Coulter Counter is still a practical, time-effective device for monitoring the particulate content of liquid samples in cavitation research when great accuracy is not required and the electrical conductivity of the major portion of the particulate population in the sample can be estimated.

The population of particulates obtained with the two techniques examined here are in agreement with previous comparable data from the literature within the expected experimental and statistical errors. They also confirm that the number concentration density distribution of particulates in the range covered by our investigation decreases approximately with the fourth power of the particle size, as often reported in the literature. Both the holographic and Coulter Counter results indicate an increase in particle concentration near the bottom of the thermocline, in agreement with the zooplankton population measurements made by Pieper and Holliday, 1984. The holographic data also indicate similar behaviour for the bubble concentration, although their relatively large statistical indetermination makes them less conclusive.

Further study is necessary to exactly clarify the dependence of the tensile strength of liquids on their nuclei content and therefore to deduce scaling laws for cavitation phenomena. This is especially true in the case of particles, whose effect on the liquid susceptibility is not yet fully understood. However, the concentration of particles and bubbles in a liquid still provides an upper bound for the number of potentially active cavitation nuclei. Much higher concentrations of particles were detetected in the ocean, according to the holographic analysis,

than in typical cavitation test facilities [Billet, 1985]. These differences should be taken into consideration in trying to relate laboratory results to prototype operation. Finally, the bubble concentration density distributions indicate that the average tensile strength of the ocean waters examined in this study should be on the order of a few thousand Pascals, with a minimum expected value of about one hundred Pascals.

10. ACKNOWLEDGEMENTS

A field experiment must necessarily rely on the assistance and cooperation of many parties. Special thanks to to Professor J. Katz of Purdue University, to Elton Daly and staff of Caltech's W.M. Keck Laboratory of Hydraulics and Water Resources, and to the Captain and crew of the R/V Seawatch. Raymond Moberly together with Doug Gray resuscitated Caltech's Coulter Counter and later cooperated in the analysis of the samples and the reduction of the data. Sheldon Green assisted in the ocean tests and carried out a large portion of the holographic reconstruction. Esther (Cindy) Morss and Richard Arrieta provided valuable help during experimentation. This work has been supported by the Office of Naval Research under Contract No. N00014-83-K-0506 and by a Fellowship for Technological Research administered by the North Atlantic Treaty Organization - Consiglio Nazionale delle Ricerche, Italy, Competition No. 215.18/11 of 9.24.1984. Their support is gratefully acknowledged.

11. REFERENCES

Bader H, 1970, "The Hyperbolic Distribution of Particle Sizes", J. Geophysical Research, Vol. 75, No. 15, pp. 2822-2830.

Billet M.L., 1985, "Cavitation Nuclei Measurements - A Review", ASME Cavitation and Multiphase Flow Forum, Albuquerque, N.M.

Carder K.L., Beardsley G.F. Jr. and Pak H., 1971, "Particle Size Distributions in the Eastern Equatorial Pacific", J. Geophysical Research, Vol. 76, No. 21, pp. 5070-5077

Carder K.L., Steward R.G. and Betzer R.P., 1982, "In Situ Holographic Measurement of the Sizes and Settling Rates of Oceanic Particulates", J. Geophysical Research, Vol. 87, No. C8, pp. 5681-5685.

Collier R.J., Burckhardt C.B. and Lin. L.H., (1971), Optical Holography, Academic Press Inc., New York.

De Velis J.B., Parrent G.B. Jr. and Thompson B.J., (1966), "Image Reconstruction with Fraunhofer Holograms", J. Optical Society of America, 56, 4, 423-427.

Hunt J.R., 1980, "Coagulation in Continuous Particle Size Distributions: Theory and Experimental Verification", Ph. D. Thesis, California Institute of Technology.

Johnson B.D. and Cooke R.C., 1981, "Generation of Stabilized Microbubbles in Seawater", Science, Vol. 213, pp. 209-211.

Katz J., O'Hern T.J. and Acosta A.J., 1984, "An Underwater Holographic Camera System for Detection of Microparticulates", ASME Cavitation and Multiphase Flow Forum, New Orleans, LA.

Knapp R.T., Daily J.W. and Hammitt F.G., 1970, Cavitation, McGraw Hill.

Medwin H., 1977, "In Situ Acoustic Measurements of Microbubbles at Sea", J. Geophysical Research, Vol. 82, No. 6, pp. 971-976

Mulhearn P.J., 1981, "Distribution of Microbubbles in Coastal Waters", J. Geophysical Research, Vol. 86, No. C7, pp. 6429-6434.

Oba R. et al., 1981, "Cavitation Nuclei Measurements by a Newly Made Coulter Counter without Adding Salt in Water", Report of the Institute of High Speed Mechanics, Vol. 43, No. 340.

Oldenziel D.M., 1982, "A New Instrument in Cavitation Research: the Cavitation Susceptibility Meter", ASME J. Fluids Engineering, Vol. 104, pp. 136-142.

Pieper R.E. and Holliday D.V., 1984, "Acoustic Measurements of Zooplankton Distributions in the Sea", J. Cons. int. Explor. Mer, Vol. 41, pp. 226-238.

Sheldon R.W., Prakash A. and Sutcliffe W.H., Jr., 1972, "The Size Distribution of Particles in the Ocean", Limnology and Oceanography, Vol. XVII, No. 3, pp. 327-340

Shen Y.T., Gowing S. and Pierce R., 1984, "Cavitation Susceptibility Measurements by a Venturi", ASME International Symposium on Cavitation Inception-1984, New Orleans, LA.

Thorpe S.A., 1982, "On the Clouds of Bubbles Formed by Breaking Wind-Waves in Deep Water, and Their Role in Air-Sea Gas Transfer", Phil. Trans. R. Soc. Lond. A, Vol. 304, pp. 155-210.

Zsolnay A. et al., 1986, "Environmental Parameters in Exuma Sound and the Straits of Florida", Naval Ocean Research and Development Activity Technical Note 252.

TABLE 1

NUMBER CONCENTRATION (Number per ml) [TOTAL NUMBER COUNTED]							
Test Location	**Depth (m)**	**Radius Range (μm)** 10–15	15–20	20–25	25–30	30–40	40–50
off Long Point	3	15 [15]	–	–	–	–	–
off Long Point	6	3.3 [7]	–	–	–	–	–
off Long Point	15	1.6 [5]	–	–	–	–	–
off Long Point	23	0.6 [1]	–	0.6 [1]	–	–	–
off Long Point	30	8.3 [10]	–	–	–	–	–
off Long Point	32	2.5 [4]	0.6 [1]	0.6 [1]	–	–	–
off East Catalina	27	1.1 [1]	–	1.1 [1]	–	–	–
off East Catalina	32	2.2 [2]	–	–	0.03 [3]	–	0.01 [1]

Table 1. Holographic results of bubble concentrations in number per ml. The total number of bubbles counted in each radius range, N_g, is indicated in brackets. The estimated relative r.m.s. error of the bubble number concentration is $1/\sqrt{N_g}$.

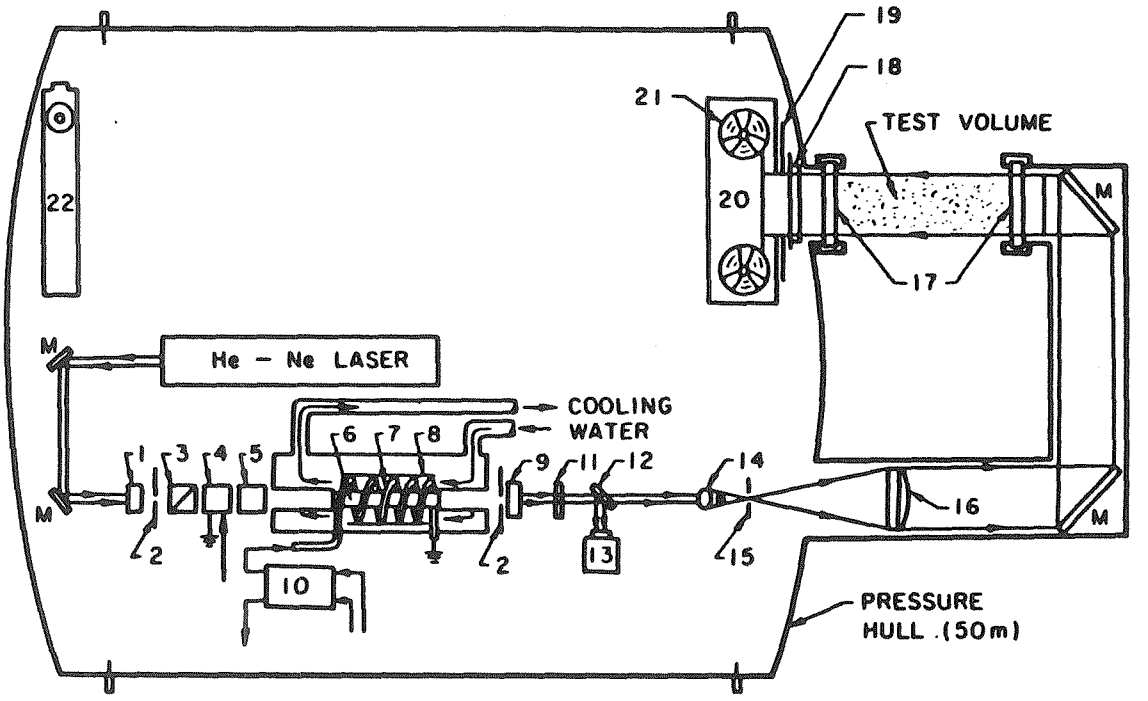

1. BACK MIRROR
2. IRIS APERTURE
3. POLARIZER
4. POCKELS CELL
5. POLARIZER (OPTIONAL)
6. RUBY ROD
7. XENON FLASH LAMP
8. REFLECTOR
9. FRONT MIRROR-SAPPHIRE ETALON
10. TRIGGER TRANSFORMER
11. NEUTRAL DENSITY FILTER
12. BEAM SPLITTER (4% REFLECTIVITY)
13. PIN DIODE
14. MICROSCOPE OBJECTIVE
15. SPATIAL FILTER - 10μ PINHOLE
16. COLLIMATING LENS
17. GLASS WINDOWS
18. INTERFERENCE FILTER
19. SHUTTER
20. AUTOMATIC FILM DRIVE
21. HOLOGRAPHIC FILM SPOOLS
22. AUTO COLLIMATOR
M. MIRROR

Figure 1. Line drawing of the holographic camera system mounted inside the submersible hull.

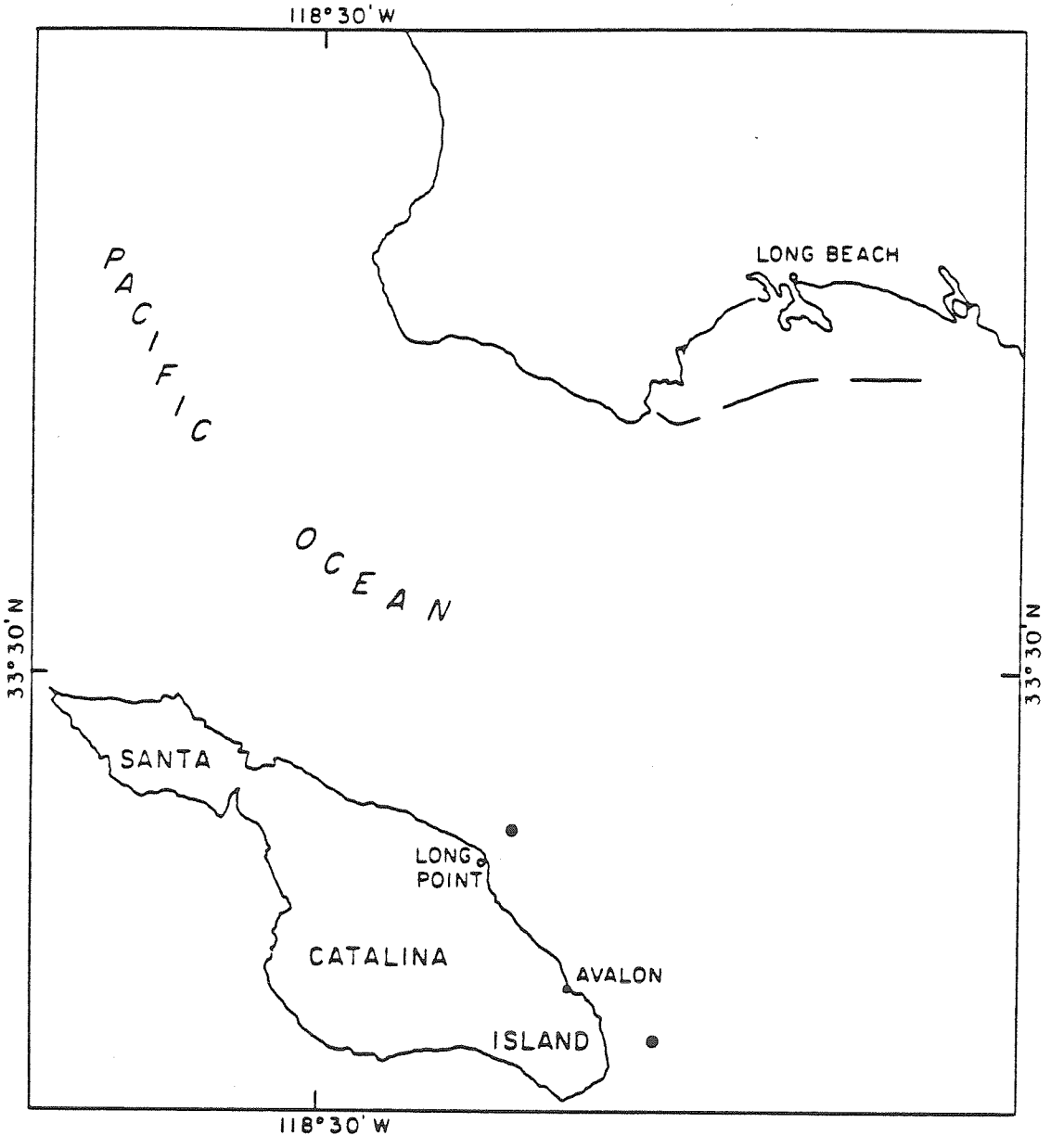

Figure 2. Map of the Los Angeles coastal area indicating the two test sites, off Long Point at 33°24′47″ N, 118°21′45″ W and east of Santa Catalina Island at 33°18′30″ N, 118°17′12″ W.

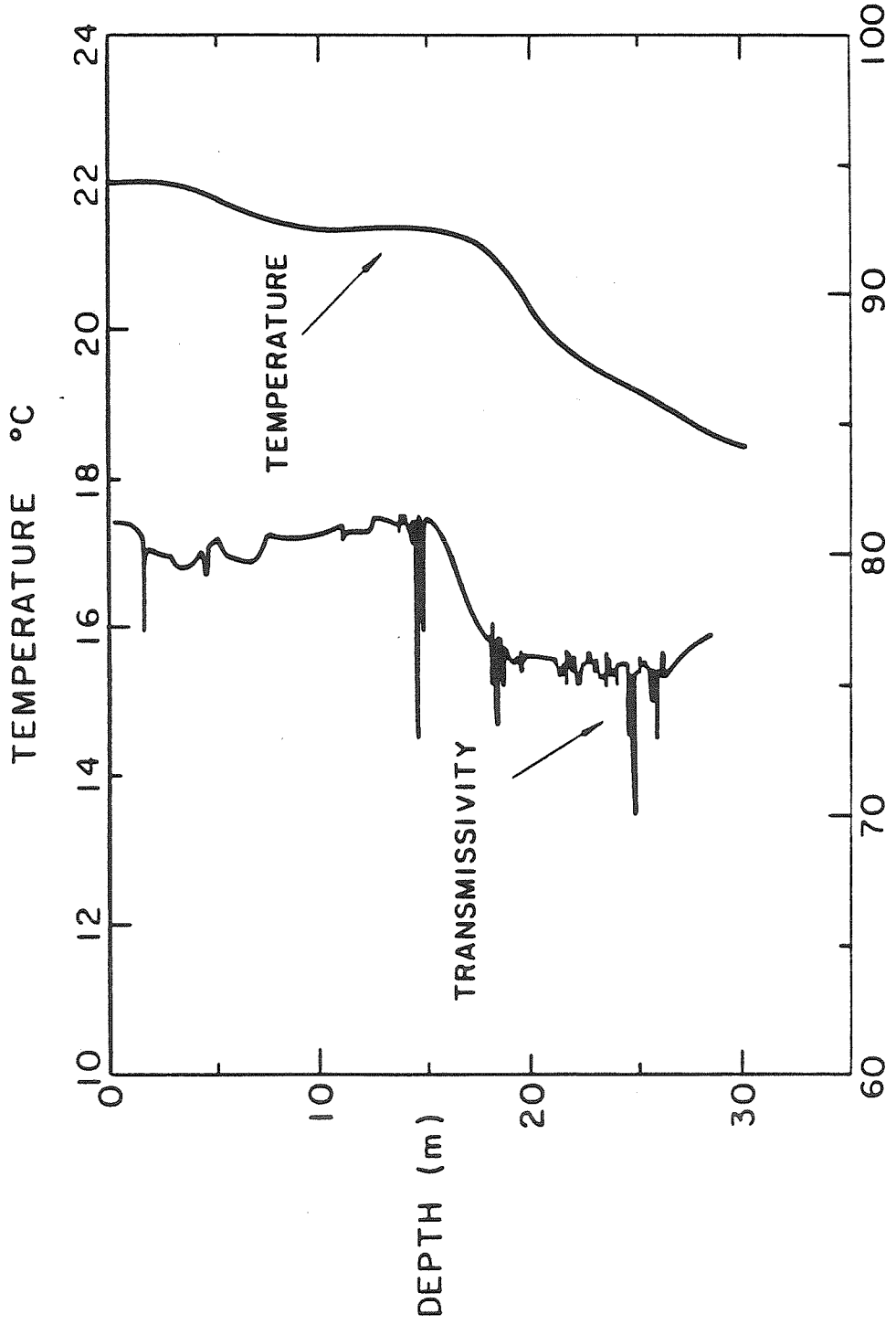

Figure 3. Temperature and transmissivity profiles for the test site off Long Point, Santa Catalina Island.

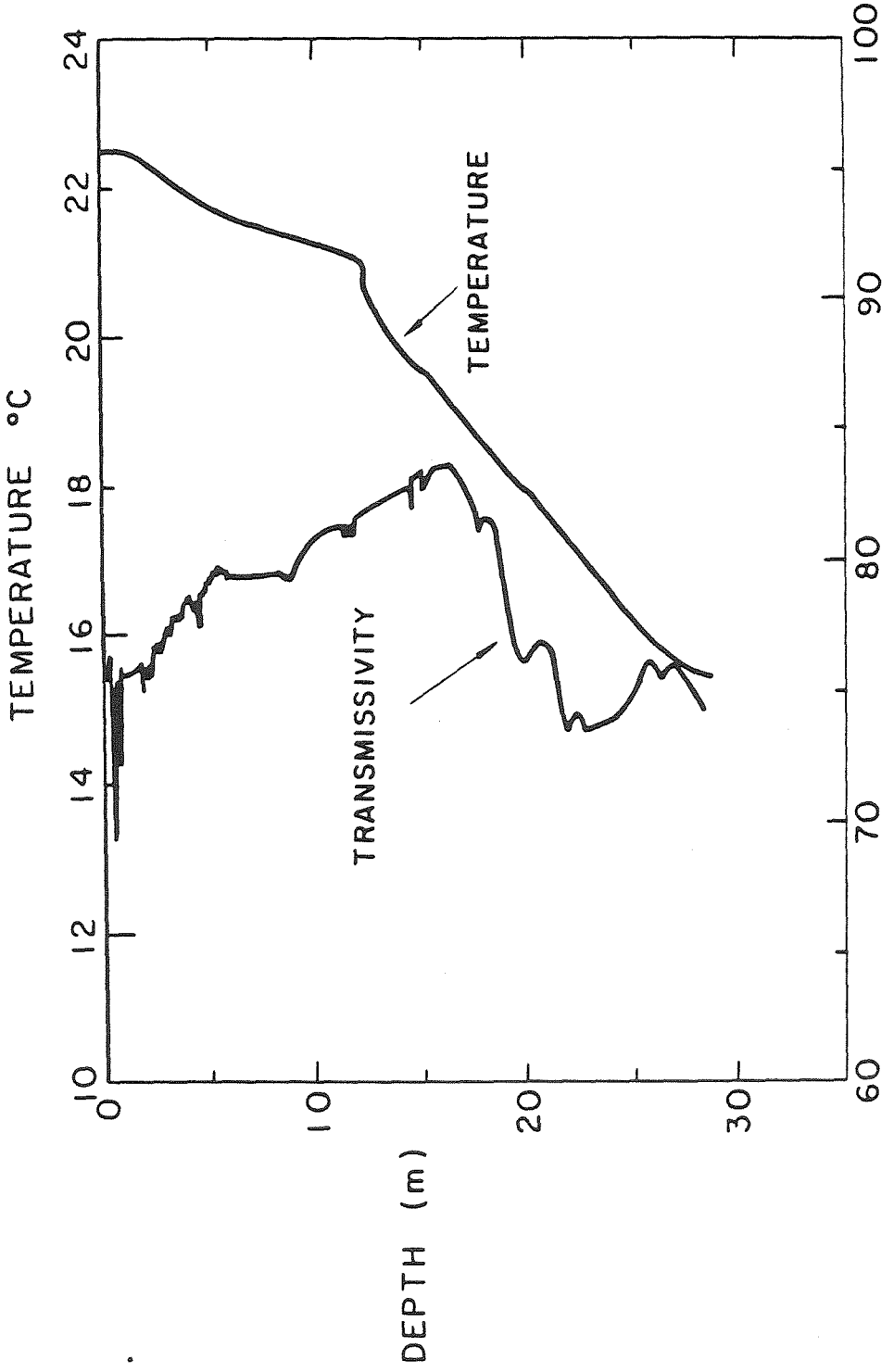

Figure 4. Temperature and transmissivity profiles for the test site off east Santa Catalina Island.

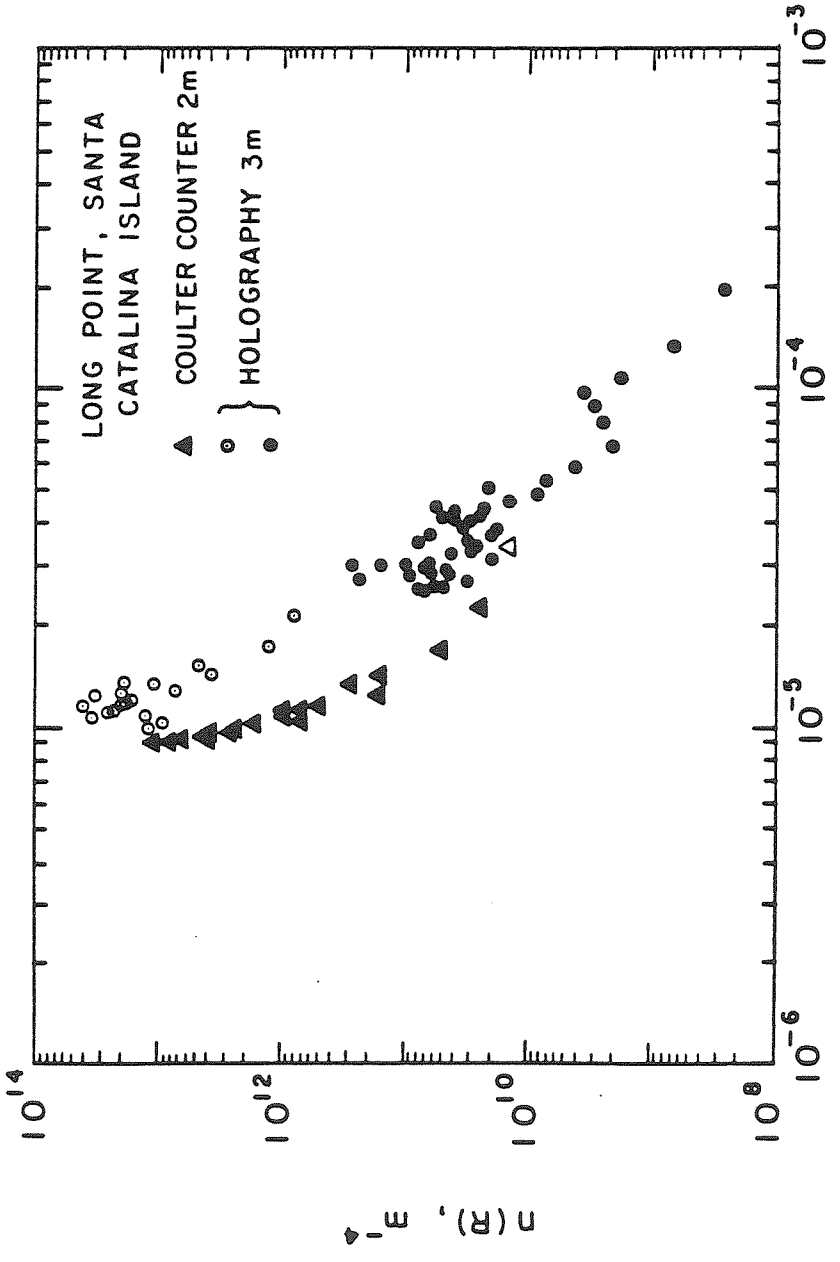

Figure 5. Number concentration density distributions of particulates, $n(R)$, in the waters off Long Point, Santa Catalina Island, as a function of the particle radius, R. The number of radius counts per group is $N_g = 4$ and the expected r.m.s. error is 50%. Holographic data (squares) were recorded at 3 m depth with sampling volumes: 1 (open symbols) and 150 ml (solid symbols). Coulter Counter data (triangles) were obtained analyzing 20 ml water samples from 2 m depth with different sensitivity: high (solid symbols) and low (open symbols).

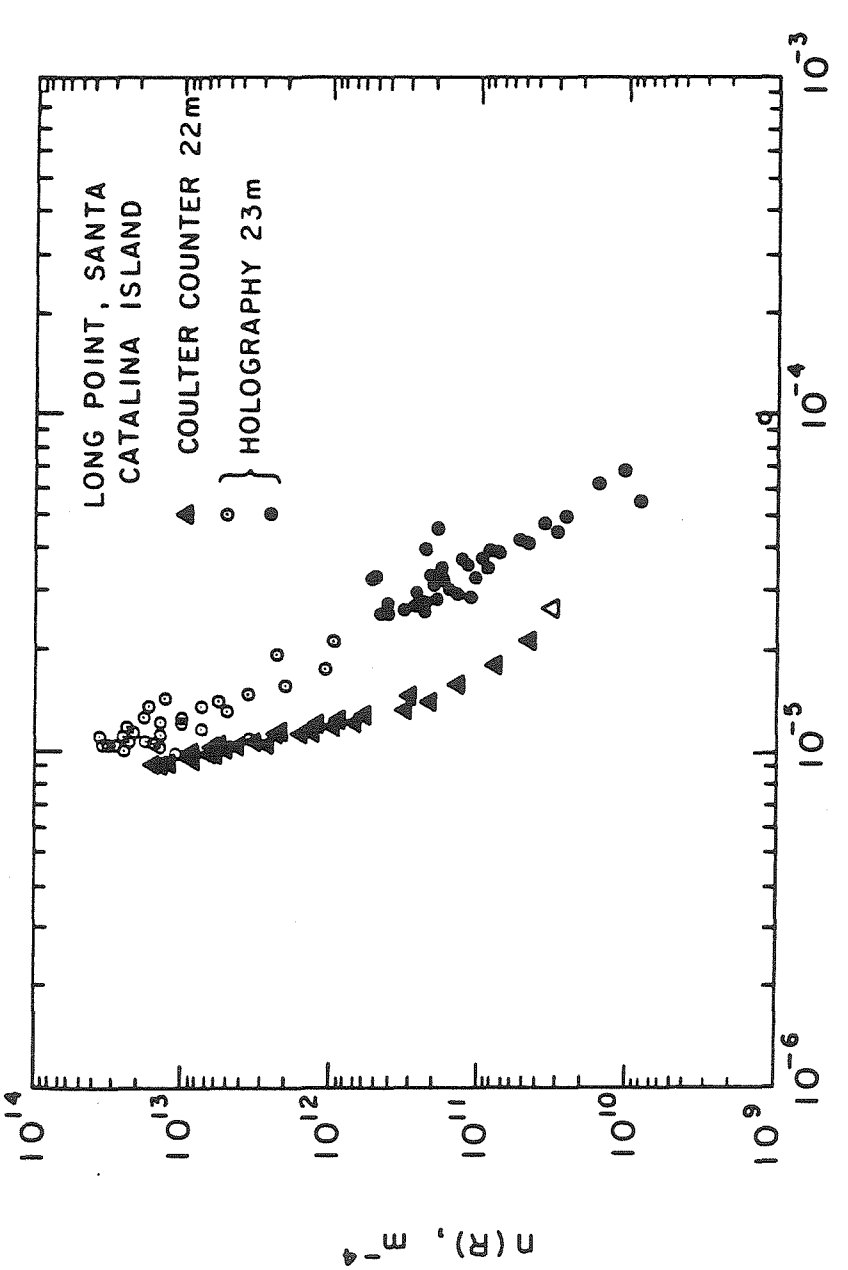

Figure 6. Number concentration density distributions of particulates, $n(R)$, in the waters off Long Point, Santa Catalina Island, as a function of the particle radius, R. The number of radius counts per group is $N_g = 4$ and the expected r.m.s. error is 50%. Holographic data (circles) were recorded at 23 m depth with sampling volumes: 1.6 (solid symbols) and 54 ml (open symbols). Coulter Counter data (triangles) were obtained analyzing 20 ml water samples from 22 m depth with different sensitivity: high (solid symbols) and low (open symbols).

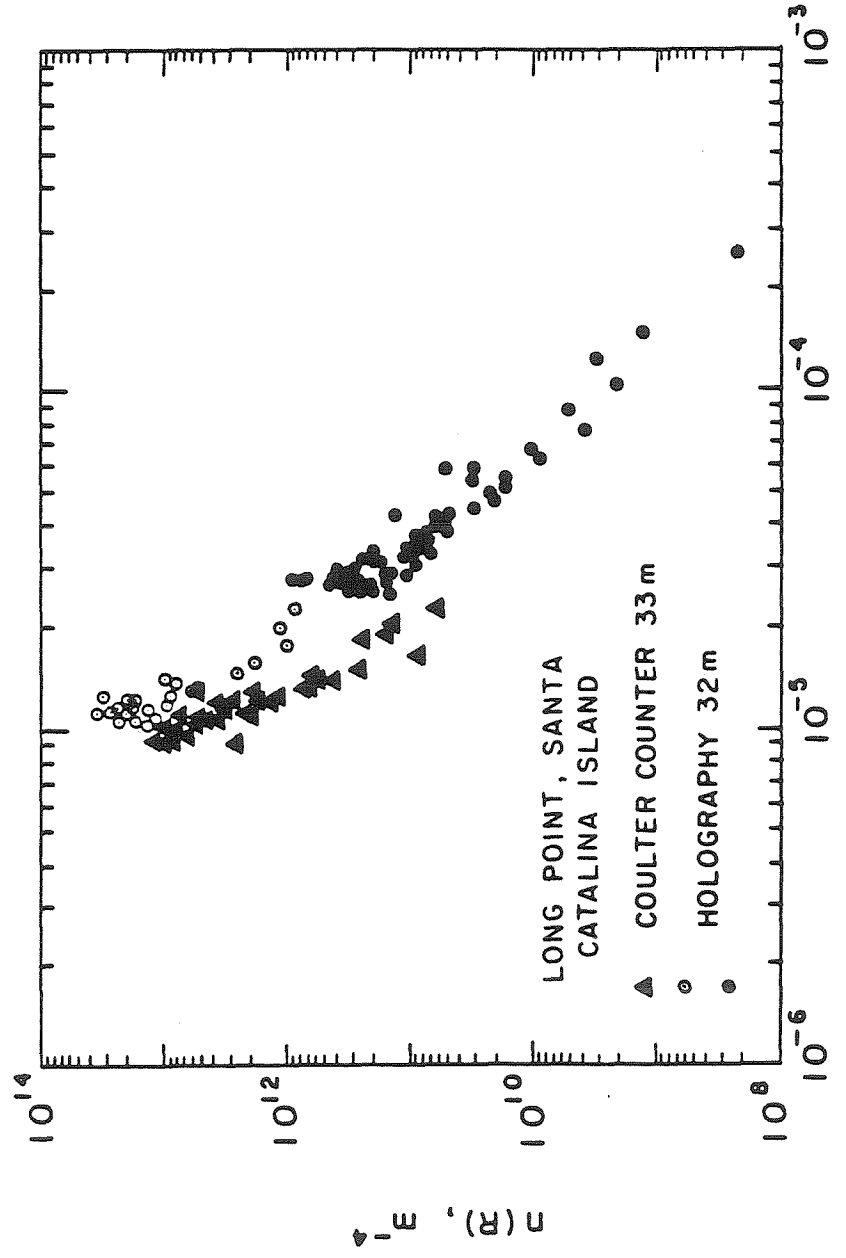

Figure 7. Number concentration density distributions of particulates, $n(R)$, in the waters off Long Point, Santa Catalina Island, as a function of the particle radius, R. The number of radius counts per group is $N_g = 4$ and the expected r.m.s. error is 50%. Holographic data (circles) were recorded at 32 m depth with sampling volumes: 1.6 (open symbols) and 79 ml (solid symbols). Coulter Counter data (triangles) were obtained analyzing 20 ml water samples from 33 m depth with different sensitivity: high (solid symbols) and low (open symbols).

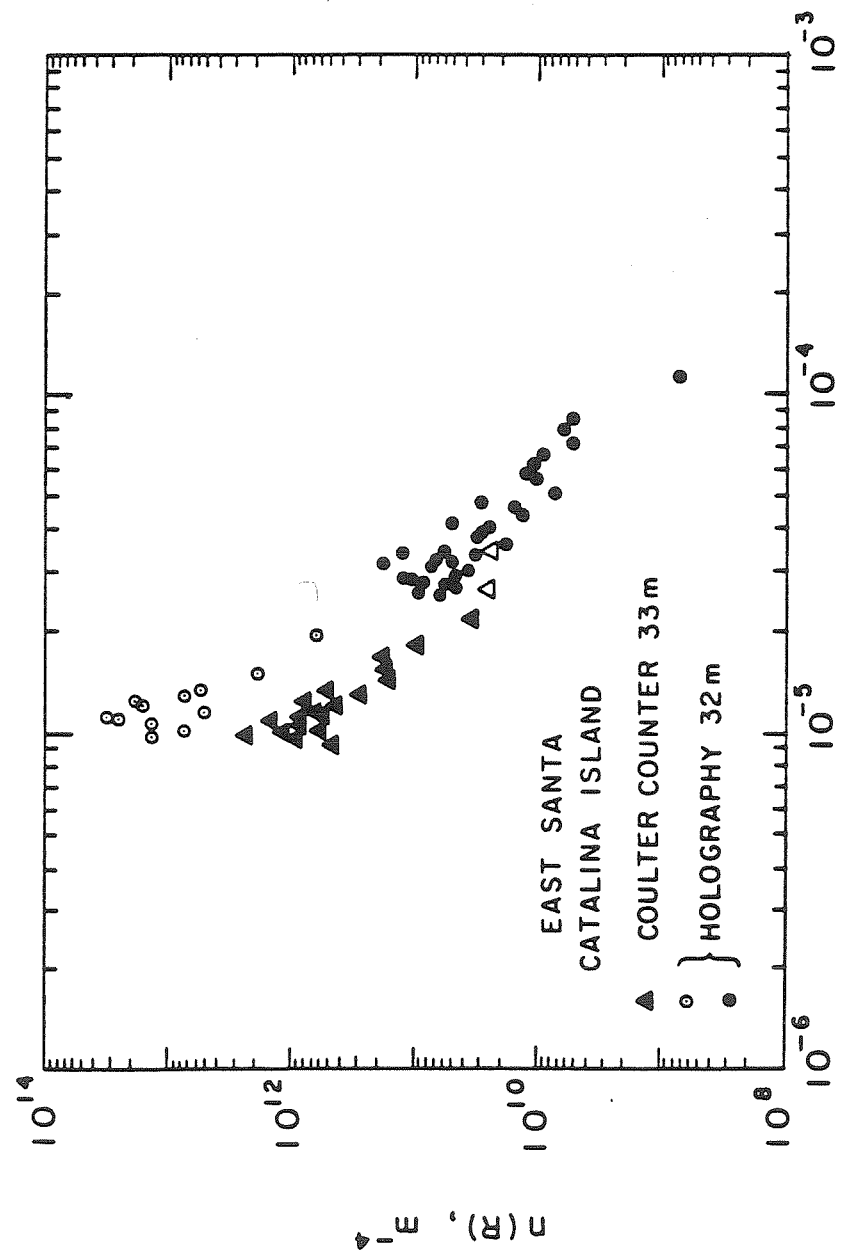

Figure 8. Number concentration density distributions of particulates, $n(R)$, in the waters off east Santa Catalina Island as a function of the particle radius, R. The number of radius counts per group is $N_g = 4$ and the expected r.m.s. error is 50%. Holographic data (squares) were recorded at 32 m depth with sampling volumes: 0.9 (open symbols) and 100 ml (solid symbols). Coulter Counter data (triangles) were obtained analyzing 20 ml water samples from 33 m depth with different sensitivity: high (solid symbols) and low (open symbols).

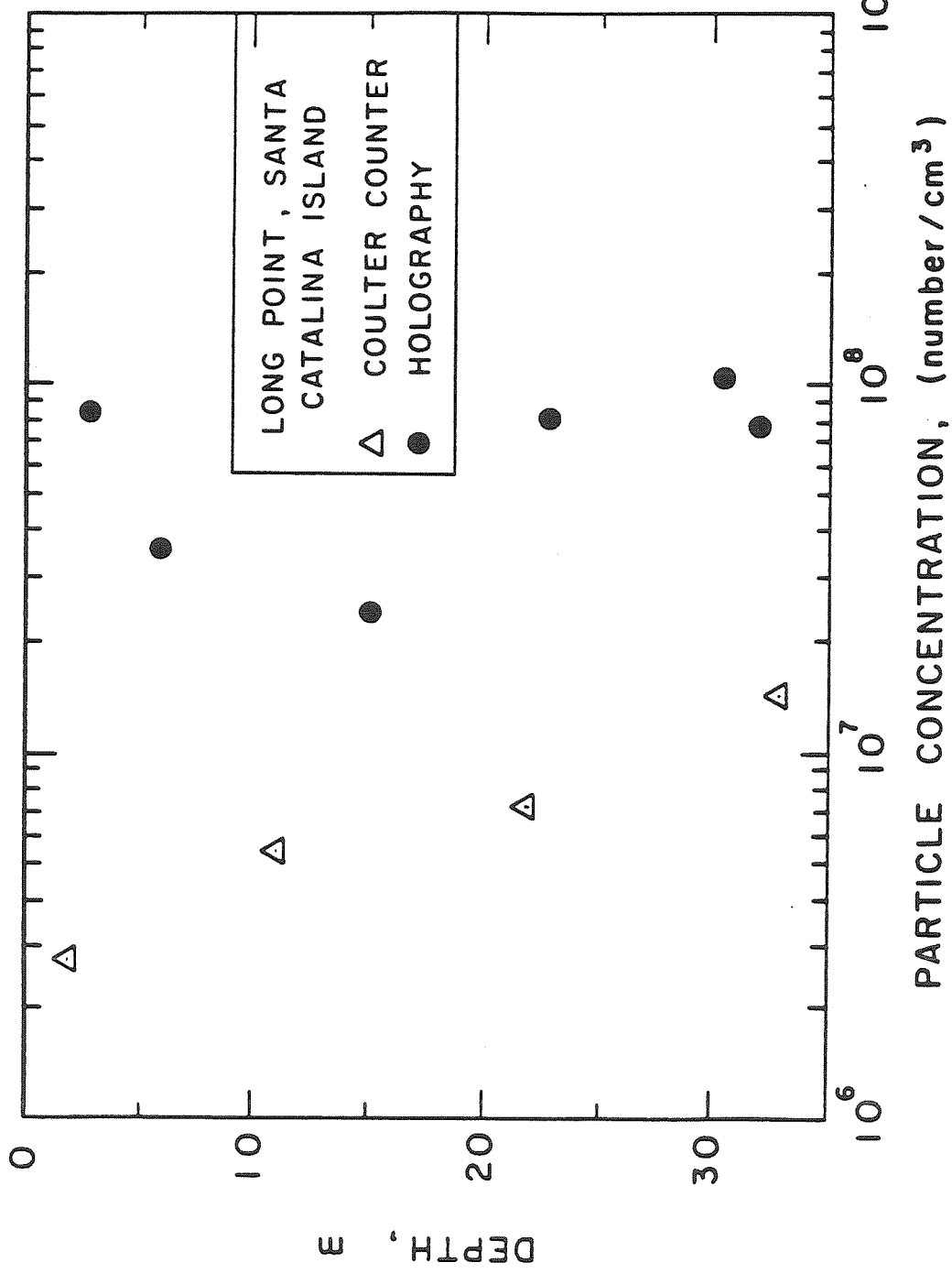

Figure 9. Particle number concentration depth profiles off Long Point, Santa Catalina Island from holographic (circles) and Coulter Counter data (triangles) in the radius range from 10 to 50 μm.

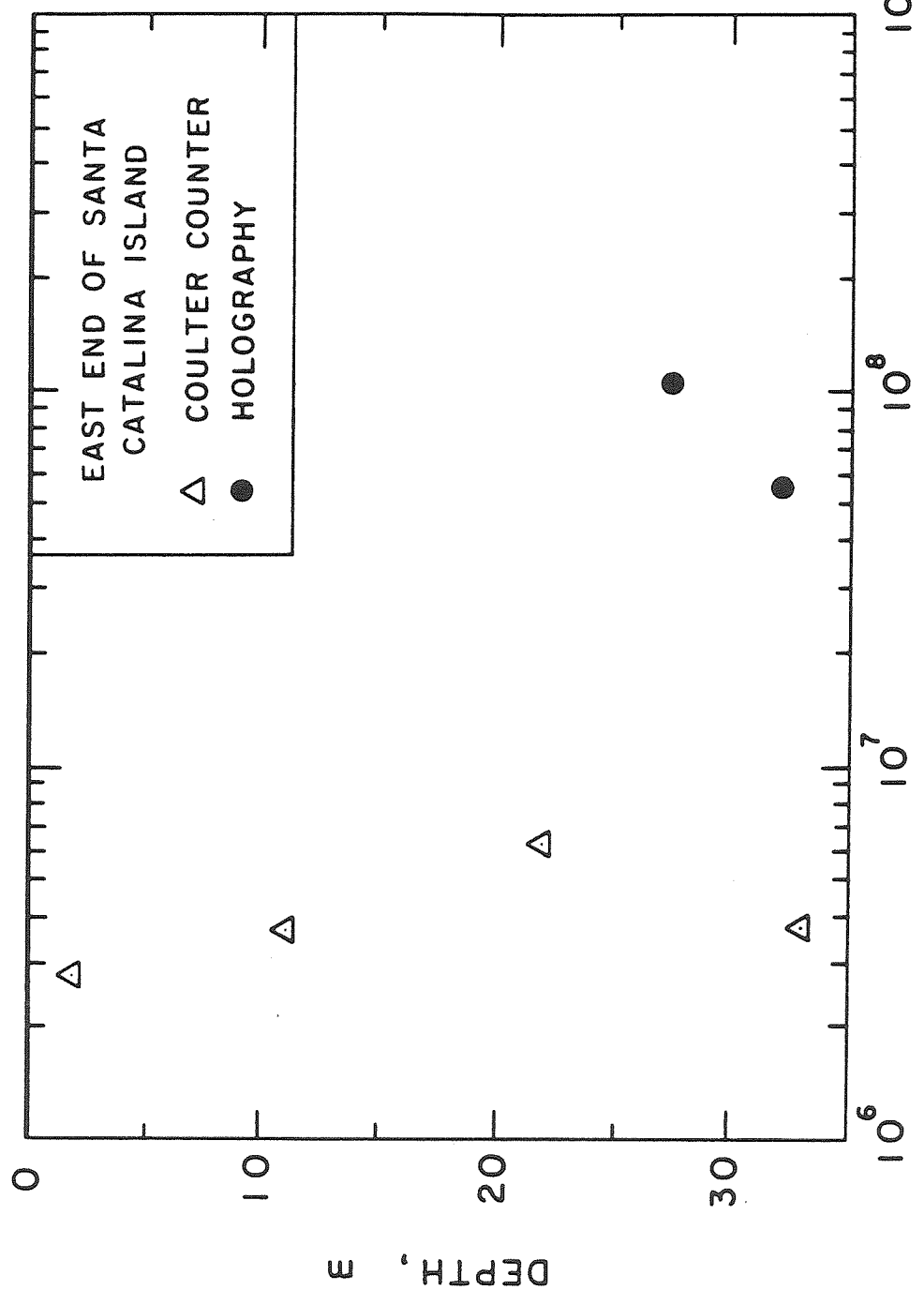

Figure 10. Particle number concentration depth profiles off east Santa Catalina Island from holographic (circles) and Coulter Counter data (triangles) in the radius range from 10 to 50 μm.

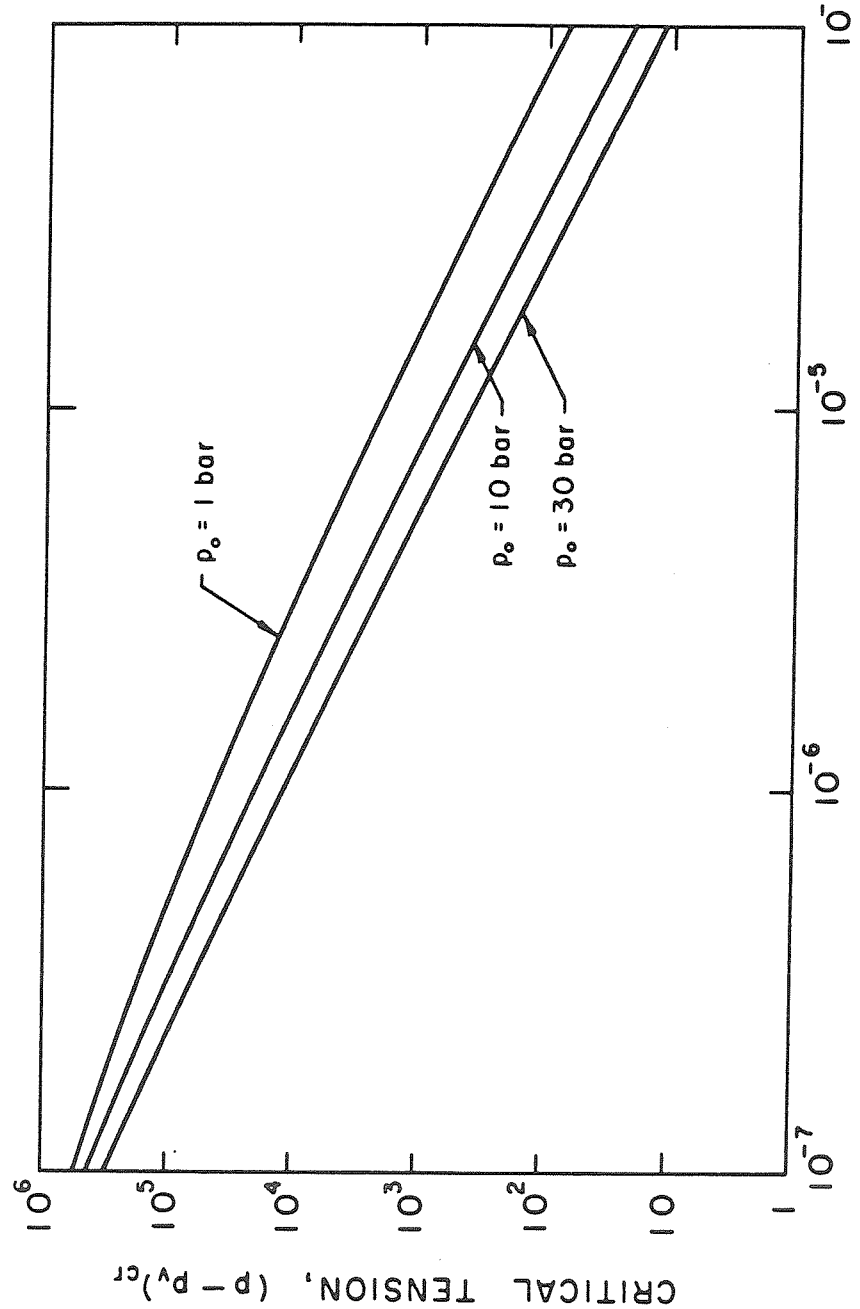

Figure 11. Critical tension, $(p_v - p)_{cr}$, of an isolated air bubble in unbounded water as a function of its static equilibrium radius, R_o, at various external pressures: $p_o = 1$ bar (upper curve), $p_o = 10$ bar (intermediate curve) and $p_o = 30$ bar (lower curve) with $T = 20\,^{\circ}\mathrm{C}$ (surface tension $S = 0.073\,\mathrm{N/m}$ and vapor pressure $p_v = 1919\,\mathrm{Pa}$).

Part II

LINEARIZED DYNAMICS OF BUBBLY AND CAVITATING FLOWS WITH BUBBLE DYNAMICS EFFECTS

Appendix 4.

ON THE ACOUSTICAL DYNAMICS OF BUBBLE CLOUDS *

by

L. d'Agostino and C.E. Brennen

1. INTRODUCTION

Recently Mørch [1980, 1981], Chahine [1982 a, 1982 b] and others have focused attention on the dynamics of a cloud or cluster of cavitating bubbles and have expanded on the work of van Wijngaarden [1964, 1972] and others. Unfortunately, there appear to be a number of inconsistencies in this recent work which will require further study before a coherent body of knowledge on the dynamics of clouds of bubbles is established. For example, Mørch and his co-workers [1980, 1981, 1982] have visualized the collapse of a cloud of cavitating bubbles as involving the inward propagation of a shock wave: it is assumed that the bubbles collapse virtually completely when they encounter the shock. This implies the virtual absence of non-condensable gas in the bubbles and the predominance of vapor. Yet in these circumstances the mixture in the cloud will not have any real sonic speed. As implied by a negative L.H.S. of equation (9), the fluid motion equations for the mixture would be *elliptic* not *hyperbolic* and hence shock wave solutions are inappropriate.

One can visualize several kinds of bubble interaction which could influence the dynamics of a cloud of bubbles. The combined response of the bubbles to an external pressure change will result in volume changes leading to a global

* presented at the 1983 ASME Cavitation and Multiphase Flow Forum

accelerating, velocity field. Associated with this velocity field would be pressure gradients which would determine the pressure encountered by individual bubbles within the mixture. It can be shown that such global interactions usually dominate any pressure perturbation experienced by one bubble due to the growth or collapse of a neighbor. The early work of Chahine [1982 a] does not reflect this fact, though in a later paper [Chahine, 1982 b] he does begin to consider the global motion.

We do not intend to resolve these questions in this brief note, but feel it necessary to indicate the lack of established literature on finite clouds of bubbles. In the present note we only wish to delineate the response of a spherical cloud of bubbles to harmonic pressure fluctuations far from the cloud.

2. BASIC EQUATIONS

A number of simplifying assumptions are made in order to construct a soluble set of equations which nevertheless model the interactions between the bubbles and the fluid. First, the relative motion between bubbles and the surrounding fluid is neglected: the limitations this imposes will be discussed in a later publication. Then it follows that velocity, $\underline{v}(\underline{x},t)$, must satisfy the continuity equation

$$\nabla \cdot \underline{v} = \frac{\eta}{1+\eta\tau}\frac{D\tau}{Dt} \tag{1}$$

where η is the number of bubbles per unit volume of the liquid (assumed incompressible with density ρ), $\tau(\underline{x},t)$ the volume of an individual bubble and D/Dt is the material derivative, defined as usual by $\partial/\partial t + \underline{v}\cdot\nabla$. Continuity is written in this form rather than in terms of the void fraction $\alpha = \eta/(1+\eta\tau)$ for the following reasons. Since relative motion is neglected, the population η must satisfy $D\eta/Dt = 0$. Hence the solution of the equations is greatly simplified by considering only those flows in which the population is piecewise constant in a finite number of prescribed material regions. Then, if the values of population η in each of the prescribed material regions is known initially, η remains at those values throughout the motion.

In the equation of motion:

$$\rho \frac{D\underline{v}}{Dt} = -(1+\eta\tau)\nabla p \tag{2}$$

external body forces have been neglected, as have viscous terms. The pressure, $p(\underline{x},t)$, and velocity $\underline{v}(\underline{x},t)$, are defined as the corresponding quantities in the absence of local perturbations caused by the growth of any individual bubble. It is interesting to point out that, due to the particular form of the boundary conditions, the Navier-Stokes equations for the flow considered later are satisfied by an irrotational solution. Hence, the only error introduced by the neglect of viscous terms in equation (2) is related to the small change of the viscosity caused by the presence of the bubbles.

Finally, the bubble volume $\tau = 4\pi R^3/3$ or, more conveniently, its radius $R(\underline{x},t)$, is determined by the Rayleigh-Plesset equation:

$$\frac{p_B - p}{\rho} = R\frac{D^2R}{Dt^2} + \frac{3}{2}\left(\frac{DR}{Dt}\right)^2 + \frac{2S}{\rho R} \tag{3}$$

where viscous effects on the bubble growth have been neglected. Here S is the surface tension and p_B is the pressure within the bubble, consisting of partial pressures of the vapor, p_v, and non-condensable gas, p_G. The former is assumed constant (neglecting thermal effects) and the non-condensable gas is assumed to consist of a constant mass which behaves with a polytropic index q so that $p_G = p_{Go}(R_o/R)^{3q}$ where p_{Go} is the gas partial pressure at a reference radius, R_o. Furthermore, if the reference state is an equilibrium state, then the equilibrium pressure in the liquid is:

$$p_o = p_{Go} + p_v - \frac{2S}{R_o} \tag{4}$$

The system of equations (1), (2), and (3) could in theory be solved for $p(\underline{x},t)$, $\underline{v}(\underline{x},t)$ and $\tau(\underline{x},t)$ when supplemented by suitable boundary conditions and the piecewise constant population, η. In practice the non-linearity of the system causes great difficulties in all but the simplest flows.

3. DYNAMICS OF A BUBBLY CLOUD IN A LIQUID

The problem we now address is that of a spherical cloud of bubbles in an unbounded liquid at rest at infinity as shown in Fig. 1. We only consider the case of very low void fraction, so that $\eta\tau \ll 1$ and the expression $(1+\eta\tau)$ appearing in (1) and (2) can be approximated as unity: then the equations (1) and (2) become:

$$\frac{1}{r^2}\frac{\partial}{\partial r}(r^2 v) = \eta\frac{DR^3}{Dt} \tag{5}$$

$$\frac{\partial v}{\partial t} + v\frac{\partial v}{\partial r} = -\frac{1}{\rho}\frac{\partial p}{\partial r} \tag{6}$$

The radius of the cloud is $A(t)$, where $A(0) = A_o$ is known. The size of the bubbles inside the cloud is a function of both position r and time t, namely $R(r,t)$. For simplicity it is assumed that initially all the bubbles have the same size, $R(r,0) = R_o$. Furthermore we assume that the population per unit liquid volume, η, is uniform and known from the initial conditions. Indeed, if the number of bubbles in the cloud is N, then $\eta = 3N/4\pi(A_o^3 - NR_o^3)$. Outside the cloud where $r \geq A(t)$ there are no bubbles ($\eta = 0$) and the equations reduce to familiar form.

We examine first the linearized form of these equations which will simultaneously provide the response of the cloud to small oscilliations in the pressure at infinity $p_\infty(t)$, and provide the basis for the study of the motion of a cloud in equilibrium when subject to a change in p_∞ which can be represented by a Fourier series or a Fourier integral. Then:

$$R(r,t) = R_o\left[1+\varphi(r,t)\right]; \qquad r < A(t) \tag{7}$$

where $\varphi \ll 1$. Under these circumstances it is readily shown that, since the velocity v is of the order of φ (equation (5)), then the convective component of the material derivative is of order φ^2 and D/Dt can be replaced by $\partial/\partial t$ if only terms of order φ are to be considered. Then it follows from the Rayleigh equation (3) that to order φ:

$$p(r,t) = p_o - \rho R_o^2\left(\frac{\partial^2\varphi}{\partial t^2} + \omega_B^2\right); \qquad r < A(t) \tag{8}$$

where:

$$\omega_B^2 = 3q\frac{p_{Go}}{\rho R_o^2} - \frac{2S}{\rho R_o^3} \tag{9}$$

and ω_B is the natural frequency of oscillation of a single bubble in an infinite liquid [van Wijngaarden, 1972; Knapp, Daily and Hammit, 1970].

If it is assumed that the bubbles are in stable equilibrium in the initial or mean state (p_{Go}, R_o) so that $3qp_{Go} > 2S/R_o$ [Knapp, Daily and Hammit, 1970; Zwick, 1954], then ω_B is real. Finally, upon substitution of (7) and (8) into (5) and (6) and elimination of $v(r,t)$, one obtains the following equation for the function $\varphi(r,t)$ in the domain $r < A(t)$:

$$\frac{1}{r^2}\frac{\partial}{\partial r}\left[r^2\frac{\partial}{\partial r}\left(\frac{\partial^2\varphi}{\partial t^2} + \omega_B^2\varphi\right)\right] - 4\pi\eta R_o\frac{\partial^2\varphi}{\partial t^2} = 0 \tag{10}$$

The incompressible single phase flow outside the bubble cloud ($r \geq A(t)$) must have the standard classical solution of the form:

$$v(r,t) = \frac{C(t)}{r^2}; \qquad r \geq A(t) \tag{11}$$

$$p(r,t) = p_\infty(t) + \frac{\rho}{r}\frac{dC(t)}{dt} + O(C^2(t)); \qquad r \geq A(t) \tag{12}$$

where $C(t)$ is of perturbation order. It follows that, to the first order in $\varphi(r,t)$ the continuity of $v(r,t)$ and $p(r,t)$ at the interface between the cloud and the pure liquid results in the following boundary condition for $\varphi(r,t)$:

$$\left(1 + A_o\frac{\partial}{\partial r}\right)\left(\frac{\partial^2\varphi}{\partial t^2} + \omega_B^2\varphi\right)_{r=A_o} = \frac{p_o - p_\infty(t)}{R_o^2\rho} \tag{13}$$

The linearized solution of equation (10) for small periodic oscillations of frequency ω of the far field pressure in the liquid $p_\infty(t) = p_o + \Re\{\tilde{p}_\infty e^{i\omega t}\}$ takes the form:

$$\varphi(r,t) = -\frac{1}{\rho R_o^2}\Re\left\{\frac{p_\infty}{\omega_B^2 - \omega^2}\frac{e^{i\omega t}}{\cos\lambda A_o}\frac{\sin\lambda r}{\lambda r}\right\}; \qquad r < A_o \tag{14}$$

where:

$$\lambda^2 = 4\pi\eta R_o\frac{\omega^2}{\omega_B^2 - \omega^2} \tag{15}$$

Another possible solution involving $(\cos \lambda r)/\lambda r$ has been eliminated since $\varphi(r,t)$ must clearly be finite as $r \to 0$. Therefore in the domain $r < A_o$:

$$R(r,t) = R_o - \frac{1}{\rho R_o} \Re \left\{ \frac{\tilde{p}_\infty}{\omega_B^2 - \omega^2} \frac{e^{i\omega t}}{\cos \lambda A_o} \frac{\sin \lambda r}{\lambda r} \right\} \tag{16}$$

then:

$$v(r,t) = \frac{1}{\rho} \Re \left\{ i \frac{\tilde{p}_\infty}{\omega} \frac{1}{r} \left(\frac{\sin \lambda r}{\lambda r} - \cos \lambda r \right) \frac{e^{i\omega t}}{\cos \lambda A_o} \right\} \tag{17}$$

$$p(r,t) = p_o - \Re \left\{ \tilde{p}_\infty \frac{\sin \lambda r}{\lambda r} \frac{e^{i\omega t}}{\cos \lambda A_o} \right\} \tag{18}$$

The entire flow has therefore been determined in terms of the prescribed quantities A_o, R_o, η, ω and p_∞.

4. RESULTS

We examine first the natural modes and frequencies of oscillation of the cloud. From (14) note that if $\tilde{p}_\infty$ were zero, oscillations only occur if:

$$\omega = \omega_B \quad \text{or} \quad \lambda_n A_o = (2n-1)\frac{\pi}{2}, \quad n = 0, 1, 2, \ldots \tag{19}$$

It follows from the expression (15) for λ that the natural frequencies, ω_n, of the cloud are: $\omega_\infty = \omega_B$, namely the natural frequency of an individual bubble in an infinite liquid, and:

$$\omega_n = \omega_B \left(1 + \frac{16 \eta R_o A_o^2}{\pi (2n-1)^2} \right)^{-1/2} ; \qquad n = 1, 2, \ldots \tag{20}$$

which is an infinite series of frequencies of which ω_1 is the lowest. The higher frequencies approach ω_B as n tends to infinity.

The lowest natural frequency, ω can be written in terms of the initial void fraction $\alpha_o = \eta \tau_o/(1 + \eta \tau_o) \simeq \eta \tau_o$ (which must be much less than unity for the validity of the analysis) as:

$$\omega_1 = \omega_B \left(1 + \frac{12 \alpha_o A_o^2}{\pi^2 R_o^2} \right)^{-1/2} \tag{21}$$

Hence, the natural frequencies of the cloud will extend to frequencies much smaller than the individual bubble frequency, ω_B, if the initial void fraction, α_o, is much larger than the square of the ratio of bubble size to cloud size ($\alpha_o \gg R_o^2/A_o^2$). If the reverse is the case ($\alpha_0 \ll R_o^2/A_o^2$), all the natural frequencies of the cloud are contained in a small range just below ω_B.

The amplitude of the radial velocity oscillations is proportional to the slope of these curves. Since each bubble is supposed to react to a uniform far field pressure, the validity of the model is limited to wave numbers, n, such that $n \ll A_o/R_o$. Note that the first mode involves almost uniform oscillations of the bubbles at all radial positions within the cloud. Higher modes involve amplitudes of oscillation near the center of the cloud which become larger and larger relative to the amplitudes in the rest of the cloud. In effect, an outer shell of bubbles essentially shields the exterior fluid from the oscillations of the bubbles in the central core, with the result that the pressure oscillations in the exterior fluid are of smaller amplitude for the higher modes.

Fig. 3 shows the forced response amplitude of the bubbles at the center ($r = 0$) and surface of the cloud ($r = A_o$) as a function of frequency, ω, for a typical case of $\alpha_o A_o^2/R_o^2 = 10$. Note the decline in the response at the surface relative to that in the center of the cloud for frequencies less than ω_B. Also note the nodes in the surface response at frequencies between the natural frequencies. The response of the cloud to frequencies greater than ω_B is quite different as illustrated in Fig. 4. Note that, while the entire cloud responses in a fairly uniform manner for $\omega < \omega_B$, only a surface layer of bubbles exhibits significant response when $\omega > \omega_B$. In the latter case the entire core of the cloud is essentially shielded by this outer layer.

5. REFERENCES

Chahine G.L., 1982 a, "Pressure Field Generated by the Collective Collapse of Cavitation Bubbles", IAHR Symp. on Operating Problems of Pump Stations and Power Plants, Amsterdam, Neth., Vol. 1, Paper No. 2.

Chahine G.L., 1982 b, "Cloud Cavitation Theory", 14th Symposium on Naval Hydrodynamics, August 1982, Session I, p. 51.

Hansson I., Kedriniskii V., and Mørch K.A., 1981, "On the Dynamics of Cavity Clusters", J. Phys. D:Appl. Phys., Vol. 15, pp. 1725-1734.

Knapp R.T., Daily J.W. and Hammitt F.G., 1970, "Cavitation", McGraw Hill.

Mørch K.A., 1980, "On the Collapse of Cavity Cluster in Flow Cavitation", Proc. 1st Int. Conf. on Cavitation and Inhomogeneities in Underwater Acoustics, Springer Series in Electrophysics, Vol. 4, pp. 95-100.

Mørch K.A., 1981., " Cavity Cluster Dynamics and Cavitation Erosion", ASME Cavitation and Polyphase Flow Forum. 1981. pp. 1-10.

Mørch K.A., 1982, " Energy Considerations on the Collapse of Cavity Cluster", Applied Scientific Research, 38, p.313.

van Wijngaarden L., 1972, "One-Dimensional Flow of Liquids Containing Small Gas Bubbles", Ann. Rev. Fluid Mech., Vol. 4, pp. 369-396.

van Wijngaarden L., 1964, "On the Collective Collapse of a Large Number of Gas Bubbles in Water", Proc. 11th Int. Cong. Appl. Mech., Springer-Verlag, Berlin, pp. 854-861.

Zwick S.A., 1954, "The Growth and Collapse of Vapor Bubbles", Calif. Inst. of Tech. Hydro. Lag. Rep. 21-19.

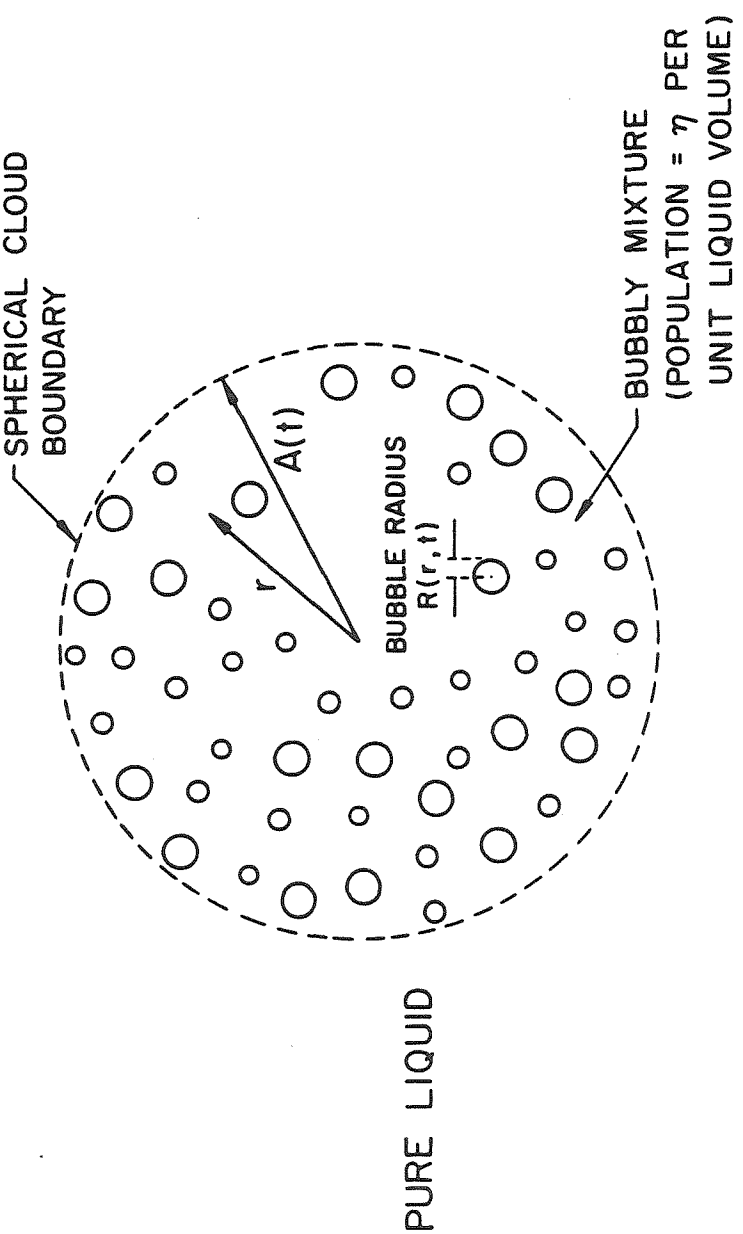

Figure 1. Schematic of a spherical cloud of bubbles.

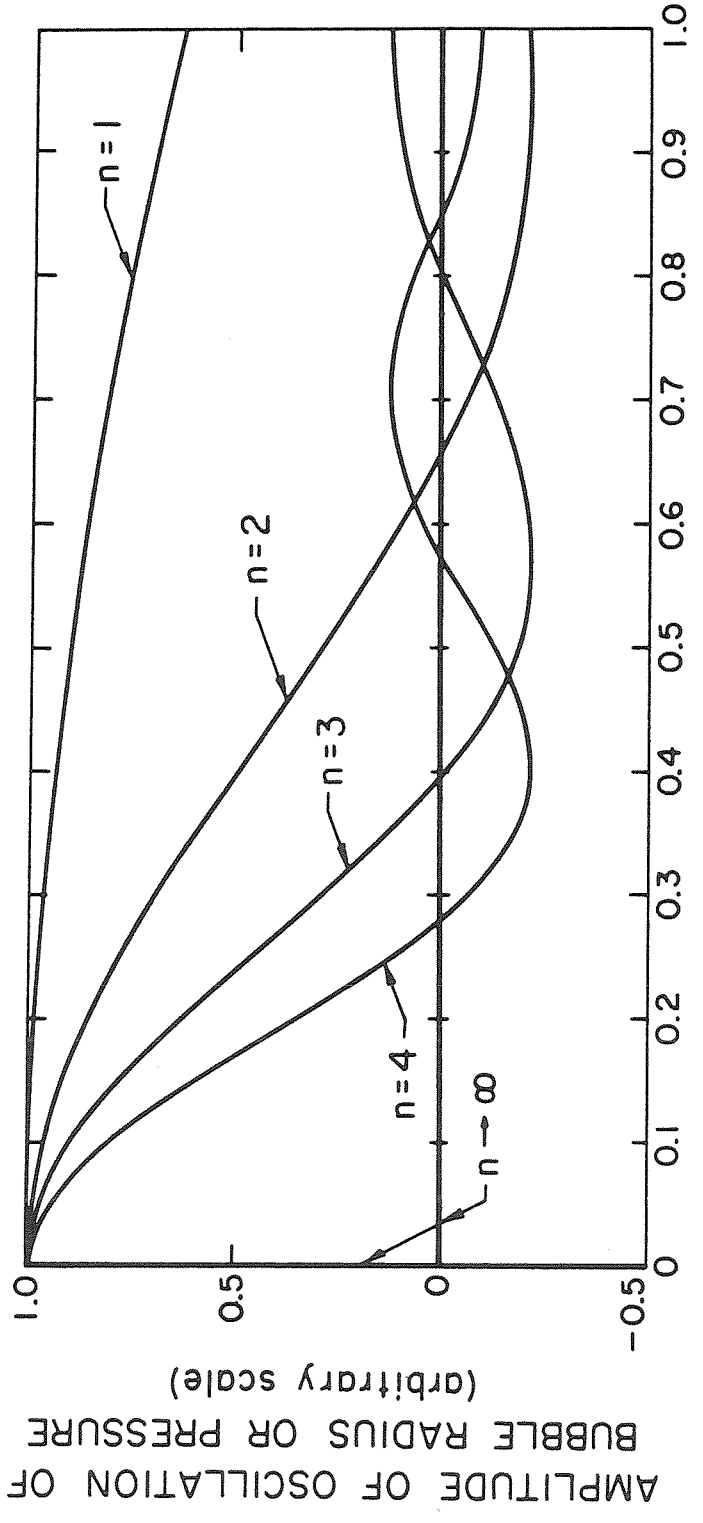

Figure 2. Natural mode chapes as a function of radial position within the bubble cloud. The arbitrary vertical scale represents the amplitude of the bubble radius oscillations and the of the pressure oscillations for modes $n = 1, 2, 3, 4$ and $n \to \infty$. The slopes of these waves are proportional to the radial velocity oscillations.

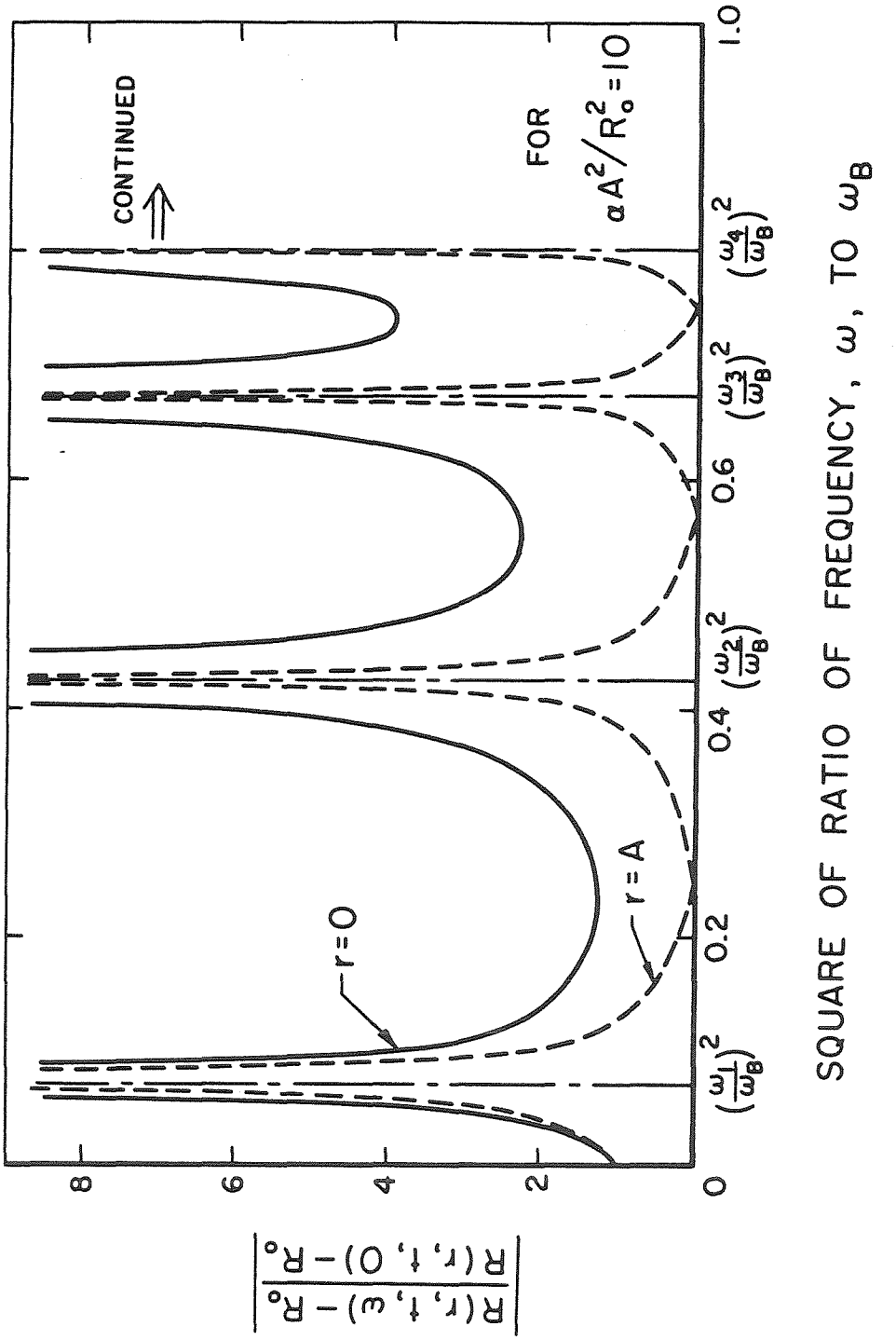

Figure 3. Forced response of a bubble cloud as a function of $(\omega/\omega_B)^2$. Amplitudes of the normalized bubble radius oscillations at the center ($r = 0$) and surface ($r = A_o$) of the cloud are shown for the case of $\alpha_o A_o^2/R_o^2 = 10$.

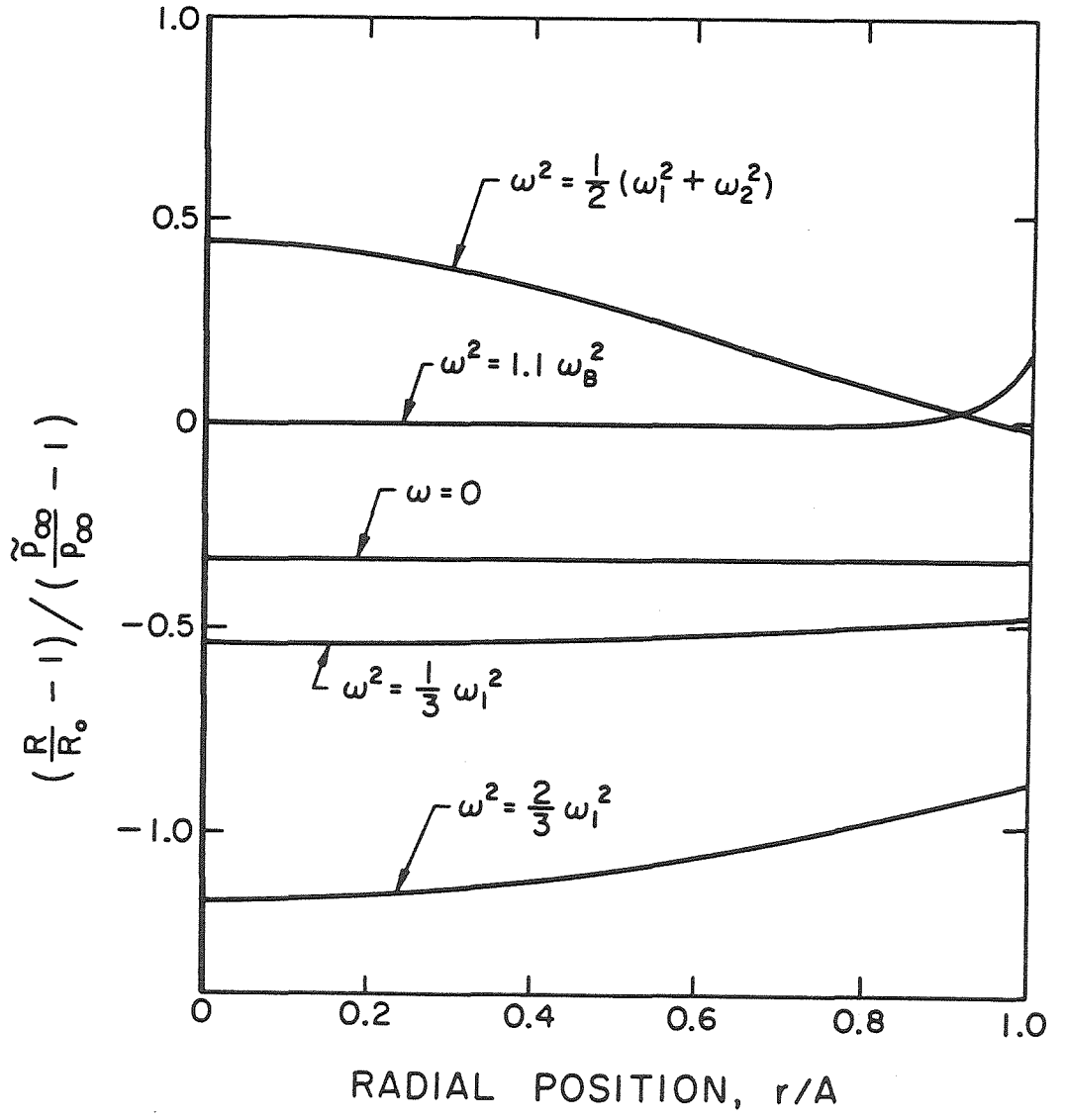

Figure 4. Forced response of the bubble radius oscillations as a function of radial position within the cloud for various frequencies, ω, as indicated (for the case $\alpha_o A_o^2/R_o^2 = 10$).

Appendix 5.

LINEARIZED DYNAMICS OF TWO-DIMENSIONAL BUBBLY AND CAVITATING FLOWS OVER SLENDER SURFACES*

by Luca d'Agostino, Christopher E. Brennen and Allan J. Acosta

California Institute of Technology
Pasadena, California 91125

1. INTRODUCTION

This paper represents part of a study of the rôle of the dynamics of bubble volume changes in the fluid mechanics of bubbly or cavitating flows. Specifically it investigates the effects of the inclusion of the bubble dynamic response in two-dimensional steady flows over surfaces with slender profiles. One of the practical objectives of this study is a better understanding of the global effects of many bubbles in cavitating flows. Traditionally bubbly cavitating flows have been analyzed starting with a calculated or measured pressure distribution from the non-cavitating or single phase flow around, say, a hydrofoil. This is then applied as a known input to the Rayleigh-Plesset equation in order to calculate the bubble volume as a function of position along a streamline. This traditional approach neglects the interactive effect which the bubble growth may have on the pressure distribution, an effect which will increase in magnitude with the number and the extent of the bubbles. While the traditional approach may have

* submitted to the Journal of Fluid Mechanics on 10.29.1987

validity close to cavitation inception when only an occasional bubble occurs, it clearly loses validity as the cavitation becomes more extensive. Significant alterations will occur in the pressure distribution and in the geometry of the region of cavitation. In water tunnel tests Gates, 1977, observed that laminar separation of the boundary layer on a hemispherical-nosed body was delayed and ultimately eliminated by increasing the number of small bubbles or nuclei present. Moreover, separate tests in which the free stream velocity was varied suggest that the above phenomenon was not caused by the "turbulence" produced by the bubbles. Rather the observations suggest that the bubbles alter the pressure distribution in such a way as to delay separation. These observations have critical consequences for cavitation inception estimations because of the intimate relation between the cavitation inception number and the coefficient of pressure at the laminar separation point [Arakeri and Acosta, 1973]. More recent experimental observations by Arakeri and Shanmuganathan, 1985, and Billet, 1986, have also helped identify the bubble interaction effects in cavitating flows. The photograph and acoustic measurements of Arakeri and Shanmuganathan clearly demonstrate that increasing the number of bubbles decreases their growth and results in a decline of the noise produced per bubble.

One of the objectives of this paper is to provide some guidance as to the nature of these alterations. Despite the extensive linearizations inherent in the analysis we believe that the results convey some qualitative understanding of the nature of the changes which occur in a real cavitating flow.

. The last few decades have seen extensive research on the dynamics of bubbly flows [van Wijngaärden, 1968, 1972]. Early studies based on space averaged equations for the mixture in the absence of relative motion between the two phases [Tangren, Dodge and Seifert, 1949] do not consider bubble dynamic effects. This approach simply leads to an equivalent compressible homogeneous medium. In a classic paper Foldy, 1945, accounted for the dynamics of individual bubbles treating them as randomly distributed point scatterers. Assuming that

the system is ergodic, the collective effect of bubble dynamic response on the flow is then obtained by taking the ensemble average over all possible configurations. An alternative way to account for bubble dynamic effects is to include the Rayleigh-Plesset equation in the space averaged equations. Both methods have been successfully applied to describe the propagation of one-dimensional disturbances through liquids containing small gas bubbles [Carsternsen and Foldy, 1947; Fox, Curley and Larson, 1955; Macpherson, 1957; Silberman, 1957].

However, because of their complexity, there are few reported examples of the application to specific flow geometries of the space averaged equations which include the effects of bubble response [van Wijngaärden, 1964]. One exception is the shock wave in a bubbly medium. A number of authors have studied this one-dimensional and time-independent (or slowly varying) flow; a good review of the current state of knowledge of bubble dynamic effects on the structure and evolution of shock waves can be found in Noorddzij, 1973. Noorddzij and van Wijngaärden, 1974, have shown that the additional inclusion of relative motion between the bubbles and the liquid can lead to some interesting evolutionary effects and permanent wave solutions. However in the present program we focus attention on one or two-dimensional time dependent flows. In two earlier notes [d'Agostino and Brennen, 1983; d'Agostino, Brennen and Acosta, 1984] we considered the one-dimensional time dependent linearized dynamics of a spherical cloud of bubbles subject to an harmonic pressure field and the two-dimensional steady flow of a bubbly liquid over wave-shaped surfaces. The results clearly show that the fluid motion can be critically controlled by bubble dynamic effects. Specifically, the dominating phenomenon consists of the combined response of the bubbles to the pressure in the surrounding liquid, which results in volume changes leading to a global accelerating velocity field. Associated with this velocity field is a pressure gradient which in turn determines the pressure encountered by each individual bubble in the mixture. Furthermore, it can be shown that such global interactions usually dominate any local pres-

sure perturbations experienced by one bubble due to the growth or collapse of a neighbor (see Section 7).

In the present work the same approach, generalized with the inclusion of dissipative effects in the dynamics of the bubbles, is first applied to steady two-dimensional flows over wave-shaped surfaces (for which there exist well established solutions for the compressible and incompressible cases) and then is extended to the case of arbitrarily shaped surfaces with slender profiles. Despite all its intrisic limitations, the following linear analysis indicates some of the fundamental phenomena involved and represents a useful basis for the study of the such flows with non-linear bubble dynamics, which we intend to discuss in a later publication.

2. BASIC EQUATIONS

Following the same approach previously indicated in our earlier notes [d'Agostino and Brennen, 1983; d'Agostino, Brennen and Acosta, 1984], several simplifying assumptions are introduced to obtain a soluble set of equations which still reflects the effects of bubble dynamic response. The relative motion of the two phases is neglected, although its inclusion is also possible (the limitations this imposes are discussed in Section 7). The liquid is assumed inviscid and incompressible, with density, ρ, and constant population, β, of bubbles per unit liquid volume. Also, all damping mechanisms in the dynamics of the bubbles are initially neglected. Then, if external body forces are unimportant, the velocity, $\underline{v}(\underline{x})$, and the pressure, $p(\underline{x})$, (defined as the corresponding quantities in the liquid in the absence of local perturbations due to any neighbouring bubbles), satisfy the continuity and momentum equations in the form:

$$\nabla \cdot \underline{v} = \frac{\beta}{1+\beta\tau}\frac{D\tau}{Dt} \tag{1}$$

$$\rho\frac{D\underline{v}}{Dt} = -(1+\beta\tau)\nabla p \tag{2}$$

where $\tau(\underline{x})$ is the individual bubble volume and D/Dt indicates the Lagrangian derivative. Finally, under the additional hypothesis that the bubbles remain spherical, it follows that $\tau = 4\pi R^3/3$, with the bubble radius, $R(\underline{x})$, determined by the Rayleigh-Plesset equation, [Plesset and Prosperetti, 1977; Knapp, Daily and Hammit, 1970]:

$$\frac{p_B - p}{\rho} = R\frac{D^2R}{Dt^2} + \frac{3}{2}\left(\frac{DR}{Dt}\right)^2 + \frac{2S}{\rho R} \tag{3}$$

Here S is the surface tension and p_B is the bubble internal pressure, which consists of the partial pressures of the vapor, p_v, and non-condensable gas, p_G. Neglecting thermal and mass diffusion effects within the bubbles, p_v is assumed constant and p_G is expressed by the polytropic relation of index q: $p_G = p_{Go}(R/R_o)^{3q}$, where p_{Go} is the gas partial pressure at the reference radius R_o

Equations (1), (2) and (3), together with suitable boundary conditions, represent, in theory, a complete system of equations for $\underline{v}(\underline{x})$, $p(\underline{x})$ and $\tau(\underline{x})$. However, in practice their highly non-linear nature requires further simplifications for a closed form solution to be attained even for very simple flows.

3. DYNAMICS OF BUBBLY FLOWS OVER SURFACES WITH SLENDER PROFILE

We consider first the problem of a two-dimensional inviscid flow of a bubbly liquid over a wave-shaped surface, as shown in Fig. 1. Let the wall profile be defined in complex notation by the equation: $\eta(x) = \varepsilon \exp(ikx)$ with $k\varepsilon \ll 1$ and let the subscript o indicate the unperturbed condition corresponding to $\varepsilon = 0$. Then, if the flow velocity is U_o and assuming, for simplicity, that all the bubble have the same radius, R_o, the undisturbed pressure in the liquid is:

$$p_o = p_{Go} + p_v - \frac{2S}{R_o} \tag{4}$$

We limit our analysis to the case of very low void fraction ($\beta\tau \ll 1$), so that the expression $1 + \beta\tau$ in equations (1) and (2) can be approximated as unity.

We also make use of first order small perturbation theory, writing the velocity components as $u(x,y) = U_o + u'(x,y)$ and $v(x,y) = v'(x,y)$, with u' and v' much smaller than U_o. Here the pressure changes are not restricted to be small with respect to the equlibrium pressure because large perturbations of the pressure can result from the velocity field generated by the bubble volume changes, even though only small modifications of the fully wetted velocity field actually occur in low void fraction flows. Then equations (1), (2) and (3) reduce to:

$$\frac{\partial u'}{\partial x} + \frac{\partial v'}{\partial y} = 4\pi\beta U_o R^2 \frac{\partial R}{\partial x} \tag{5}$$

$$\rho U_o \frac{\partial u'}{\partial x} = -\frac{\partial p}{\partial x} \tag{6}$$

$$\rho U_o \frac{\partial v'}{\partial x} = -\frac{\partial p}{\partial y} \tag{7}$$

$$p = p_v + p_{Go}\left(\frac{R_o}{R}\right)^{3q} - \frac{2S}{R} - \rho U_o^2\left[R\frac{\partial^2 R}{\partial x^2} + \frac{3}{2}\left(\frac{\partial R}{\partial x}\right)^2\right] \tag{8}$$

Finally, eliminating u' and v' from (5), (6) and (7) and using (8), one obtains the following equation for $R(x,y)$:

$$\nabla^2\left\{R\frac{\partial^2 R}{\partial x^2} + \frac{3}{2}\left(\frac{\partial R}{\partial x}\right)^2 + \frac{1}{\rho U_o^2}\left[\frac{2S}{R} - p_{Go}\left(\frac{R_o}{R}\right)^{3q}\right]\right\} - \frac{4\pi\beta}{3}\frac{\partial^2 R^3}{\partial x^2} = 0 \tag{9}$$

where ∇^2 is the two-dimensional Laplacian. Furthermore, the linearized kinematic condition at the wall: $v(x, y_w)/U_o = d\eta/dx$ results in the following boundary condition for $R(x,y)$:

$$\frac{\partial}{\partial y}\left\{R\frac{\partial^2 R}{\partial x^2} + \frac{3}{2}\left(\frac{\partial R}{\partial x}\right)^2 + \frac{1}{\rho U_o^2}\left[\frac{2S}{R} - p_{Go}\left(\frac{R_o}{R}\right)^{3q}\right]\right\}_{y=y_w} = \frac{d^2\eta}{dx^2} \tag{10}$$

where y_w is the ordinate of the wall profile corresponding to $\varepsilon = 0$. In addition the solution is required to be periodic in x with wave number k.

The non-linear equations (9) and (10) do not have any known analytical solution. In order to investigate their fundamental behaviour, we therefore examine the linearized form of these equations for small changes of the bubble

radius: $R(x,y) = R_o[1+\varphi(x,y)]$, where $\varphi(x,y) \ll 1$. Then, to the first order in φ:

$$\nabla^2\left(\frac{\partial^2\varphi}{\partial x^2} + \frac{\omega_B^2}{U_o^2}\varphi\right) - 4\pi\beta R_o\frac{\partial^2\varphi}{\partial x^2} = 0 \tag{11}$$

$$\frac{\partial}{\partial y}\left(\frac{\partial^2\varphi}{\partial x^2} + \frac{\omega_B^2}{U_o^2}\varphi\right)_{y=y_w} = \frac{1}{R_o^2}\frac{d^2\eta}{dx^2} \tag{12}$$

where ω_B is the natural frequency of oscillation of a single bubble in an unbounded liquid, [Plesset and Prosperetti, 1977; Knapp, Daily and Hammit, 1970]:

$$\omega_B^2 = 3q\frac{p_{Go}}{\rho R_o^2} - \frac{2S}{\rho R_o^3} \tag{13}$$

If the bubbles are in stable equilibrium in their mean or unperturbed state, then $3qp_{Go} > 2S/R_o$ and ω_B is real. The linearized solution of equation (11) for the case of an unbounded bubbly flow over a wave-shaped wall is:

$$\varphi(x,y) = k\varepsilon\frac{1-\alpha_o}{3\alpha_o}\frac{1-G^2}{G}e^{ikx-Gky}; \qquad y \geq 0 \tag{14}$$

Here G is the principal square root (with non-negative real and imaginary parts) of:

$$G^2 = 1 - M^2 = 1 - \frac{3\alpha_o}{1-\alpha_o}\frac{U_o^2/R_o^2}{\omega_B^2 - k^2U_o^2} \tag{15}$$

where M can be shown to be the flow Mach number based on the sonic speed corresponding to the frequency $\omega = kU_o$ experienced by each bubble during its motion past the wavy surface. The other possible solution involving $\exp(ikx + Gky)$ has been eliminated since in the subsonic regime $\varphi(x,y)$ must be finite as $y \to +\infty$ and in the supersonic regime no disturbance can propagate from the wall in the upstream direction. Therefore in the domain $y \geq 0$:

$$R(x,y) = R_o + R_o k\varepsilon\frac{1-\alpha_o}{3\alpha_o}\frac{1-G^2}{G}e^{ikx-Gky} \tag{16}$$

$$u(x,y) = U_o + U_o k\varepsilon\frac{e^{ikx-Gky}}{G} \tag{17}$$

$$v(x,y) = iU_o k\varepsilon e^{ikx-Gky} \tag{18}$$

$$p(x,y) = p_o - \rho U_o^2 k\varepsilon \frac{e^{ikx-Gky}}{G} \tag{19}$$

In the case of a wave-shaped channel of semi-width b, the symmetry about the centerline $y = b$ provides the second boundary condition for the velocity: $v(x,b) = 0$ and the linearized solution of equation (11) takes the form:

$$R(x,y) = R_o + R_o k\varepsilon \frac{1-\alpha_o}{3\alpha_o} \frac{1-G^2}{G} \frac{\cosh Gk(b-y)}{\sinh Gkb} e^{ikx} \tag{20}$$

$$u(x,y) = U_o + U_o k\varepsilon \frac{\cosh Gk(b-y)}{\sinh Gkb} \frac{e^{ikx}}{G} \tag{21}$$

$$v(x,y) = iU_o k\varepsilon \frac{\sinh Gk(b-y)}{\sinh Gkb} e^{ikx} \tag{22}$$

$$p(x,y) = p_o - \rho U_o^2 k\varepsilon \frac{\cosh Gk(b-y)}{\sinh Gkb} \frac{e^{ikx}}{G} \tag{23}$$

Due to the linear nature of the problem, the above solution can readily be generalized to the case of surfaces with arbitrary slender boundaries. If the wall profile is denoted by $\eta(x)$ and $H(k)$ is the Fourier transform of $\eta(x)$ such that in complex notation:

$$\eta(x) = \int_0^{+\infty} H(k) e^{ikx}\, dk \tag{24}$$

then the linearized solution $f(x,y)$ of equation (11) admits the following integral representation:

$$f(x,y) = \int_0^{+\infty} H(k) f_k(x,y,k)\, dk \tag{25}$$

where $f_k(x,y,k)$ is the corresponding wavy surface solution for given k and $\varepsilon = 1$. Thus, for instance, the normalized bubble radius for the semi-infinite and channel flow cases is:

$$\varphi(x,y) = \int_0^{+\infty} H(k) \frac{1-\alpha_o}{3\alpha_o} \frac{1-G(k)^2}{G(k)} e^{ikx-G(k)ky}\, dk \tag{26}$$

$$\varphi(x,y) = \int_0^{+\infty} H(k) \frac{1-\alpha_o}{3\alpha_o} \frac{1-G(k)^2}{G(k)} \frac{\cosh G(k)k(b-y)}{\sinh G(k)kb} e^{ikx}\, dk \tag{27}$$

respectively. The integrands in the above equations have integrable square root singularities corresponding to the sonic condition $k = k^*$ and to the bubble resonance condition $k = k_B$. The latter also corresponds to the essential singularity

due to the pole of G which appears in the argument of the exponential and hyperbolic functions. In equation (27) the additional singularities due to the finite wall spacing $k = k_n$ behave as simple poles. Therefore the above integrals are difficult to compute numerically in their current form. In physical terms this reflects the fact that the present theory allows the bubble radius response to grow unbounded at bubble resonance conditions. As shown later, this difficulty is eliminated by the introduction of dissipative effects which limit the bubble response and generate a complex G^2, thus removing the singularity from the real axis.

Energy dissipation in bubbly flows naturally originates from various sources such as viscosity, heat and mass transfer in the two phases and sound radiation from the bubbles. In particular, viscous effects occur due to the interaction of the flow with the boundaries, to the relative velocity of the two phases, or as a consequence of the motion induced by the volume changes of the bubbles. In the further development of the theory of bubbly liquids over surfaces with slender profiles we only consider the most important forms of damping occurring in the dynamics of the bubbles. However, to the same order of approximations used here, the inclusion of the relative motion is indeed possible, as we intend to discuss in a later work where we consider the simultaneous solution of the fluid dynamic equations for the two phases with the relevant interaction terms. The results of this analysis show that the relative motion slightly modifies the expression of the Mach number parameter G^2 and generates as expected additional damping, but that its overall effects on the flow are usually quite small.

In order to account for dissipation effects in bubble dynamics, the Rayleigh-Plesset equation (3) is modified as suggested by Prosperetti, 1984:

$$\left(1-\frac{\dot{R}}{c}\right)R\ddot{R}+\frac{3\dot{R}^2}{2}\left(1-\frac{\dot{R}}{3c}\right)= \\ =\left(1+\frac{\dot{R}}{c}\right)\frac{p_R(t)+p(t+R/c)}{\rho}+\frac{R}{\rho c}\frac{dp_R(t)}{dt} \qquad (28)$$

where $p_R(t)$ is the liquid pressure at the bubble surface, related to the internal pressure p_B (assumed uniform) by:

$$p_B(t) = p_R(t) + \frac{2S}{R} + 4\mu\frac{\dot{R}}{R} \tag{29}$$

Here dots denote Lagrangian time derivatives, μ is the viscosity and c the speed of sound of the pure liquid. Linearization for small steady state changes under the action of a periodic pressure perturbation $p(t) = p_o(1 - \sigma \exp i\omega t)$ leads to modelling each individual gas bubble as a linear harmonic oscillator:

$$\ddot{\varphi}(t) + 2\lambda\dot{\varphi}(t) + \omega_{B\omega}^2\varphi(t) = \delta\sigma e^{i\omega t} \tag{30}$$

with internal pressure: $p_B(t) = p_{Bo}[1 - \phi\varphi(t)]$ where:

$$2\lambda = \frac{4\mu}{\rho R_o^2} + \frac{\omega^2 R_o}{c} + \frac{p_{Bo}}{\rho\omega R_o^2}\Im(\phi) \tag{31}$$

$$\omega_{B\omega}^2 = \frac{p_{Bo}}{\rho R_o^2}\left(\Re(\phi) - \frac{2S}{R_o p_{Bo}}\right) \tag{32}$$

$$\delta = \frac{p_o}{\rho R_o^2}\left(1 - i\frac{\omega R_o}{c}\right) \tag{33}$$

$$\phi = \frac{3\gamma\theta^2}{\theta[\theta + 3(\gamma-1)A_-] - i3(\gamma-1)(\theta A_+ - 2)} \tag{34}$$

$$A_\pm = \frac{\sinh\theta \pm \sin\theta}{\cosh\theta - \cos\theta} \tag{35}$$

and $\theta = R_o\sqrt{(2\omega/\chi_G)}$ is the ratio of the bubble radius to the bubble thermal diffusion length. The three terms of the effective damping coefficient, λ, respectively represent the contributions of the viscous, acoustical and thermal dissipation, while $\omega_{B\omega}$ is the effective natural frequency of the oscillator when excited at frequency ω. Finally, the complex parameters δ, ϕ and σ account for the magnitude ratio and phase difference between the related quantities. In particular, $\Re(\phi)/3$ can be interpreted as the effective polytropic exponent of the gas in the bubble [Prosperetti, 1984].

By means of the Galilean transformation $\underline{x} = \underline{v}(\underline{x})t + const.$ the above theory can be readily applied to the case of a bubbly flow over a wave-shaped surface. Here the frequency of the Lagrangian pressure change experienced by each bubble during its motion is: $\omega = kU_o$ and the following linearized approximations: $D/Dt \simeq U_o(\partial/\partial x)$, $D^2/Dt^2 \simeq U_o^2(\partial^2/\partial x^2)$ can be used to express the Lagrangian derivatives in the Eulerian coordinates. Upon the assumption of a $2\pi/k$-periodic behaviour in the x-direction, damping can be incorporated in the theory for the linearized dynamics of bubbly flows over surfaces with slender profile. The previous approach simply leads to the same formal expressions (16)-(27) of the solution for the flow quantities, with a generalized definition of the Mach number parameter:

$$G^2 = 1 - M^2 = 1 - \frac{3\alpha_o}{1-\alpha_o}\frac{(1 - ikU_oR_o/c)U_o^2/R_o^2}{\omega_{B\omega}^2 - k^2U_o^2 + i2\lambda kU_o} \tag{36}$$

which now becomes complex. It can be shown that $\Im(G^2) \geq 0$, thus, with the same convenction as before, $\Re(G) \geq 0$ and $\Im(G) \geq 0$.

The entire flow has therefore been determined in terms of the material properties of the phases, the geometry of the wall profile and of the assigned quantities: β, R_o, U_o and p_o.

4. RESULTS FOR UNDAMPED BUBBLE DYNAMICS

We now examine the nature of the above solution considering first the undamped case. From equations (16) and (20) note that the bubble response is singular when:

(i) $G^2 = 0$ and therefore the flow Mach number is equal to unity (sonic condition);

(ii) $(kU_o/\omega_B)^2 = 1$, namely the exciting frequency experienced by each bubble during its motion is equal to the natural frequency of an individual bubble in an infinite liquid (bubble resonance condition). In addition, the channel flow is also singular when:

(iii) $Gkb = in\pi; \qquad n = 0, \pm 1, \pm 2, \ldots$

The above conditions can be interpreted in two different ways according to whether the free stream velocity or the wall wave number is assumed to be the independent variable. The former is the natural approach to the analysis of a given geometrical configuration at different flow regimes; the latter reflects the point of view used in deducing the solution for a more complex wall shape in terms of linear superposition of the different harmonic components of the wall profile.

Since the population is related to the initial void fraction $\alpha_o = \beta\tau_o/(1 + \beta\tau_o)$, G^2 can be considered as a function of the reduced frequency kU_o/ω_B and one of the following two parameters: $3\alpha_o/k^2R_o^2$ when the wall geometry is fixed, or $3\alpha_o U_o^2/\omega_B^2 R_o^2$ when the flow velocity is constant. Consequently, equations (i) and (ii) can be used to deduce either the free stream velocities or the wall wave numbers which respectively correspond to sonic and bubble resonance conditions:

$$U_o^{*2} = \frac{\omega_B^2/k^2}{1 + 3\alpha_o/k^2R_o^2}; \qquad k^{*2} = \frac{\omega_B^2}{U_o^2}\left(1 - \frac{3\alpha_o U_o^2}{\omega_B^2 R_o^2}\right) \tag{37}$$

$$U_{oB}^2 = \frac{\omega_B^2}{k^2}; \qquad k_B^2 = \frac{\omega_B^2}{U_o^2} \tag{38}$$

Similarly, for channel flow, conditions (iii) define the natural modes of the system, leading to infinite series of free stream velocities or wall wave numbers:

$$U_{on}^2 = \frac{\omega^2}{k^2}\left(\frac{1 + 3\alpha_o/k^2R_o^2}{1 + (n\pi/kb)^2}\right) \tag{39}$$

$$k_n^2 = \frac{1}{2}\left[k^{*2} - \frac{n^2\pi^2}{b^2} + \sqrt{\left(k^{*2} - \frac{n^2\pi^2}{b^2}\right)^2 + 4\frac{n^2\pi^2}{b^2}\frac{\omega_B^2}{U_o^2}}\right] \tag{40}$$

where $n = 0, 1, 2, \ldots$ For large n these series respectively converge to the free stream velocity and the wall wave number corresponding to the bubble resonance conditions. For small n the behaviour of these series is regulated by the values

of $3\alpha_o/k^2R_o^2$ or $3\alpha_o U_o^2/\omega_B^2 R_o^2$, which account for the relative importance of compressibility effects in the flow. When these parameters are of order unity or larger, the lower terms of the above series will in general extend to values much smaller than the ones given by the bubble resonance condition (ii), thus indicating that the natural modes can occur at comparatively low frequency. On the other hand, when the reverse is the case, compressibility effects are less significant, and all the terms of these series are contained in a small range below bubble resonance conditions. In this case all the natural modes of the system occur with a frequency only slightly lower than the bubble resonance frequency.

The occurrence of bubble resonance and the presence of a finite sound speed divide the flow solutions in three different regimes, namely: subsonic $(0 < G^2 < 1)$, supersonic $(G^2 < 0)$ and super-resonant $(G^2 > 1)$. As we shall see later, this has significant consequences on the behaviour of the flow. In the subsonic regime the wall disturbances can propagate in the upstream direction and the flow parameters resemble the ones of an incompressible flow, with the bubble response essentially in phase with the excitation. On the other hand, in the supersonic flows, where the perturbations cannot travel upstream, the typical delayed response of compressible flows appears and internal modes occur in the presence of suitable boundary conditions. Finally, in super-resonant flows the bubbles do not have time to respond as quickly as the excitation requires and the flow shows again the characteristics of incompressible flows, although the bubble response in this case tends to be out of phase with respect to the excitation.

The bubble response is maximum near bubble resonance conditions and, when damping is present, tends to be more localized in the proximity of the excitation source. The propagation of disturbances is also strongly affected by the dispersive nature of the sonic speed reflected in the frequency dependence of the Mach number parameter G^2 in equations (15) and (36). In general the wall profile can excite the flow over a wide range of frequencies, depending on

its shape and on the free stream velocity. The spectral components of the wall profile excitation for which the flow is more nearly sonic tend to travel larger distances before being attenuated. Usually the sonic regime is close to the bubble resonance condition and its effects are therefore difficult to isolate, unless the parameters $3\alpha_o/k^2R_o^2$ or $3\alpha_o U_o^2/\omega_B^2 R_o^2$ are of order unity. For this to happen relatively large flow velocities and void fractions are in general necessary, as discussed in Section 7.

Let us consider first the case of fixed wall geometry and variable free stream velocity. Then the behaviour of the parameter G^2 as a function of the reduced frequency is shown in Fig. 2 for some typical values of $3\alpha_o/k^2R_o^2$. Note that all curves start from unity at the origin and tend to move away from their horizontal asymptote $G^2 = 1$ (corresponding to the incompressible flow case) as the value of $3\alpha_o/k^2R_o^2$ increases. Also note that G^2 always changes sign at sonic and bubble resonance conditions, i.e. at the transition between different flow regimes. The corresponding amplitudes of bubble radius oscillations at the wall ($kx = \pi/4$ and $y = 0$) for the case of a semi-infinite flow with $k\varepsilon/2\pi = .01$ are shown in Fig. 3, which also shows the migration of the sonic singularity from the bubble resonance condition towards the origin for increasing values of the parameter $3\alpha_o/k^2R_o^2$. Finally, the bubble radius response in the case of the channel flow is significantly different, as illustrated by Fig. 4, because of the presence of the additional resonances (iii) introduced by the finite spacing between the boundaries.

We assume next that the free stream velocity is fixed and the wall wave number is allowed to vary. In this case the curves representing the parameter G^2 as a function of the reduced frequency, now shown in Fig. 5, again display the tendency to move away from the horizontal asymptote $G^2 = 1$ as the value of the parameter $3\alpha_o U_o^2/\omega_B^2 R_o^2$ increases. However, the value at the origin now depends on the free stream velocity and can be either positive, zero or negative according to whether the flow is respectively subsonic, sonic or supersonic. The

normalized bubble radius response amplitudes at the wall ($kx = \pi/4$ and $y = 0$) for the case of a semi-infinite flow with $k\varepsilon/2\pi = .01$ are shown in Fig. 6. Here, as expected from the above considerations, when the free stream velocity increases the sonic resonance moves from the bubble resonance conditions to the origin and finally disappears for supersonic flows.

The parameter G^2 also controls another important aspect of the flow, namely the penetration of wall induced disturbances in the y-direction, which equations (16) and (20) show to be inversely proportional to $\Re(G)k$. In effect, when $\Re(G)$ is considerably larger than unity the response of the layer of bubbles near the wall essentially shields the rest of the mixture, with the result that the penetration of the disturbances induced by the wall is significantly reduced. On the other hand, as $\Re(G)$ approaches zero near sonic conditions, the perturbations due to the wall tend to affect the whole flow.

5. RESULTS WITH BUBBLE DAMPING

In general terms the introduction of energy dissipation in the bubble dynamics has the consequence of bounding the bubble response at the resonance condition, of providing smooth transitions between the various regimes and of eliminating higher order internal modes. In the rest of this section we consider the case of air bubbles ($\gamma = 1.4$, $\chi_G = 0.0002\,\mathrm{m^2/s}$) in water ($\rho = 1000\,\mathrm{kg/m^3}$, $\mu = 0.001\,\mathrm{N\,s/m^2}$, $S = 0.0728\,\mathrm{N/m}$, $c = 1485\,\mathrm{m/s}$). The other relevant flow parameters are: $p_o = 10^5\,\mathrm{Pa}$, $R_o = 0.001\,\mathrm{m}$, $\varepsilon = 0.001\,\mathrm{m}$ and, when applicable, $k = 20\pi\,\mathrm{m^{-1}}$, $U_o = 250\,\mathrm{m/s}$. Further comment on the dimensionless variables and practical values of both the dimensionless and dimensional variables is included at the end of Section 7.

In the damped case the effective bubble resonance frequency, $\omega_{B\omega}(\omega)$, equation (32), is a function of the exciting frequency, $\omega = kU_o$, and extends from the value corresponding to isothermal conditions in the bubbles ($\omega = 0$ and $\phi = 3$), equal to the definition in the absence of damping, to the isentropic value reached

in the limit for $\omega \to +\infty$. In what follows, normalization has been carried out with respect to the bubble resonance frequency, ω_B, defined as the solution of the equation: $\omega_B = \omega_{B\omega}(\omega_B)$. This choice has no special meaning, but preserves the occurrence of bubble resonance for $kU_o/\omega_B = 1$, with the advantage of making the plots for the damped case more readily comparable to the corresponding ones in the absence of damping.

We now examine the solution for the flow over wave-shaped surfaces with damped bubble dynamics. Since most of the phenomena manifest in the undamped solutions are still relevant, we will limit ourselves to the illustration of the main differences introduced by the inclusion of dissipative effects. Let us again consider first the case of fixed wall geometry and variable free stream velocity. The parameter $|G^2|$ in Fig. 8 no longer goes to zero and infinity at sonic and bubble resonance conditions; instead it passes through a minimum and a maximum, which separate the various flow regimes. The different behaviour of the solution in the subsonic, supersonic and super-resonant regimes is now reflected in the relative importance of the real and imaginary parts of G^2, which change rapidly at the transition from one regime to the next, as shown in Fig. 9. In particular, the comparatively large value of $\Im(G^2)$ is related to the propagation of flow disturbances from the wall in the downstream direction at a relatively shallow angle, which is typical of the supersonic regime. On the other hand, the large value of $\Re(G^2)$ reflects the fact that "compressibility effects" are relatively unimportant and that flow disturbances propagate away from the wall in a nearly normal direction, as happens in the subsonic and super-resonant cases. As expected, the flow response is no longer singular when energy dissipation is taken into account. The amplitudes of the bubble radius oscillation at the wall ($y = 0$) for a semi-infinite flow are shown in Fig. 10 and simply display a first maximum at sonic conditions and a second more pronounced one corresponding to the bubble resonance. Similarly, in the the bubble radius response of Fig. 11 for the channel flow case, all but the lowest resonances due to the

internal motion are virtually eliminated by the presence of dissipative effects. The same phenomena were manifest when the free stream velocity is fixed and the wall wave number is allowed to vary.

In all cases, increasing the void fraction substantially decreases the amplitude of bubble growth. As mentioned in the introduction, this phenomenon has been observed experimentally by Arakeri and Shanmuganathan, 1985, and by Billet, 1986. It has important consequences for cavitation damage and noise.

Clearly bubbly flows produce lifting forces on the boundaries when their shape determines a net vertical displacement of the flow. They also always produce surface drag even in the absence of viscous effects at the boundaries. This is another important consequence of the compressible nature of bubbly flows, which determines the transfer of energy from the flow velocity to the bubble motion under the influence of the perturbations induced by the wall. Indeed, as we shall see later, not all boundary shapes produce lift, but any deviation from a straight wall profile generates a drag force. As an example, the drag coefficient $C_D = 2D/\varepsilon\rho U_o^2$ based on the drag per unit depth D on a wall wave length in a semi-infinite bubbly flow is plotted in Fig. 12 for three values of the void fraction parameter $3\alpha_o U_o^2/\omega_B^2 R_o^2$. For increasing free stream velocities the drag is initially zero, reaches a maximum near the sonic condition and finally tends to zero in the super-resonant regime where compressibility effects asymptotically vanish. The lift on a wall wave length in the same flow is identically zero, since no net vertical displacement of the flow is produced by a full period of the wall profile.

Significant analogies exist between the results shown here for the case of bubbly flows over slender profiles and the the ones previously obtained for the linearized dynamics of clouds of bubbles [d'Agostino and Brennen, 1983]. In both flows the dispersive behaviour due to bubble dynamics effects is controlled by similar parameters, G^2 and λ^2, which depend on the bubble population and the excitation frequency. These parameters also determine the elliptic or

hyperbolic nature of the solution, the penetration of external disturbances and the occurrence of the natural mode shapes and frequencies of the flow.

Finally, as a concluding remark, it is easily verified that the above theory reduces (as expected) to the first order perturbation solutions for incompressible and homogeneous compressible flows in the limit for zero void fraction or free stream velocity and zero wall wave number, respectively.

6. RESULTS FOR A SINGLE, GAUSSIAN-SHAPED BUMP

We now consider a semi-infinite bubbly flow over a slender surface with a Gaussian-shaped profile $\eta(x) = \varepsilon \exp(-x^2/2a^2)$ of maximum height $\varepsilon \ll a$. The Fourier transform, as defined by equation (24), is: $H(k) = \sqrt{2/\pi}\varepsilon a e^{-k^2a^2/2}$. As shown earlier, the solution for this flow is expressed by the inverse Fourier integrals (25). When dissipative effects are included the integrands have no singularities and are readily computed. It is convenient also in this case to define characteristic parameters whose values are related to the importance of sonic and bubble resonance effects. By analogy with the solution for a harmonic profile we can anticipate that $2\pi/k$ will now be replaced by $2a$ and the relevant parameters in the case of a Gaussian bump are: $3\alpha_o a^2/\pi^2 R_o^2$ for the sonic condition and $(U_o\pi/a\omega_B)^2$ for the bubble resonance condition.

The bubble radius response at the wall ($y = 0$) is shown in Fig. 13 for $3\alpha_o a^2/\pi^2 R_o^2 = 1$ and for three values of the bubble resonance parameter, $(U_o\pi/a\omega_B)^2$. Note that for the lower value of the bubble resonance parameter the bubble radius response is essentially in phase with the expected behaviour of the pressure at the wall in the fully wetted flow case. Bubble inertial effects are only reflected in the small delay which makes the curve slightly asymmetric with respect to the plane $x = 0$. However, when $(U_o\pi/a\omega_B)^2 = 1$ bubble dynamic effects become more important and the bubbles no longer have the time to respond as in the previous case. The bubble radius simply goes through a minimum corresponding to the positive slope of the profile, followed by a maximum and a

slow return to the unperturbed free stream conditions. For the larger value of the bubble resonance parameter the bubble response is furtherly delayed and the bubbles are excited into damped oscillations which slowly subside further downstream.

The bubble radius response in the channel flow case is illustrated in Fig. 14 for $kb = \pi$, where the situation is modified by the presence of the internal flow modes of the system introduced by the finite spacing between the boundaries. For the lower value of the bubble resonance parameter the behaviour is similar to the semi-infinite flow case. For higher values of $(U_o\pi/a\omega_B)^2$ this similarity is only restricted to the early stages of the bubble radius response. Later the internal flow modes of the system are excited and they variously interact to produce the more complex oscillatory behaviour of the downstream portion of the flow.

The propagation of wall induced disturbances inside the semi-infinite flow over a Gaussian-shaped profile is illustrated in Fig. 15 which shows the bubble radius response at increasing distances from the wall: $y = 0$, $5a/\pi$ and $10a/\pi$. The values of the parameters $3\alpha_o a^2/\pi^2 R_o^2 = 1$ and $(U_o\pi/a\omega_B)^2 = 1$ have been chosen in order to make both compressibility and bubble resonance effects important in this case. Hence the attenuation is relatively small, while the time delay of the bubble radius response at increasing distances from the wall is significant. Also note the inhibiting action that the proximity of the wall plays on the amplitude of the bubble radius oscillations in the downstream part of the flow.

The pressure distribution at the wall in the semi-infinite flow configuration, shown in Fig. 16 for $(U_o\pi/a\omega_B)^2 = 1$ and for three values of the void fraction parameter $3\alpha_o a^2/\pi^2 R_o^2$, is similar to the bubble radius response, but exhibits a faster decay of the oscillations in the downstream region of the flow. Even a relatively small increase of the void fraction has a significant influence on the pressure distribution at the wall. In particular it is interesting to observe that

increasing the void fraction values moves the minimum pressure point downstream; hence one would expect the laminar separation point to be similarly displaced downstream in real viscous flows. This consequence of the compressibility of the bubble mixture may well be responsible for the observed delay and even suppression of separation in travelling bubble cavitating flows over headforms with increased bubble content [Gates, 1977]. The lift and drag coefficients, $C_L = 2L/\varepsilon\rho U_o^2$ and $C_D = 2D/\varepsilon\rho U_o^2$, generated by the above pressure distributions are illustrated in Fig. 17 and Fig. 18 as a function of the reduced frequency parameter $(U_o\pi/a\omega_B)^2$ for three values of the void fraction parameter $3\alpha_o a^2/\pi^2 R_o^2$. Here L and D are the lift and drag per unit depth on the wall profile. The behaviour of these coefficients is typical of compressible flows, with peaks near sonic conditions, followed by a rapid drop in the super-resonant regime, where only a thin layer of bubbles close to the boundary responds to the exitation.

7. LIMITATIONS

We now briefly examine the restrictions imposed to the previous theory by the various simplifying assumptions that have been made. Specifically we will discuss the limitations due to the introduction of the continuum model of the flow, to the use of the linear perturbation approach in deriving the solution, to the neglect of the relative motion between the phases and of the local pressure perturbations in the neighborhood of each individual bubble. In what follows we will refer to the wavy surface solution in the absence of damping, since it represents the most conservative case and the basis of the generalization to slender profiles of arbitrary shape.

The perturbation approach simply requires that $\varphi \ll 1$ in equation (14), a constraint that can be satisfied far from the sonic and bubble resonance conditions with proper choice of $k\varepsilon$ and $U_o/\omega_B R_o$. This is probably the most restrictive limitation of the present analysis.

For the continuum approach to be valid, the two phases must be minutely dispersed with respect to the shortest characteristic length of the flow, here either the wall wave length or the penetration of the wall disturbances in the y-direction. Hence the bubble equilibrium radius is required to satisfy the most restrictive of the two conditions: $kR_o \ll 1$ and $\Re(G)kR_o \ll 1$.

In order to estimate the error associated to the neglect of local pressure effects due to the dynamic response of each individual bubble, we consider the pressure perturbation experienced by one bubble as a consequence of the growth or collapse of a neighbor:

$$\Delta p = \rho \left\{ \frac{R}{s} \left[R \frac{D^2 R}{Dt^2} + 2 \left(\frac{DR}{Dt} \right)^2 \right] - \frac{R^4}{2s^4} \left(\frac{DR}{Dt} \right)^2 \right\} \tag{41}$$

where $s = O(R_o/\alpha_o^{1/3})$ is the average bubble spacing and $R = R_o(1+\varphi)$ is given by equation (16) or (20). To the same order of approximation used to develop the present analysis, comparison with the global pressure change expressed by equation (19) or (23) then shows that the local pressure perturbations are unimportant if:

$$\alpha_o^{1/3} \left| \frac{k^2 U_o^2/\omega_B^2}{1 - k^2 U_o^2/\omega_B^2} \right| \ll 1 \tag{42}$$

Far from bubble resonance regime, this condition is generally satisfied in low void fraction flows.

Finally, in order to assess the error introduced by the neglect of the relative velocity between the two phases, let us consider the equation of motion for a bubble of negligible mass [Voinov, 1973] with Stokes' viscous drag:

$$\frac{D\underline{v}}{Dt} - \frac{1}{3}\frac{D\underline{v}_B}{Dt} + \frac{1}{R}\frac{DR}{Dt}(\underline{v} - \underline{v}_B) = \frac{2\nu}{R^2}(\underline{v} - \underline{v}_B) \tag{43}$$

where $\underline{v}$ is the velocity of the liquid, $\underline{v}_B$ is the velocity of the bubble and ν is the kinematic viscosity of the liquid. Linearizing as before and assuming for both the relative velocity $\underline{v}_r = (\underline{v} - \underline{v}_B)$ and the velocity of the liquid a $2\pi/k$-periodic solution in the x-direction, one obtains:

$$\left| \frac{\underline{v}_r}{\underline{v} - \underline{v}_o} \right| = \frac{2}{\sqrt{1 + (6\nu/kR_o^2 U_o)^2}} \ll 1 \tag{44}$$

Hence we expect that relative motion effects are unimportant when $kR_o^2U_o/\nu \ll 1$. Using the continuum hypothesis $kR_o \ll 1$, this condition actually requires that $R_oU_o/\nu = O(1)$, which is already implicit in the assumption of Stoke's viscous drag. Thus the relative motion between the phases can be neglected as long as Stoke's expression correctly represents the drag on the bubbles. On the other hand, the above analysis does not allow us to assess to what extent this choice is justified. However, the more general simultaneous solution of the equations of motion for both phases, which we intend to discuss in a later publication, shows that the effect of relative motion is smaller than the above would suggest. It simply leads to a modified expression of the parameter G^2 involving a factor where unity is added to the void fraction multiplied by the square of the right hand side of equation (44). The presence of the void fraction multiplier further reduces the estimate of the effect of relative motion.

We now briefly dicuss the conditions for the effects of bubble dynamics and compressibility to become significant, showing that in general relatively high flow velocities and void fraction are required. As mentioned earlier, compressibility effects are expected to be important when the void fraction parameter $3\alpha_o a^2/\pi^2 R_o^2$ is of order unity or greater, i.e. when: $\alpha_o \geq O(R_o^2/a^2)$. For the validity of the present theory the typical dimension of the flow, a, must be much larger than the bubble size, R_o, say $a/R_o \geq 10$. Hence appreciable compressibility and bubble interaction effects can take place when the void fraction is of the order of 0.01 or larger, a situation which can easily occur in practice. On the other hand, bubble dynamics effects become important when the reduced frequency parameter $(U_o\pi/a\omega_B)^2$ is of order unity or larger, i.e. when $U_o \geq O(a\omega_B)$. Consider, for example, the case of air bubbles in water. Usually the surface tension has little influence on the bubble natural frequency, thus from equation (13): $\omega_B = O(\sqrt{p_o/\rho R_o^2})$, where for bubbles in equilibrium at about atmonspheric pressure $\sqrt{p_o/\rho} \simeq 10\,\mathrm{m/s}$. Hence bubble dynamic effects are significant when $U_o \geq O((a/R_o)\sqrt{p_o/\rho})$, which requires the flow velocity

to be of the order of 100 m/s or larger. Velocities of this magnitude are rare for objects moving inside liquids. The present linear theory therefore suggests that, unlike compressibility effects, important bubble dynamic phenomena are unlikely to be observed in most practical applications. However, the non-linear response of the bubbles is characterized by much larger time scales and therefore bubble dynamic effects may still occur in practice at substantially lower speeds than indicated by the present linear analysis.

8. CONCLUSIONS

As anticipated in the introduction and confirmed by the present theory, the dynamics of the bubbles is strongly coupled through the pressure and velocity fields with the overall dynamics of the flow. The presence of the bubbles is responsible for the the occurrence of bubble resonance phenomena and for the drastic modification of the sonic speed in the medium, which decreases and becomes dispersive (frequency dependent). The sonic and bubble resonance conditions lead in turn to the identification of three different flow regimes, here designated as subsonic, supersonic and super-resonant.

The inertial and resonance effects become important when the residence time of the bubbles is comparable to their typical response time: in the flows discussed here it is required that the reduced frequency parameters $(kU_o/\omega_B)^2$ for the flows with harmonic excitation or $(U_o\pi/a\omega_B)^2$ in the case of Gaussian excitation are of order unity. For this to happen relatively large flow velocities and bubble sizes are in general necessary.

Similarly, the effects related to the sonic regime become important and significantly separated from the bubble resonance condition when the void fraction parameter ($3\alpha_o/k^2R_o^2$ for the flow over a wavy wall with fixed geometry, $3\alpha_o U_o^2/\omega_B^2 R_o^2$ for the flow over a wavy wall with fixed free stream velocity, or $3\alpha_o a^2/\pi^2 R_o^2$ in the case of the Gaussian bump) is of order unity. For this to happen relatively large flow velocities and void fractions are in general necessary.

In the present work only the energy dissipation occurring in the dynamics of the bubbles has been considered, which represents the most important damping mechanism in bubbly flows. Additional contributions to the energy dissipation from the relative motion between the bubbles and the surrounding liquid can be included in the model, but their effects are expected to be small.

The results of this investigation reveal a number of qualitative effects which may be of importance in real cavitating flows around headforms or hydrofoils. First an increase in the population of nuclei or bubbles causes a substantial reduction of the amplitude of growth of the bubbles as they are convected through a low pressure region. We have already noted that such a phenomenon has been observed experimentally by Arakeri and Shanmuganathan, 1985, and by Billet, 1986. This in turn could substantially reduce the acoustic noise or damage potential. Secondly the compressibility of the flow produces a delay in the minimum pressure (and therefore in any laminar separation), a phenomenon noticed in the experiments of Gates, 1977. This shift in the pressure distribution can also generate drag and similar changes in the lift coefficient could be anticipated for lifting surfaces. It remains to be seen whether this could help explain the well-known changes in lift and drag which result when cavitation is present.

The present theory has been derived under fairly restrictive simplifying assumptions involving the flow geometry and the linearization of both the velocity field and the bubble dynamics. Therefore it is not expected to provide a quantitative description of the behaviour of steady bubbly flows over slender surfaces, except perhaps in the acoustical limit. Large bubble radius perturbations occur in most flows of practical interest; hence the most crucial limitation in the present paper is the linearization of the bubble dynamics, while the assumption of small velocity perturbations is likely to be more widely justified. If all the above linearizations were omitted only numerical solutions could be realistically attempted. However, if only the hypothesis of linear bubble dynamics is abandoned, the development of quasi-linear theories might be possible and would

have a much broader applicability.

Even the very simple geometry of the flows considered here can nevertheless provide an introduction to the study of flows of great technical interest. Flows with similar geometry occur in many fields of applied hydrodynamics such as the study of propellers, lifting surfaces, pump blades, and yet general theories have only been developed in the fully wetted and supercavitating cases. In these flows the above theory might shed some light on the behaviour of the lift, drag and moment coefficients of the profiles, on the influence of the presence of the bubbles on boundary layer development, flow separation and on other boundary viscous effects, on the problem of cavitation inception and its the correlation to the nuclei number distribution of the liquid, and on the possible choice of more suitable parameters and laws for cavitation scaling. Finally, other more direct applications include the production and propagation of noise in cavitating flows.

9. ACKNOWLEDGEMENTS

The authors would like to thank Cecilia Lin for her help in drawing the pictures. This work was supported by the Naval Sea System Command General Hydromechanics Research Program Administered by the David Taylor Naval Ship Research and Development Center under Contract No. N0014-75-C-0378, by the Office of Naval Research under contract No. N00014-83-K-0506 and by a Fellowship for Technological Research administered by the North Atlantic Treaty Organization - Consiglio Nazionale delle Ricerche, Italy, Competition No. 215.15/11 of 11.5.1982. Their support is gratefully aknowledged.

10. REFERENCES

Arakeri, V. H. and Acosta, A. J., 1973, "Viscous Effects in the Inception of Cavitation on Axisymmetric Bodies", ASME J. Fluid Eng., Vol. 95, p. 519.

Arakeri, V. H. and Shanmuganathan, V., 1985, "On the Evidence for the Effect of Bubble Interference on Cavitation Noise", J. Fluid Mech., Vol. 159, pp.

131-150.

Billet, M., 1986. Personal communication.

Carsternsen, E. L., and Foldy, L. L., 1947, "Propagation of Sound through a Liquid Containing Bubbles", J. Acoust. Soc. Am., Vol. 19, pp. 481-501.

d'Agostino, L. and Brennen, C. E., 1983, "On the Acoustical Dynamics of Bubble Clouds", ASME Cavitation and Multiphase Flow Forum, pp. 72-75.

d'Agostino, L., Brennen, C. E. and Acosta, A. J., 1984, "On the Linearized Dynamics of Two-Dimensional Bubbly Flows over Wave-Shaped Surfaces", ASME Cavitation and Multiphase Flow Forum, pp. 8-13.

Foldy, L. L. 1945, "The Multiple Scattering of Waves", Phys. Rev., Vol. 67, pp. 107-119.

Fox, S. E., Curley, S. R. and Larson, G. S., May 1955, "Phase Velocity and Absorption Measurements in Water Containing Air Bubbles", J. Acoust. Soc. Am., Vol. 27, No. 3, pp. 534-539.

Gates, E. M., 1977, "The Influence of Free Stream Turbulence, Free Stream Nuclei Population and a Drag Reducing Polymer on Cavitation Inception on Two Axisymmetric Bodies", Ph. D. thesis, Calif. Inst. of Tech.

Knapp, R. T., Daily, J. W. and Hammit, F. G., 1970, "Cavitation", McGraw Hill.

Macpherson, J. D., 1957, "The Effect of Gas Bubbles on Sound Propagation in Water", Proc. Phys. Soc. London, Vol. 70 B, pp. 85-92.

Muir, J. F. and Eichhorn, 1963, "Compressible Flow of an Air-Water Mixture through a Vertical Two-Dimensional Converging-Diverging Nozzle", Proc. Heat Trans., Fluid Mech. Inst., Standford, Standford University Press.

Noorddzij L., 1973, "Shock Waves in Mixtures of Liquids and Air Bubbles", Doctoral thesis, Technische Hogeschool, Twente, Netherlands.

Noorddzij L. and van Wijngaärden, L., 1974, "Relaxation Effects, Caused by Relative Motion, on Shock Waves in Gas-Bubble/Liquid Mixtures", J. Fluid Mech., vol. 66, part 1, pp. 115-143.

Plesset, M. S. and Prosperetti, A., 1977, "Bubble Dynamics and Cavitation", Ann. Rev. Fluid. Mech., Vol. 9, pp. 145-185.

Prosperetti, A., 1984, "Bubble Phenomena in Sound Fields: Part One", Ultrasonics, March 1984, pp. 69-78.

Silberman, E., 1957, "Sound Velocity and Attenuation in Bubbly Mixtures Measured in Standing Wave Tubes", J. Acoust. Soc. Am., Vol. 18, No. 8, August, pp. 925-933.

Tangren, R. F., Dodge, C. H., and Seifert, H. S., 1949, "Compressibility Effects in Two-Phase Flows", J. Appl. Phys., vol 20, pp. 637-645.

Voinov, O. V., 1973, "Force Acting on a Sphere in an Inhomogeneous Flow of an Ideal Incompressible Fluid", Plenum Publishing Coorp., transl. from Zhurnal Prikladnoi Mekhaniki i Tekhnicheskoi Fiziki, No. 4, pp. 182-184, July-August 1973.

van Wijngaärden, L., 1964, "On the Collective Collapse of a Large Number of Gas Bubbles in Water", Proc. 11th Int. Congr. Appl. Mech., Springer-Verlag, Berlin, pp. 854-861.

van Wijngaärden, L., 1968, "On the Equations of Motion of Mixtures of Liquid and Gas Bubbles", J. Fluid Mech., Vol. 33, part 3, pp. 465-474.

van Wijngaärden, L., 1972, "One-Dimensional Flow of Liquids Containing Small Gas Bubbles", Ann. Rev. Fluid. Mech., Vol. 4, pp. 369-396.

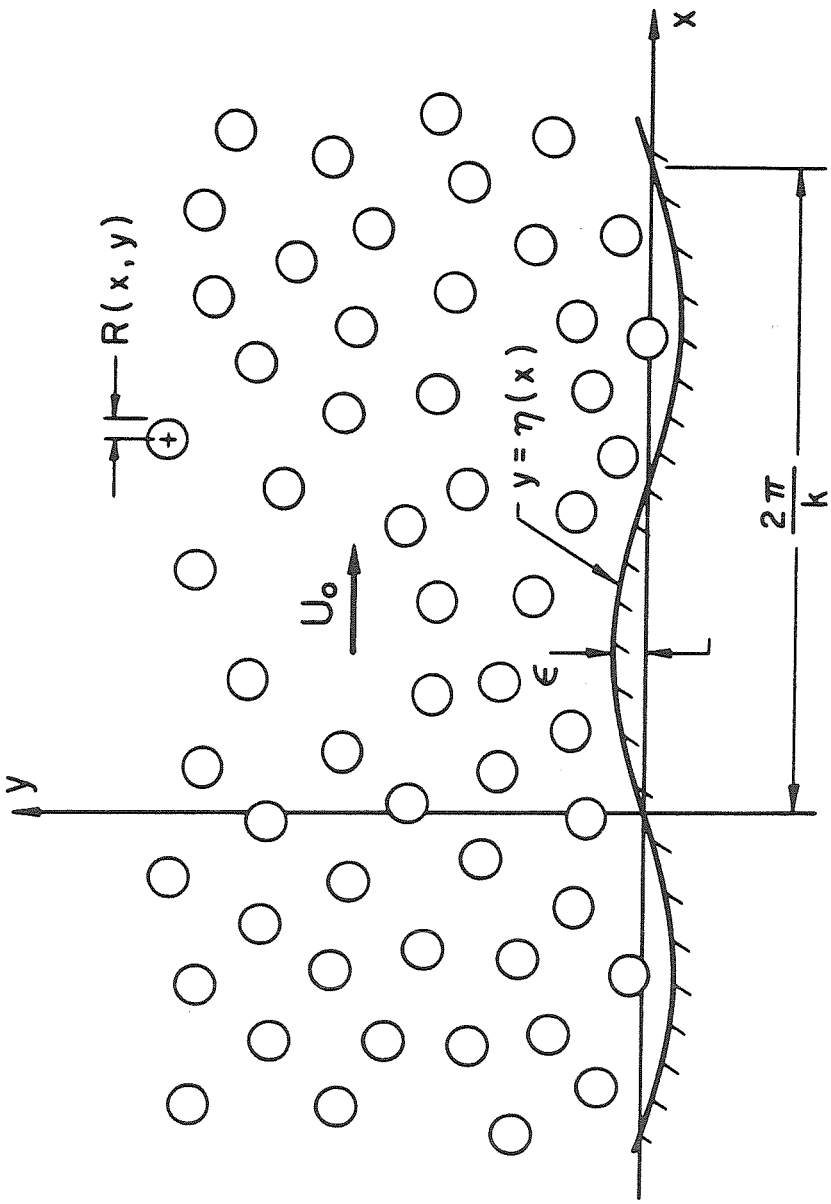

Figure 1. Schematic of a bubbly liquid flow over a wave-shaped surface.

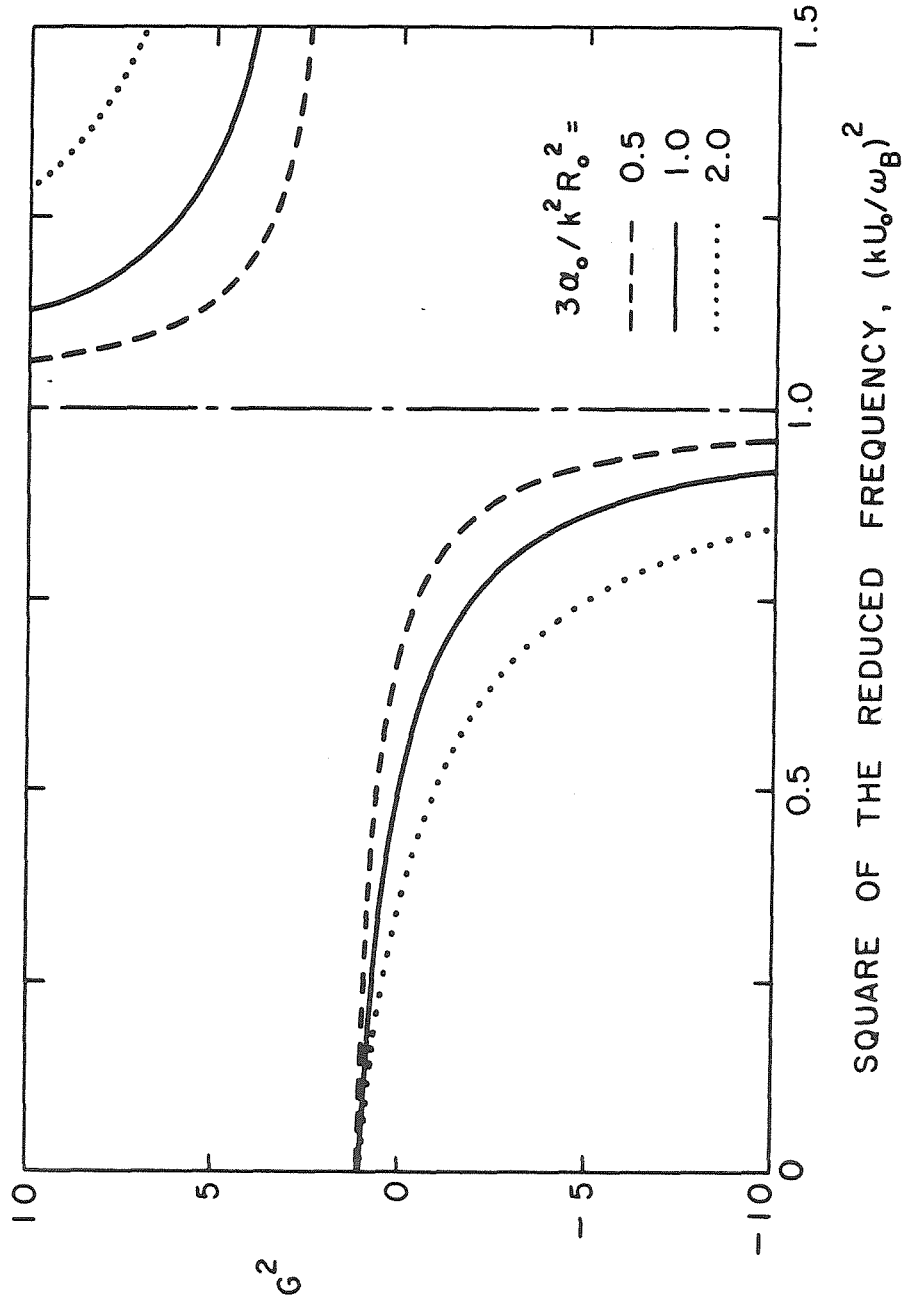

Figure 2. Parameter G^2 v/s the square of the reduced frequency, $(kU_o/\omega_B)^2$, for different values of $3\alpha_o/k^2R_o^2 = 0.5$ (broken line), 1 (solid line) and 2 (dotted line).

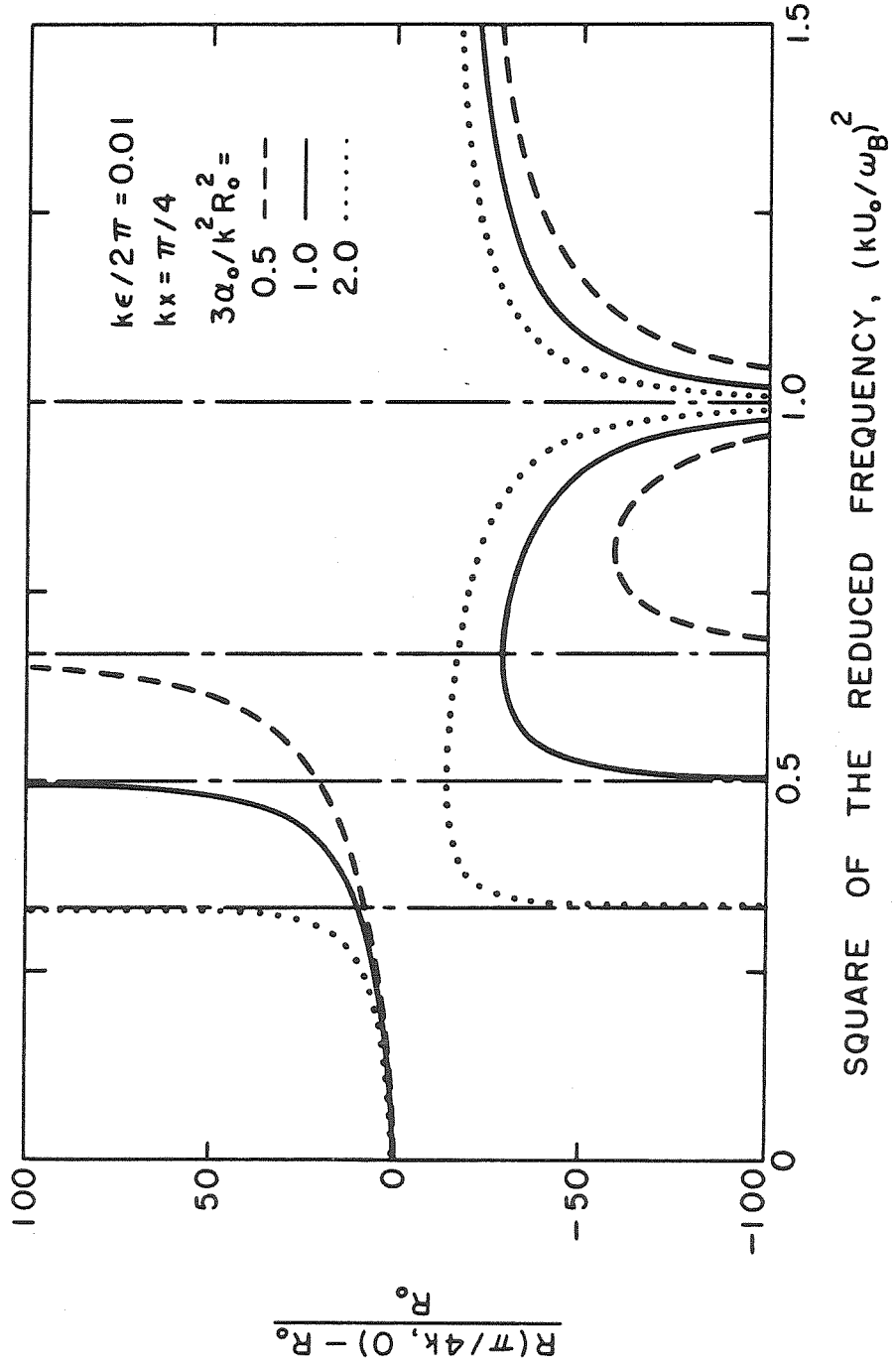

Figure 3. Response of a semi-infinite undamped bubbly flow over a wave-shaped wall as a function of the square of the reduced frequency, $(kU_o/\omega_B)^2$. Normalized amplitudes of the bubble radius oscillations at the wall ($kx = \pi/4$ and $y = 0$) are shown for different values of the parameter $3\alpha_o/k^2R_o^2 = 0.5$ (broken line), 1 (solid line) and 2 (dotted line).

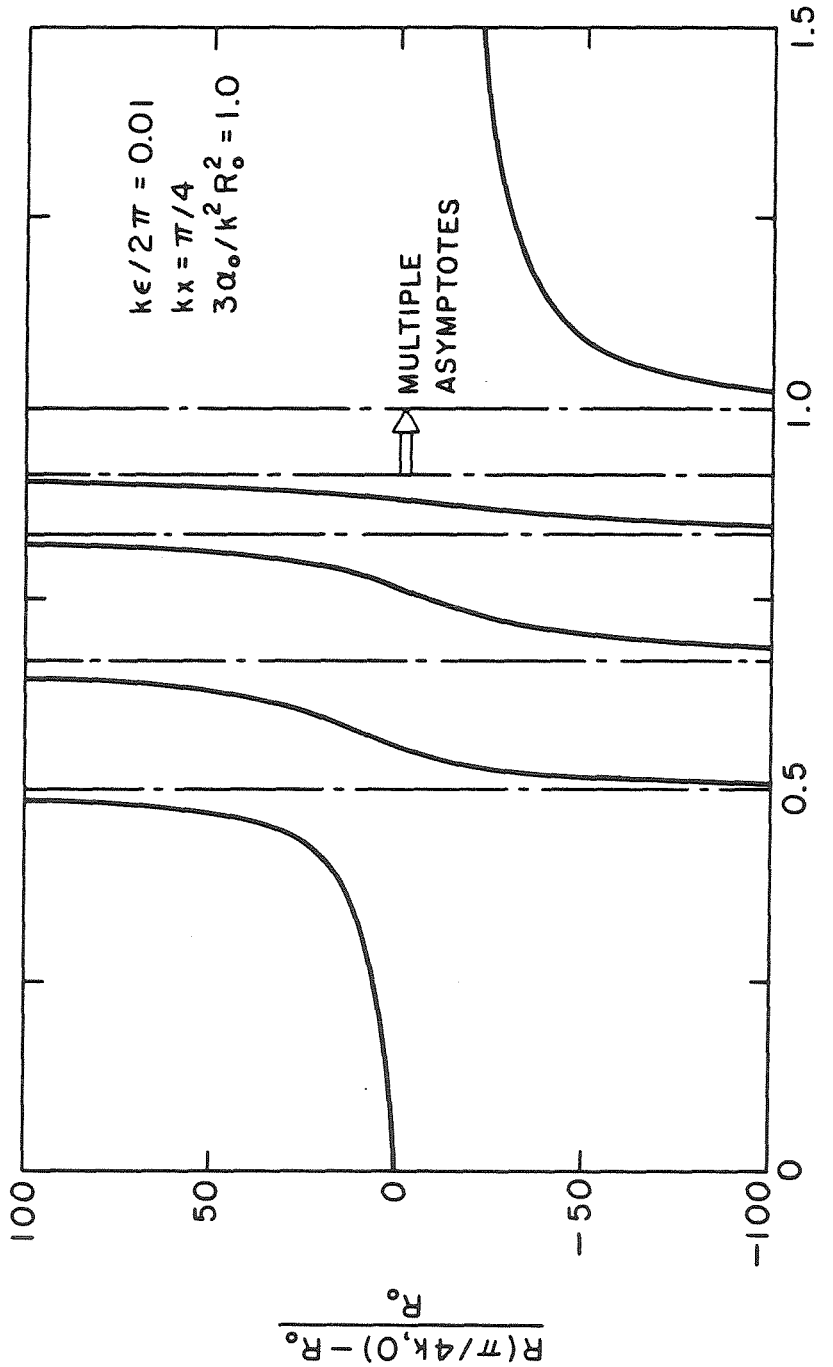

Figure 4. Response of an undamped bubbly flow in a symmetric wavy wall channel as a function of the square of the reduced frequency, $(kU_o/\omega_B)^2$. Normalized amplitudes of the bubble radius oscillations at the wall ($kx = \pi/4$ and $y = 0$) are shown for $3\alpha_o/k^2R_o^2 = 1$ and $kb = \pi$.

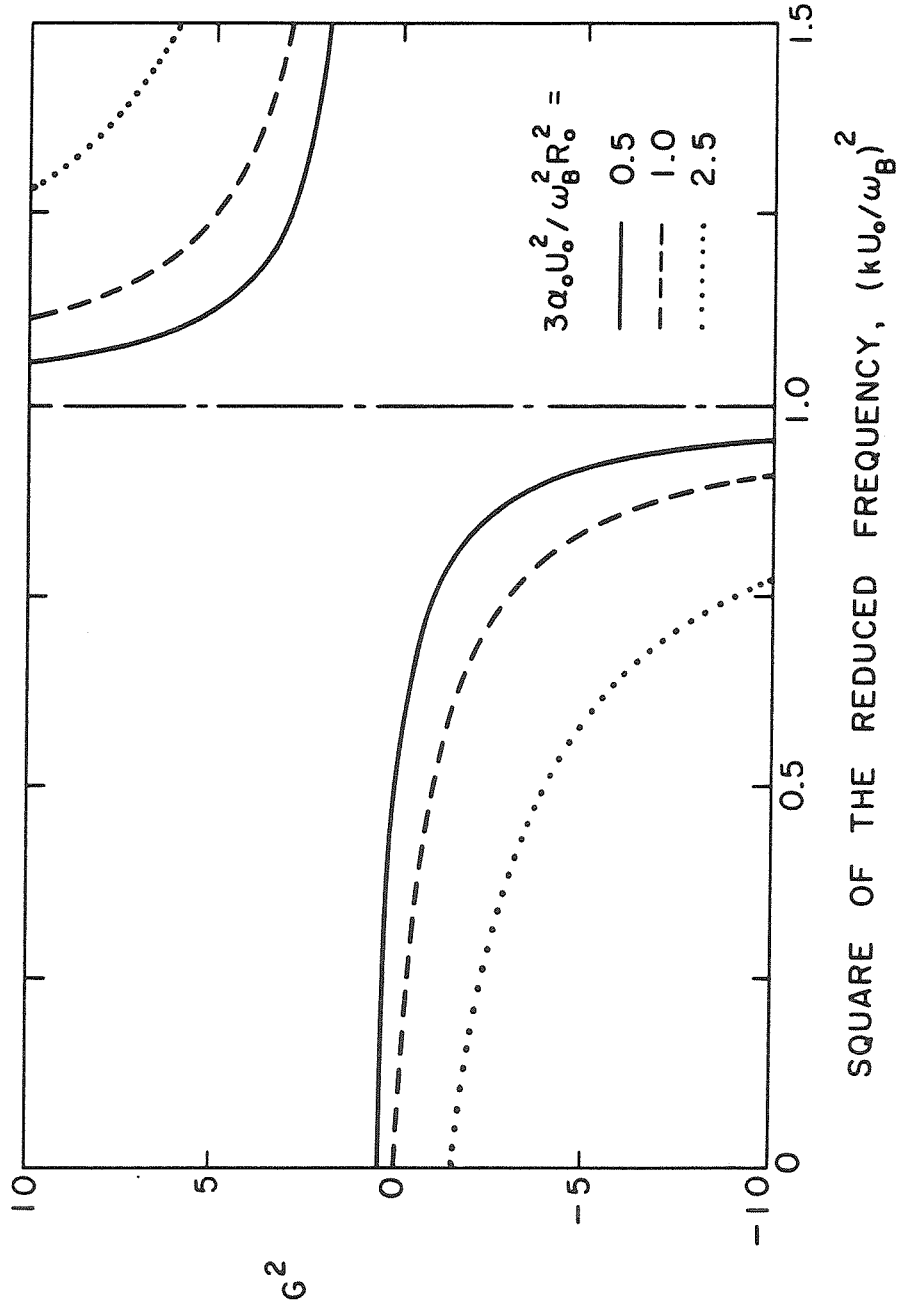

Figure 5. Parameter G^2 v/s the square of the reduced frequency, $(kU_o/\omega_B)^2$, for different values of $3\alpha_o U_o^2/\omega_B^2 R_o^2 = 0.5$ (solid line), 1 (broken line) and 2.5 (dotted line).

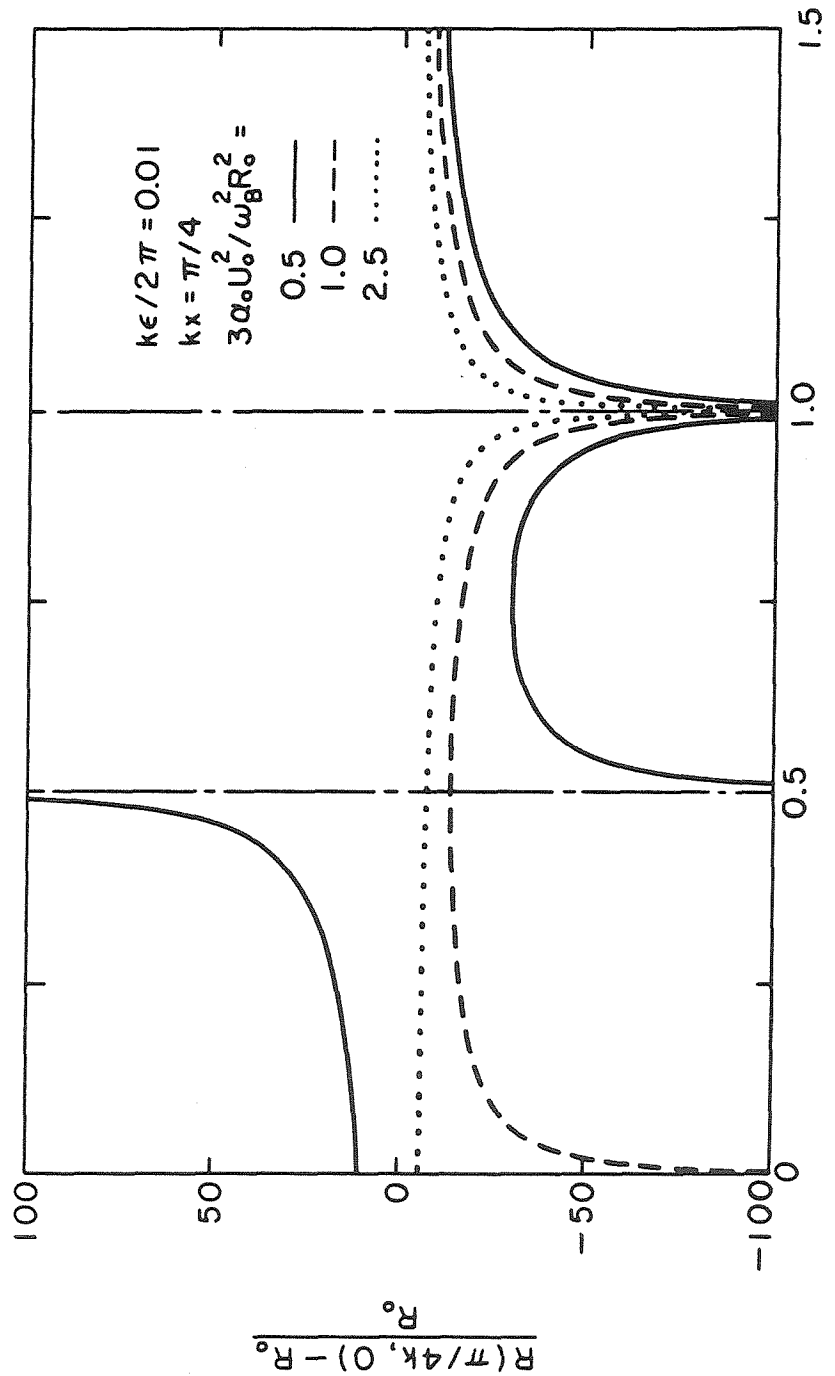

Figure 6. Response of a semi-infinite undamped bubbly flow over a wave-shaped wall as a function of the square of the reduced frequency, $(kU_o/\omega_B)^2$. Normalized amplitudes of the bubble radius oscillations at the wall ($kx = \pi/4$ and $y = 0$) are shown for different values of the parameter $3\alpha_o U_o^2/\omega_B^2 R_o^2 = 0.5$ (solid line), 1 (broken line) and 2.5 (dotted line).

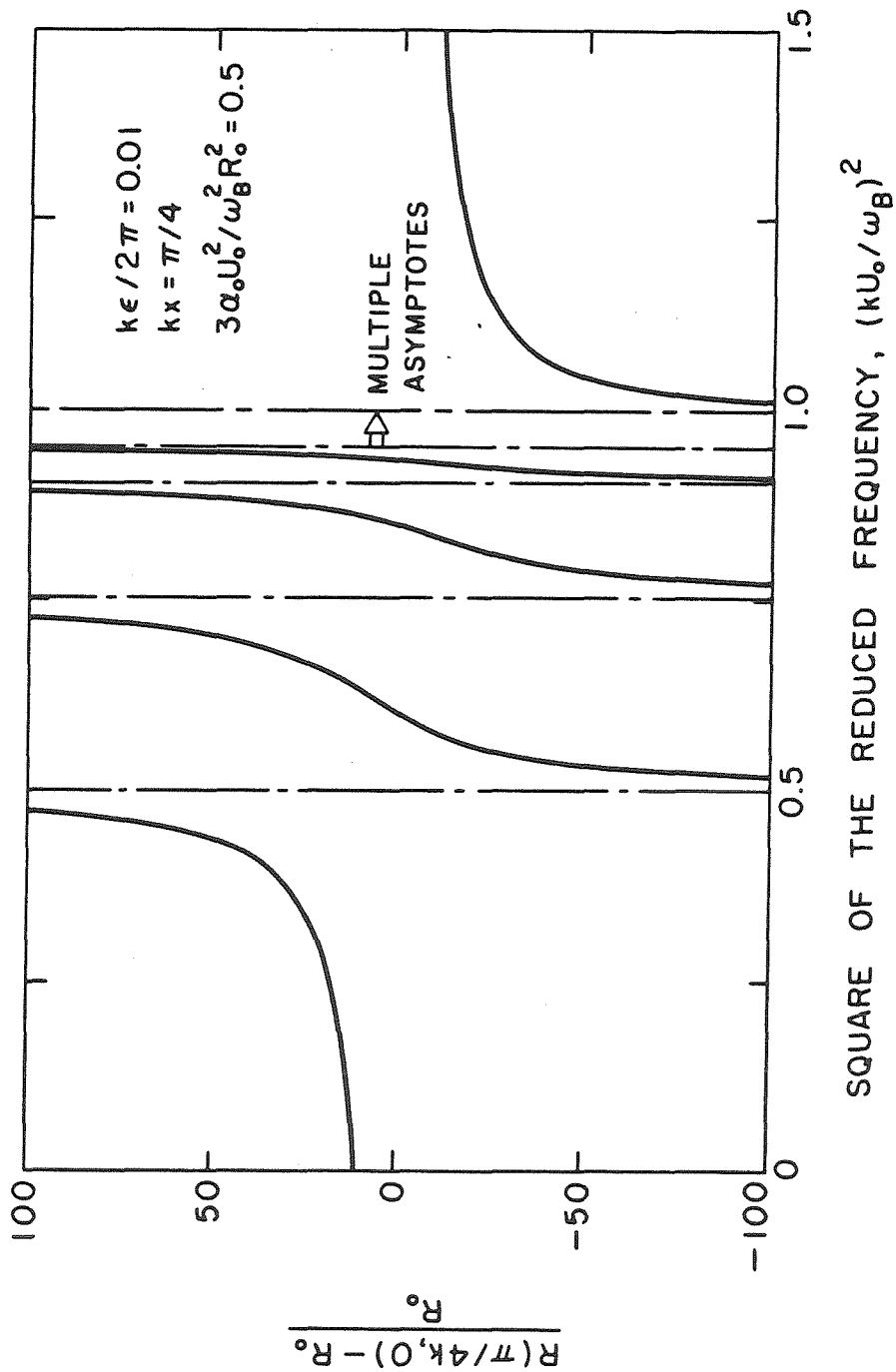

Figure 7. Response of an undamped bubbly flow in a symmetric wavy wall channel as a function of the square of the reduced frequency, $(kU_o/\omega_B)^2$. Normalized amplitudes of the bubble radius oscillations at the wall ($kx = \pi/4$ and $y = 0$) are shown for different values of the parameter $3\alpha_o U_o^2/\omega_B^2 R_o^2 = 0.5$ and $kb = \pi$.

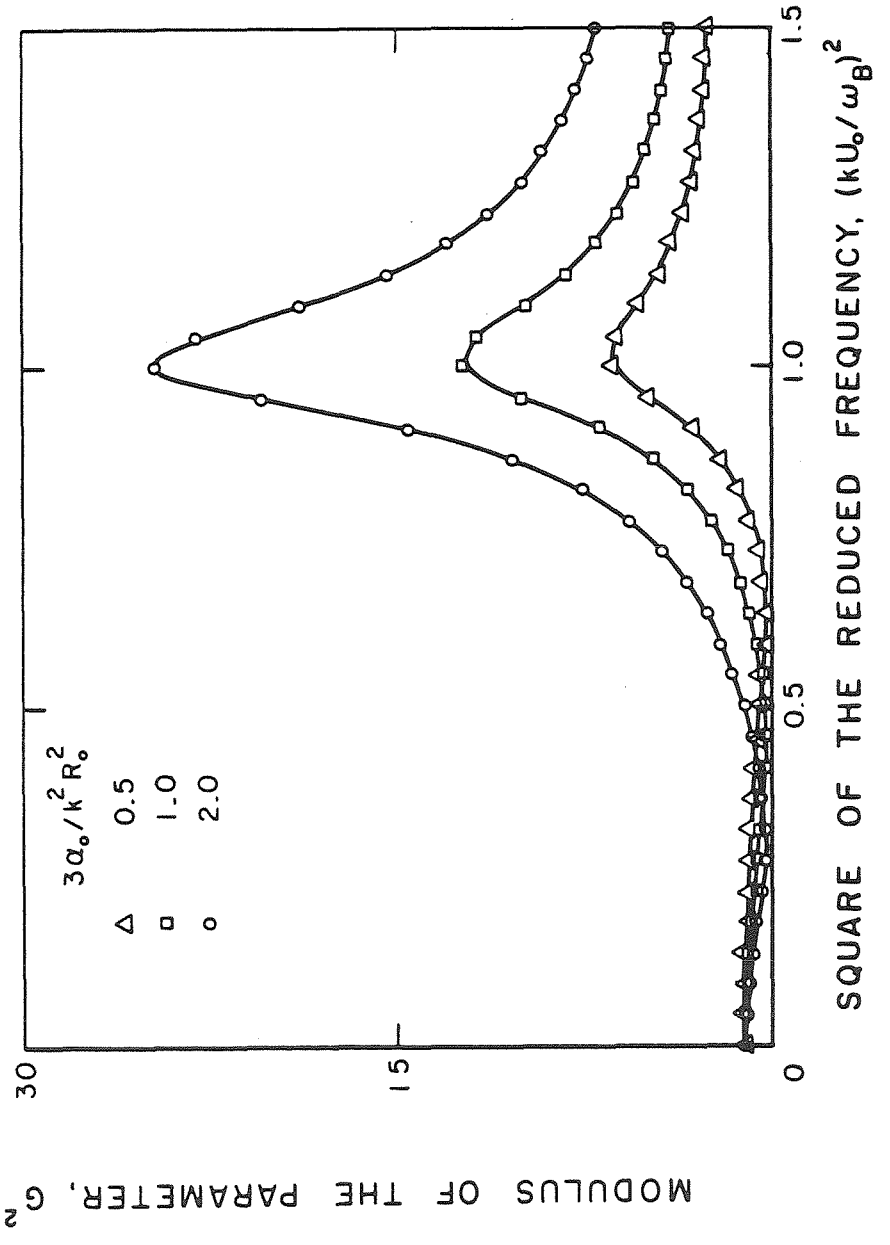

Figure 8. Modulus of the parameter G^2 v/s the square of the reduced frequency, $(kU_o/\omega_B)^2$, for different values of $3\alpha_o/k^2R_o^2 = 0.5$ (triangles), 1 (squares) and 2 (circles).

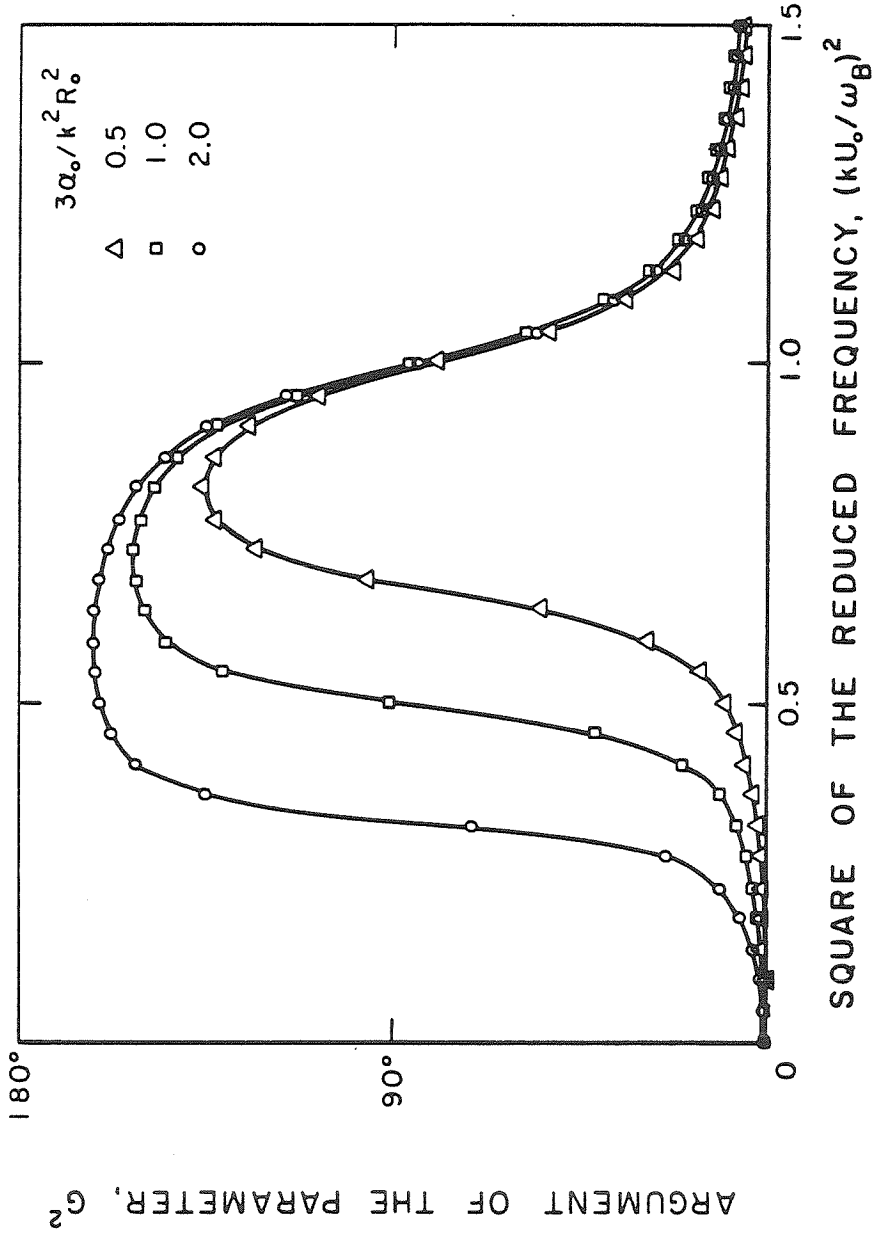

Figure 9. Argument of the parameter G^2 v/s the square of the reduced frequency, $(kU_o/\omega_B)^2$, for different values of $3\alpha_o/k^2R_o^2 = 0.5$ (triangles), 1 (squares) and 2 (circles).

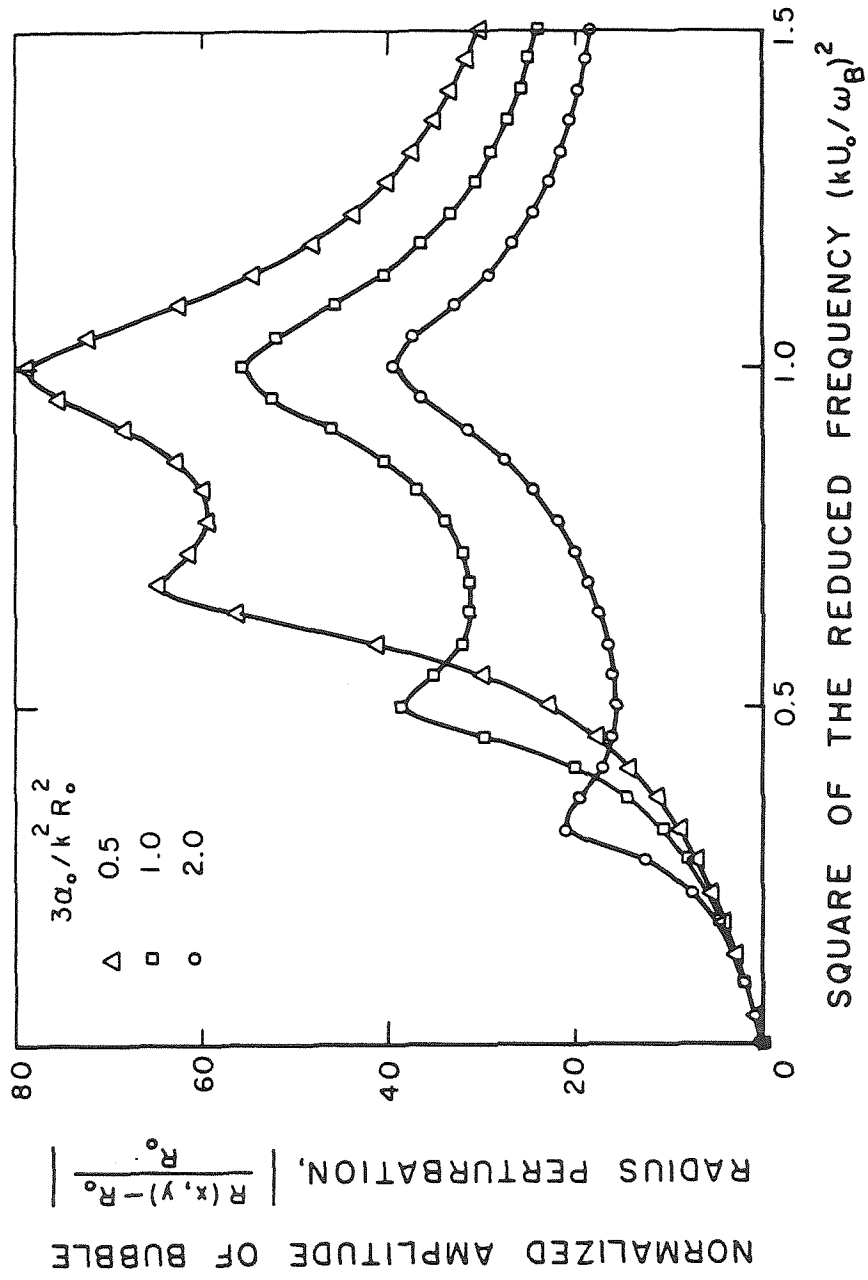

Figure 10. Response of a semi-infinite damped bubbly flow over a wave-shaped wall as a function of the square of the reduced frequency, $(kU_o/\omega_B)^2$. Normalized amplitudes of the bubble radius oscillations at the wall ($y = 0$) are shown for different values of the parameter $3\alpha_o/k^2R_o^2 = 0.5$ (triangles), 1 (squares) and 2 (circles).

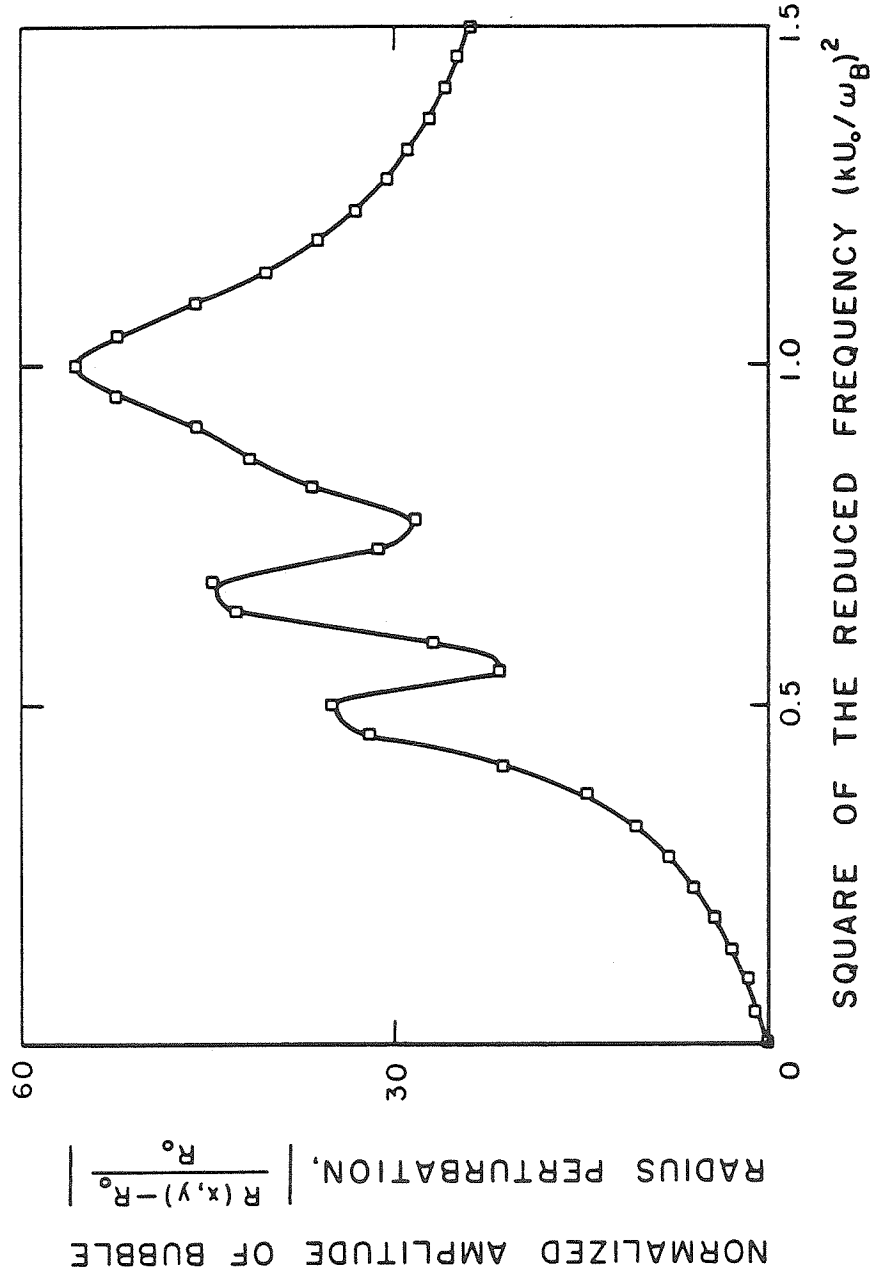

Figure 11. Response of a damped bubbly flow in a symmetric wavy wall channel as a function of the square of the reduced frequency, $(kU_o/\omega_B)^2$. Normalized amplitudes of the bubble radius oscillations at the wall ($y = 0$) are shown for $3\alpha_o/k^2R_o^2 = 1$ and $kb = \pi$.

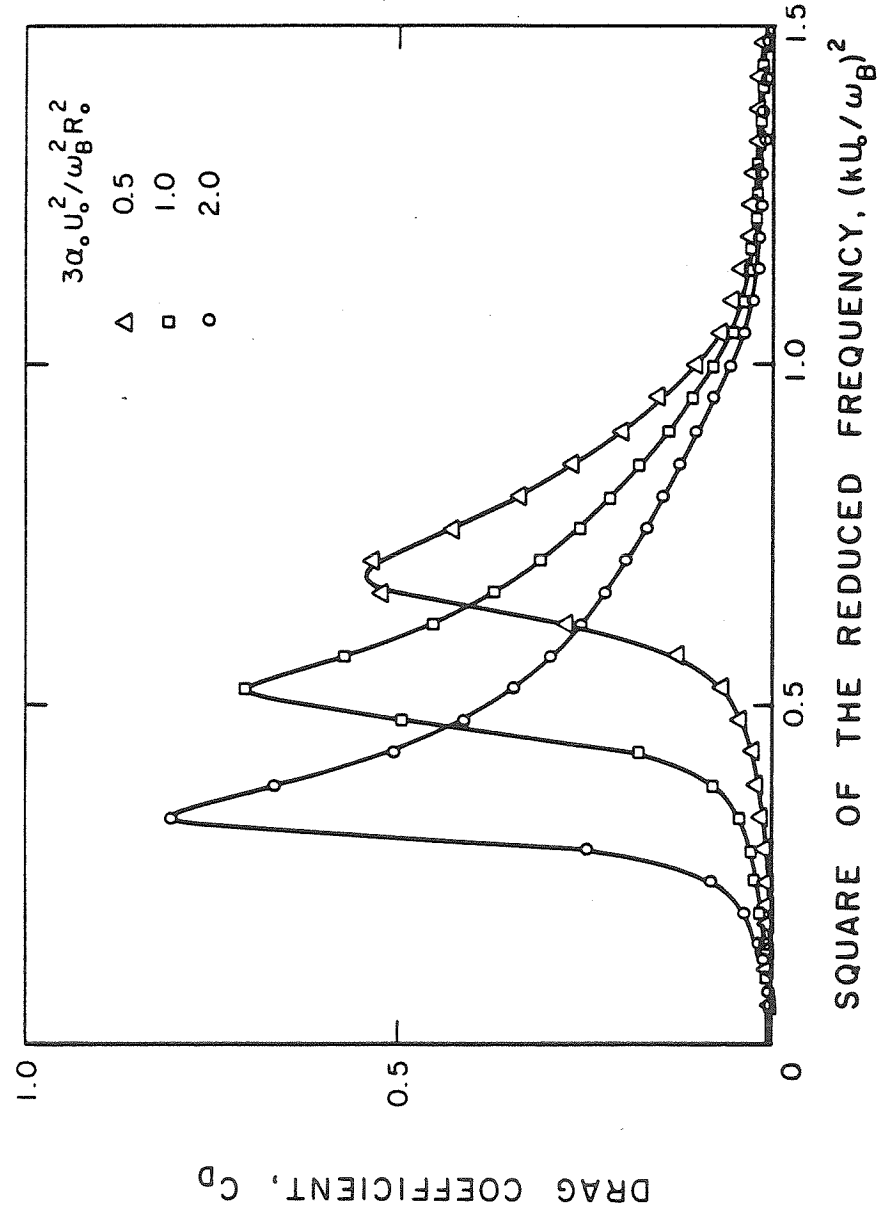

Figure 12. Drag Coefficient $C_D = 2D/\varepsilon\rho U_o^2$ in a semi-infinite damped bubbly flow over a wave-shaped wall as a function of the square of the reduced frequency, $(kU_o/\omega_B)^2$ for different values of the parameter $3\alpha_o U_o^2/\omega_B^2 R_o^2 = 0.5$ (triangles), 1 (squares) and 2 (circles).

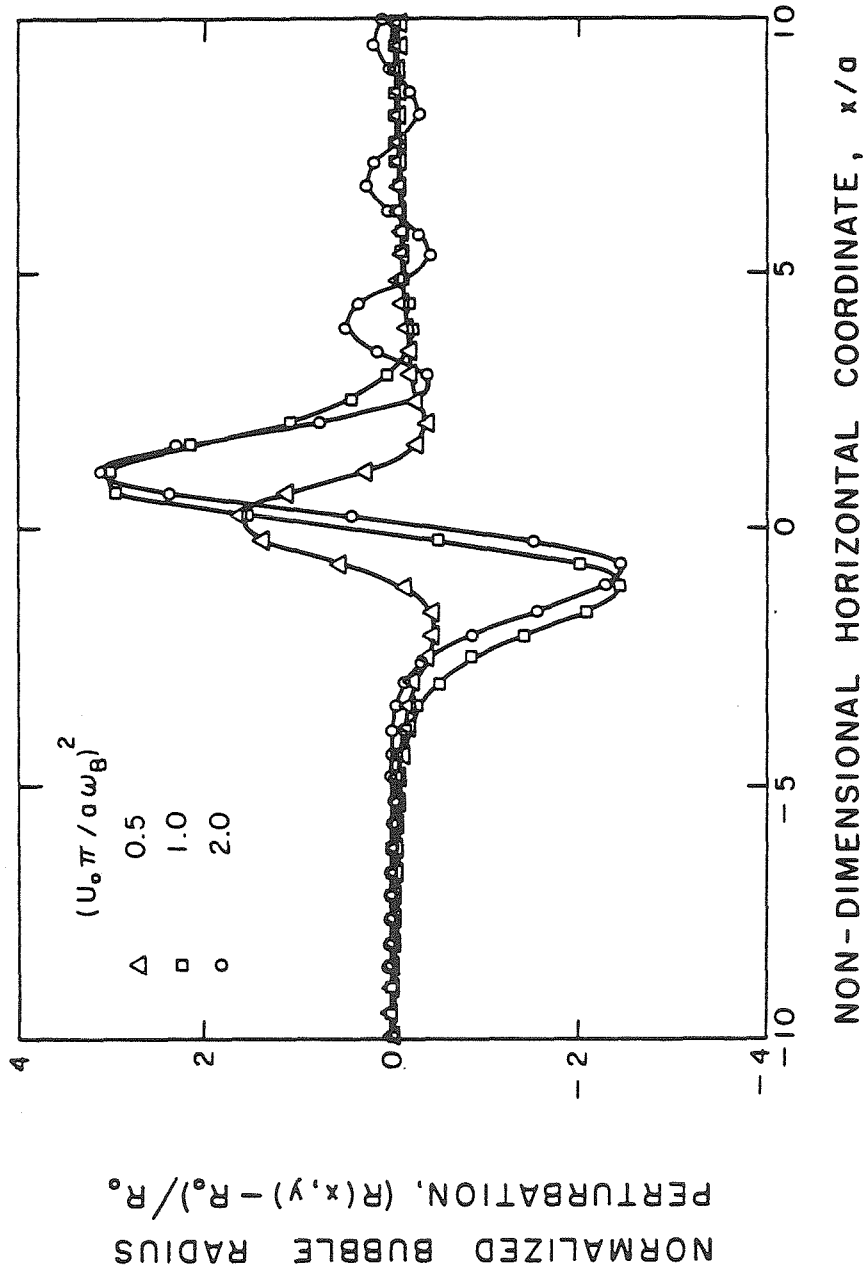

Figure 13. Response of a damped semi-infinite bubbly flow over a Gaussian-shaped profile as a function of the non-dimensional horizontal coordinate, x/a. Normalized amplitudes of the bubble radius oscillations at the wall ($y = 0$) are shown for $3\alpha_o a^2/\pi^2 R_o^2 = 1$ and for $(U_o\pi/a\omega_B)^2 = 0.5$ (triangles), 1 (squares) and 2 (circles).

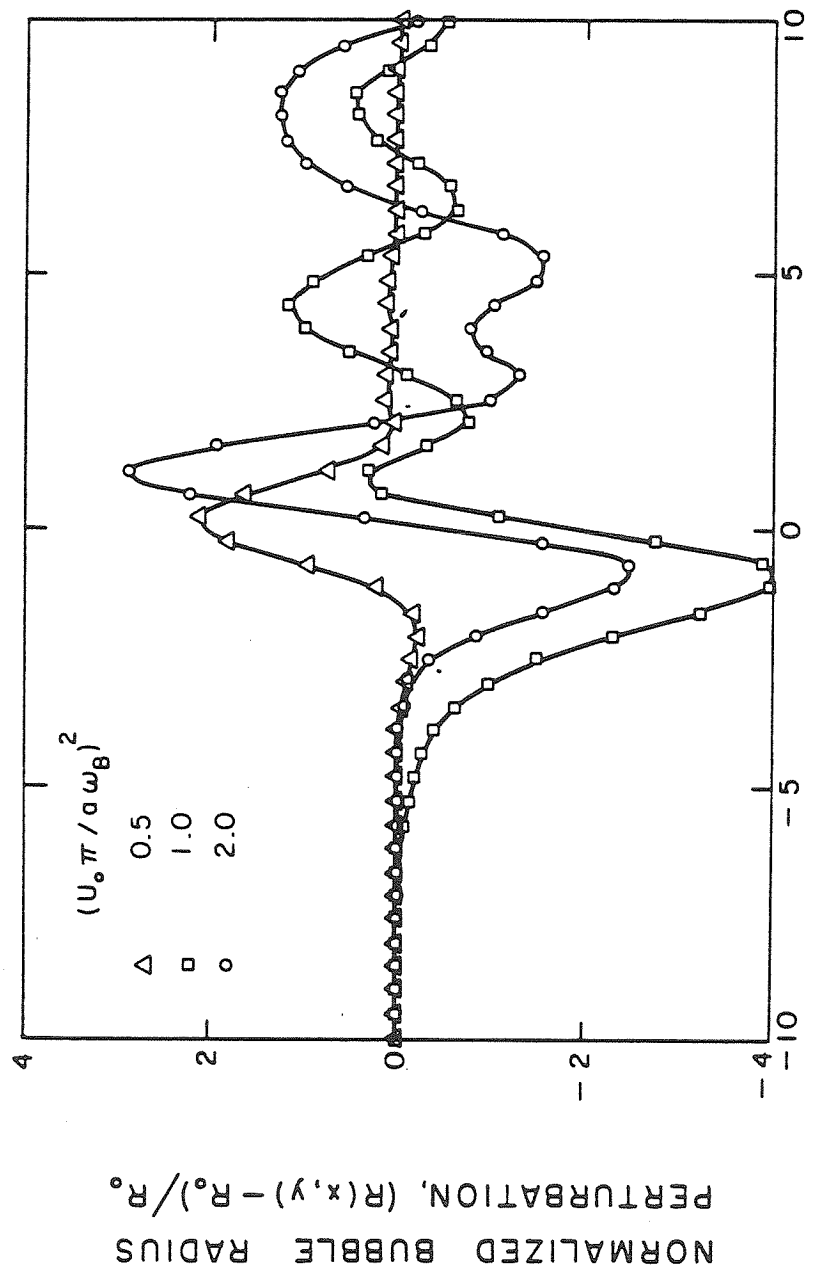

Figure 14. Response of a damped bubbly flow in a symmetric channel with Gaussian-shaped profile as a function of the non-dimensional horizontal coordinate, x/a. Normalized amplitudes of the bubble radius oscillations at the wall ($y = 0$) are shown for $3\alpha_o a^2/\pi^2 R_o^2 = 1$, $kb = \pi$ and for $(U_o\pi/a\omega_B)^2 = 0.5$ (triangles), 1 (squares) and 2 (circles).

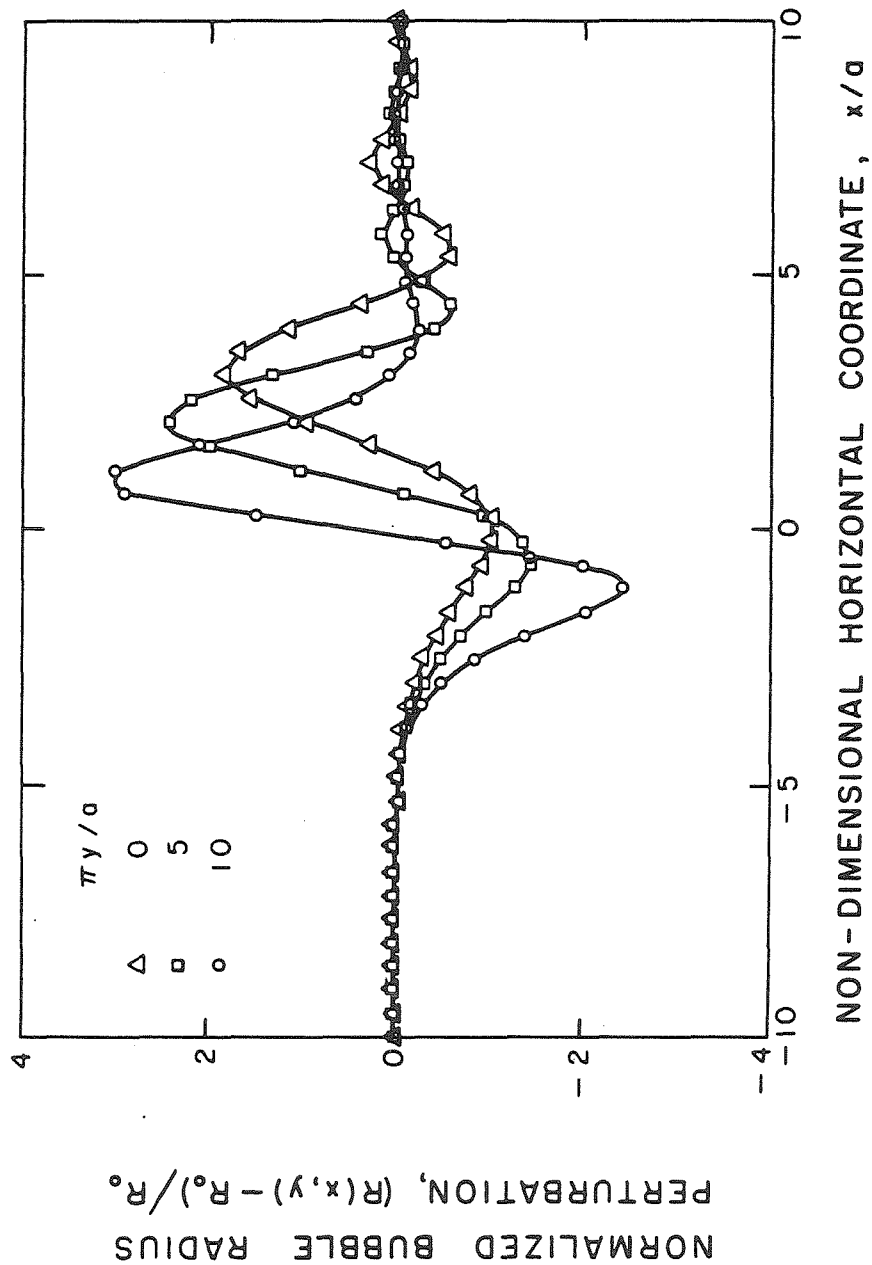

Figure 15. Response of a damped semi-infinite bubbly flow over a Gaussian-shaped profile as a function of the non-dimensional horizontal coordinate, x/a. Normalized amplitudes of the bubble radius oscillations at various distances from the wall are shown for $3\alpha_o a^2/\pi^2 R_o^2 = 1$, $kb = \pi$, $(U_o\pi/a\omega_B)^2 = 1$ and $\pi y/a = 0$ (triangles), 5 (squares) and 10 (circles).

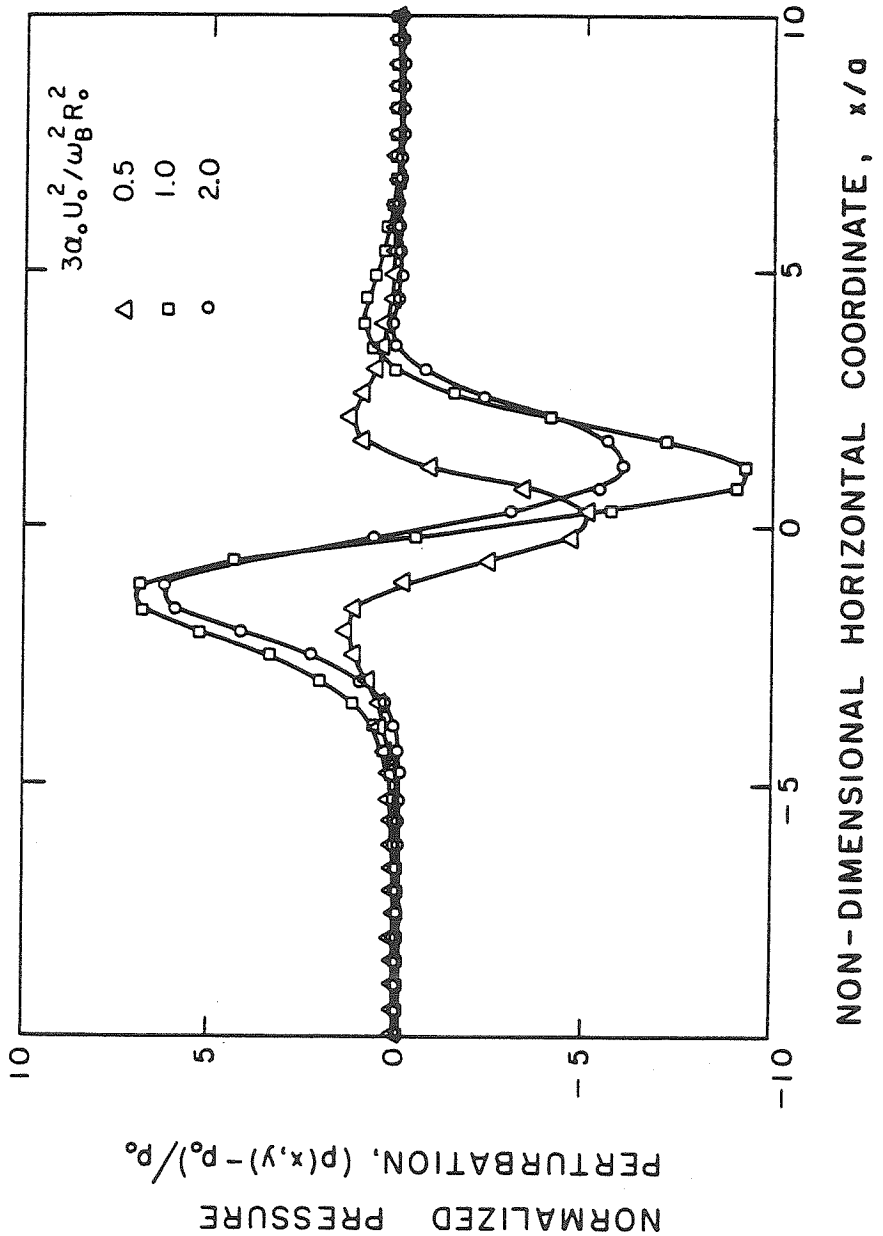

Figure 16. Response of a damped semi-infinite bubbly flow over a Gaussian-shaped profile as a function of the non-dimensional horizontal coordinate, x/a. Normalized amplitudes of the pressure perturbation at the wall $y = 0$ is shown for $(U_o\pi/a\omega_B)^2 = 1$ and for three different values of the parameter $3\alpha_o U_o^2/\omega_B^2 R_o^2 = 0.5$ (triangles), 1 (squares) and 2 (circles).

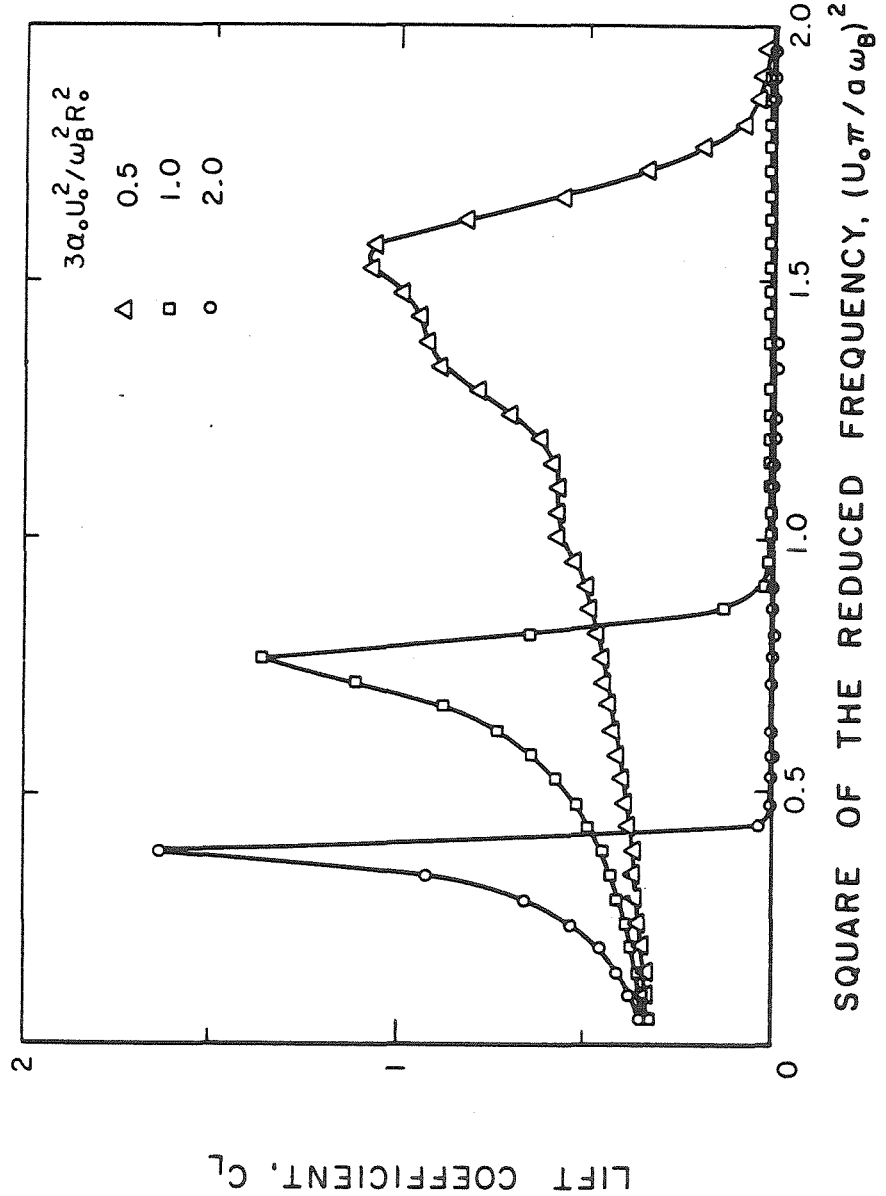

Figure 17. Lift Coefficient $C_L = 2L/\varepsilon\rho U_o^2$ in a semi-infinite damped bubbly flow over a Gaussian-shaped profile as a function of the reduced frequency parameter $(U_o\pi/a\omega_B)^2$ for three different values of the parameter $3\alpha_o U_o^2/\omega_B^2 R_o^2 =$ 0.5 (triangles), 1 (squares) and 2 (circles).

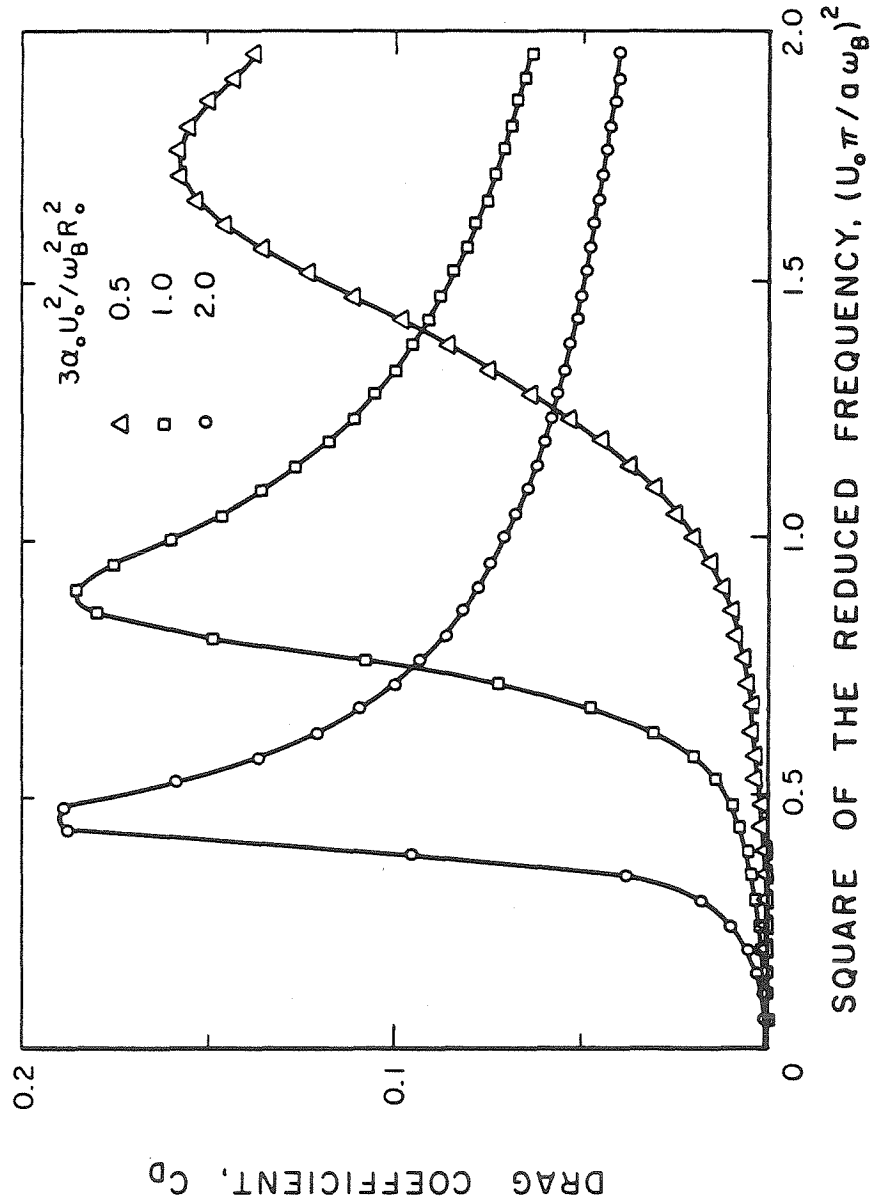

Figure 18. Drag Coefficient $C_D = 2D/\varepsilon\rho U_o^2$ in a semi-infinite damped bubbly flow over a Gaussian-shaped profile as a function of the reduced frequency parameter $(U_o\pi/a\omega_B)^2$ for three different values of the parameter $3\alpha_o U_o^2/\omega_B^2 R_o^2 =$ 0.5 (triangles), 1 (squares) and 2 (circles).